Author:
Reyes Paredes, David A

Title:
Low Cost Millimetre Wave Over-the-Air Testing Method For 5G and Beyond

Low Cost Millimetre Wave Over-the-Air Testing Method For 5G and Beyond

By

DAVID ARTURO REYES PAREDES

Department of Electrical and Electronic Engineering
UNIVERSITY OF BRISTOL

A dissertation submitted to the University of Bristol in accordance with the requirements of the degree of DOCTOR OF PHILOSOPHY in the Faculty of Engineering.

SEPTEMBER 2020

Abstract

In order to deliver the high capacity and throughput goals for 5G and beyond wireless connectivity, the effective use of Millimetre Wave (mmWave) spectrum is necessary. When compared to sub-6 GHz spectrum, these higher frequencies incur greater attenuation due to path loss and blockages, necessitating the use of directional antennas at both ends of the communications link. These are most likely to be implemented by means of an antenna array and beamformer in a highly integrated form within the RF transceiver. In such compact devices, antenna connectors are typically not available, thus negating the use of connective testing methodologies. Further, the mmWave operational environments synonymous with 5G New Radio (NR), are known to be highly dynamic in both spatial and temporal domains, hence the need for effective low cost mmWave Over-the-Air (OTA) testing for both product development, optimisation and compliance testing.

The novel millimetre wave OTA architecture described herein, importantly facilitates the excitation of the Device Under Test (DUT) from multiple dynamic angles of illumination, thus representing realistic operating conditions for 5G NR, as well as the handover operation between multiple access points (APs). The method exploits the reflective properties of the ellipse, overcoming the pin-point focal regions by means of multiple discrete plane reflectors configured on an ellipsoidal frame. The evolved architecture offers a test zone commensurate with integrated mmWave antennas and beamformers as well as compliance with the testing specifications of the 3GPP standardisation body. The research presented is based on theoretical analysis and ray tracing to develop the highly novel solution, culminating with a series of practical measurements.

The technique developed offers a low-cost novel solution for testing devices operating at mmWaves frequencies (e.g. 28 GHz) with screen size of up to 7 inches ($\approx$ 18 cm). The laboratory-based prototype offers multi-source excitation and a test zone volume of 20 cm by 20 cm by 20 cm. The main advantage of this method is that the multiple signals illuminating the DUT can be generated from a single location by an individual two-dimensional (2D) phase antenna array conformed by multiple sub-arrays. To mimic real link conditions the feeder antenna must be connected to a base station emulator in order to stimulate the DUT with the test signals. If required, an optional channel emulator can create temporal, and frequency fading conditions. With a 2D array facet, it is possible to electronically beam steer the signals in both azimuth and elevation from the source point. The signals will be redirected by means of one or more reflectors towards the DUT, thereby creating a 3D spatially addressable stimulus. This architecture can be readily enhanced to improve the characteristics of the test zone through the use of specially shaped reflector, active reflectarrays or active metasurfaces.

Dedication and acknowledgements

To my wife Karen, my daughter Isabel, my parents Eugenio and Alicia and my brother Paul for their untiring love and support.

I would like to express my deepest gratitude to Prof. Mark Beach, Dr. Moray Rumney and Dr. Geoffrey Hilton for the encouragement, assistance and guidance and whose knowledge and expertise were extensively shared for the success of this thesis.

I would like to thank to Keysight Technologies Inc, especially to Roger Nichols and his team for giving me the opportunity of developing this project in partnership with the company and the multiple occasions given to acquire and share the knowledge that resulted from this research.

My special thanks to the Ecuadorian Government that through the National Secretariat of Science, Technology and Innovation (SENESCYT) funded my studies through the Scholarship Program "Convocatoria Abierta 2014".

This work was supported by the Engineering and Physical Sciences Research Council [grant numbers EP/I028153/1 and EP/L016656/1] and the University of Bristol

AUTHOR'S DECLARATION

I declare that the work in this dissertation was carried out in accordance with the requirements of the University's Regulations and Code of Practice for Research Degree Programmes and that it has not been submitted for any other academic award. Except where indicated by specific reference in the text, the work is the candidate's own work. Work done in collaboration with, or with the assistance of, others, is indicated as such. Any views expressed in the dissertation are those of the author.

SIGNED: ..... DATE: .....

TABLE OF CONTENTS

List of Tables

Table **Page**

List of Figures

List of Abbreviations

2D	two-dimensional
2G	2nd Generation of mobile communication
3D	three-dimensional
3G	3rd Generation of mobile communication
3GPP	The 3rd Generation Partnership Project
4G	4th Generation of mobile communication LTE
5G	5th Generation of mobile communication
AAoA	Azimuth Angle of Arrival
AAoD	Azimuth Angle of Departure
AAS	Active Antennas Systems
AC	Anechoic Chamber
ACLR	adjacent channel leakage ratio
AoA	Angle of Arrival
AoD	Angle of Departure
ASA	Angular Spread Arrival
ASD	Angular spread of Departure
BLER	Block Error Rate
BS	Base Station
CATR	Compact Antenna Test Range
CDMA	Code Division Multiple Access
CE	Channel Emulator
CIR	Channel Impulse Response
CQI	Channel Quality Indicator
CSI	channel system information
CTIA	Cellular Telephone Industries Association

D2D	Device to Device
DFF	Direct Far-Field
DL	Downlink
DPR	Discrete Plane Reflector
DUT	Device Under Test
EAoA	Elevation Angle of Arrival
EAoD	Elevation Angle of Departure
ECDF	empirical cumulative distribution function
ECR	Elliptical Cylinder Reflector
EFIE	electric field integral equation
EIRP	Effective Isotropic Radiation Pattern
EIS	Effective Isotropic Sensitivity
eMBB	Enhanced Mobile Broadband
ERR	Ellipsoid of Revolution Reflector
EVM	Error Vector Magnitude
FA	feeder antenna
FF	Far-Field
FR1	Frequency Range 1
FR2	Frequency Range 2
FSPL	Free Space Path Loss
gNB	next generation NodeB
GO	Geometric Optics
GPRS	General Packet Radio Service
GSCM	Geometry-based Stochastic Channel Model
GSM	Global System for Mobile communication
ICNIRP	International Commission on Non-Ionizing Radiation Protection
IF	intermediate frequency
IFF	Indirect Far-Field
ITU	International Telecommunications Union
KPI	Key Performance Indicators

LNA	low noise amplifier
LOS	Line of Sight
LTE	Long-Term Evolution
MIMO	multiple-input multiple-output
mMTC	Massive Machine-Type Communications
mmWave	Millimetre Wave
MoM	method of moments
MPAC	Multi-probe Anechoic Chamber
MS	Mobile Station
NF	Near-Field
NLOS	Non-Line of Sight
NR	New Radio
NSA	Non-standalone
NYU	New York University
O2I	Outdoor to Indoor
OTA	Over-the-Air
PA	power amplifier
PAS	Power Angle Spectra
PDP	Power Delay Profile
PDSCH	Physical Data Shared Channel
PO	Physical Optics
PRACH	Physical Random Access Channel
QZ	Quiet Zone
RC	Reverberation Chamber
RCS	Radar Cross Section
RF	Radio Frequency
RMa	Rural Macrocell
RRM	Radio Resource Management
RSRP	Received Signal Radiation Power
RTS	Radiated Two Stage
Rx	Receiver

SAR	specific absorption rate
SCM	Stochastic Channel Model
SCME	Spatial Channel Model Extension
SIMO	single-input multiple-output
SINR	Signal Interference to Noise Ratio
SISO	single-input single-output
SL	spatial lobe
SNR	Signal to Noise Ratio
SSCM	Statistical Spatial Channel Model
TC	time cluster
TIS	Total Isotropic Sensitivity
TRP	Total Radiated Power
TRxPs	transmission reception points
Tx	Transmitter
TZ	Test Zone
UE	User Equipment
UL	Uplink
UMa	Urban Macro-cellular
UMi	Urban Micro-cellular
UMTS	Universal Mobile Telecommunications Service
uRLLC	Ultra-Reliable and Low Latency Communications
V2V	Vehicle to Vehicle
VNA	Vector Network Analyzer
ZSA	Zenith Spread of Arrival

CHAPTER 1

INTRODUCTION

1.1 Motivation

The demand for high data rate wireless communications and the number of mobile users has been steadily growing, therefore the fifth generation (5G) mobile technology is being rolled-out to satisfy this demands. The International Telecommunications Union (ITU) proposed a set of target Key Performance Indicators (KPI) that 5G networks and 5G devices must achieve [1], and to address these challenges, technologies such as Massive multiple-input multiple-output (MIMO) and Millimetre Wave (mmWave) frequencies have risen as solutions capable to deal with the data connected society.

The concept behind Massive MIMO is to employ a Base Station (BS) with a large number of antennas (antenna arrays) that will simultaneously serve many User Equipment (UE) at the same time and with the same frequency resources, which can significantly improve the spectral efficiency of the wireless networks for sub-6 GHz spectrum [2]. On the other hand, mmWave technology makes use of frequencies between 30 to 300 GHz[1] where exists large amounts of available spectrum that can be used to deliver high data rate, low delays, and reliable communications [3]. As explained later mmWave devices also employ beamforming antenna array technology.

Up until now 2G, 3G, and 4G cellular mobile UEs had been implemented with many devices offering antennas port connectors. These can be used to evaluate the performance of the device bypassing the antennas facet and testing separately the baseband circuitry and RF circuitry port antenna. To test single-input single-output (SISO) UE requirements, the radiated RF performance of the UE is evaluated by sampling the radiated performance of the device in its surroundings.

[1]The range of frequencies defined by 3GPP know as sub-6 GHz are Frequency Range 1 (FR1) : 410 to 7125 MHz and mmWave Frequency Range 2 (FR2): 24250 to 52600 MHz

The 3D characterisation of the transmit performance of the UE is computed with the data captured from the spatially distributed power measurements. The Total Radiated Power (TRP) is than calculated by integrating all the power values obtained, this parameter gives information about the radiation efficiency of the antenna of the device. The receiver is characterised by the Total Isotropic Sensitivity (TIS) metric, by measuring the required downlink power to achieve a specific throughput [4–6]. Further details of these parameters are described in Chapter 3.

With the incorporation of MIMO into 4G UEs,[2] it was necessary to test the radiated performance in a different way, and this test have to be performed Over-the-Air (OTA). OTA testing is a general principle to measure the radiated performance of wireless devices that includes the impact of the antenna facet. In theory it is possible to characterise antennas and antennas arrays separately from the device by connecting test devices to the port of the antenna with a coaxial cable in a fully instrumented anechoic chamber [7]. However, in practical UE designs, this involves intrusive modifications to the device that render the results nearly useless and certainly not suitable for validating end-to-end device conformance. At mmWave frequencies, direct antenna measurement is even less likely as antennas will be highly integrated into the device [4, 8, 9]. e.g Figure 1.1 below shows a fully integrated extended-range mmWave antenna module built specifically for 5G Fixed Wireless Access(FWA) consumer premises equipment (CPE), whose size is comparable to the United States one-cent coin.

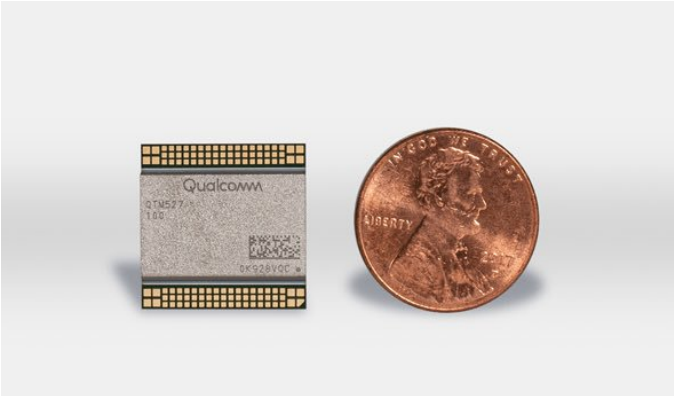

Figure 1.1: Qualcomm QTM527 5G extended range mmWave Antenna module

To accurately measure the performance of a Device Under Test (DUT) OTA, it should be located at a minimum measurement distance based on the largest dimension of the antenna system (or the diameter of the antenna) . This distance is known as the far field region of the antenna where an ideal plane wave is generated. At low frequencies, typical measurement distances are quite small e.g the far-field of a DUT with a 150 mm antenna diameter would be around 300 mm. Additional factors to determine this distance are fully described in [10]. At mmWave frequencies, the far-field distance can be much larger e.g. a DUT with a 150 mm antenna diameter at 60 GHz would give a far-field distance of 9 m. As it would be extremely

[2]MIMO means multiple antennas in the device

expensive and complicated to have a dedicated infrastructure that big, it is necessary to evaluate if this criterion still holds for high frequencies and to come up with new techniques to measure the characteristics and performance of devices operating at centimetre and millimetre wave frequencies [4]. Currently, two techniques are mostly used to test the MIMO OTA performance of 4G UE being Multi-probe Anechoic Chamber (MPAC) and the Radiated Two Stage (RTS) method, which have both been standardized and are summarized in Chapter 3 and extensively described in [11].

Communicating at mmWave frequencies results in additional propagation impairments such as additional path loss [12] (e.g. The path loss at 3.4 GHz (frequency assigned in UK for 5G) is approximately 20 dB smaller than at 30 GHz). Also, these high frequencies experience higher penetration losses as well as greater susceptibility to blockages (e.g., foliage, vehicles, people, etc.) [13]. To mitigate these effects, the BS and the UE will employ Active Antennas Systems (AAS) incorporating phased array antennas. Due to the shorter wavelengths at mmWave, these multi-element active antennas can be physically compact making integration with the Radio Frequency (RF) transceiver electronics viable. The AAS provides dynamic and adaptive electronic beam steering functions, providing the high-gain directional antenna patterns needed to mitigate the path loss, as well as enabling spatial re-use for higher capacity and density [14].

To maintain a reliable connection, the UE must offer dynamic three-dimensional (3D) antenna pattern control and rapid reconfiguration [14]. This functionality presents new challenges when compared with legacy sub-6GHz mobile devices regarding product conformance testing [15]. Moreover, the small size of the AAS makes the provision of antenna connectors for conductive testing unlikely; thus, the testing of 5G mmWave frequency devices necessitates a radically different approach. Most likely this has to be performed with OTA methodologies [16].

Radio performance evaluation of both BS and UEs is essential as it is required in different phases of a product's development, starting from early research prototypes, design optimization, and actual product approval for rollout. These are critical step specially if beam forming technology present because exploiting the spatial domain is new for cellular systems. Therefore, optimising the beam forming control of such devices is critical to system performance. OTA testing methods have some advantages over field trials such as repeatability, reliability, measurement and cost efficiency, thus the evaluation method ought to mimic realistic propagation conditions to accurately assess the performance of the UE in the field [7]. However, OTA testing also has a number of challenges, such us the UE antenna arrays do not provide access to their RF ports, requires a well-controlled environment to test the performance of the devices, realistic emulation of real-life conditions, among others. These will be discussed in detail in subsection 3.8.

This thesis proposes new OTA test methods capable of emulating 3D spatially dynamic channels for mmWave devices and access point technology. These methods are based on the reflective properties of the ellipse and show the evolution of the design and prototyping of elliptical cylinder reflectors, as well as discrete plane reflectors evenly distributed along a part-ellipsoid

curvature. These offer a cost-effective means of emulating a sparse spatially dynamic mmWave propagation channel, with the DUT experiencing real-life channel conditions. Theoretical and practical characterisation of the infrastructure validate the test method which is a potential candidate for testing Radio Resource Management (RRM) (described in subsection [3.7.5]) and demodulation requirements of 5G mmWave mobile devices in dynamic spatial environments that could be proposed to be included as one of the test methods within the Release 16 study item on testability at 3GPP [16, 17].

1.2 Key Contributions

The key contributions of this thesis are summarised as follows:

1. Novel design, implementing, detailed characterisation and modelling of two over the air test methods; one based on elliptical cylinder reflectors and the other based on discrete plane reflectors distributed in a ellipsoidal structure.
2. A methodology to evaluate the performance of 5G New Radio (NR) mmWave frequency devices through the generation of simultaneous dynamic signals that arrive at the device under test with different angles of arrival in both azimuth and elevation planes.
3. Algorithm to place and distribute a set of discrete plane reflectors of a certain size to create a test zone sufficiently large to allocate typical sized smartphone devices.
4. Development of a ray tracing tool to aid analyse the distribution of the electromagnetic fields from the different types of reflectors explored during the development of the thesis.
5. Implementation and validation of prototypes of the proposed OTA test methods with real active antenna from the company Anokiwave [18].

The work presented in this thesis has led to some publications in international conferences, publication in a book and submission of a journal paper, as well as a potential patent application. A list is included in below.

1. CDT Annual Student Research Conference at Engineers' House, Bristol on 23rd September 2017, presentation titled "Over the air (OTA) validation of 5G millimetre wave devices' active antenna performance"
2. Cambridge and Wireless "Radio technology for 5G-making it work" in Bristol - UK on 18th September 2018, presentation title "Novel 5G Over-the-Air test method for millimetre wave frequency devices".
3. CDT Annual Student Research Conference at Engineers' House, Bristol on 28th September 2018, poster title: "Over-the-Air test method for 5G mmWave frequency devices"

4. 8th COST IRACON meeting in Podgorica - Montenegro on 1st - 3rd October 2018, paper title "Novel Over-the-Air test method for 5G mmWave devices with beam forming capabilities"

5. 2018 IEEE Global Communications Conference: GLOBECOM 2018, 9th - 13th December 2018, Abu Dhabi, UAE, paper title "Over-the-Air Test Method for 5G mmWave Devices with Beamforming Capabilities" [16].

6. 10th COST IRACON Oulu - Finland on 4th - 6th September 2019, paper title "Novel Over-the-Air Test Method for 5G Millimetre Wave devices, based on Elliptical Cylinder Reflectors"

7. 2019 IEEE 90th Vehicular Technology Conference: VTC2019 Fall 22-25 September 2019, Honolulu, Hawaii, USA, paper title "Novel Over-the-Air Test Method for 5G Millimetre Wave devices based on Elliptical Cylinder Reflectors" [19].

8. 2018 12th European Conference on Antennas and Propagation: EuCAP 2018, December 2018, London, UK., paper title "Non-intrusive characterization of 60GHz antenna array, using packet measurements" [4].

9. IWPC 4G&5G Antenna Evolution, Edinburgh, Nov 2019

1.3 Thesis Overview

The thesis is organised as follows:

Chapter 2 covers some relevant background theory. It introduces the basic principles of a 5G technology, summarises the existing 5G channel models and provides the definitions of three large scale parameters that are of concern of this study such as line of sight probability, path loss and clustering. Furthermore, provides basic information about active antennas, and the different types of beamforming technologies since the millimetre wave 5G NR UE as well as the feeder antenna used during this thesis heavily rely on this kind of devices.

Chapter 3 presents an overview of existing Over the Air test methods to test the performance of 2G, 3G and 4G mobile devices as well a description of the measurement metrics. It also includes an analysis of the drawbacks of the methods when tried to be used for testing mmWave frequency devices. Furthermore, it discusses the challenges faced to test mmWave 5G devices, with special focus in beamforming, radio resource management and demodulation. The analysis also includes prior art that has some relation with the use of ellipsoid reflectors.

Chapter 4 describes the ray tracing simulator developed to design and evaluate the proposed test methods. It was based on Geometric Optics principles, in order to model the electromagnetic fields of the signals. The approach followed is called Forward-Ray Tracing, consists in casting rays from the transmitter in all directions.

Chapter 5 covers the analytical analysis the ellipsoid and elliptical cylinder reflectors used within the elliptical based architecture. Basic definitions about of the ellipse and the required geometrical customisations to achieve the desired test zone volume. Furthermore, the analysis of angles of arrival, angles of departure, dimensions of the test zone volume for each type of reflector is described, finalizing with the pros and cons of the two candidate architectures is appraised.

Chapter 6 describes the design and simulations of the test method that further improves the test zone volume by using discrete plane reflector. The description of the algorithm used to distribute the plane reflectors to create the desired three-dimensional spatial environment is discuses. Similarly, to the other test methods the angles of arrival, angles of departure, dimensions of the test zone volume is also described, finalizing with the pros and cons of the three candidate architectures.

Chapter 7 describes the implementation of two prototypes: an elliptical cylinder reflector, and a set of plane discrete reflectors. Experimentally shows the applicability of the proposed method for mmWave OTA testing and shows the Test Zone size achieved with the prototypes.

Chapter 8 concludes the thesis with a series of recommendations regarding the application of this method and discusses ideas for future work inspired by its outcomes.

CHAPTER 2

THE ROAD TO 5G AND BEYOND: THE NEED FOR MILLIMETRE WAVE CHANNEL MODELS

2.1 Introduction

Each generation of wireless mobile communications has contributed to fulfil a communication need and address a specific set of key performance indicators. For example, the first generation (1G) of mobile wireless devices was the first automatic analogue cellular system mainly capable of executing analogue phone calls. Later on, the second generation (2G) employed digital modulation techniques for voice and messaging as well as circuit-switched data connections at up to 9600 bits/s. The most deployed technologies worldwide were Global System for Mobile communication (GSM) and Qualcomm IS-95 with its Code Division Multiple Access (CDMA). Next the General Packet Radio Service (GPRS) was developed to allow aggregation of several carriers for higher speed, packet-switched applications such as always-on internet access[20]. The incorporation of higher data transmission rates and internet were the main attributes of the third-generation mobile cellular system the technical specifications of the network were based on the GSM and was known as the Universal Mobile Telecommunications Service (UMTS). GSM used a power-efficient constant envelope modulation scheme Gaussian Minimum Shift Keying (GMSK). Broadband internet, and applications were added in 3.5G, to the faster broadband internet and lower latency in what is known as Long-Term Evolution (LTE) which is the fourth generation (4G). LTE uses Orthogonal Frequency Division Multiplexing (OFDM) for the downlink. OFDM is used as a digital multi-carrier modulation method enabling spectrum flexibility for wide carriers with high peak rates.

Mobile broadband in combination with billions of consumer devices between mobile phones, laptops, tablets, etc. have enabled people to communicate mostly in any part at any time by

digital audio and video phone calls, emails, social media, music and video streaming, control and monitor appliances, internet of things (IoT), etc. As the number of devices, applications and services increase so does the demand of data transmission over current mobile networks that will soon struggle to cope with it. Therefore, the 5th Generation of mobile communication (5G) is being developed to address these shortages, in particular data capacity. Some of the prime benefits of 5G devices will be attaining significantly faster low latency data access. 5G will support Massive Machine-Type Communications (mMTC), Enhanced Mobile Broadband (eMBB), Ultra-Reliable and Low Latency Communications (uRLLC) [21].

According to the ITU in [1, 22] some of KPI network-level capabilities that 5G must attain are:

- Latency: 1 millisecond end-to-end round-trip delay for specific applications
- Mobility: up to 500 [Km/h]
- Connection density: 106 [devices/km^2]
- User experience data rates: 10-100 [Mbits/s]
- Spectrum efficiency 1x to 3x
- Peak data rate: 1 - 20 [Gbit/s]
- Area traffic capacity: 1-10 [Mbit/s/m^2]
- Network energy efficiency

Potential use cases for this technology are: Virtual Reality that could be used either for entertainment or practical applications like automation of production; telemedicine namely medical monitoring and remote surgery. In the automotive domain, it is expected that 5G will enable fast and reliable communications between the traffic infrastructure and the driving vehicles in order to increase safeness on the roads. Machine-to-Machine (M2M) connectivity is another possibility, although it already exists more complex and demanding devices may be developed, etc.

Different technologies are being investigated that will enable 5G technology to achieve the expected capabilities previously mentioned, more specifically for the air-interface Massive MIMO and mmWaves are predominately the main technologies being considered. [2, 3, 12]. 5G NR will be deployed in two main frequency ranges. FR1 comprises all the frequencies from 450 MHz to 7.125 GHz and FR2 from 24.25 GHz to 52.6 GHz. At higher frequencies there exist more spectrum available to fulfil the demand of high data rates by having bandwidths of up to 400 MHz per carrier.

Prior to the development of a new methodology to test the performance of 5G mmWave devices it is important to understand the characteristics of the wireless channel at these high frequencies to emulate their behaviour in a controlled environment and facilitate performance optimisation. In general, the dynamics of the mmWave channel shifts from an omnidirectional operation that

of dynamic spatial focusing. In this section a brief description of the existing channel models is discussed. Also, main large-scale parameters such as path loss, delay spread, number of clusters, angles of departure and arrival are described

2.2 5G Channel Models

Common propagation scenarios described in the literature are Rural Macrocell (RMa), Urban Micro-cellular (UMi), Urban Macro-cellular (UMa), Indoor, and Outdoor to Indoor (O2I) environments, being these of higher priority, and scenarios such as Device to Device (D2D), Vehicle to Vehicle (V2V) among others are also being researched. A UMi scenario is considered an open area in the order of 50m to 100m, where a Transmitter (Tx) can be placed at heights between 3m to 20m and the Receiver (Rx) might be anywhere between 1.5m to 2.5m also in height. The expected distance between cells is between 100m to 200m. In a UMa scenario, the BS are mounted at 25m to 35m and the expected coverage area is between 200m and 500m. For indoor scenarios, the BS is mounted at 2m or 3m, and the height of the Rx is 1.5m and the area is about $500m^2$. Mobility in the horizontal plane is considered to be 3km/h for all scenarios [23, 24].

The existing channel models are listed below:

- The technical report TR38.901 [23] published by 3GPP covers the modeling of the physical layer of both the UE and the access network of 3GPP systems and captures the channel models for frequencies from 0.5 GHz up to 100 GHz. It is based on the 3D Stochastic Channel Model (SCM), supports scenarios such as UMi street canyon, UMa, Indoor, and RMa. The maximum bandwidth supported is up to 10% of the centre frequency but no larger than 2 GHz. This channel model only covers static channels [23].

- 5GPPP released the “Measurement Result and Final mmMAGIC Channel Models”, after conducting extensive multi-frequency channel measurements and simulations campaigns, covering various 5G propagation scenarios, some of them were contributions to the models being developed by 3GPP and ITU and QuaDRIGa [25]. The channel model is a Geometry-based Stochastic Channel Model (GSCM) whose baseline is the latest 3GPP channel model [23] with additional features which covers a frequency range from 6 to 100 GHz and it is focused on the modeling of frequency-dependent large scale parameters, ground reflection effects, cluster and sub-paths, small-scale fading, blockage, building penetration, etc. It is extensively detailed in [26].

- The New York University (NYU) has developed a Statistical Spatial Channel Model (SSCM) developed using time clusters and spatial lobes to generate multipath parameters for omnidirectional and directional Channel Impulse Response (CIR) and their corresponding Power Angle Spectra (PAS) based on real measurements at multiple frequencies from 28 to 73 GHz. Supported scenarios are UMi, UMa, and RMa, and these are applicable

for a wide range of frequencies from 0.5 to 100 GHz [27]. With the data collected from the measurement campaigns, they were able to develop a statistical channel model fully detailed in [28].

- Mobile and wireless communications Enablers for the Twenty-twenty Information Society (METIS) consists of three channel models, map-based (ray tracing), stochastic, and a hybrid model. The models were derived from measurements and simulations. Supported frequencies in the models are from 0.45 GHz to 70 GHz. The stochastic model is specified in separated frequency bands. The supported bandwidth for the stochastic model for frequencies below 6GHz is up to 100 MHz and 1GHz specifically for 60 GHz, and 10% of the centre frequency for the map-based model. Depending on the model used certain propagation scenarios are supported. The map-based model is suitable for evaluating massive MIMO, advanced beamforming and for pathloss modeling for device to device (D2D) and vehicle to vehicle (V2V). The stochastic model is a GSCM further development from WINNER/3GPPP that provides multi-dimensional shadowing maps, mmWave parameters, direct sampling of the PAS and frequency dependent pathloss. The channel models are antenna independent. The particularity of this channel model is that instead of proposing a unique value for each parameter, it is proposed a range of a minimum and maximum values [29].

- The Millimetre-Wave Evolution for Backhaul and Access (MiWEBA) project developed a quasi-deterministic channel model, which combines a geometry-based approach for a limited number of multipath components and a stochastic approach. The scenarios considered in the channel model are classified in access (open area, street canyon, and Indoor), backhaul/front haul (above roof top, street canyon), and D2D (open area, street canyon, and Indoor), etc. It is stated that that mmWave CIR is comprised of a few strong rays, a number of relatively weak random rays, and flashing rays. The model is limited for 60 GHz [30].

- The quasi-deterministic radio channel generator (QuaDRIGa) channel model is based on the Wireless World Initiative for New Radio (WINNER+) channel model and the 3GPP-3D channel model, it is a GSCM. The channel parameters are determined stochastically, based on statistical distributions obtained from measurements. The frequency range supported is from 2 to 6 GHz, with a maximum bandwidth of 100 MHz. In QuaDRIGa each scattering cluster is approximated by 20 individual scatters. Depending on the angular spread and amount of diffuse scattering the typical number of clusters for Line of Sight (LOS) scenarios are around 10 and for Non-Line of Sight (NLOS) are around 20 [25].

2.2.1 Millimetre Wave channel characteristics

2.2.1.1 Path loss

Among all different channel models found in literature, mainly there are three path loss models considered. 3GPP models and the ones based on it use the Alpha-Beta-Gamma (ABG) model with an additional dependency on base station and terminal heights, and with a LOS breakpoint. NYU considers the Close-In (CI) free space reference distance PL model with a 1m reference distance and an extra attenuation term to account for atmospheric conditions, and the last model is the Close-In free space reference distance model with frequency-dependent path loss exponent (CIF) [24, 27].

The CI model is given by

$$PL^{CI}(f,d)[dB] = FSPL(f,1m)[dB] + 10n\log_{10}(d) + AT[dB] + X_{\sigma}^{CI} \tag{2.1}$$

Where d is the 3D distance between Tx and Rx in metres, f is the frequency in Hz and n is the pathloss exponent, AT is the attenuation term in dB induced by atmosphere, FSPL denotes the free space path loss and X_{σ}^{CI} is a zero-mean Gaussian random variable with standard deviation σ in dB. The ABG model is given by

$$PL^{ABG}(f,d)[dB] = 10\alpha\log_{10}(d) + \beta + 10\gamma\log_{10}(f) + X_{\sigma}^{ABG} \tag{2.2}$$

where α captures how the path loss increase as the distance between Tx and Rx varies in metres, β is a floating offset value in dB, γ captures the path loss variation over the frequency f in GHz, and X_{σ}^{ABG} is the Shadow Fading deviation term in dB. The CIF model is an extension of the CI model and uses a frequency-dependent path loss exponent given by:

$$PL^{CIF}(f,d)[dB] = FSPL(f,1m)[dB] + 10n\left(1 + b\left(\frac{f-f_o}{f_o}\right)\right)\log_{10}\left(\frac{d}{1m}\right) + X_{\sigma}^{CIF} \tag{2.3}$$

where n is the path loss exponent, b is an optimization parameter that captures the slope or linear frequency dependency of the path loss exponent that balances at the centroid of the frequencies being modelled, fo is a fixed reference frequency [24].

From the literature in [31, 32] is has been shown that the ABG, CI, and CIF models are all very comparable in prediction accuracy when large data sets exist, even though the ABG model requires more model parameters. The CI and CIF models are physically tied to the transmitter power via the utilization of a 1-m close-in free-space reference distance that has inherent frequency dependency over the entire microwave and mmWave band.

Fig. 2.1 shows the PL calculated at 28 GHz for distances from 30m to 1000m for UMi LOS scenario using equations extracted from 3GPP, mmMAGIC and NYU channel models.The NYUSIM and mmMAGIC models estimate approximately 5-dB more signal power at 1 km when compared to 3GPP [31].

Fig. 2.2 shows the PL calculated at 28 GHz for UMi NLOS scenario, where is shown that the 3GPP NLOS path loss crosses over and becomes greater than the NYU CI path loss at distances

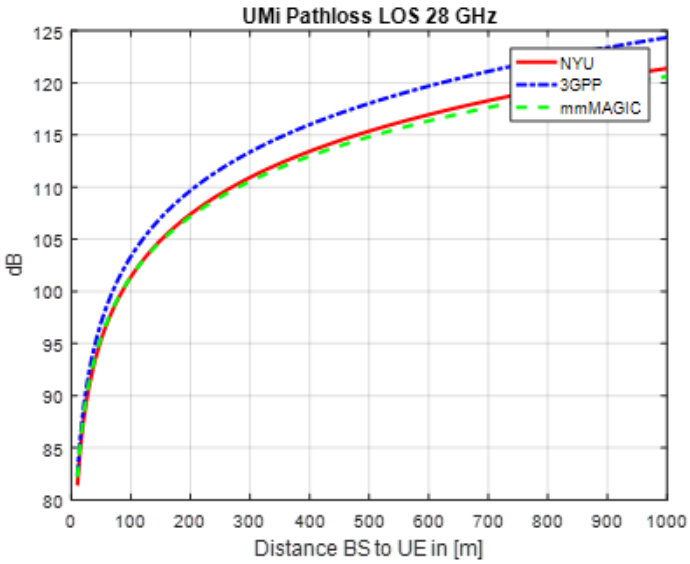

Figure 2.1: Comparison of pathloss from 3GPP, mmMAGIC and NYU for LOS scenarios

greater than 200 m [31]. The mmMAGIC model [26] shows larger attenuations compared with the other two models.

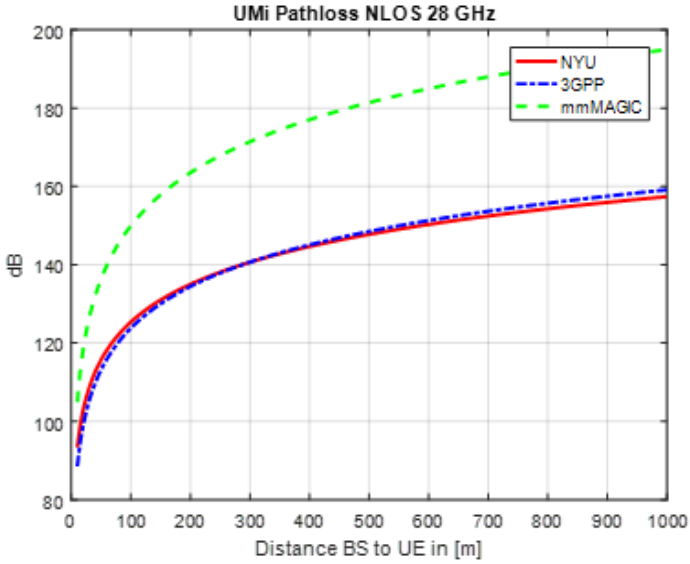

Figure 2.2: Comparison of pathloss from 3GPP, mmMAGIC and NYU for NLOS scenarios

2.2.1.2 Line of sight probability

In the context of mobile communications, a Line of Sight (LOS) link can be thought as a straight path between the BS and the UE in a three-dimensional space when unobstructed by any objects. On the other hand, a Non-Line of Sight (NLOS) is the indirect path from the BS and the UE also

in three dimensional space. LOS is the ideal condition for mobile communications because the transmitted signal is received with best possible signal strength without exposing any obstacles. In NLOS, there are many obstacles such as buildings, forest, cars, people, etc. In this case, the transmitted signal by the BS reaches the UE weakened or vice-versa.

Models for the probability of LOS are needed to predict the likelihood that a UE is within a clear LOS of the BS, or in an NLOS region due to obstructions. LOS propagation will offer more reliable performance in mmWave communications as compared to NLOS conditions, given the greater diffraction loss at higher frequencies compared to sub-6 GHz bands where diffraction is a dominant propagation mechanism [12]. Line of Sight (LOS) probability model is a function of the separation distance between the transmitter and receiver. It can also be a function of the TX and RX heights. It is inherited from the previous LOS probability model derived for sub-6 GHz bands by 3GPP [32]

The LOS probability model proposed by the 3GPP 3D channel model for the UMi is given by equation 2.4. If the two-dimensional distance d_{2D} between BS and UE is less or equal than 18 m then the probability is 1. Thus, the equation below is given by distances greater than 18 m.

$$P_{LOS} = \frac{18}{d_{2D}} + \exp\left(-\frac{d_{2D}}{36}\right)\left(1 - \frac{18}{d_{2D}}\right) \tag{2.4}$$

For UMa scenarios the LOS probability is also 1 when the distance $d_{2D} \leq 18m$, for larger distances it is given by equation 2.5. The height of the user terminal h_{UT} is considered 1.5 m

$$P_{LOS} = \left[\frac{18}{d_{2D}} + \exp\left(-\frac{d_{2D}}{63}\right)\left(1 - \frac{18}{d_{2D}}\right)\right]\left(1 + C'(h_{UT})\frac{5}{4}\left(\frac{d_{2D}}{100}\right)^3 \exp\left(-\frac{d_{2D}}{150}\right)\right] \tag{2.5}$$

where

$$C'(h_{UT}) = \left(\frac{h_{UT} - 13}{10}\right)^{1.5} \tag{2.6}$$

The LOS probability is derived with assuming antenna heights of 3m for indoor, 10m for UMi, and 25m for UMa. The other models for indoor scenarios and RMa are fully described in Table 7.4.2.1 in [23].

A comparison between the LOS probability models form 3GPP and NYUSIM is given in [32, 33] for UMi and UMa scenarios and is shown in Fig. 2.3 (Source: [34]), where it was found that the 3GPP model has a non-zero tail at distances of several hundred metres, which should not be the case in urban environments where numerous obstructions such as buildings exist. For distances smaller than 160 m, NYUSIM predicts a larger LOS probability compared to 3GPP for both UMi street canyon and UMa scenarios. The LOS probability impacts the estimated spectral efficiency because LOS links have stronger signals compared to the NLOS scenarios due to higher diffraction losses.

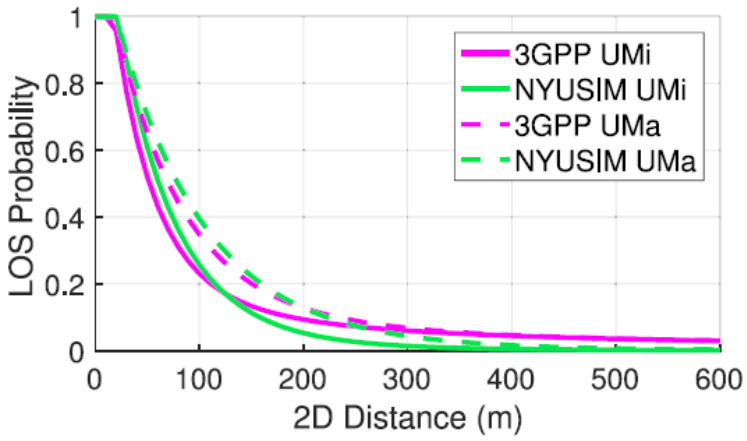

Figure 2.3: Comparison of LOS probability models in the 3GPP channel model and NYUSIM in UMi and UMa scenarios for a UE height of 1.5 m.

2.2.1.3 Clusters

The 3GPP and NYUSIM channel models have adopted two different approaches to define the clusters. 3GPP considers that the clusters are characterised by a joint delay-angle probability density function, which means that a group of travelling multipaths must depart from a unique Angle of Departure (AoD) and must arrive with a unique Angle of Arrival (AoA). This combination is centred around the mean propagation delay [23, 32, 34].

On the other hand, NYUSIM defines the cluster by using two concepts: time cluster (TC) and spatial lobe (SL) to describe multipath behaviour in omnidirectional Channel Impulse Response (CIR). "TCs are composed of multipath components traveling close in time and arriving from potentially different directions in a short propagation time window. SLs denote primary directions of departure or directions of arrival where energy arrives over several hundred nanoseconds" [32, 34, 35]. A SL may contain many multipath components arriving in a space with different time delays. According to 3GPP the number of clusters in a LOS scenario is 12 and for a NLOS scenario should be 19, each of which contains 20 multipaths [23]. Whereas, according to NYUSIM in [34, 36] the number of TC is only up to 5 and the number of SLs yields up to 6.

According to 3GPP, the characteristics within each cluster are RMS delay spread of around 5 ns, the Angular spread of Departure (ASD) must be in the order of 3 degrees, the Angular Spread Arrival (ASA) is 17 degrees and the Zenith Spread of Arrival (ZSA) is 7 degrees. On the other hand, NYUSIM channel model shows a mean ASD of 6.7 degrees, a mean Angular Spread Arrival (ASA) of 6.7 degrees, and a mean ZSA of 1.8 degrees [23, 37]

2.2.2 Blockages aspects

As mentioned before mmWave will suffer from large-scale blockage effects due to buildings, foliage, cars or any obstacle in between the BS and the UE, therefore it is important to consider

how blockages produced by the human body affect the overall performance of the communication link. Particularly the hands will have a great impact on the radiated performance due to the proximity to the antenna in the handset it may change the impedance of the antennas [38]. According to the measurement performed in [39], the penetration of mmWave through the human body is very low showing high losses around 20 to 40 dB. A complementary analysis made in [40] showed that more than 90% of the transmitted power is absorbed by the dermis and epidermis layers of the body. However, according to measurements carried out by the author have shown that the hand and the human body appear to be extremely reflective similar to metal which contradicts what was stated by [39].

In [41] the effects of the hands over the radiation pattern were analysed at 15GHz (candidate frequency was chosen by NTT DoCoMo), considering that the UE has two arrays on the top and three different locations of the hands single hand, dual hand, and single finger touching close to antenna array. For the two first cases the efficiencies of the arrays were similar as if the terminal was in free space, for the second case the coverage efficiency degraded and can be see that the main beam of one of the arrays is reflected to the other one, and the radiation pattern is totally altered by the finger that is on one of the arrays. This particular analysis in [41] helps to confirm the importance of performing OTA measurements with the entire UE including the antennas, because the human body and particularly the hand will represent a considerable issue while keeping a good communication quality within the upcoming 5G technology.

Before any devices are introduced into the consumer market, it must comply with exposure guidelines set by governments. According to [40] the specific absorption rate (SAR) measurement commonly used for current cellular technologies cannot longer be used for mmWave frequencies due to at these frequencies the energy absorption is confined to the surface layers of the skin, therefore power density should be utilized for compliance applications as it is suggested by the International Commission on Non-Ionizing Radiation Protection (ICNIRP). In [42] the ICNIRP stated that for “Frequencies from 10 MHz to 300 GHz, heating is the major effect of absorption of electromagnetic energy, and temperature rise of more than 1 - 2 degrees centigrade can have adverse health effects such as heat exhaustion and heat stroke”. Additionally, suggested that the power density limits are 10 W/m2 for the general public and 50 W/m2 for the occupational group. With those limits taken into account the maximum radiated power for future 5G UE was determined in [43], that it would be around 15dBm and 18 dBm which is approximately 6 dB below than current UEs radiated power operating in 3G and 4G LTE technologies. This reduction in the maximum radiated power represents a problem with the range of coverage and capacity that 5G terminals will face, due to the propagation characteristics of mmWave frequencies.

2.3 Active Antenna Arrays and Beamforming

Beamforming refers to the ability of an array of antennas to focus the radiated energy along a specific direction in the space. It also performs the function of spatial filtering. This is achieved by adjusting the amplitude and phase of each element of the array through signal processing so that at particular angles the signals will experience a constructive interference while others experience a destructive interference. The device that controls the phases and amplitudes of the different excitation currents of each antenna is known as the beamforming network.

Beamforming is required to address the challenges of higher path losses experienced at high frequencies such as mmWaves, improving the link budget and enabling mobility. In order to maintain a call, the UEs must be capable of searching and tracking the signals, as well as to discover and switch to the strongest multipath. Therefore, being able to steer the beam in 3D as efficiently as possible is a basic requirement.

In the following subsections a brief description of the three main types of beamforming (analogue, digital, and hybrid) is given.

2.3.1 Analogue beamforming

Analogue beamforming is done at RF level, the beamforming network consists of elements that control the phases and amplitudes of the signal [44, 45]. Figure 2.4 shows an analogue beamformer receiver with a linear antenna array used to produce a unique beam that can be steered in a particular direction. To do so complex weights are applied to the signal from each antenna in the array. By varying the amplitude (relative amplitude of weight a_k) the width of the beam can be changed and also the side lobe levels are controlled. The direction of the beam depends on the antenna elements spacing, and the phase-shifts (θ_k) between the antenna elements. In this case, a power combiner is used to add up all the received signals at each antenna.

This configuration is used either if the device is transmitting or receiving, so the beamforming network can distribute the signal from the transmitter to the antennas or from the antennas to the receiver. In receiver mode, the signals from the antennas add coherently if the signals arrive in the correct region of space. The output $y(t)$ is given by a linear combination of the data of the K elements at a time t, as equation (2.7):

$$y(t) = \sum_{k=1}^{K} W_k^* x_k \tag{2.7}$$

Where, x_k is the signal from the k^{th} antenna which is multiplied by the corresponding weight $W_k^* = e^{j \sin\theta_k}$, and θ_k is the phase shift. In transmitter mode the baseband signal is first modulated and then amplified and split among the available antenna elements. The drawback of this system is that can only handle one data stream and generates one single beam [46].

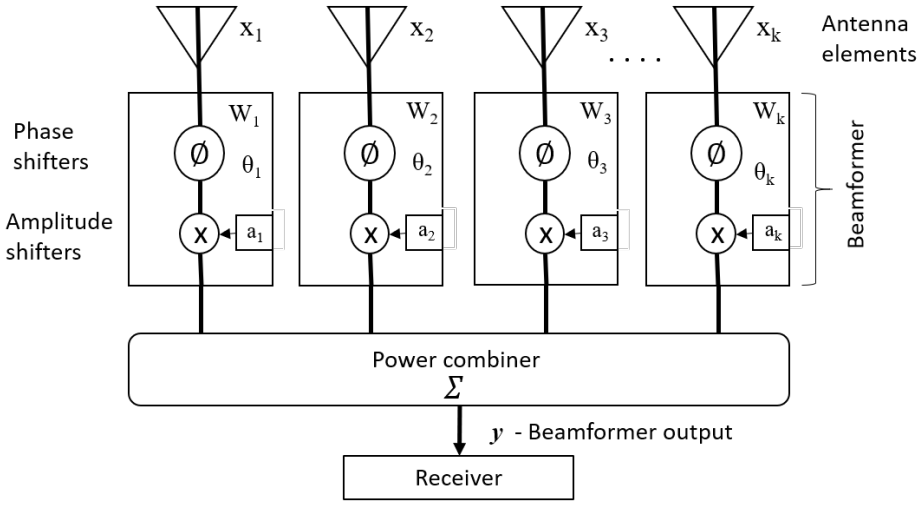

Figure 2.4: Analogue beamforming receiver

2.3.2 Digital beamforming

The digital approach of beamforming refers to the fact that instead of using analogue phase shifters and attenuators fixed methods to weighting the signals, the changes are done digitally directly to the signal at a base band level. In digital beamforming the incoming RF signal is split into two streams of binary base band signals representing I (in-phase) and Q (quadrature) channels. The signals at base band represent the amplitudes and phases of signals received at each at each antenna element of the array. The beamforming is done weighting this base band (digital) signals, adjusting either their phase or the amplitude, or both. So, when they are added together they form the desired beam. The receiver performs a down-conversion, filtering and amplification of the signal so that the analogue to digital converter (ADC) can work. There are many configurations to perform digital beamforming, such as element-space, beam space, two-dimensional, etc [44]. Beam-space beamforming is a method is used to produce multiple orthogonal beams through performing digital signal processing. The weighted outputs are generated by a set of beam-space combiners, by means of the interpolation between individual beams in order to fine-steer the resultant beam, perform a linear combination of the output beams to synthesize a shaped beam or low side lobes pattern, and a combination of some beams to create nulls in the interference direction.

A high-level architecture of a digital beamforming method is show in Fig. 2.5 (Source: [47]), where the system requires $Nx \times Nz$ RF chains, one per antenna element, but the difference would be that the weights to the phase are applied digitally.

Even though this architecture is more flexible, it also means that is more demanding in terms of cost due to the number of RF chains, and also in terms of power, and these two are particular relevant for mmWave due to the devices will require large number of antenna elements.

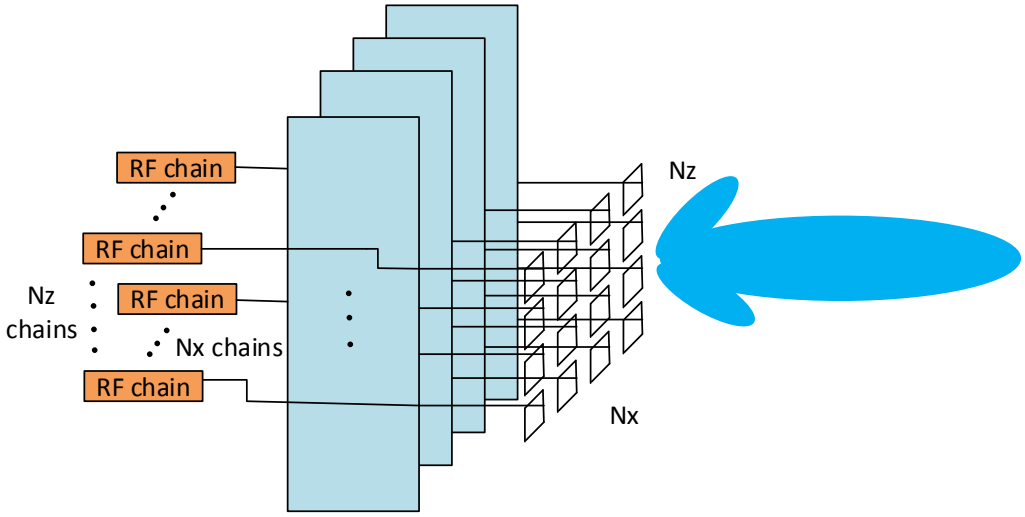

Figure 2.5: Digital beamforming

2.3.3 Hybrid beamforming

Using conventional digital beamforming for large antenna arrays is not practical because for implementation it requires a dedicated radio frequency chain for each antenna element [48]. For example an antenna array of 8 by 8 antenna elements would need 64 RF chains, this implies that the solution would be expensive and consumes high amounts of power. Therefore, hybrid methods are being developed, like in [48] in which the beamformer is built combining baseband beamformer (digital) and RF beamformer (analogue) using phase shifters. With hybrid beamforming the number of RF chains is twice the total number of data streams desired, an example of the architecture is shown in Fig. 2.6 (Source: [47]).

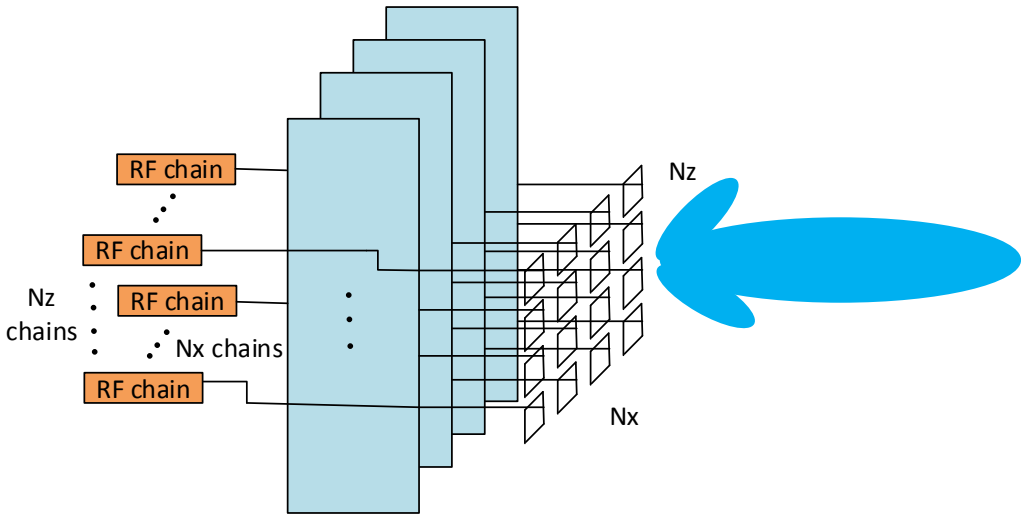

Figure 2.6: Hybrid beamforming for mmWave

2.4 Conclusions

In this chapter a description of the definitions of 5G technology [1, 23, 49], existing channel models and a summary of the different beamforming methods used in active antenna arrays given. Some of the purposes of 5G NR are to connect larger number of devices, enable new services, and empower new user experiences by efficiently make use of the available free spectrum. 5G NR will incorporate advanced wireless technologies such as massive MIMO and mobilizing millimetre wave frequencies as well as optimized waveforms and multiple access techniques inherited from the orthogonal frequency-division multiplexing (OFDM) family. Scalable numerology will address different spectrum bands according to the different deployment models of the networks. Among the envisioned use cases of 5G are: enhanced Mobile Broadband is one of them, intended to deliver high data rates, massive Machine Type Communications whose focus is to be able to connect large number of devices to one base station and Ultra-Reliable and Low Latency Communications where devices rely on very low latency to perform their tasks. Possible applications are industry automation, vehicle to infrastructure communications or autonomous driving. There are two frequencies ranges designated in 5G NR, known as FR1 corresponding to the range of 410 MHz to 7125 MHz and FR2 corresponding to 24250 MHz and 52600MHz. However, technically speaking millimetre waves frequencies is the band of spectrum between 30 GHz and 300 GHz that could be used in order to meet the target specifications of the upcoming 5G and possibly 6G technologies.

Although mmWave frequencies promise a large spectrum availability, they also bring a lot of challenges that must be addressed, such as higher path loss, few dominant multipath components, and higher susceptibility to blockages, amongst others. Based on the channel models described above it is possible to conclude that effectively at mmWave frequencies the energy with which the mobile terminals must work is very sparse and that for line of sight scenarios no more than 4 strong clusters signals will arrive at the receiver, and a maximum of 6 cluster is true for non- line of sight scenarios. The multipaths arriving at the terminal can come from any place depending on the position of it and how fast the user is moving. Therefore, in order to mimic what could happen in real life a great variety of angles of arrival in elevation, and azimuth must be created, in that way, the device terminal will be able to be evaluated as if it would be in real-life conditions.

To overcome the additional path loss of mmWaves compared to sub 6 GHz systems it will be required to use very directional and high gain, turning the common known scenario of how well is the quality of the signal at the UE to achieve high data rate transmissions, to where is the signal? since there will be less energy to detect, which takes the working scenario to a whole new level where the devices must be able to search for the signal, acquire the signal, and finally track the signals while the user moves to avoid losing connectivity. For this to work 5G mmWave handsets will incorporate beamforming techniques. Antenna control and beamforming algorithms are being developed to operate in real-time in order to combat the effects of dynamically changing environment in mmWave, which need to be tested in conjunction the antennas and device circuitry in its final form factor, in order to corroborate that the device can work adequately in this harsh

environment.

CHAPTER 3

PERFORMANCE TEST METHODS

3.1 Introduction

Since the early days of wireless communications and up until now most performance testing of the Mobile Station (MS) or User Equipment (UE) has been done in a conductive manner [15]. This means directly connecting cables to the device's temporary antenna port RF connectors to the test equipment, these antenna ports connectors are used for conformance testing. This kind of tests give an idea of how the terminal is working, however do not consider the antenna's performance and interaction with the propagation environment. Therefore, this is only a partial wireless test of the performance of the device. In the case of the antenna being faulty or performing poorly, this was not noticed as was the case that afflicted the iPhone 4 known as the 'grip of death' that occurred when the signal levels of the terminal drop due to hand obstruction, position and motion [50]. Apart from the fact that the device would not work properly, faulty devices also can cause problems to the network with a reduction in the overall network capacity being directed by a phone with poor RF sensitivity [51].

The wireless association, Cellular Telephone Industries Association (CTIA), was the first organization to publish in October 2001 the first "Test Plan for Mobile Station Over the Air" [10], which was the method of measurement for radiated RF power and receiver performance. Initially, the test was standardized for single-input single-output (SISO) devices. Later, in 2006 the 3GPP, adopted CTIA's test method and published their specifications for SISO devices 3GPP "Measurements of Radio Performances for UMTS Terminals in Speech Mode" [38]. The standardization of tests for multiple-input multiple-output (MIMO) devices, started in 2007, and and this remains as an open and ongoing work item [51], and many new methods have been proposed and evaluated. This important evolution in wireless system design and test will be

further discussed in the following sections.

The goal of OTA testing is to perform radiated measurements of a wireless device as a unique element (terminal with mounted antennas inside an emulated propagation environment), thus characterising the device performance alongside a defined test methodology and predefined performance metrics. Currently, there is a good understanding among industry and many facilities have been built to perform OTA testing for 2G, 3G and 4G mobile devices working in frequencies up to 7 GHz. Traditional metrics used to evaluate the performance of the devices are Total Radiated Power (TRP), Total Isotropic Sensitivity (TIS), Throughput, Antenna Efficiency, antenna correlation, Block Error Rate (BLER), among others [10, 17, 52–54].

With the upcoming 5G technology, OTA tests methods will be inevitably needed as one of the enabling technologies to bring mmWave connectivity into service. Here high gain, very directive, narrow beams with adaptive steering antennas arrays will be used to compensate the high path loss of the signal, fundamental to the operation of such systems. Therefore, it is very important to design a test method which allows hardware emulation of real-life dynamic scenarios where the characteristics of active array antenna systems embedded in the UE and at the BS can be effectively and robustly tested.

3.2 Definition of Near Field and Far Field

Testing the performance of the devices can be realized either in the radiated Near-Field (NF) region also known as Fresnel region of the DUT or in the Far-Field (FF) region also called Fraunhofer region, as stated in [55]. The far field region is usually considered as the distance were the curvature of the spherical wavefront at the edge of the device under test has a phase difference of 22.5 degrees compared to the centre of the device [56]. Not all performance tests can be done with the DUT placed in either region or with a unique method, hence it is necessary to define what requirements can be tested by each candidate. The minimum measurement distance between the probe antenna and the DUT to be in the near field is given by equation (3.1) [56]

$$M_{dist} > 0.63 * \sqrt{\frac{D^3}{\lambda}} \tag{3.1}$$

where D is the antenna diameter of the DUT, and λ is the wavelength.

And the far-field distance boundary is given by equation (3.2)

$$M_{dist} > \frac{2 * D^2}{\lambda} \tag{3.2}$$

Typically, the near-field measurements are used to measure the TRP of the device, the peak Effective Isotropic Radiation Pattern (EIRP), and the adjacent channel leakage ratio (ACLR).

The far-field measurements allow to further detailed characterisation of the device compared to near-field. Parameters such as Error Vector Magnitude (EVM), power spectrum, Block Error Rate (BLER), throughput, etc [15]. The methodology proposed in this thesis offers a highly novel solution for the performance testing of the Beam Management features of the devices, as well as the Radio Resource Management (RRM) requirements specially for dynamic channels. Depending on the size of the DUT the measurement distance using traditional test methods can be too large. A comparison of the different measurement regions boundaries for 28 GHz and 39 GHz is shown in Fig. 3.1.

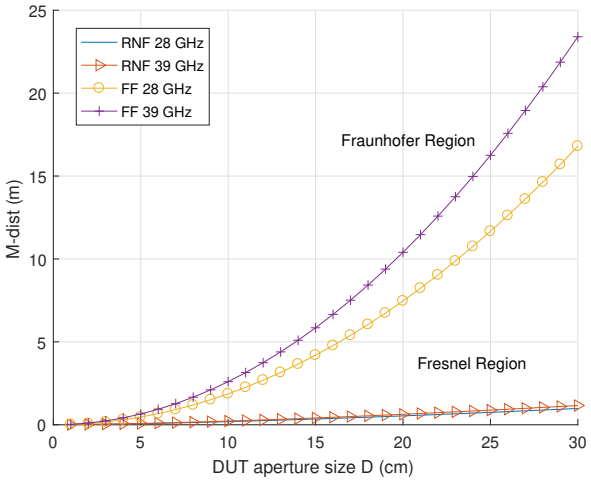

Figure 3.1: Measurement distances with respect to DUT antenna diameter

Considering that an average DUT antenna diameter is 15 cm, it can be observed that at 28 GHz the far-field region would be at approximately 4.2 m and for 39 GHz it would be at approximately 5.8 m. The near-field region for such devices would be at approximately 41 cm. Based on these results, it was considered that the dimensions of the proposed OTA test method should be chosen such that the measurement distance between the probe antenna and the DUT is 4.1 m, which approximates the far-field distance. Further details are given in chapters 5 and 6.

3.3 Conductive test method

Traditionally the performance of a wireless device's antenna has been measured in a passive way obtaining its radiation pattern in an anechoic chamber [51]. The device's conformance and performance testing are done through connecting a pair of cables into the device's temporary antenna port connectors. The test system comprises of BS emulator, a wireless channel emulator, and the DUT as illustrated in Fig. 3.2.

The BS signal emulator generates RF signals and associated control, which are fed to the channel emulator which reproduces a wireless signal propagation environment based on path

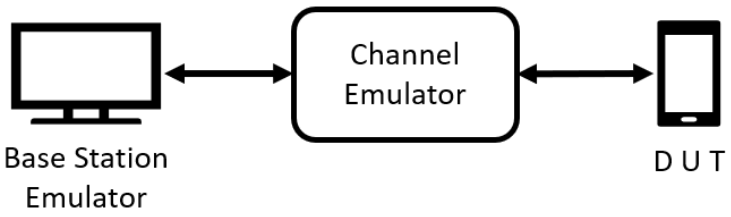

Figure 3.2: Conductive test method block diagram.

loss, fading and Doppler spread. These signals are directly connected to the DUT. This help to characterize the SISO UE under controlled and repeatable conditions without the influence of the antenna [10], although this is the major shortcoming of this technique.

However, as mentioned before by bypassing the antennas it is not possible to have a complete picture of how the device will perform in real conditions. Nevertheless, for early phones, it was not much of a problem since they usually operated in one band and had customised antenna with a fixed length according to its operation band and had intrinsically a good performance. In today's and upcoming networks obtaining the desired dynamic antenna pattern response from mobile devices is crucial because these are becoming thinner, with larger screens which require larger batteries, meaning there is less space for the RF components that could mean a compromise in performance, due to more elements interfering with the radiation characteristics of the device and have a larger impact at high frequencies.

3.4 Over the Air test methods for SISO and MIMO devices

There are two SISO OTA test methods currently approved for sub 6 GHz systems, which are the anechoic chamber and the Reverberation Chamber (RC) [51]. There are two further methods approved for MIMO OTA testing being the Multi-probe Anechoic Chamber (MPAC) and the Radiated Two Stage (RTS) method. However, to emulate an evolving dynamic angle of arrival test environment at mmWave frequencies, none of the above methods can be directly used because they are not either technically capable or would be very expensive to implement[19].

3.4.1 Multi-Probe Anechoic Chamber

MPAC testing method is capable of emulating multipath environments. Testing is performed within an anechoic chamber, where a set of probe antennas are placed in a ring distribution inside surrounding the DUT. Each antenna transmits signals with a specific temporal and spatial characteristics for testing MIMO devices, produced by the BS emulator and the Channel Emulators. The minimum number of antennas for a full ring must be 8 [10], each of one must be separated 45 degrees and the applicable channel model is the Spatial Channel Model Extension (SCME) Urban Macro / Urban Micro cell (UMa / UMi). For the case of a Single cluster, minimum

3 probes are needed [11]. The channel emulator appropriately distributes the signals with the desired properties of fading, correlation, delay, etc. The 8 or more antennas configuration placed as a ring allows to generate an arbitrary number of clusters with related angle spreads. Figure 3.3 depicts a 2D setup, where the ring of probes is located in the azimuth plane only. A 3D configuration could be built when emulation of the elevation domain is also required. However generally, this is not required for devices up to 4G technology because the received signal [11, 51].

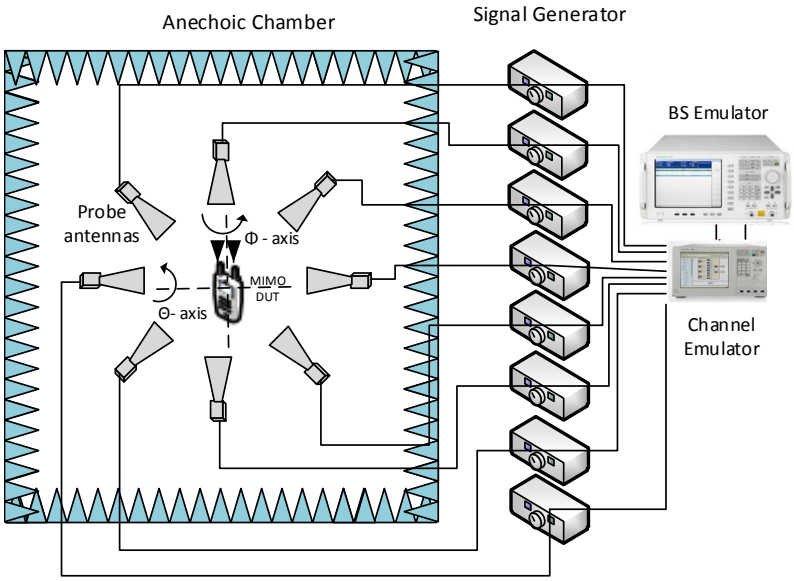

Figure 3.3: Multi-probe anechoic chamber setup

Importantly for the research being consider here, a Quiet Zone (QZ) inside of the ring can be defined. This is the area where the signal strength and the phases are carefully controlled and illuminate the DUT with nearly uniform amplitude and phase [11]. Inside of the QZ, there is a smaller Test Zone (TZ) as shown in Fig. 3.4. The TZ is defined as the area within which the correlation of the test signals can be controlled to create an arbitrary 2D spatial channels. TZ must be larger than the maximum antenna separation on the DUT [15]. Current 4G devices support 2x2 or 4x4 MIMO whose antennas locations are usually unknown, and the radiation pattern is considered quasi-omnidirectional with unknown polarisation, therefore the TZ ought to be larger than the physical dimension of the DUT. With 8x2 probes provide an ideal test zone of 0.7λ, rising to 1.6λ with 16x2 probes [11, 57, 58]. The size of the TZ is determined by the number of probes, the more the larger it becomes, and their angular separation. Additionally, the size of the Test Zone (TZ) is determined by the angular spacing of the probes and the minimum number of probes is approximated by $K = 2\lceil 2\pi r + 1 \rceil$, where r is the radius of the cylinder test zone in wavelengths, and $\lceil . \rceil$ is the integer ceiling operator [59, 60].

The MPAC method could be used in principle for testing devices above 6 GHz but it presents two important issues from the implementation point of view. The first issue is the practically

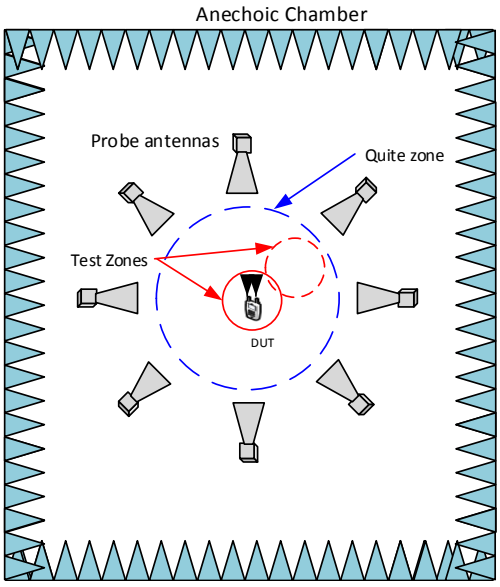

Figure 3.4: Multi-probe anechoic chamber illustrating Quiet Zone and Test Zone locations

achievable TZ size, which depends upon the angular spacing of the probes. The second issue is that for higher frequencies a 3D environment must be emulated, and therefore additional probes must be added in elevation. To create a sufficiently large TZ at mmWave frequencies might require over 100 probes in 2D azimuth alone, plus more in elevation. This many antennas installed in an anechoic chamber will lead to unwanted mutual coupling between probes which will affect the minimum size of the chamber [19, 61]. Further, a non-technical concern with a full 3D MPAC is the complexity and high cost of multiple millimetre wave RF hardware chains.

3.4.2 Reverberation Chamber (RC)

A Reverberation Chamber (RC) is a metallic cavity, which is used to emulate a rich multipath environment. By definition, a reverberation chamber is “a metallic cavity or cavities that can emulate an isotropic multipath environment which represents a reference environment for systems designed to work during fading, similar to how the free space “anechoic” reference environment is used for test of Line-of-sight systems” [11, 38]. The reproduced channel is a Rayleigh-fading channel with isotropic scattering and is clearly not a realistic case for mmWave operation. The test setup is comprised of a BS simulator connected to a switch which will distribute the signals to the different antennas located in walls and roof. Additionally, it has mechanical metallic stirrers and a rotating platform where the DUT is held. This method has limited channel modelling capabilities. The Power Delay Profile (PDP) is limited to a single decaying exponential, the Doppler spectrum, and maximum Doppler is limited by the speed of motion of the stirrers and is difficult to obtain a repeatable MIMO fading correlation on the downlink waveform [51] as shown in Fig. 3.5 (Source:[11]).

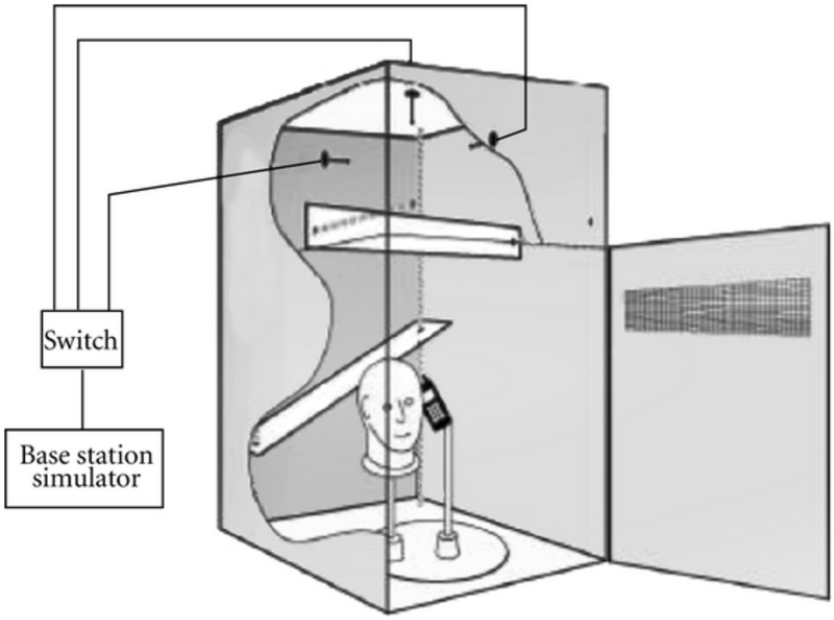

Figure 3.5: Reverberation Chamber setup.

Previously mentioned limitations are addressed by adding a channel emulator connected between the antennas and the BS simulator. The channel emulator will help to improve the PDP being programmed with fading taps set at the desired excess delays. The fading taps will also allow higher Doppler spreads. Furthermore, the correlation of the fading downlink MIMO transmission paths could be adjusted. This method can accurately emulate the PDP of a Spatial Channel Model Extension (SCME) [11]. A general setup is shown in Fig. 3.6 (Source:[11]).

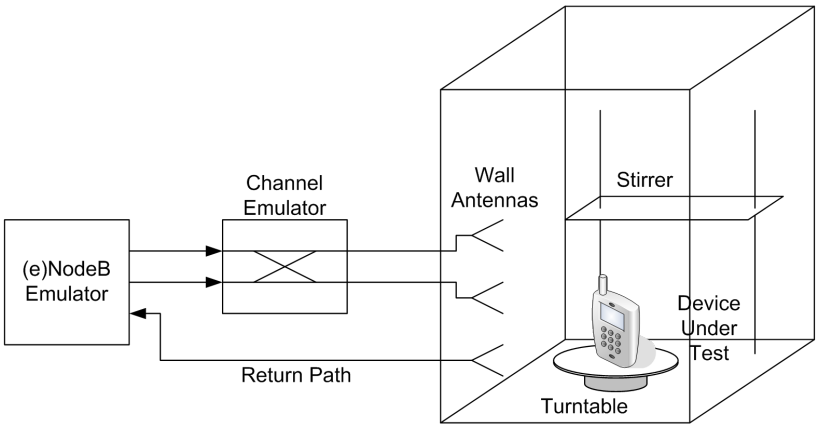

Figure 3.6: Test setup using channel emulator for a 2x2 MIMO configuration

3.4.3 Radiated Two Stage

In the Radiated Two Stage (RTS) method, the first stage required is the accurate measurement of the far-field radiation pattern of the MIMO antennas. One way of doing this is directly connecting a Vector Network Analyzer (VNA) to the antenna if available, the second way requires the mobile to have a special test mode to measure individual antenna's amplitude and relative phase response. Figure 3.7 illustrates a high-level implementation of this method.

For the second stage, the radiation patterns are convolved (mathematically combined) with the chosen MIMO OTA channel model in a channel emulator. The channel model may be chosen from the correlation or geometry approximations. The test signal obtained represents the faded downlink signal what the DUT would have received if it had been placed in the radiated field. This signal is fed to the DUT through the antenna connectors bypassing the antennas. In this method, it is assumed that the far-field pattern of the MIMO antennas fully captures the mutual coupling of the antenna arrays and the influence on the radiated performance. These measurements are conducted in an anechoic chamber [11, 51]).

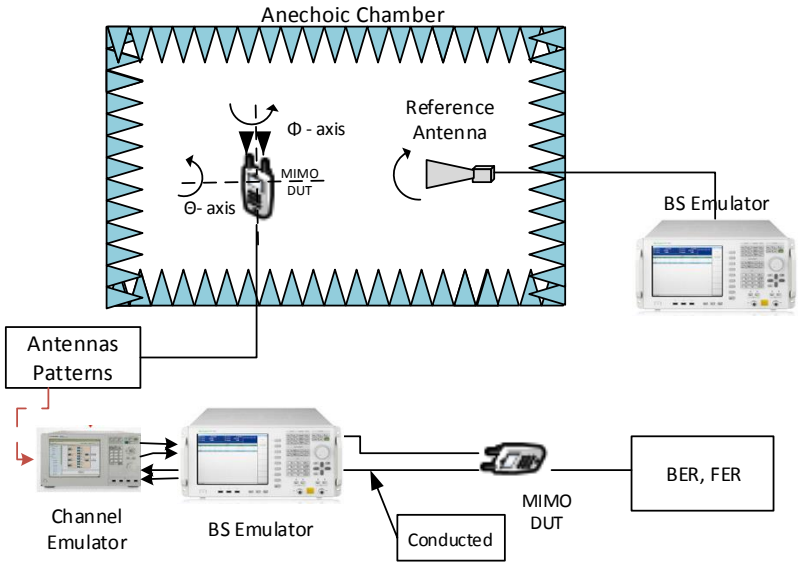

Figure 3.7: Radiated Two-stage method setup.

3.5 OTA test methods for 5G devices with static channels

3.5.1 Direct Far-Field

The Direct Far-Field (DFF) method is the simplest OTA test method and is optimised for a single direction of arrival. It is included here as it is the basic component of the more complex methods that emulate spatially dynamic environments. The method consists of an anechoic chamber

where the DUT is mounted in a positioner that rotates in azimuth and elevation planes relative to the probe antenna. Depending on the size or location of the antennas and the frequency of operation the required distance for the DUT to be in the far-field with respect to the probe varies significantly. The DUT antenna must be placed at the centre of the probe antennas TZ, and this must be done for each independent antenna array needed to be characterised, or to avoid this a larger distance is required and the DUT is centred on the TZ. Due to the path losses at mmWave frequencies, it has been determined by 3GPP that for RF tests the DFF method is restricted to a maximum antenna antenna diameter of 5cm at 43 GHz [15, 17], although this restriction may be relaxed for demodulation and Radio Resource Management requirements where the level of accuracy is less critical.

3.5.2 Indirect Far-Field

As its name suggests the Indirect Far-Field (IFF) is the opposite of the DFF because the probe antenna is not looking directly to the DUT. The most common setup used in this method is known as a Compact Antenna Test Range (CATR) system, which is a standardized method by the 3GPP [62] used to characterise the radiation parameters of antennas and devices in a very small space. Conceptually it consists of a probe antenna whose diverging beam illuminates a parabolic reflector. Usually the probe antenna is situated at the focus point of the reflector [56]. The parabolic reflector collimates the original diverging beam and directs it to the DUT. The advantage of this system is that the collimated beam has a quasi-uniform amplitude and phase across its extent. This uniform amplitude emulates an ideal plane-wave front which illuminates to the DUT. The quiet zone of a CATR has typically a cylindrical shape as seen in Fig. 3.8 (Source: [63]). Another advantage of this method is that it has a smaller footprint compared with a DFF methods and also has lower path loss. Commonly the CATR are used to measure the Effective Isotropic Radiation Pattern (EIRP), TRP and Effective Isotropic Sensitivity (EIS). Furthermore, validation of beamforming and beam steering is also possible but only for static cases, which is an expensive disadvantage. To characterize the DUTs the system requires that the entire radiating volume of the device be within the quiet zone. The DUT is placed on top of a rotating positioner that allows to capture the radiated fields as a function of azimuth and elevation angles. This configuration is reciprocal so that the device can be measured either in transmit or receive mode without re positioning [64].

3.5.3 Base line measurement setup

The baseline measurement setup [17] for testing UE RRM characteristics is based on the Direct Far Field method, where the DUT is located at an equal distance from two or more probe antennas connected to emulated next generation NodeB (gNB) sources. The probes are distributed in a semicircle formation at different angular spacing from 30^o to 180^o in 30^o increments. The DUT is mounted in a positioner system with two degrees of freedom within the quiet zone, which is

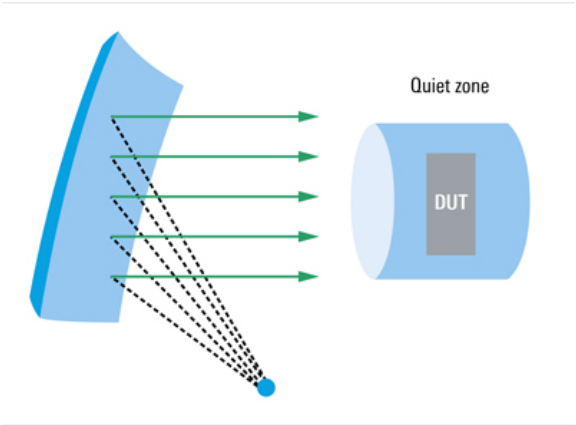

Figure 3.8: Illustration of a compact antenna test range

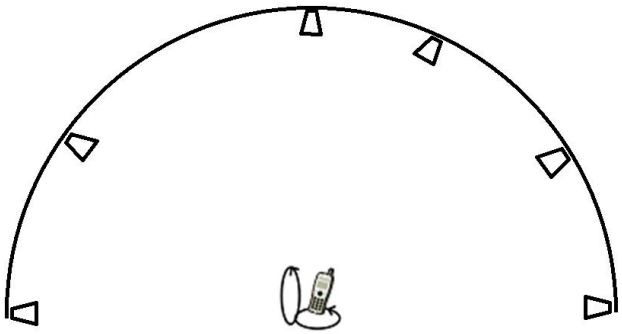

Figure 3.9: Baseline measurement setup of RRM characteristics

located at the centre of the rotational axes as shown in Fig. 3.9 (Source: [17]). For release 15 the maximum number of simultaneously active angles of arrival is two. The method allows emulation of multi-path fading propagation conditions as tapped delay line with no angular spread per cluster. The metrics for DUT RRM testing that the system needs to support are not yet fully defined by 3GPP [17, 65].

3.5.4 Simplified Sector Multi-probe Anechoic Chamber

The Simplified Sector Multi-probe Anechoic Chamber (SS-MPAC) method is a derivation of the legacy 2D MPAC method and addresses the issues of Test Zone (TZ) size at mmWave, and 3D capability, within a simplified implementation and has been proposed to 3GPP. Firstly, to address the issue with the number of probe antennas and to provide 3D coverage, only one sector of the 3D sphere is emulated. The system is then further simplified by the need to drive only a few (4 or 8) of the probes at any one time to limit the cost of channel emulator hardware. This method is useful for testing massive MIMO base stations where a sectorised approach is sufficient and is also a potential solution for testing handsets in dynamic angle of arrival environments such as Physical Random Access Channel (PRACH) testing during call setup and handover. That said, a

sectorised approach is not ideal for the UE where full 3D is required. The large number of probes are located approximately at an equal distance from the DUT with a certain angular spacing, aiming to achieve amplitude and phase coherence, the latter being a complicated target to achieve. The probe antennas will be connected to switches responsible for activating and deactivating a sub-set of the probe antennas which are fed by fading channel emulators that may require additional components such as power amplifiers, up/down converters, etc. For base station testing, a UE emulator would reproduce the testing signal [19, 61, 66]. An illustration of the components of the SS-MPAC test method are shown in Fig.3.10 (Source: [61]).

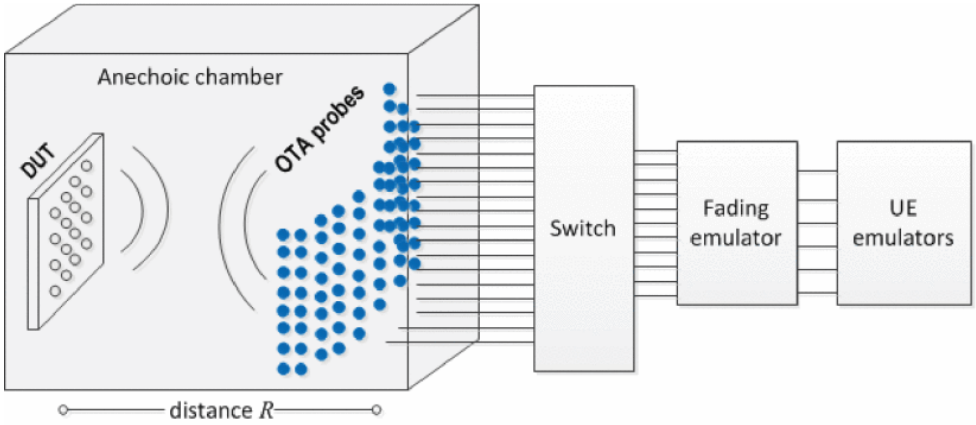

Figure 3.10: Simplified Sector Multi-probe Anechoic Chamber

3.6 Prior art using ellipsoid reflectors for OTA

As will be described and discussed below, the solution proposed in this thesis is based on the reflective properties of an ellipse. Therefore, in addition to investigating currently used and under development OTA test methods, a search for prior art concerning the use of ellipsoid reflectors was conducted because the intention was to file a patent of the proposed measurement method.

The initial proposal for a low cost mmWave OTA solution was to use of a continuous ellipsoid surface conceived in early 2018. However, prior art describing an elliptical test solution for similar technology was found. The patent US 2014/0327586 A1 [67] from 2014, whose applicant was The Howland Company from Buford, GA, US, patented a test chamber for measuring TRP, TIS, and antenna efficiency by using a “Reflective Ellipsoid Chamber” (see Fig. 3.11) (Source: [67]). This is a continuous elliptical surface with pin-point focal placement of the components and was designed to allow measurement of total radiated power, total isotropic sensitivity as well as antenna efficiency (see chapter 4 and 5 for analysis and measurement of similar structures). As stated in the patent the advantage of this system was the ability to collect all of the energy radiated by a device, in every direction, at a single point. It was not intended to create multiple directional signals with different angles of arrival. The disadvantage of this method is that

placement of the device is critical on the alignment of the antenna‘s phase centre with the focal points. Depending on the size of the chamber, small misalignments of the transmitter or receiver antennas from the focal points will cause the expected convergent signal (rays) to be offset by centimetres from the other focal point. Furthermore, as it is a full ellipsoid chamber undesirable secondary reflections will be produced, and precise measurements cannot be made, specially controlling the angles of arrival of the signals, because a full ellipsoid will create a isotropic environment. Controlling the angular distribution of the signals is particularly important for 5G mmWave devices since they will have multiple antenna modules spatially separated to create a spherical coverage and avoid blocking but objects such as a human hand. Thus, the apparatus described in the Howland patent would not work for millimetre wave device technology with directive beams for either the measurements they describe or for our intended OTA. Moreover, this approach was not followed up with commercialization. However, as the patent mentions an ellipsoid reflector in it, it was decided that any form of ellipse to shape a chamber for antenna measurements is unlikely to be patentable.

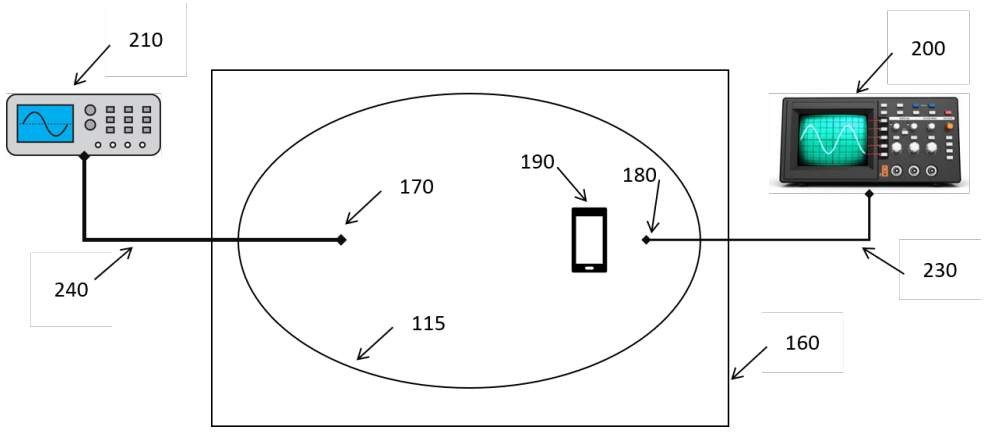

Figure 3.11: Reflective Ellipsoid Chamber from Howland

In 2013 with the patent number US8 395 558 B2, titled “Millimeter-wave Reflector Antenna System and Methods for Communication using Millimeter-wave signals” the company Intel Corporation [68] also refers to the use of discrete elliptical arc surfaces. The setup is illustrated is Fig. 3.12 (Source: [68]) . One of the goals of this system is to use multiple reflectors that combine both circular arc in the first plane and elliptical arcs in a second plane to shape the reflected beam such that it has a diverging directivity pattern in the azimuth plane, and a substantially non-diverging directivity pattern in the elevation plane. Thus, achieving a steerable beam antenna beam over a beam-scanning angle generated by a chip-array antenna.

More recently the company Rohde & Schwarz has a published patent on Over the Air test Systems and Method for Testing a device under test number US 2019 0162780 A1 [69]. This again describes an elliptical test structure and a with a continuous reflecting surface facing (claim 7) and in claim 11 use of a partially elliptical shaped reflector. Figure 3.13 (Source: [69]) shows a

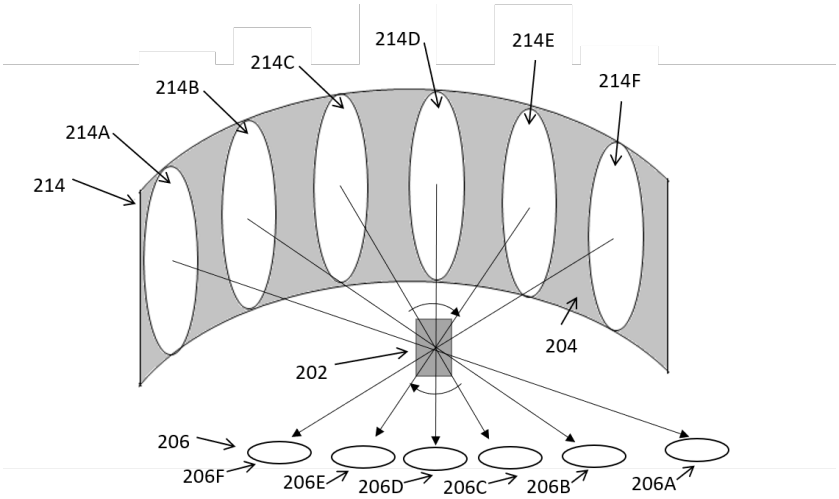

Figure 3.12: Millimetre-wave Reflector Antenna System and Methods for Communication using Millimetre-wave signals

schematic of test system mentioned in the patent. The test system comprises an elliptical (16), the measurement antenna (14) and a device under test (18) located at the focal points, shielding member of the main lobe (42), and a positioner among other elements fully described in the patent. This system is intended for testing a DUT in a wireless communication environment which enables to test the receiving properties of the device from different impinging angles of the signals. It is important to notice that claim 16 “signals are received in the far field” according to the author of this thesis, this claim is not accurate, as it would be analysed and shown in later chapters an elliptical surface will not produce this effect. This again describes an elliptical test structure and a with a continuous reflecting surface facing (claim 7) and in claim 11 use of a partially elliptical shaped reflector. Further, this system is very susceptible to physical misalignments. In order accurately test the performance of smartphones like size devices, the reflected rays should have covered the whole Test Zone area and device and this system will not offer the OTA testing zone required.

3.7 Figures of merit

Previously some of the figures of merit such as TRP, and TIS among others used in current OTA test methods and were mentioned, thus in this section a summary of the principal measurements is detailed.

3.7.1 Effective Isotropic Radiation Power (EIRP)

The EIRP is the actually transmitted power-level. The EIRP of each polarisation $EIRP_\theta$ and $EIRP_\phi$ is calculated by adding the composite loss of the entire transmission path and the

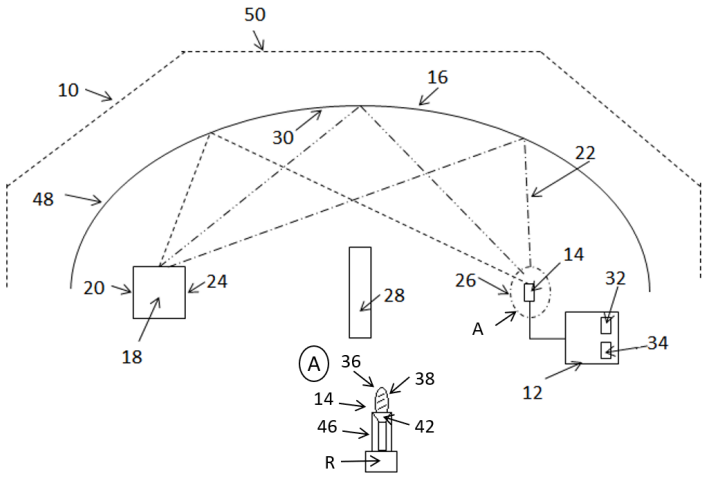

Figure 3.13: Schematic of the test system in the Rohde & Schwarz patent

measured power in logarithmic scale. The procedure to measure the beam peak direction in transmission mode of the UE is found with a 3D EIRP scan, individually for each orthogonal polarisation. The step size of the grid is 2.5 degrees which is equivalent to 10224 sample points. To make this measurement the beam of the DUT must be locked during the entire test. The mean power of the modulated signal is captured with either a spectrum analyser, power meter or a gNB emulator. The total EIRP is the sum of both polarisations as given by 3.3

$$EIRP = EIRP_\theta + EIRP_\phi \tag{3.3}$$

3.7.2 Total Radiated Power (TRP)

The TRP is a measure of how much power the antenna actually radiates, when non-idealities such as mismatch and losses in the antenna are taken into account. The TRP is defined as the integral of the power transmitted in different directions over the entire radiation sphere [38] is given by 3.4:

$$P_{TRP} = \frac{1}{4\pi} \oint \left(P_{tx} G_\theta(\Omega; f) + P_{tx} G_\phi(\Omega; f) \right) d\Omega \tag{3.4}$$

Where P_{tx} is the transmit power, $G_\theta(\Omega; f)$ and $G_\phi(\Omega; f)$ are the polarisation components of the gain pattern for the handset antenna measured at the frequency f, and Ω is the solid angle describing the direction.

The TRP value for the uniform measurement grid is calculated using [17]

$$TRP = \frac{\pi}{2NM} \sum_{i=1}^{N-1} \sum_{j=0}^{M-1} \left[EIRP_\theta(\theta_i, \phi_i) + EIRP_\phi(\theta_i, \phi_i) \right] sin(\theta_i) \tag{3.5}$$

Where N is the number of angular intervals in the nominal theta range from 0 to π and M is the number of angular intervals in the nominal phi range from 0 to 2π.

The TRP values for the constant density grids are calculated using:

$$TRP = \frac{1}{N}\sum_{i=1}^{N-1}\left[EIRP_{\theta}(\theta_i,\phi_i) + EIRP_{\phi}(\theta_i,\phi_i)\right] \tag{3.6}$$

where N is the number of measurement points.

3.7.3 Effective Isotropic Sensitivity (EIS)

By definition, the beam peak direction in reception mode is where the maximum total component of Received Signal Radiation Power (RSRP) is found [17]. It is found with a 3D RSRP scan individually for each orthogonal polarisation with the same number of sample points as 3D EIRP scan. EIS_{θ} is the power level for the θ-polarisation at which the throughput exceeds the requirements for the specified reference measurement channel. EIS_{ϕ} is the power level for the ϕ-polarisation at which the throughput exceeds the requirements for the specified reference measurement channel The resulting EIS for the total component is given by 3.7

$$EIS = \left[\frac{1}{EIS_{\theta}} + \frac{1}{EIS_{\phi}}\right]^{-1} \tag{3.7}$$

3.7.4 Error Vector Magnitude (EVM)

"The Error Vector Magnitude is a measure of the difference between the reference waveform and the measured waveform. This difference is called the error vector. Before calculating the EVM, the measured waveform is corrected by the sample timing offset and RF frequency offset. Then the carrier leakage shall be removed from the measured waveform before calculating the EVM" [70].

The beam is locked during the entire test toward that direction the maximum total component of EIRP is found. The EVM_{θ} and EVM_{ϕ} for the θ and ϕ-polarisations of the modulated signal arriving is measured with signal analyser, or gNB emulator. The results of the EVM_{θ} and EVM_{ϕ} are compared against the test requirement. If either meets the requirement, it is considered that the UE passes [17].

3.7.5 Radio Resource Management (RRM) testing

In the 3GPP technical report 38.810 several testing methodologies for NR UE are described, as well as the procedures for testing the UE RRM, demodulation and channel system information (CSI) requirements. In this technical report it is also detailed suitable OTA test methods for static scenarios whereas for dynamic scenarios the requirements are still to be determined. For sub 6 GHz frequency bands it is assumed that antenna connectors are available at the DUT and OTA

testing is considered as the baseline approach for 5G NR UE RRM, demodulation and CSI test methodology. Performing conductive tests using an intermediate frequency IF testing excludes all components which operate at the radio frequency such as RF filters, duplexers, transmit receive switch, low noise amplifier (LNA),power amplifier (PA), analogue beamforming phase shifting elements etc., and the algorithms which control such components from the test. Therefore, testing the performance of these must be performed via OTA methods [17].

Some of the capabilities that a UE RRM baseline measurement setup shall fulfil are listed below

- Emulation of up to 2 NR transmission reception points (TRxPs). For Non-standalone (NSA) NR devices, the test setup shall emulate in addition 1 LTE cell. The emulated LTE cell provides a stable LTE signal without precise propagation modelling or path loss control between it and the DUT. No performance verification for LTE carriers is supported.

- N dual-polarised antennas transmitting the signals from the emulated gNB sources to the DUT. The antennas transmit into the test zone in such a way that signal polarisation does not prevent the DUT receiving a consistent, predictable power level. Wanted and noise (AWGN) signals can be transmitted from one or both active probes.

- Test method shall allow modelling of propagation conditions between the DUT and the emulated gNB sources such as static multi-path fading propagation conditions.

For the case of UE demodulation and CSI testing some of the key aspects that the baseline setup should be capable of are listed below:

- The test is conducted in an anechoic chamber, and shall be performed in the radiative near field or in the far field

- The test method shall allow modelling of multi-path fading propagation conditions between the DUT and the emulated gNB sources, and static propagation conditions. The Baseline setup includes a capability to select the best UE beam during initial call setup. For setups intended for measurements of UE demodulation and CSI characteristics in NSA mode, an LTE link antenna is used to provide the LTE link to the DUT. The LTE link antenna provides a stable and noise-free LTE signal without precise path loss or polarisation control. No performance verification for LTE carriers is supported.

- The test system shall allow modes noise emulation for UE demodulation testing such as simulation of fixed SNR conditions at the DUT, and emulation of noise-free conditions at the DUT

3.7.6 Definition of the Test Zone volume

For indirect far field test systems such as the compact antenna test range previously mentioned in subsection 3.5.2 and in [17], an standardized definition of the Quiet Zone (QZ) is the region with an amplitude taper of less than 1 dB, amplitude ripple of ±0.5dB in amplitude and ±5 deg in phase [71]. These specifications allow the representation of a pseudo plane waves and are illustrated in Fig. 3.14 (Source: [71]). The amplitude taper is measured as the variation of a second-degree polynomial function, which is obtained by means of a least squares best fit through the amplitude data over a cut through the QZ in dB. Similarly, the amplitude ripple is measured by determining the variation of the amplitude about the second-degree polynomial fit also expressed in dB. And the phase ripple is the deviation from a best fit straight line over the QZ expressed in degrees [72].

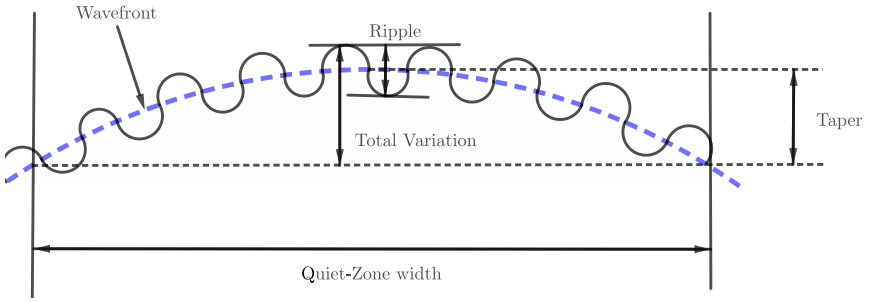

Figure 3.14: Illustration of amplitude taper and amplitude ripple specifications in the Quiet-Zone

In IFF systems the amplitude taper in the quiet zone is produced mainly by the antenna pattern of the feeder and the space attenuation due to propagation of the signal. As the feeder antenna is not isotropic, nor a perfect source point, its pattern has a directivity which means that the amplitude of the signal varies with direction. Thus, the portion of the feed pattern that illuminates the surface reflector, is directly transferred into the quiet zone, thus causing additional deviations from the ideal uniform plane wave [72].

Ideally the low-cost OTA test method should also be able to approximate a far-field like signal at the test zone volume from different angles of arrival. These mandatory characteristics will be analysed for each type of candidate system with different reflectors in the following subsections. The candidate system should be able to generate a test zone volume sufficiently large to allocate real-life mobile devices such as smartphones. According to the recommendations of 3GPP the QZ for smartphones shall be considered a sphere with radius of $R = 10$ cm [55]. However, the Test Zone evaluated here is a cube centred at one of the focal points of the ellipse whose edge length E_{TZ} is twice the radius of the sphere, thus $E_{TZ} = 2R = 20$cm. Both the 3GPP QZ and the TZ are illustrated in Fig. 3.15.

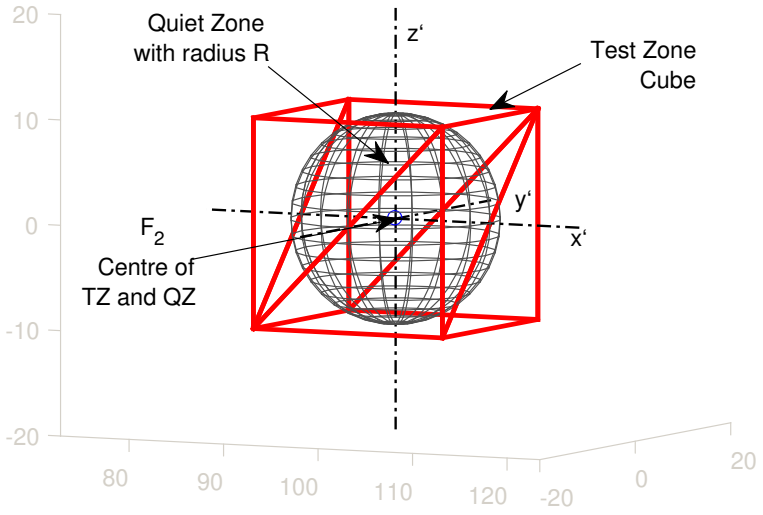

Figure 3.15: Test Zone volume and Quiet Zone illustration (Axis given in cm)

3.8 Challenges for testing 5G NR devices

To ensure mmWave devices perform effectively several challenges exist related to OTA measurements, mainly because UEs are expected to perform beamforming to acquire and track the signals transmitted by the base station. Thus, proposing and validating a robust method to test moving beams, in the presence of interference and scattering is a significant challenge.

The simplest operating environment for a 5G mmWave device is when the UE is in direct line of sight of the BS and the signal arrives at the UE from a constant angle. A more likely scenario is when one or more signals arrive at the UE from different directions due to static reflectors (e.g., walls, windows) or from different BS. These types of scenarios can be emulated by the 3GPP baseline RRM measurement setup [17] as previously described. However, the most typical operating scenarios are when the UE is moving, or the reflected signals are produced from moving objects such as vehicles, moving people or even just by the movements of the human hand. These spatially dynamic scenarios result in the UE having to constantly search and acquire suitable cells or BS, as well as tracking signal direction, switching between beams and cells, and providing feedback on signal conditions in order to maintain the call or data session active.

In comparison with sub 6 GHz systems, space is a new measurement dimension which is added in 5G. In typical operating environments, an effective mmWave test method must be able to emulate both static and dynamic three dimensional (3D) real-life environments with at least two simultaneous variable angles of arrival. Further, as the signal direction can change direction very rapidly, it would be best to avoid having mechanically moving parts, as these add complexity and normally do not respond sufficiently fast for this application. In addition, the system should

be compact and cost-effective to be affordable by industrial and academic laboratories working on 5G mmWaves technologies [16].

Another important challenge is that the UEs will include several individual active antenna modules, each of which needs to be characterised. The characterisation of this modules should be tested individually as well as jointly which increases the difficulty and the time required to test the UE during production.

Testing the performance of UEs could be performed in two ways. The first approach is known as “white box”. This is based on prior knowledge of the positioning of the antenna array module or modules. The position(s) can be known either if the manufacturer of the device provides the designs of the device or by near-field scanning. The advantage of this approach is that the phase centre of the device can be placed at the centre of the test zone, obtaining very accurate results. Also, as the “D” antenna diameter is known the far-field distance can be reduced. The second approach is known as “black box”. In this case the position of the antenna modules are not required, and the centre of the DUT is placed at the centre of the test zone. For this approach the far field region is at a longer distance because “D” is much larger, but the device does not need to be repositioned for testing. Figure 3.16 shows some examples of the possible location of the antenna modules, where the double arrow is showing the length of “D” depending on the configuration of the antenna modules. However, for conformance testing only the “black box” approach would be used as the device manufactures prefer not to declare the antenna structure [15].

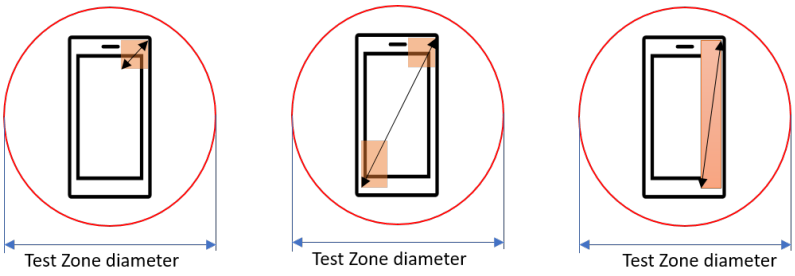

Figure 3.16: DUTs inside test zone showing the length of the “D” antenna diameter depending on the position of the antenna arrays.

3.9 Conclusions

As 5G technology evolves to work at mmWave frequencies OTA testing becomes essential because the active antenna systems which are highly integrated with the DUT therefore it will be physically impossible to connect the DUTs to the test equipment by cables.

The MPAC method technically could be used for testing devices above 6GHz but it presents some important issues especially from the implementation point of view:

1. The first one corresponds to the Quite Zones and the Test Zone sizes, which depend upon the size of the anechoic chamber, the number of probes, and the angular distribution of them.

2. The second one is that for higher frequencies a 3D environment must be built and therefore a second ring has to be added with its corresponding probes.

3. Directly related to the two previous points is the necessity of connecting a channel emulator to each probe antenna.

4. A large number of antennas installed in an anechoic chamber will suffer from mutual coupling, therefore adequate separation between them is required and this again will affect the size of the chamber.

All these factors coincide in one non-technical concern which is extremely high costs of implementation. Technically speaking the size of the test zone with 8x2 probes separated 45 degrees has a test zone of 0.7λ to 1λ, that for the case of 2600 MHz gives approximate 12 cm, whereas for 30 GHz it will reduce to approximately 25 mm which is extremely small and impossible to fit any physical device.

The RTS method is a cost effective method for sub 6 GHz and mainly relies on measuring the antenna pattern which in the second stage will be convolved with the required channel, like this it is possible to create the adequate signal to be used for testing the DUT. Systems working at frequencies above 6 GHz will rely on steerable antennas and there is not an obvious role in black box conformance testing of devices.

The main issue of the RC method is that although it can create stochastic reflections, there is no way to specifically control the direction of each reflection and that mainly the environment recreated is isotropically. Test have been carried out in investigating the feasibility of extending the frequencies of RC to 40 GHz. The chamber transfer function was measured obtaining more than 20 dB of loss for frequencies above 28 GHz with respect to sub 6 GHz with an unloaded chamber. Loading the chamber with absorbers increases the losses the given RMS Delay Spread varies from 70 to 43 ns at 28 GHz. The tests conclude that acceptable and realistic loss level is achievable, no control over the direction of arrival has been done and this is a very important feature that must be evaluated to 5G devices.

The standardisation bodies must define all the required measurement metrics related to testing the operation and performance of the beamforming such as beamforming gain, beam tracking ability, Error Vector Magnitude on the beam centre etc, these cannot be performed in a cable conductive way, therefore new suitable test methods are required.

CHAPTER 4

RAY TRACING ALGORITHM

4.1 Introduction

In order to design and analytically evaluate the proposed OTA candidate architectures, a ray tracing algorithm was developed in MATLAB. Here, the Forward-Ray Tracing method was adopted, which consists in casting rays from a source point (in this case from the focal point where the feeder antenna or transmitter is located) until they reach an object. The algorithm only considered specular reflections, and not diffuse reflections, thus, assuming that there was only one reflected ray for each incident ray.

The surfaces considered in this model for the reflectors exhibit an ideal electric conducting property (ability of a material to conduct electrical current) also referred as Perfect Electric Conductor (PEC). The electric conductivity of metals such as, aluminium and copper used in the prototype as the reflectors are in the order of $10^7 - 10^8$ (Siemens/ metre). It is assumed that the electromagnetic field below or behind the surface of a PEC material is zero, which means that the wave is completely reflected. According to the boundary conditions, the tangential components of the electric field must vanish at all points along the interface [56].

Ray launching Geometrical Optics techniques are applicable to high-frequency field problems and used to compute electromagnetic scattering from large objects, usually in the range of twenty wavelengths or higher[73]. It is an asymptotic method ("methods for expanding functions, evaluating integrals, and solving differential equations which become increasingly accurate as some parameter approaches a limiting value"[74]) which uses principles of Geometric Optics (GO) to calculate the scattered fields. It is important to note that the term scattered fields and reflected fields throughout the remainder of this thesis mean the same and would be used interchangeably. High frequency fields exhibit a local plane wave nature where the properties of the medium and scatterer size vary little over an interval on the order of a wavelength[73].

A flow chart of the main building blocks of the ray tracing algorithm is shown in Fig. 4.1. Firstly, the variables such as the dimensions of the ellipse, frequency, angular granularity of the rays and the kind of reflector to be analysed are defined. Secondly, the candidate architecture to be analysed is specified which includes the creation of the reflectors, calculation of the electric (E) fields of the transmitter antenna, creation of the receiver plane which represents the test zone area, and the translation to the corresponding focal points is performed. Thirdly, the rays are launched following the previously defined antenna pattern. If the ray intersects the reflector then a second ray is launched from that point with the corresponding direction of reflection. Lastly, the second ray looks if it intersects the receiver plane. If true, parameters such as amplitude, phase, angles of departure, arrival, total distance of the ray, intersecting point at the receiver plane are calculated, stored and displayed. A detailed description of the subroutines and algorithms is given in the following subsections.

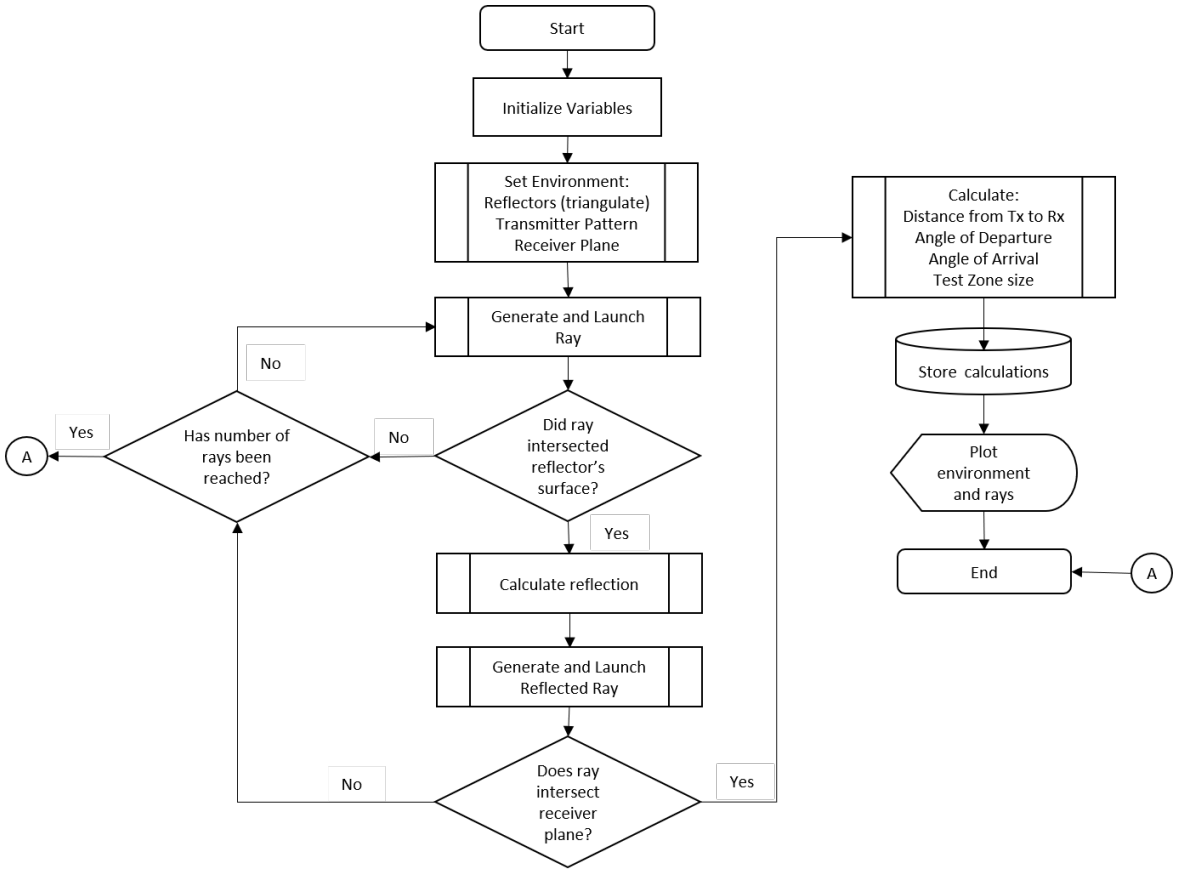

Figure 4.1: Flowchart of customized ray tracing algorithm for mmWave OTA analysis.

4.2 Specification of Candidate Architecture

This consists of calculating the reflectors, the feeder antenna pattern and the receiver plane positions. The mathematical expressions and algorithms used to compute all these elements are described below.

4.2.1 Transmitter radiation pattern

As the proposed OTA test methods are based on reflectors, they require a radiating element that will illuminate them, which in general terms could be accomplished by kind of antenna for example slot antennas, open-ended waveguides, horn antennas, lens antennas, etc. The radiation fields are determined from the shape and size of the antenna. In this thesis, this was analysed for the effects of a pyramidal horn antenna as it was adopted in later experimental validation work described in chapter 7.

4.2.1.1 Point source

A point source can be used as the feeder antenna because it radiates equally in all directions as depicted in Fig. 4.2. In terms of GO it radiates a spherical wavefront. The field radiated by a point source is given by eq. (4.1) [56].

$$E(\theta,\phi) = \frac{e^{-jkr}}{r} \tag{4.1}$$

Where, k is the wavenumber and r is a distance from the source point.

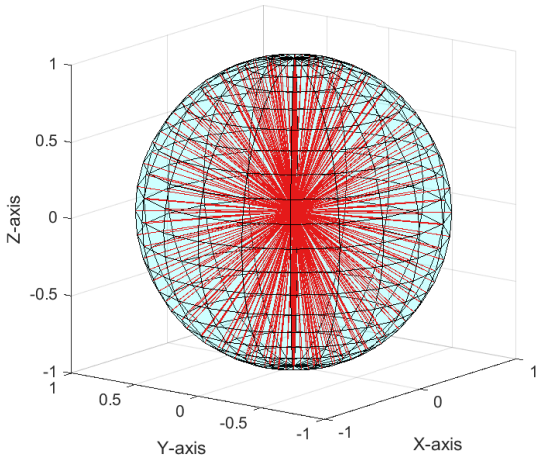

Figure 4.2: Representation of a Source Point, and the rays being propagated from it (axis normalised to a unit scale of 1).

4.2.1.2 Pyramidal horn antenna

A pyramidal horn antenna (see Fig. 4.3, Fig. 4.4, Fig. 4.5 (Source: [56] Chapter 13)) was used to test and characterise the prototypes later on, therefore it was modelled as the feeder of the ray tracing algorithm. The tangential components of the E- and H- fields over the aperture of a horn pyramidal antenna can be mathematically approximated by (4.2) and (4.3) respectively [56].

$$E = -j\frac{kE_o e^{-jkr}}{4\pi r}[sin\phi(1+\cos\theta)I_1 I_2] \tag{4.2}$$

$$H = j\frac{kE_o e^{-jkr}}{4\pi r}[cos\phi(1+\cos\theta)I_1 I_2] \tag{4.3}$$

where, k is the wavenumber, r is the distance to the observation point. The terms I_1 and I_2 are given by (4.4) and (4.5)

$$\begin{aligned} I_1 = \frac{1}{2}\sqrt{\frac{\pi\rho_2}{k}}(e^{j(k_x'^2\rho_2/2k)}\{[C(t_2')-C(t_1')]-j[S(t_2')-S(t_1')]\} \\ +e^{j(k_x''^2\rho_2/2k)}\{[C(t_2'')-C(t_1'')]-j[S(t_2'')-S(t_1'')]\}) \end{aligned} \tag{4.4}$$

$$I_2 = \frac{1}{2}\sqrt{\frac{\pi\rho_2}{k}}(e^{j(k_x'^2\rho_2/2k)}\{[C(t_2')-C(t_1')]-j[S(t_2')-S(t_1')]\}) \tag{4.5}$$

where t_1', t_2',t_1'',t_2'', k_x' and k_x'' are give by and C and S are the complex Fresnel integrals which are tabulated in Appendix IV of [56].

$$t_1' = \sqrt{\frac{1}{\pi k\rho_2}}\left(-\frac{ka_1}{2}-k_x'\rho_2\right) \tag{4.6}$$

$$t_2' = \sqrt{\frac{1}{\pi k\rho_2}}\left(+\frac{ka_1}{2}-k_x'\rho_2\right) \tag{4.7}$$

$$k_x' = k\sin\theta\cos\phi+\pi/a_1 \tag{4.8}$$

$$t_1'' = \sqrt{\frac{1}{\pi k\rho_2}}\left(-\frac{ka_1}{2}-k_x''\rho_2\right) \tag{4.9}$$

$$t_2'' = \sqrt{\frac{1}{\pi k\rho_2}}\left(+\frac{ka_1}{2}-k_x''\rho_2\right) \tag{4.10}$$

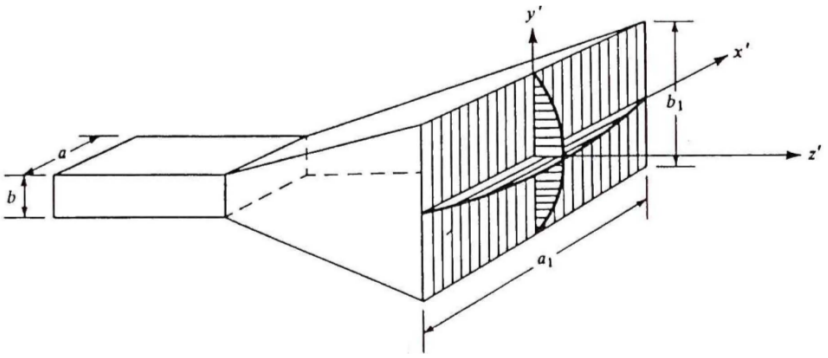

Figure 4.3: Pyramidal horn

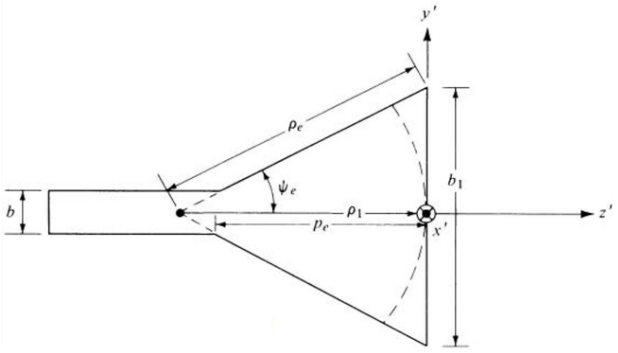

Figure 4.4: E-plane view of the pyramidal horn

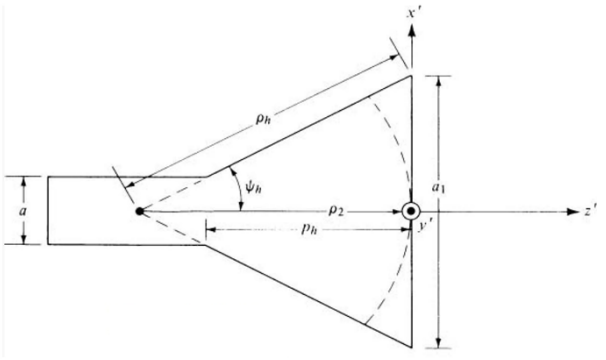

Figure 4.5: H-plane view of the pyramidal horn

(4.11) $$k_x'' = k \sin\theta \cos\phi - \pi/a_1$$

where ρ_1, and ρ_2 are the distances shown in Fig. 4.2 and Fig. 4.3.

The dimensions chosen of the antenna where based on the measurements taken from the Flann dual polarized horn antenna, model DP241 AB, that was used during the tests of the prototype. The aperture of the antenna was symmetrical, thus $a_1 \approx a_2 \approx 4\lambda$ and the lengths of $\rho_1 \approx \rho_2 \approx 9\lambda$. With these dimensions, the calculated beamwidth was approximately 15 degrees and the directivity was 21 dBi. The beam pattern of the antenna measured in the anechoic

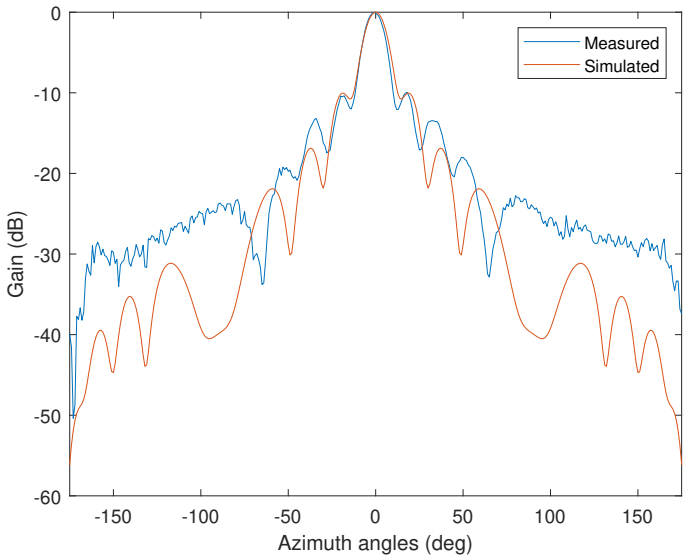

Figure 4.6: 2D field pattern of pyramidal horn measured and simulated (Gain relative to boresight)

chamber and the simulated with eq. 4.2 is shown in Fig. 4.6.

The instantaneous E-field intensity is a complex number and is measured in Volts per metre (V/m). The instantaneous H-field intensity is also a complex number and is measured in Amperes per metre (A/m).

4.2.2 Directivity and Gain

The directivity of the antenna is defined as the ratio between the radiation intensity $U(\theta,\phi)$ of the antenna in a given direction to the radiation intensity averaged over all directions. The average radiation intensity is the total radiated power P_{rad} over 4π (see eq. 4.12). The directivity is often measured in logarithmic scale (dBi isotropic decibels) [56].

$$D(\theta,\phi) = \frac{\text{radiation intensity}}{\text{total radiated power}} = \frac{4\pi U(\theta,\phi)}{P_{rad}} \tag{4.12}$$

The gain of the antenna is closely related to the directivity but takes into account the efficiency of the antenna. It is defined as "the ratio of the intensity, in a given direction, to the radiation intensity that would be obtained if the power accepted P_{in} by the antenna were radiated isotropically. The radiation intensity corresponding to the isotropically radiated power is equal to the power accepted by the antenna divided by 4π" (see eq. (4.13) [56].

$$G(\theta,\phi) = \frac{\text{radiation intensity}}{\text{total accepted (input) power}} = \frac{4\pi U(\theta,\phi)}{P_{in}} \tag{4.13}$$

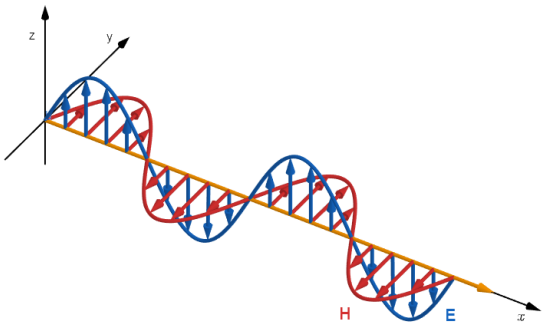

Figure 4.7: Linearly polarized electromagnetic wave propagating in the x-axis direction. The blue arrows represent the time-varying E-fields parallel to the $z-axis$, and the red arrow represent the H-fields.

The antenna radiation efficiency η of the antenna relates the total power radiated from the antenna P_{rad} to the power accepted by the antenna P_{in}. It only takes into account the losses of the antenna itself such as conductive and dielectric losses and do not consider matching. Thus, directivity and gain are related according to eq. (4.14)

$$G(\theta,\phi) = \eta \cdot D(\theta,\phi) \tag{4.14}$$

4.2.3 Polarisation

The electromagnetic waves have certain polarisation that is given by the orientation of the E-field in the space and is perpendicular to the direction of propagation. For the case of the pyramidal horn antenna the electromagnetic wave is linearly polarised, meaning that the wave oscillates in a single direction. Linear polarization can be defined as vertical, horizontal or slanted, however it depends on the orientation of the coordinate system. Fig. 4.7 illustrates a vertically linear polarised electromagnetic wave propagating along the x-axis direction. There are other forms of polarisation such as circular and elliptical. Circular polarization is achieved with two E-fields with the same amplitude oscillating 90 degrees out of phase, and orthogonal to each other. In general, the figure that the electric field vector traces is an ellipse and linear and circular polarisation are special cases of the elliptical polarisation [56].

In a radio link the maximum power transfer occurs when the transmitter and receiver are co-polarised, namely both are oriented in such a way to have the same polarization. When the antennas are positioned in orthogonal polarisation are known to be cross-polarised and the performance of the link will be reduced due to polarisation losses. The E- and H -field components of the pyramidal horn antenna used for the simulations is illustrated in Fig. 4.8. It can be seen that the two fields are perpendicular to each other and the largest components are along the $x-$ axis.

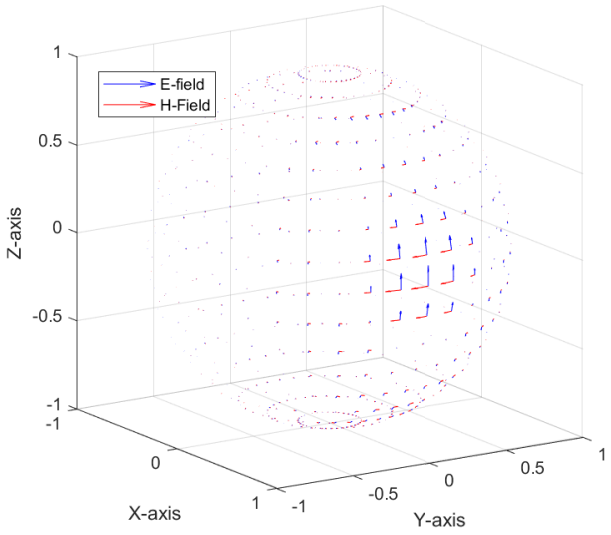

Figure 4.8: Electric (E) and Magnetic (H) fields of the horn antenna, boresight pointing in the direction of y-axis

4.2.4 Rotation and translation algorithm

Once the fields of the feeder antenna have been determined, they are converted from spherical coordinates to Cartesian coordinates, which will have the form of $A = [A_x, A_y, A_z]$, where A represents either the E- or H- fields. Next, these points are oriented to the corresponding angles of departure in azimuth and elevation and finally translated to the defined focal point that can be either F_1 or F_2. A translation is a geometric transformation that moves every point of the figure by the same distance in a given direction.

As the ray tracing algorithm deals with points, vectors, lines and planes, being the last two a set of points in the Euclidean space it is important to have a way to rotate these points or vectors about the axes of the coordinate system. For example, for the case under study it is required to point the antenna pattern of the transmitter and receiver devices in azimuth and elevation planes to adequately transmit and receive signals. To perform a rotation, it is required to have the vector represented as a column vector $\mathbf{v}$, and a rotation matrix $\mathbf{R}$. The rotation is performed by multiplying the matrix and the vector as $\mathbf{Rv}$.

The rotation matrix $\mathbf{R}$ is composed of three basic rotation matrices: As it is seen in Fig. 4.9 $\boldsymbol{R}_x(\alpha)$ rotates the point or vector an angle α in a counterclockwise direction, this rotation is also known as roll (eq. 4.15). Similarly, the matrix $\boldsymbol{R}_y$ rotates a point or vector an angle β in a counter clockwise direction,this rotation is also known as pitch (eq. 4.16). And the matrix $\boldsymbol{R}_z(\gamma)$ rotates a point or vector an angle γ in a counter clockwise direction this rotation is also known as yaw (eq. 4.17). If it is required to rotate the vector in any direction in a 3D space the order of multiplication of the basic rotation matrices is important, thus the rotation matrix is given by

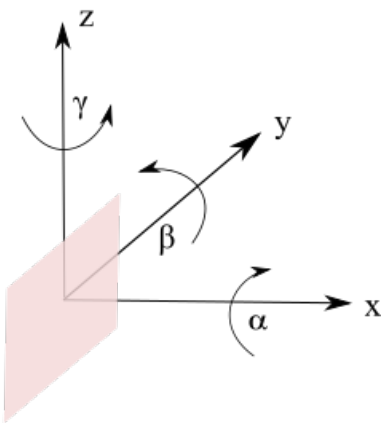

Figure 4.9: Angles of the rotation matrix **R**

$$\mathbf{R} = \boldsymbol{R}_z(\gamma)\boldsymbol{R}_y(\beta)\boldsymbol{R}_x(\alpha)$$

(4.15)
$$\boldsymbol{R}_x(\alpha) = \begin{bmatrix} 1 & 0 & 0 \\ 0 & \cos(\alpha) & -\sin(\alpha) \\ 0 & \sin(\alpha) & cos(\alpha) \end{bmatrix}$$

(4.16)
$$\boldsymbol{R}_y(\beta) = \begin{bmatrix} \cos(\beta) & 0 & \sin(\beta) \\ 0 & 1 & 0 \\ -\sin(\beta) & 0 & cos(\beta) \end{bmatrix}$$

(4.17)
$$\boldsymbol{R}_z(\gamma) = \begin{bmatrix} \cos(\gamma) & -\sin(\gamma) & 0 \\ \sin(\gamma) & cos(\gamma) & 0 \\ 0 & 0 & 1 \end{bmatrix}$$

The implementation of the algorithm in pseudocode is shown in appendix A.

4.2.5 Ray

A ray can be defined as a line which has an origin $\mathbf{O} = (x_o, y_o, z_o)$ and a direction vector **D**, the former is a point and the latter is a vector. Any point $P(t) = (x, y, z)$ on the line in 3D mathematically can be represented by the parametric equation 4.18.

(4.18)
$$\mathbf{P}(t) = \mathbf{O} + t * \mathbf{D};$$

Where t is the distance from the origin of the ray to the desired P point, and the normalized direction vector $\mathbf{D} = (E - O)/||(E - O)||$. The ray is illustrated with its constituents in Fig 4.10.

4.2.6 Reflectors

Depending on the type of reflector being analysed the appropriate algorithm should be selected. The possible options are the ellipsoid reflector, elliptical cylinder reflector and the discrete plane reflector. The first two reflectors will be fully described and analysed in chapter 5 and the latter in chapter 6. It is important to mention that in order to calculate the intersection of the rays with the reflector's surfaces, all these were first triangulated by using a 3D Delaunay triangulation algorithm [75].

4.2.7 Receiver Plane

As previously mentioned, a plane was used to represent the test zone area. In general, a plane is defined as a flat surface that extends infinitely. In 3D a plane can be determined in a number of ways such as a line and a point, two parallel lines, two intersecting lines, or three non-collinear points. In Cartesian coordinate the plane can be represented in the genearl form by:

$$a \cdot x + b \cdot y + c \cdot z + d = 0 \tag{4.19}$$

where a, b,and c are the components of the normal vector $\mathbf{N}$, and d is a constant.

Any point on a plane determined by three points $S_1 = (x_1, y_1, z_1,)$, $S_2 = (x_2, y_2, z_2,)$, and $S_3 = (x_3, y_3, z_3,)$ forming a triangle (see Fig. 4.10) can be represented as

$$\mathbf{S}_1 + \mathbf{S}_{12} \cdot u + \mathbf{S}_{13} \cdot v, \quad u, v \in \mathbb{R} \tag{4.20}$$

Where $\mathbf{S}_{12} = \mathbf{S}_2 - \mathbf{S}_1$ is the vector pointing from S_1 to S_2, and $\mathbf{S}_{13} = S_3 - S_1$ is the vector pointing from S_1 to S_3, u and v are the barycentric coordinates of the triangle . The normal vector of the plane can be calculated with the cross product of the two vectors $\mathbf{N} = \mathbf{S}_{12} \times \mathbf{S}_{13}$.

Similar to the case of the feeder antenna the receiver plane needs to be positioned at the other focal point opposite to the feeder. Depending on the central angle of arrival of the reflected signal the orientation of the receiver plane is calculated as its normal is parallel to the signal.

4.2.8 Ray to Triangle Intersection

In the Euclidean space a line and a plane can either intersect in a single point (see Fig. 4.10) or be parallel to each other. These are parallel if the dot product of the normal vector of the plane with the direction vector of the ray is equal to 0, thus $\mathbf{N} \cdot \mathbf{D} = 0$. If true it means that $\mathbf{N}$ is perpendicular to $\mathbf{D}$, otherwise the intersection point $\mathbf{S}_{int}$ is found by setting the point in the line equation (4.18) equal to the point in the plane equation (4.20), giving

$$\mathbf{O} + t * \mathbf{D} = \mathbf{S}_1 + \mathbf{S}_{12} \cdot u + \mathbf{S}_{13} \cdot v \tag{4.21}$$

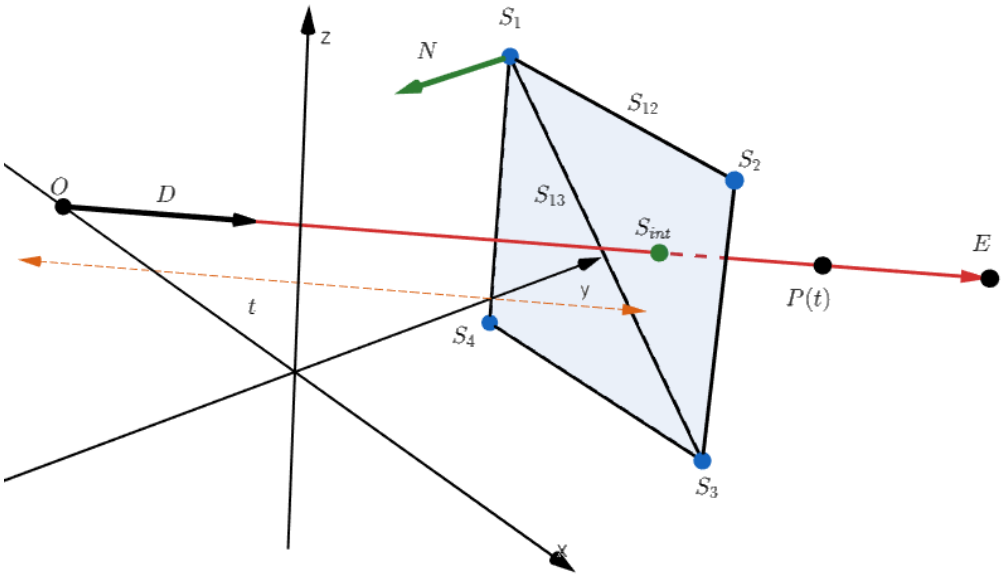

Figure 4.10: Definition of a ray, plane and intersection of a ray with the plane for the receiving DUT

Considering the dot product of **N** and **D** is different than zero, then expressing equation (4.21) in matrix form the parameters of the equations (4.18) and (4.20) can be found with

$$\begin{bmatrix} t \\ u \\ v \end{bmatrix} = \begin{bmatrix} -\mathbf{D} & \mathbf{S}_{12} & \mathbf{S}_{13} \end{bmatrix}^{-1} \begin{bmatrix} \mathbf{O} - \mathbf{S}_1 \end{bmatrix} \tag{4.22}$$

If t is in the range $[0,1]$, means that the intersection point is on the line segment between **O** and **E**. Similarly, if the parameters v and u are also in the range $[0,1]$ the intersection is on the parallelogram formed by the point $\mathbf{S}_1$ and the vectors $\mathbf{S}_{12}$ and $\mathbf{S}_{13}$. Additionally, if $(u+v) \leq 1$, means that the intersection point is inside of the triangle formed by the points $\mathbf{S}_1$, $\mathbf{S}_2$, and $\mathbf{S}_3$. Finally, the intersection point is calculated by replacing t in equation (4.18), thus giving

$$\mathbf{S}_{int} = \mathbf{O} + t * \mathbf{D} \tag{4.23}$$

In order to improve the time of finding the intersections it was used the algorithm proposed by Möller and Trumbone [76]. The advantage of this method is that it is highly vectorised, and the plane equation does not need to be computed or stored which saves time for triangulated meshes. The pseudocode of the algorithm is shown in appendix A.

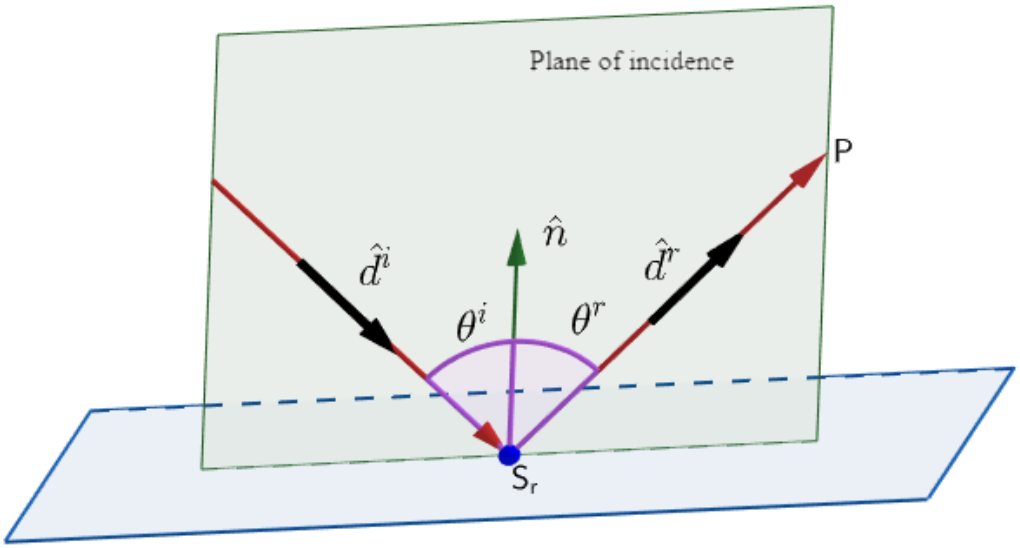

Figure 4.11: Incident and reflected rays lying on plane of incidence.

4.2.9 Ray trajectory and the Law of reflection

There are two types of reflections: specular and diffuse. The occurrence of one or the other highly depends upon the smoothness of the surface. The analysis carried out only considers perfect smooth surfaces, thus it is assumed that the amount of signal reflected is equal to the incident signal, and that only specular reflections exist. Reflections occur when the incident ray encounter a reflector or surface that does not absorb the signal energy, instead it bounces it away from the surface. The law of reflection of Snell's law stated that the angle of the incident signal θ^i is reflected with the same angle θ^r with respect to the vector normal $\hat{n}$ of the surface (see Fig 4.11), thus, $\theta^i = \theta^r$ [73].

The direction of reflection $\hat{d}^r$ of the ray can be calculated applying eq. (4.24).

$$\hat{d}^r = \hat{d}^i - 2(\hat{n} \cdot \hat{d}^i)\hat{n} \tag{4.24}$$

Where $\hat{d}^i$ is the incident unit direction vector and $\hat{n}$ is the normal unit vector of the plane. It is important to notice that the plane of incidence (which is defined as the plane containing the vector normal to the surface and the propagation vector or the incident vector) and the reflection plane are coplanar, thus $\hat{n} \times \hat{d}^i = \hat{n} \times \hat{d}^r$

4.2.10 Amplitude continuation along the reflected rays

In subsection 4.2.1.2 were described the mathematical expressions to calculate equation the E- and H- fields radiated by a horn antenna. These fields have spherical equiphase but not spherical equiamplitude [73]. When there are no scatterers the electromagnetic fields would be described

just by those expressions. Whereas, with a reflector or scatterer present, the resulting E-field is the sum of the incident field and the reflected field.

$$E^t(p) = E^i(p) + E^r(p) \tag{4.25}$$

In terms of GO the incident field considering a ray tube propagating in free space that impinges a surface at a point S_r can be described by the principal radii of curvature ρ_1^i and ρ_2^i, the initial GO field E^i at a reference point S_t and d^i is the distances from the reference point to the reflected point.

$$E^i(S_r) = E^i(S_t)\sqrt{\frac{\rho_1^i \rho_2^i}{(\rho_1^i + d^i)(\rho_2^i + d^i)}}\, e^{-jkd^i} \tag{4.26}$$

Where, $A(t^i) = \sqrt{\frac{\rho_1^i \rho_2^i}{(\rho_1^i + d^i)(\rho_2^i + d^i)}}$ is the spreading factor that governs the amplitude variation of the field along the ray path [73]. For the case of spherical wave ray tube $\rho_1^i = \rho_2^i = \rho$. The spreading of the ray tube becomes $A(d^i) = \rho/(\rho + d^i)$. It is possible to use the GO approach to calculate the reflected electromagnetic fields for high frequencies if the scatterers are sufficiently large compared to the wavelength, thus it can be assumed that the contribution of the field at a point P in the space is mainly determined from the induced currents in the neighbourhood of the reflection point S_r of the surface, known as the "*stationary phase point*" [73].

$$E^r(S_r) = -E^i(S_r) + 2(\hat{n} \cdot E^i(S_r))\hat{n} \tag{4.27}$$

Now the expression to find the reflected fields from the reflecting surface at any point P is given by

$$E^r(P) = E^r(S_r)\sqrt{\frac{\rho_1^r \rho_2^r}{(\rho_1^r + d^r)(\rho_2^i + d^r)}}\, e^{-jkd^r} \tag{4.28}$$

4.2.11 Phase continuation along the reflected rays

In a homogeneous isotropic media where the rays are seen as straight lines orthogonal to the wavefronts, the description of the phase change along the ray path is given by

$$e^{-jkt} \tag{4.29}$$

where t is the distance between the ray origin and any specific point in space, which in this case would be the reflection point S_t and k is the wave number [73].

After reflection the ray leaves the surface and continues to travel through the homogeneous medium, therefore the reflection point S_t is the new origin of the ray and will travel a distance d^r up to a particular point in space, and more specifically a point that lies on the receiver plane, and equation (4.29) can be used to calculate the phase of the reflected ray.

4.2.12 Friis Transmission equation

The Friis transmission equation (eq. 4.30) relates the power transmitted by an antenna to the power received by another antenna separated by a distance R. It assumes that the polarisation of the antennas is matched and direction of maximum directivity is aligned.

$$P_{Rx} = \frac{P_{Tx} G_{Tx} G_{Rx} \lambda^2}{(4\pi R)^2} \tag{4.30}$$

Where P_{Rx} is the received power, P_{Tx} is the transmitted power, G_{Tx} and G_{Rx} are the gain of the transmitter and receiver antennas respectively. The term $\frac{\lambda^2}{(4\pi R)^2}$ is known as the free space path loss factor which takes into account the losses due to the spherical spreading of the energy by the antenna.

4.2.13 Validation of ray tracing algorithm

To validate the ray tracing algorithm described above various shapes of reflector were compared below. To simplify the test, it was considered that the feeder was a point source and only forward propagation towards the different reflectors was accounted. The general setup consists of a source point located a point F_1 translated approximately 0.98 m along the negative $x-$axis, a reflector of with a vertical length of 0.6 m centred with respect to the $y-$axis and translated 2.05 m along the negative $x-$axis. The rays path length, amplitude of fields distribution of each ray and the phases of each ray were computed at a line parallel to the $y-$axis translated 0.98 m along the positive $x-$axis, as illustrated in Fig. 4.12, Fig. 4.13 and Fig. 4.14.

Flat reflector

It is well known that if a flat reflector is considered to be infinite in extent, then the analysis of its radiation can be realised with the image principle. This principle allows to simply replace the reflector by another identical image mirrored antenna. However, if the reflector is finite in extent this principle can still be used as a first approximation of the fields if it is large enough compared with the wavelength. In this case the reflector length has a length of 52 wavelengths. For more accurate results it is required to take into account the diffraction from the edges which produce back scattering [77]. Figure. 4.12 shows a flat or plane reflector, at its back the cyan coloured lines represent the normal vector to the surface at each point of reflection of the incident rays. It can be seen that the reflected rays diverge away from the centre of the reflector. At the reference

line (black dashed line crossing point F_2) it is observed that the reflected rays spread 4 times the length of the reflector along the vertical axis. The total (from source point to reflector plus reflector to reference line) shortest ray path length was 4.1 m and the largest was 4.27 m. If the feeder is mirrored about the plane, the same distribution of rays occurs.

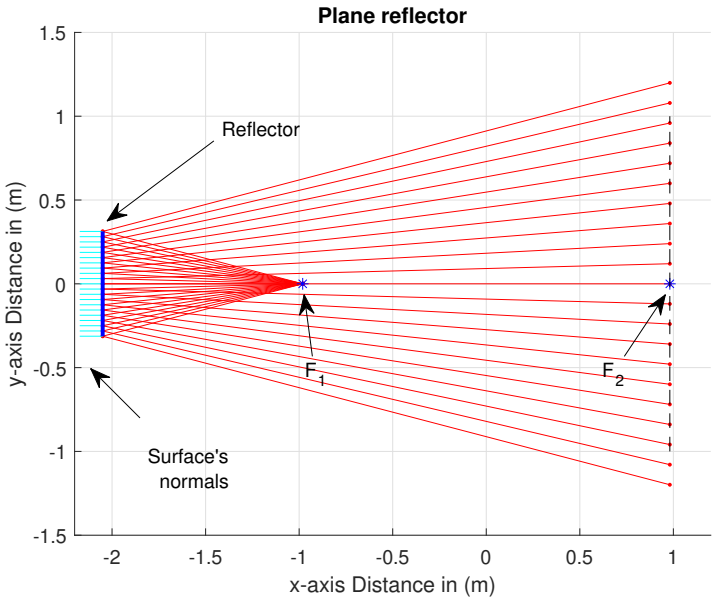

Figure 4.12: Flat reflector with a point source feeder

Parabolic reflector

The main characteristic of parabolic reflectors is that if a point source is placed at its focal point, the rays reflected by the surface will emerge as a parallel beam. These parallel rays are known to be collimated. In the same manner if a beam of parallel rays arrives at the parabolic reflector all the rays will converge at the focal point. Parabolic reflectors are commonly used in compact antenna test ranges systems because it is possible to generate nearly planar wavefronts in a very short distance, compared with the distance required to produce the same size test zone using a direct far field system. The configuration shown in Fig. 4.13 with feeder place in front of the parabola is usually known as front fed [56]. This is not the most ideal configuration but helps to illustrate the validity of the ray tracer tool. Similarly, to the flat reflector. The length of the reflector in straight line parallel to the $y-$axis is also 0.6 m. The total ray path distance travelled by each one of the rays was approximately 4.1 m at the reference line. As expected, all the reflected rays are parallel to each other, which differs with the flat reflector because its reflected rays diverged, and each ray path has a different length.

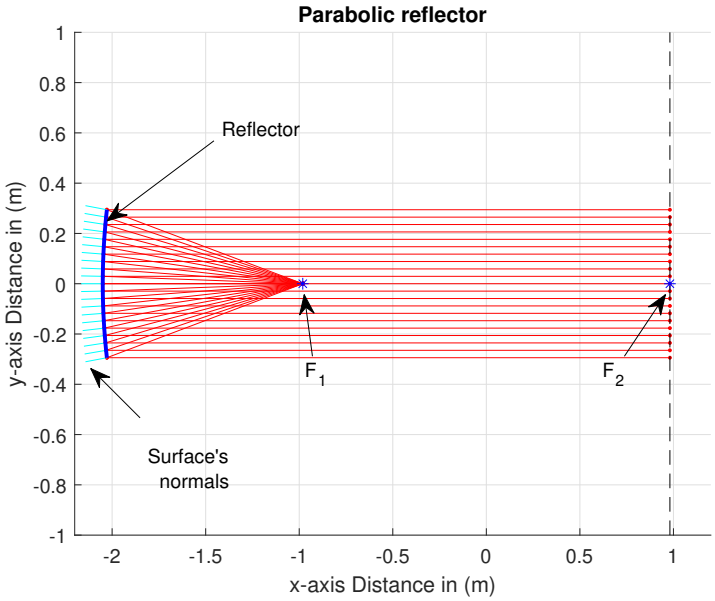

Figure 4.13: Parabolic reflector with a point source feeder

Elliptical reflector

The reflective property of the ellipse (based on geometrical optics [78]) states that if a ray is emitted from one focal point (e.g., $\mathbf{F}_1$) and meets any point $\mathbf{P}_i$ on the ellipse, it will be reflected and pass through the other focal point (e.g., $\mathbf{F}_2$) as illustrated in Fig. 4.14. Moreover, by definition the sum of the distances from the two focal points to a point on the ellipse is constant. This property directly applies to the ellipsoid reflector and partially to the other two type of reflectors ECR and DPR, with subtle differences that will be discussed further in chapters 5 and 6.

The main advantage of using a reflector with elliptical shape as will be discussed in the following chapters is that from a single source point, multiple signals (rays) can be generated that arrive at the other focal from different directions which is desired condition to test 5G NR devices. Furthermore, this is a significant advantage compared to other test methods such as the MPAC, SS-MPAC, and 3D MPAC, since it does not require multiple probe antennas with individual transceivers or complex and expensive control circuitry to switch transceivers between probes .

4.2.13.1 Comparison of the reflectors

Each one of the three reflectors previously described reflects the rays differently. In Fig. 4.15 the top subplot shows a comparison of the total path distances travelled by each ray of the three reflectors when projected at the reference line. It can be observed that the flat reflector exhibits greater spread. The difference between the maximum and minimum distances is approximately 17 cm. Considering a signal at 28 GHz, then the difference in signal strength would be approximately 0.7 dB as depicted by the orange line in the middle subplot of Fig. 4.15, which shows the magnitude

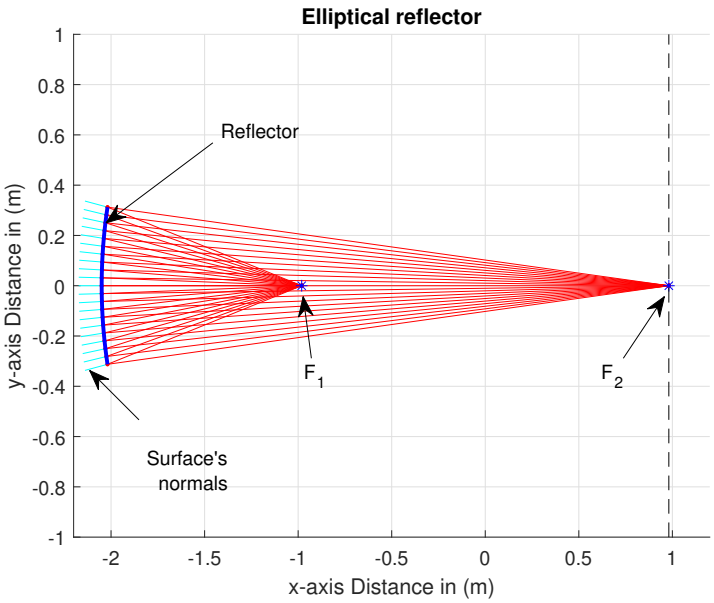

Figure 4.14: Elliptic reflector with a point source feeder

of the fields of each ray in logarithmic scale normalised to the strongest field. The subplot at the bottom shows the phase distribution of each ray. It can be observed that phases of the ray 0 to 80 and 123 to 200 fluctuate between ±180 degrees. The phase variation of the reflected rays closer to the $x-$axis is in the range of -164 degrees and 120 degrees.

All the rays of the parabolic reflector travelled approximately the same distance. The difference in length is in the order of millimetres therefore it can be considered as negligible in term of amplitude difference of the rays as shown the middle subplot of Fig. 4.15. The phase distribution is more uniform compared to the flat reflector case as seen in the bottom subplot.

For the case of the elliptical reflector one can see that the total path length of all the rays is exactly the same 4.1 m (see top subplot Fig. 4.15). Therefore, the field strength of all the rays is also exactly the same (see middle subplot Fig. 4.15) as well as the phases Fig. 4.15).

4.3 Conclusions

In this chapter a ray tracing algorithm developed in-house was described which in the following chapters will be used to perform analytical analysis of the different types of reflectors that were considered as part of the proposed OTA test method.

One advantage of the ray tracing algorithm is that it allows to quickly evaluate some basic characteristics of the test methods under consideration, and is computationally inexpensive. Furthermore, it provides with valuable information such as angles of departure, angles of arrival, spatial distribution of the electromagnetic fields, etc. The rays will roughly show the trajectory of the signals in space when transmitted from a source and the trajectory after reflection from

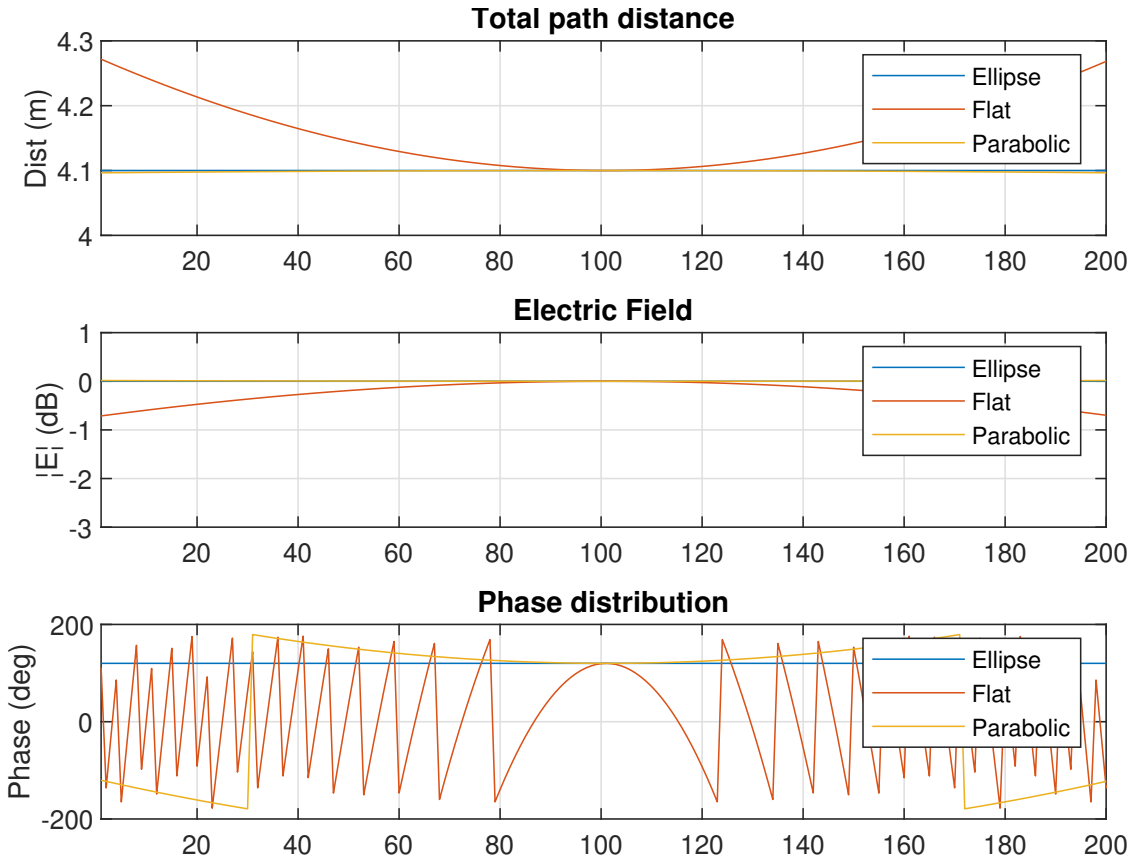

Figure 4.15: Comparison of ray path distances (top subplot), normalized electric field (middle subplot), and phase distribution (bottom subplot) from the plane reflector, parabolic reflector and elliptic reflector

obstacles. Although there are many commercially available ray tracing programs, none were available to the author of the thesis for the development of the research and normally are very costly. Therefore, developing one from scratch not only reduced costs of the project, but helped the author of this thesis to gain knowledge about this useful tool and more importantly a self-written code gives freedom to modify and create new features according to the specific needs without having to rely on third party vendors.

To validate the algorithm three reflectors were evaluated: a flat reflector, a parabolic reflector and an elliptical reflector. It was demonstrated that the reflected rays followed the theoretically expected paths. For the case of the flat reflector the reflected rays diverged away from the centre of the reflector. The parabolic reflector collimated the reflected rays, and the elliptical reflector focus the rays at the second focal point.

The ray tracing algorithm was limited to uniquely calculate specular reflections, however in real conditions it is well known that the sharp edges of the reflectors would produce diffraction of the rays which generates undesired interference with the test signals. The interested reader could complement this algorithm with geometrical theory of diffraction.

CHAPTER 5

LOW COST 5G OVER THE AIR TEST METHOD

5.1 Introduction

To overcome some of the limitations of existing OTA test methods as described in chapter 3, three new approaches were conceived and investigated. These approaches explore the use of an ellipsoid reflector, a set of elliptical cylinder reflectors, and importantly a set of discrete reflectors distributed in a part-ellipsoid structure. All these architectures offer a means of creating spatially dynamic environments to emulate real-life mmWave operational scenarios and use conditions. An active array antenna (e.g. phased array antenna) was considered as the means to generate simultaneously one or more test signals with different orientations, which after being reflected will illuminate the DUT with different angles of arrival in both azimuth and elevation planes.

This chapter begins with the description of the apparatus that is common to all the types of reflectors. Secondly, the definition of the ellipse and its previously mentioned geometrical customisations. Thirdly, the analysis of Angle of Arrival (AoA), Angle of Departure (AoD), dimensions of the Test Zone (TZ) volume for each type of reflector, and the ray path distances were calculated through consideration of the geometrical optics using the author's own ray tracing algorithm. The results of the ray tracing algorithm were complemented with electromagnetic simulations performed by the programs ANSYS Savant, used to determine the distribution of the phases and fields inside of the test zone. The Savant simulator also has a solver based on Shooting and Bouncing Rays, with many more features than the self-written algorithm. The principal work performed by Savant is determining the scattered field. The scattered field is produced by the radiation of surface currents impressed upon the scattering geometry by the incident field. The total field is reconstructed through coherent addition of the incident and scattered fields. This solver was used to determine the characteristics of the test zone volume, which was employed in

Chapters 5 and 6. Finally, the pros and cons of the three candidate architectures is appraised.

It is important to remember as was stated in Chapter 3 that the aimed size of the TZ is of approximately 20 cm, which is consistent with the latest recommendations of 3GPP that the quiet zone for smartphones shall be considered a sphere with radius of R = 10 cm [55].

5.2 General description of the low cost 5G OTA test method based on ellipsoid reflectors

The 5G mmWave OTA test method for mmWave frequency devices proposed here exploits the reflective properties of an ellipse which in terms of GO states that any ray emitted from one focal point is reflected by the surface and pass through the other focal point. Three different types of reflectors have been considered and analysed, these are: An Ellipsoid of Revolution Reflector (ERR), a set of Elliptical Cylinder Reflector (ECR) distributed in an ellipsoidal shape, and a set of Discrete Plane Reflector (DPR) evenly distributed along a part-ellipsoid structure. The schematics of the proposed mmWave OTA test methods are illustrated in Fig. 5.1, Fig. 5.2 and Fig. 5.3.

For all the cases, the analysis below consists of: One of the type of reflectors listed above, a directional feeding antenna (referred to as the feeder), and a DUT. The DUT is emulated through a horn antenna. For a full test-house implementation, the feeder would be conducted to a base station emulator to generate the test signals to stimulate the DUT's operation under real link conditions. Furthermore, if required, an optional channel emulator can create temporal, and frequency fading (path delays, Doppler spread, and fast fading). The feeder and the DUT are placed at the focal points. If only one signal is required, the feeder could also be a horn antenna with high directivity and attached to a 2D positioner to generate variable AoDs. Alternatively, if more than one signal is required, or if the AoA switching is too fast for the positioner, the feeder can be implemented using a phased array antenna with multiple RF ports, capable of generating one or more independently steerable beams (for example the Anokiwave AWA-0142-IK as used in section 7.3.1.1). If realized through a 2D array facet, it is possible to electronically beam steer the signals in both azimuth and elevation from the focal point. These signals will be redirected by means of one or more of the reflectors towards the DUT arriving at it with different AoA, thereby creating a 3D spatially addressable stimulus. This will support the real-time emulation of the spatial dynamic mmWave channel and the necessary performance characterisation of the DUT.

5.2.1 Definition of the Coordinate System

Prior to discussing the design and analysis of the reflectors, it is necessary to define the coordinates systems that will be applied through the remainder of this thesis. Two systems were used, a global and a local coordinate system. The global coordinate system is a Cartesian system of three orthogonal axis, x, y, and z, and the local coordinate systems which are the similar but

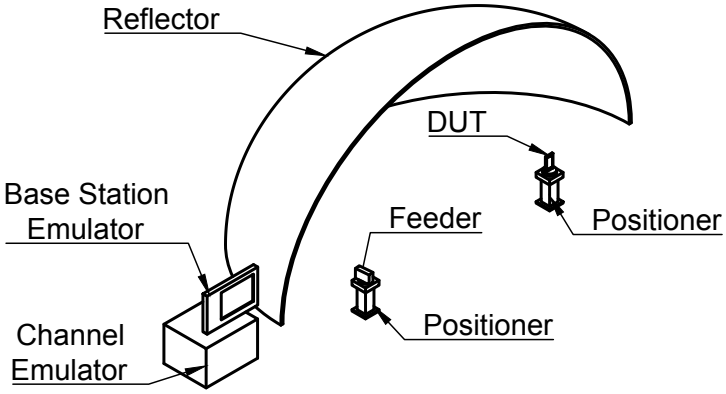

Figure 5.1: Schematic of the initial proposal for a mmWave OTA test method with ERR

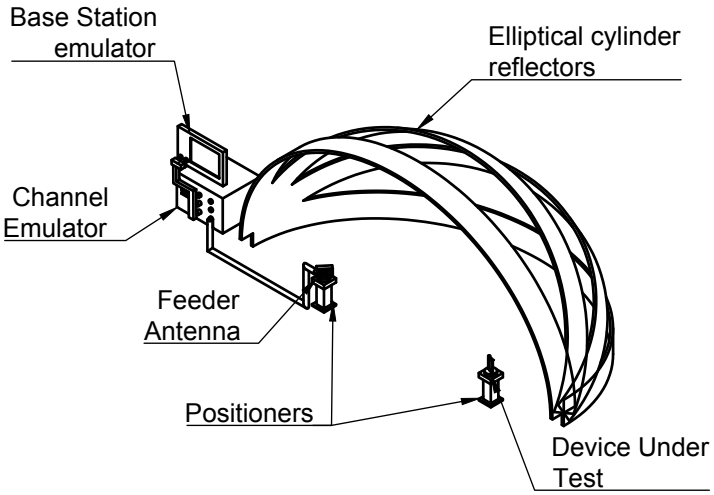

Figure 5.2: Schematic of the second proposal for a mmWave OTA test method with ECR

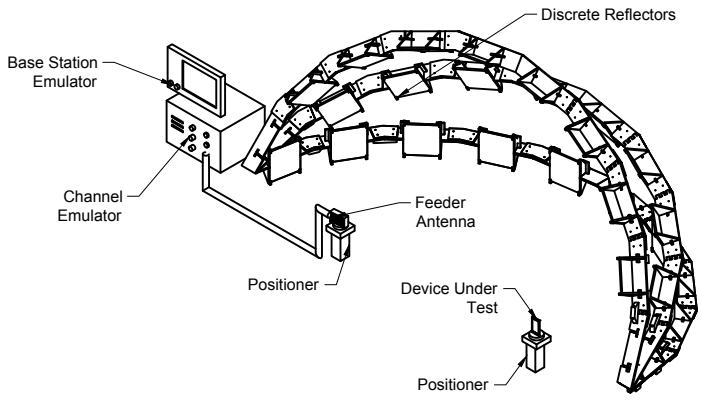

Figure 5.3: Schematic of the third and final proposal for a mmWave OTA test method with DPR

translated from the global to the focal points whose axis are denoted by x', y', and z' for $\mathbf{F}_2$ (DUT), and x'', y'', and z'' for $\mathbf{F}_1$ (Feeder) (see Fig. 5.4), although this is not fixed as the position of the DUT and the feeder can be interchangeable. For all cases and types of reflectors the centre of the base ellipse is located at the origin in the global coordinate system $O = (0,0,0)$. Furthermore, the xy-plane is considered to be the azimuth plane, and the xz-plane is the elevation plane.

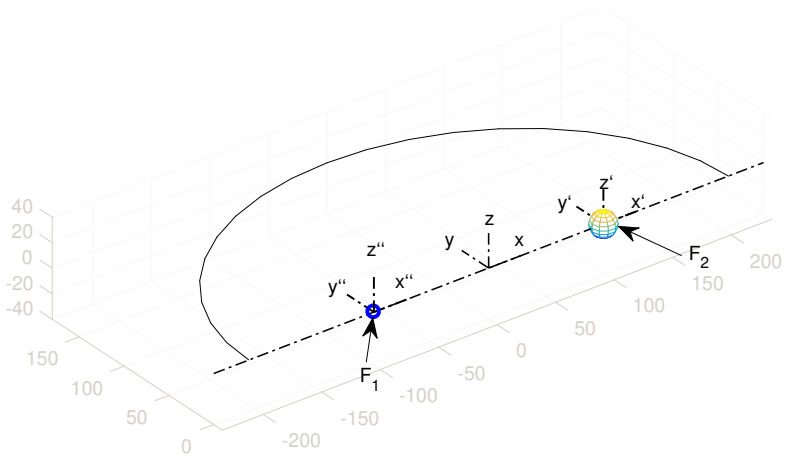

Figure 5.4: Global Coordinate System and Local Coordinate System (Distance given in cm)

5.3 Description of the ellipse, ellipsoid and elliptical cylinder

An ellipse is defined as the set of points $P(x,y,z)$ in the plane, where the sum of the distances from two points (also known as foci) F_1, and F_2 to every point P on the line is a positive constant ($|F_1P| + |PF_2| = 2a$). It is characterised by its semi-major axis a and semi-minor axis b. The distance of the focal points from the origin, it is given by $dF = \sqrt{a^2 - b^2}$. These characteristics are illustrated in Fig 5.5

An ellipse centred in the origin is mathematically defined by the equation (5.1)

$$\frac{x^2}{a^2} + \frac{y^2}{b^2} = 1 \tag{5.1}$$

An ellipsoid of revolution is a quadratic surface obtained by rotating an ellipse about one of its principal axis (see Fig 5.1 which shows a section of a full-ellipsoid) and is described by equation (5.2), where $c = b$, which means that the curvature has the same length in the $y-$ axis and $z-$ axis .

$$\frac{x^2}{a^2} + \frac{y^2}{b^2} + \frac{z^2}{c^2} = 1 \tag{5.2}$$

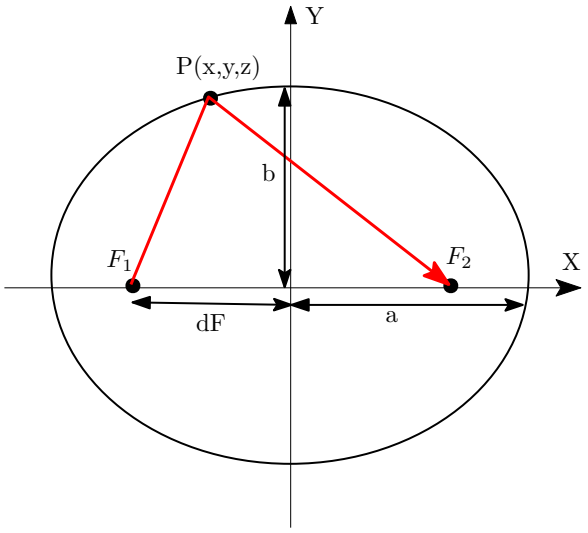

Figure 5.5: Description of the Ellipse

According to the definition of the ellipse, the length of all the rays passing across the two focal points adds up to a constant which is twice the length of the semi-major axis, and this also applies to the ellipsoid. Thus, the ray path lengths $dist_i$ of an ellipsoidal reflector described above can be calculated with equation (5.3).

$$dist_i = \sqrt{\sum_{i=1}^{n}(\mathbf{P}_i - \mathbf{F}_{1i})^2} + \sqrt{\sum_{i=1}^{n}(\mathbf{F}_{2i} - \mathbf{P}_i)^2} \tag{5.3}$$

where, point $\mathbf{P}_i = (P_{i1}, P_{i2}, P_{i3})$ is the reflection point at the reflector, $\mathbf{F}_1 = (F_{11}, F_{12}, F_{13})$ is the feeder focal point ,and $\mathbf{F}_2 = (F_{21}, F_{22}, F_{23})$ is the DUT focal point.

On the other hand, an elliptic cylinder (see Fig 5.2) can be considered as a cylinder which has an elliptical cross-section or base . The parametric equations of an elliptic cylinder of height h, semi-major axis a, and semi-minor axis b are given by equation (5.4).

$$x = a\cos\phi; \quad y = b\sin\phi; \quad z = h \tag{5.4}$$

where, x, y and z are the coordinates of any point P, and $\phi \in [0, 2\pi)$.

5.3.1 Definition of the dimensions of the ellipse

As previously mentioned, according to the definition of the ellipse the sum of the distances from the foci to any point on the ellipse is twice the length of the semi-major axis. Hence, in order to achieve the desired 4 m distance between feeder and DUT the semi-major axis (as described in section 3.2) must be $a \geq 200$ cm. A 2.5% margin was considered, therefore the chosen length of the semi-major axis was of $a = 205$ cm.

The length of the semi-minor axis b was chosen such that the feeder antenna and the DUT were sufficiently separated apart from each other to avoid any direct coupling or leakage between them. Moreover, the distance between the foci and the vertex of the ellipse with the semi-major axis would leave enough room to rotate a DUT with a antenna diameter of 20 cm. Fig. 5.6 shows the distances of the foci from the origin given by $dF = \sqrt{a^2 - b^2}$ for different lengths of b. Thus, it was decided that the foci should be located approximately at half the length of the semi- major axis $dF \approx a/2 \approx 100$ cm, which gives the length of the semi- minor axis $b = 180$ cm.

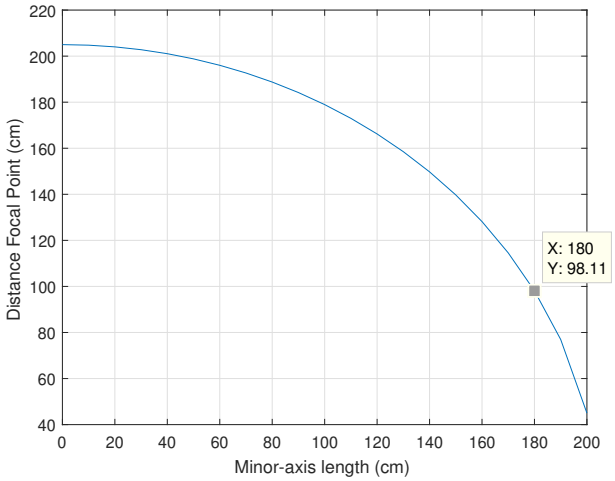

Figure 5.6: Distances of the foci from the centre of the ellipse for different lengths of b

5.4 5G OTA test method based on ellipsoid reflector

The first candidate architecture to be analysed is the ellipsoid of revolution since this would be the ideal candidate reflector because it can theoretically generate continuous AoA in both azimuth and elevation planes. This reflector is the foundation for the other two methods. Two different sections of the ellipsoid were considered. The first is a section of the ellipsoid which surrounds both the DUT and Feeder illustrated in Fig. 5.7, which will be called side ellipsoid reflector (side ERR), and the second is a section of the ellipsoid that only surrounds the feeder, this is shown in Fig 5.8, which will be referred as front ellipsoid reflector (front ERR). There are a number of considerations to take into account to design the reflectors, such that these create the right environment to test 5G mmWave NR devices. The parameters analysed in this project are the size and quality of the test zone, measurement distance, angles of arrivals, and angles of departure, which are discussed below.

5.4.1 Design of Ellipsoid Revolution Reflectors

Below a mathematical description of the two types of reflectors is given

5.4.1.1 Design Side ERR

The parametric equations that describe the side ellipsoid reflector are given by equation 5.5 an is illustrated in Fig. 5.7

$$\begin{aligned} x &= a\cos\phi\sin\theta \\ y &= b\sin\phi\sin\theta \\ z &= b\cos\theta \end{aligned} \tag{5.5}$$

for $\phi \in [0,\pi]$ and $\theta \in [0,\pi/2]$.

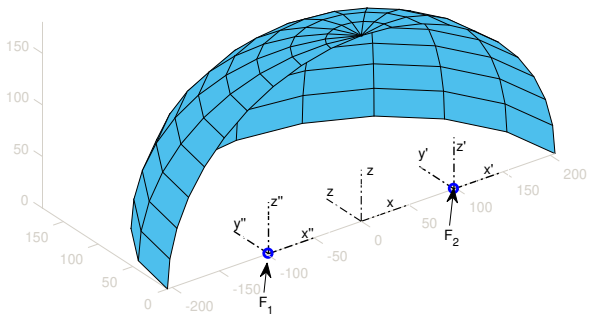

Figure 5.7: Side Ellipsoid Reflector (Dimensions in cm)

5.4.1.2 Design Front ERR

The front ellipsoid reflector is mathematically described by the same equations (5.5), but the range of the angles change to $\phi \in [\pi/2, 3\pi/2]$ and $\theta \in [0,\pi/2]$. An illustration of the reflector is shown in Fig. 5.8.

5.4.2 Angles of Arrival of ERR

The angles of arrival in the azimuth (AAoA) plane are represented by α. For the side ellipsoid reflector these are measured from the x'-axis in an anticlockwise direction towards the y'-axis, as depicted in Fig. 5.9. For the front ellipsoid reflector, the angles are measured from the y'-axis in an anticlockwise direction towards the negative x'-axis shown in Fig. 5.10.

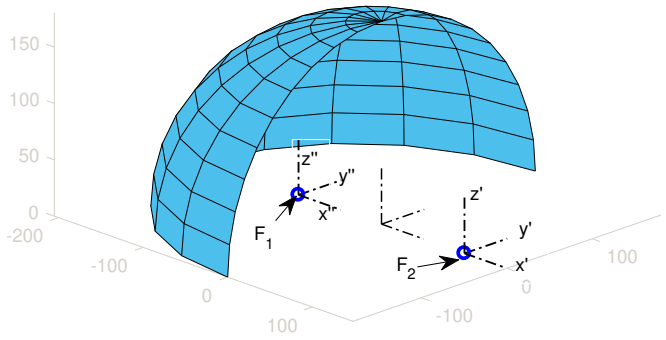

Figure 5.8: Front Ellipsoid Reflector (Dimensions in cm)

5.4.2.1 Azimuth Angles of Arrival of the Side ERR

Given that the i-th reflection point $P_i(x_i, y_i, z_i)$ on the surface of the reflector is known, the azimuth AoA α_i of any incident ray at F_2 can be found as follows:

1. Calculate the projection point $Pproj_i$ of P_i onto the xy-plane:

$$Pproj_i = P_i - (P_i \cdot \mathbf{n})\mathbf{n} \tag{5.6}$$

where $\mathbf{n}$ is the vector normal of the xy-plane.

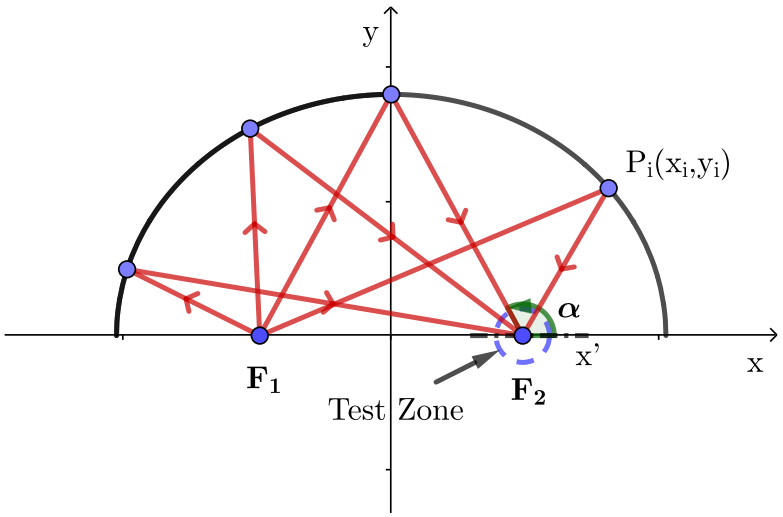

Figure 5.9: Side Ellipsoid Reflector - Azimuth AoA

2. Calculate α_i

$$\alpha_i = \cos^{-1}\left(\frac{(F_2 - Pproj_i)\cdot(-F_2)}{|F_2 - Pproj_i||F_2|}\right) \tag{5.7}$$

Theoretically the range of azimuth AoA would be $0 \geq \alpha \geq 180$ degrees.

5.4.2.2 Azimuth Angles of Arrival of the Front ellipsoid reflector

Similar to the previous analysis, if the i-th reflection point $P_i(x_i, y_i, z_i)$ on the front ellipsoid reflector is known, then the azimuth AoA α_i of any incident ray at F_2 can be found as follows:

1. Calculate the projection point $Pproj_i$ of P_i onto the xz-plane given by equation (5.6)
2. Calculate α_i

$$\alpha_i = \cos^{-1}\left(\frac{(F_2 - Pproj_i)\cdot(\mathbf{n}_{xz})}{|F_2 - Pproj_i||\mathbf{n}_{xz}|}\right) \tag{5.8}$$

where $\mathbf{n}_{xz} = (0,-1,0)$ is the normal vector to xz-plane.

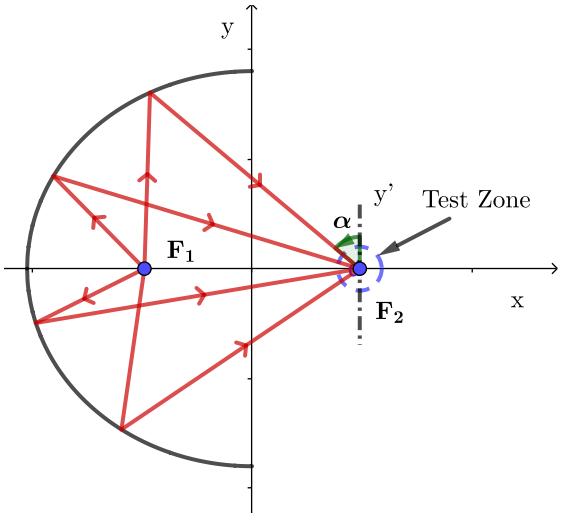

Figure 5.10: Front Ellipsoid Reflector - Azimuth AoA

Theoretically the range of the azimuth AoA's would be $28.59 \geq \alpha \geq 143.79$ degrees. However, one can note that the DUT placed in $F1$ will block part of the incident or reflected signals, depending if it is set to transmit or receive. Thus, the usable angles of arrival will depend on the physical size of the DUT.

5.4.2.3 Elevation Angles of Arrival of ERR

The angles of arrival in the elevation (EAoA) plane are represented by β which are measured from the xy-plane towards the z'-axis. These angles are calculated in the same way for both types

of reflectors. A cross section of the reflectors is depicted in Fig. 5.11, and the EAoA are calculated as follows:

Given that the i-th reflection point $P_i(x_i, y_i, z_i)$ is known, the EAoA β_i of any incident ray at F_2 can be found as follows:

1. Calculate the projection point $Pproj_i$ of P_i onto the xy-plane given by equation (5.6)
2. Calculate β_i

$$\beta_i = \cos^{-1}\left(\frac{(F_2 - Pproj_i)\cdot(F_2 - P_i)}{|F_2 - Pproj_i||F_2 - P_i|}\right) \tag{5.9}$$

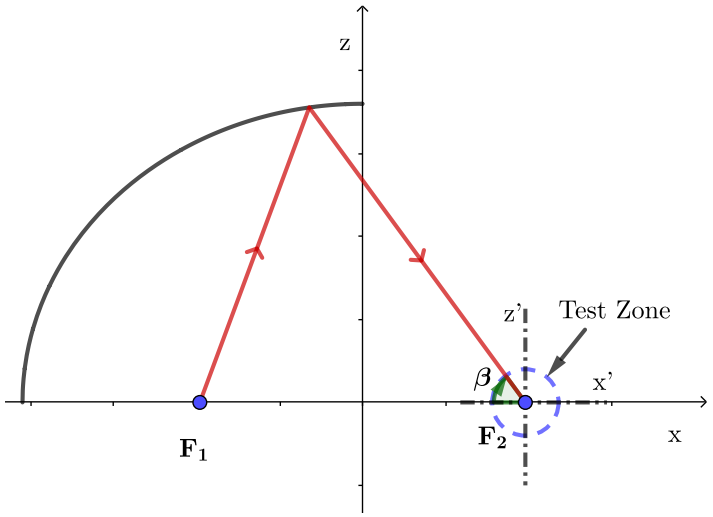

Figure 5.11: Cross-section of the ellipsoid - Elevation AoA

Thus, theoretically the range of EAoA for the side ellipsoid reflector would be $0 \geq \beta \geq 90$ degrees, and for the front ellipsoid reflector the range of EAoA is $0 \geq \beta \geq 61.41$ degrees.

5.4.3 Mapping of Angles of Departure with Angles of Arrival of ERR

The angles of departure for both types of reflectors are given by the angles that delimit the shape of the reflector, this are summarized as follows: For the side ellipsoid reflector the azimuth angles of departure (AAoD) are all the values of $\phi \in [0, \pi]$ and the elevation angles of departure (EAoD) are the values of $\theta \in [0, \pi/2]$. Similarly, for the front ellipsoid reflector the AAoD are all the values of $\phi \in [\pi/2, 3\pi/2]$ and the EAoD are the values of $\theta \in [0, \pi/2]$.

As the reflectors are continuous concave surfaces it is possible to have virtually infinite number of combinations between angles of departure in azimuth and elevation, which means that there are unlimited angles of arrival with the ranges specified above. However, the angles of illumination or departure will be limited by the amplitude and phase weights of the active array antenna used. Figure 5.12 shows some examples of the mapping of the Azimuth Angles of Departure with the Azimuth Angles of Arrival for certain values of Elevation Angles of Departure.

It is possible to observe that for elevation angles of departure below 60 degrees the curves of the AoA follow a similar quasi-linear trend, whereas for EAoD over 60 degrees there is a different trend how the AAoA and AAoD relate to each other, and this is due to the transmitted ray is being pointed close to the highest points of the reflector, which reduces the number of angles of arrival, never reaching any angle smaller than 110 degrees.

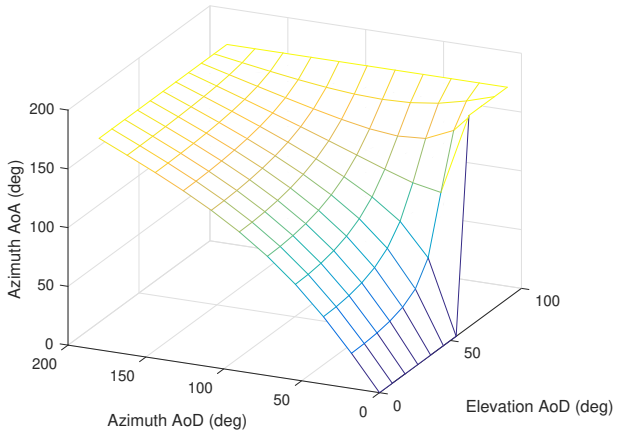

Figure 5.12: Mapping of Azimuth Angles of Departure with Azimuth Angles of Arrival

Similarly, in Fig. 5.13 it is illustrated the mapping of the elevation angles of departure with the arrival. There is not a unique relation between them since they also depend on the azimuth angle of departure. If the AAoD is fixed at 0 degrees, it can be seen that the slope with which the EAoD increase is steeper than any other EAoD, but at approximately 63 degrees it reaches a peak of the EAoA, and after it drops to similar values. Approximately from AAoD of 90 degrees to 180 degrees there is a linear trend of the ratio of change between the EAoD and EoAA.

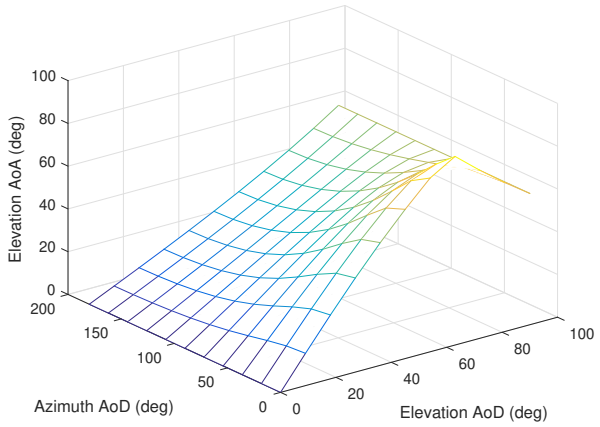

Figure 5.13: Mapping of Elevation Angles of Departure with Elevation Angles of Arrival

5.4.4 Test Zone of the ERR method

As mentioned above one of the objectives of the OTA test system is that the test zone should be sufficiently large to allocate and test mobile devices such as smartphones. Thus, determining the realizable test zone size of the system with an ERR reflector is needed.

5.4.4.1 Ray path lengths

Taking in consideration the property of the ellipse that the sum of the distances from the foci to every point on the line is constant would mean that ideally there should be an equal propagation distance from the feeder to the DUT. Thus, assuring an in-phase field superposition of the scattered fields at the DUT focal point when the reflector is illuminated by the feeder antenna whose phase centre is located at the other focal point [79]. However, in practice this requires the manufacture of a perfect reflector and additionally perfect source point as a feeder. In practice, none of these conditions are possible to fully meet because the antennas are not perfect source points and manufacturing a perfect reflector would be very expensive and depends on the manufacturing technique.

To verify the statement that the sum of the distances from the foci should be constant and as a way to test out the correctness of the simulator, the total path distance travelled by each ray from the feeder to the DUT was obtained for three AoD: 60, 100 and 150 and EAoD: 40, 30, 50 respectively. To illustrate the idea of this simulations Fig. 5.14 shows an example where the feeder has an azimuth AoD of 45 degrees and elevation AoD of 30 degrees. The red lines represent the rays being launched from the feeder focal point, and the direction of each ray is given by the radiation pattern of the antenna in black/blue. To avoid cluttering the picture, only the rays corresponding to the main lobe are shown. At the DUT focal point a blue square represents the desired TZ area of 20 cm x 20 cm. The green dots inside the TZ area are the points were the reflected rays reach the TZ area. The area covered by spatial distribution of these intersecting points gives a rough estimate of the theoretically realizable size of the TZ.

As the measurement is being done in a plane it is expected to observe small variation between the distance of rays, because some rays with large elevation angles of arrival will intersect the plane earlier, and rays with very small angles will intersect later. The range of these distance variations also directly depend on the granularity of triangulation of the reflector's surface. If the triangles comprising the reflector surface were infinitely small, then all the rays would perfectly arrive to the focal point. However, to speed up the simulations a finite number of triangles comprising the reflector was used, more specifically the reflector had 180000 vertices and 358202 faces. It can be seen in Fig. 5.15 that the mean distance is 410.02 cm, and the range of fluctuation is between 409 and 411. The largest distances also correspond to rays representing the side lobes of the used antenna pattern.

With these results one can conclude that with and ideal reflector effectively any ray being launched from one focal point, arrives to the other focal point with a constant travelled distance.

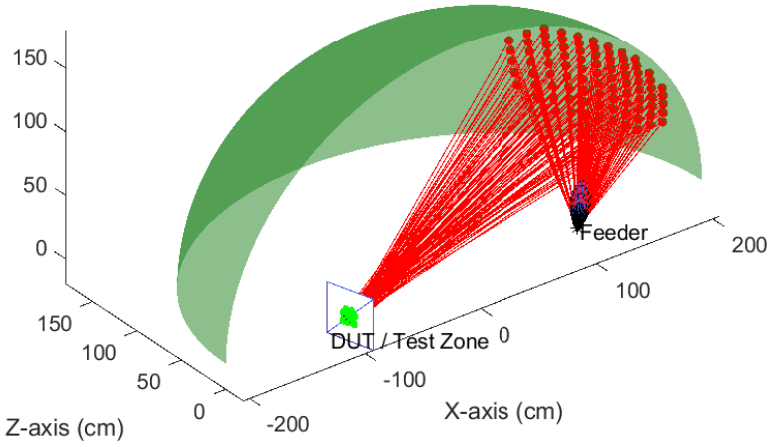

Figure 5.14: Simulation of Test Zone size of the ERR setup

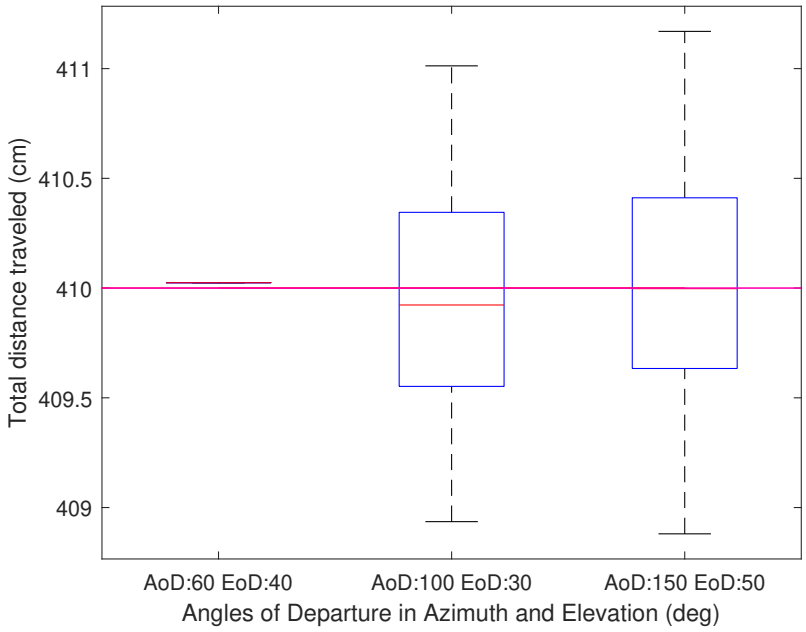

Figure 5.15: Total path distances of rays from different angles of departure

However, for the non-ideal case the total distances travel by the rays will directly depends on the accuracy with which the reflector is created.

5.4.4.2 Distribution of E-Fields in the test zone volume

The estimation of the size of the TZ was based on the spatial distribution of the E-fields evaluated over the $X'-Y'$, $X'-Z'$, and $Y'-Z'$ planes shown at the right-hand side in the Fig. 5.16. The size of the planes was 30 cm × 30 cm (ten centimetres larger than the size of the desired test zone size). To reduce the interference produced by the line of sight fields of the back and side lobes of the feeder antenna a plane with perfect absorber characteristics was placed at the origin of the global coordinate system shown in magenta colour. For an absorber structure to absorb electromagnetic energy its impedance must match with free space to minimize reflections [80].

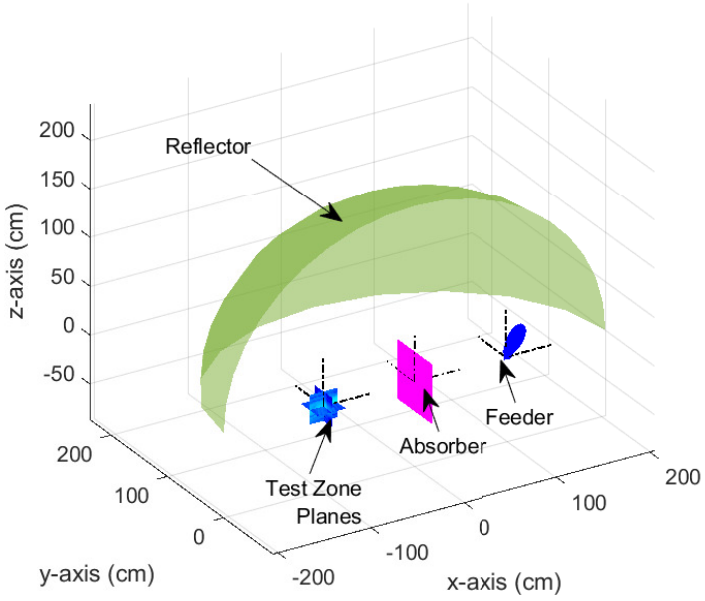

Figure 5.16: Setup for the evaluation of E-fields at the Test Zone

Several tests were performed pointing the beam to different angles to understand how the spatial distribution of the scattered E-field at the test zone behaves. The distribution of the scattered E-fields is shown in logarithmic scale normalised to zero (dB). Here two cases will be analysed as examples.

For the first case the feeder was pointed to the azimuth AoD 160 degrees and elevation of 30 degrees. The three overlapping planes are shown on the top-left plot in Fig. 5.17. Also, the desired test zone is depicted as a cube with black. Visually, it can be seen that there are contribution of energy from all directions. Looking at the $Y'-Z'$ and $X'-Y'$ planes it is notorious that the reflected signal was converging until it reached the focal point and after it diverged rapidly. The highest power level is located close to the focal point which is at the centre of the black squares. The $X'-Z'$ plane clearly shows the beam waist size of approximately 5 cm × 5 cm.

To have a better numerical idea of how the field distribution close to the focal point is, the

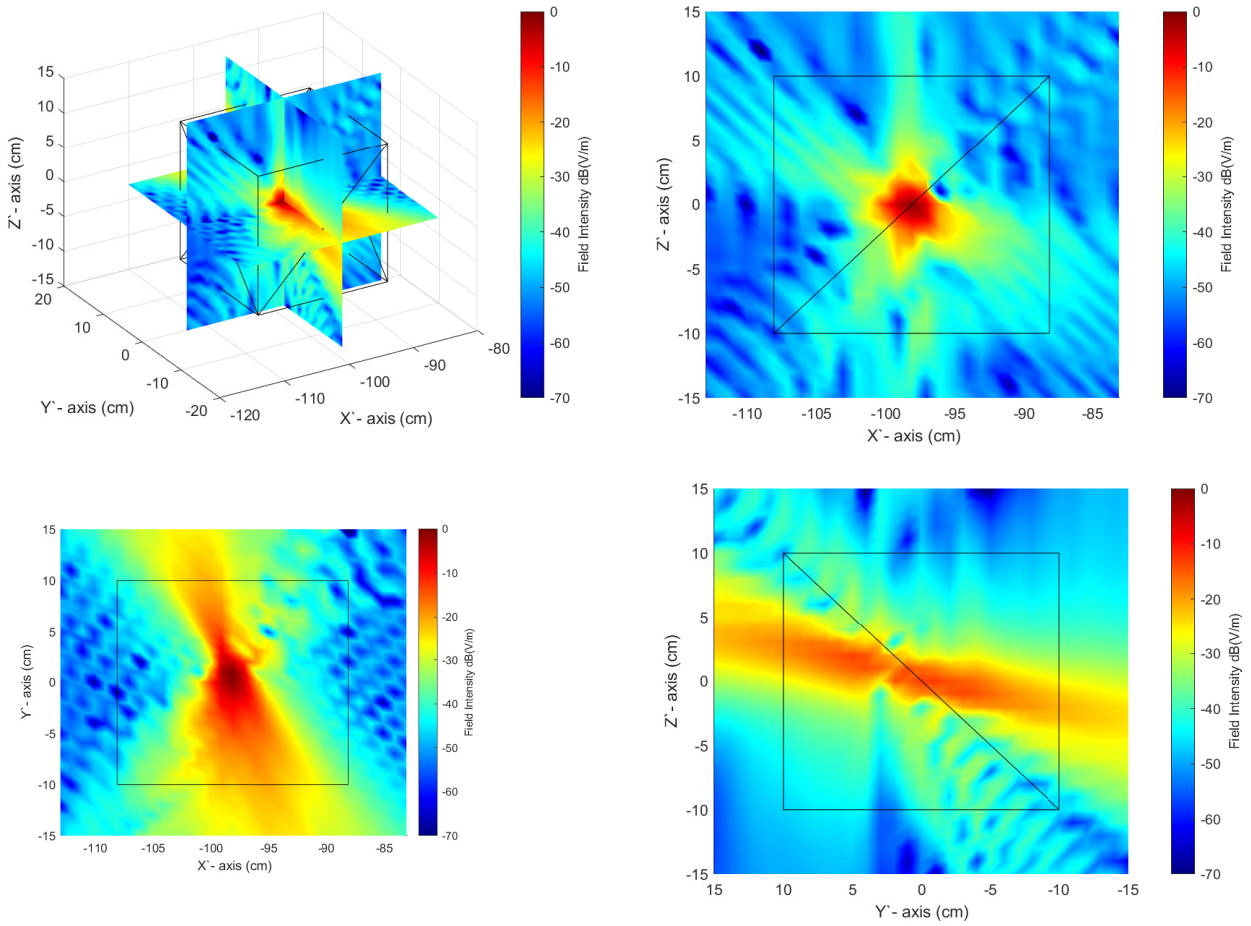

Figure 5.17: Distribution of scattered field at the Test Zone from a signal pointed to AAoD = 160 degrees and EAoD = 30 degrees (Field Intensity normalised to 0 dB)

planes were cut where they intersect to each other. The values of the E-fields extracted from the cuts are shown in Fig. 5.18. It can be seen, that in the range of -10 to 10 cm in the horizontal axis that is the size of the desired test zone volume, the difference of the levels of the E-fields is very large. At the lowest point there is a difference of approximately 60 dB. Ideally, the distribution of the fields should be uniform in amplitude and phase within the test zone.[1] If the beam waist size is measured at the -5 dB mark, then it is of approximately 5cm.

The second example is illustrated in Fig. 5.19. In this case the feeder antenna had an azimuth AoD of 0 degrees and an elevation of 30 degrees. One can observe that the scattered beam waist is wider than the previous case. This behaviour was observed repeatedly when the feeder pointed within its own quadrant, namely in the range of azimuth angles of departure of 0 to 120 degrees. From 120 to 180 degrees the beam waist was narrower. Once more in the bottom-right plot corresponding to $Y' - Z'$ plane it can be seen that the fields converged at the focal point and

[1]Uniform distribution in this context means that the amplitude and phase of the fields should be almost constant

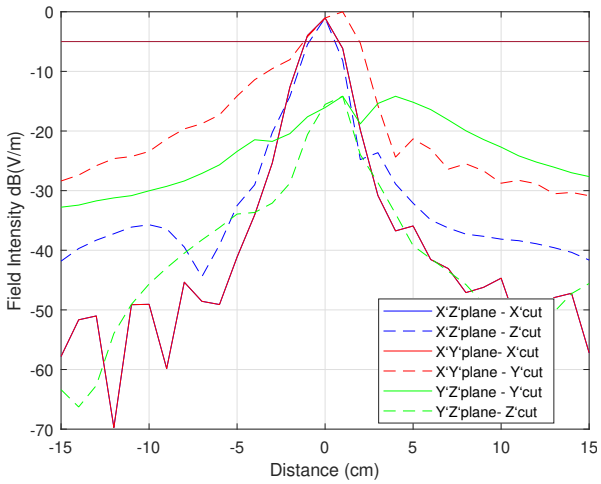

Figure 5.18: Distribution of the E-fields at the intersection lines of the three orthogonal planes

immediately diverge.

For completeness the plane cuts were also taken where the planes intersect each other and are shown in Fig. 5.20. One can observe that there is a wider distribution of the field levels. However, inside the desired region there are large variations also reaching approximately 60 dB difference. It is important to notice that the scattered signal is not perfectly converging at the focal point, therefore a wider spread of the fields is observed in $X'-Z'$ and $Y'-Z'$ planes. The converging point was moved approximately 2 cm in the positive direction of the $X'-$axis (see Fig. 5.19 top-right and bottom-left plots.)

To summarize, firstly, on the plus side it can be observed that the main advantage of using an ellipsoid reflector is that virtually one could generate signals with a large number of angles of departure and arrival from a unique point source or feeder. Secondly, after several simulations it was observed that the E-fields did follow the reflective properties of the ellipse. These converged at the focal point or close to it creating a narrow beam waist or narrow distribution of the fields levels, meaning that there were large variations within the test zone volume. Therefore, the signals at the test zone volume cannot fully illuminate a DUT with the characteristics required to test the performance of the device as suggested by the 3GPP. Hence, it was needed to evolve the design of the geometry of the reflector to enlarge the test zone volume.

5.5 5G OTA test method based on elliptical cylinder reflectors (ECR)

As will be demonstrated the characteristic of the elliptical cylinder reflector allows to have a larger test zone volume compared with the ellipsoid reflector with some restrictions. A discrete number of ECRs can be used to emulate a 3D mmWave frequency channel environment following a distribution shown in Fig. 5.2.

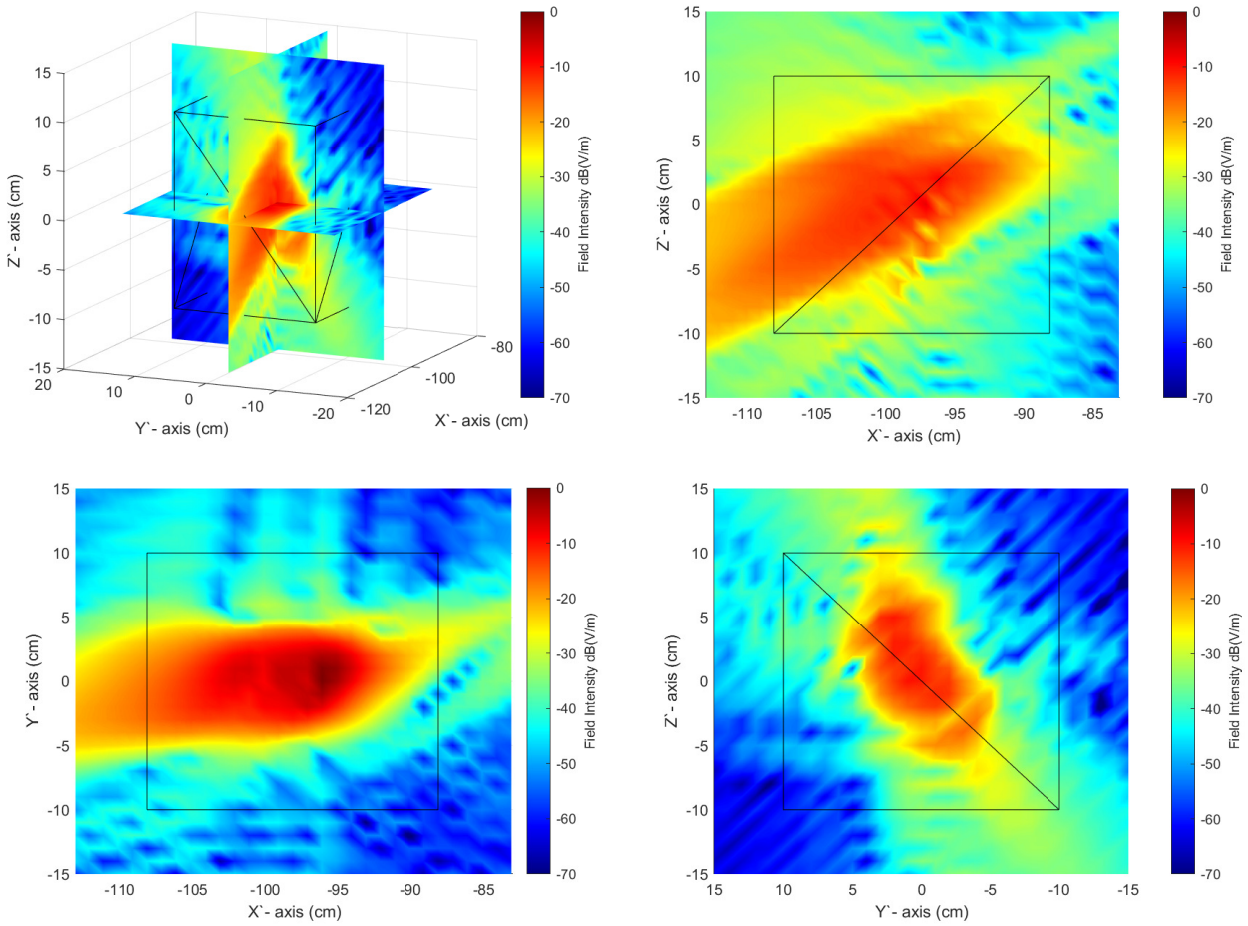

Figure 5.19: Distribution of scattered field at the Test Zone from a signal pointed to AAoD = 0 degrees and EAoD = 30 degrees (Field Intensity normalised to 0 dB)

5.5.1 Design of Elliptical Cylinder reflectors

The parametric equations that describe the side elliptical cylinder are given by equations (5.10)

$$\begin{aligned} x &= a\cos\psi \\ y &= b\sin\psi \\ z &= h \end{aligned} \tag{5.10}$$

where, x and y and z are the coordinates of any point $P(x,y,z)$, and $\psi \in [0,\pi]$ and h is the height of the reflector. As was the case for the side ellipsoid reflector, it is of interest to use just with half of the ellipse thus the reason of the range of the ψ angles. The centre of the reflector in height coincides with the x-axis of the global coordinate system. Thus, the bottom of the reflector will be located at $z = -h/2$, and the top of the reflector will be placed at $z = h/2$ as shown in Fig. 5.21.

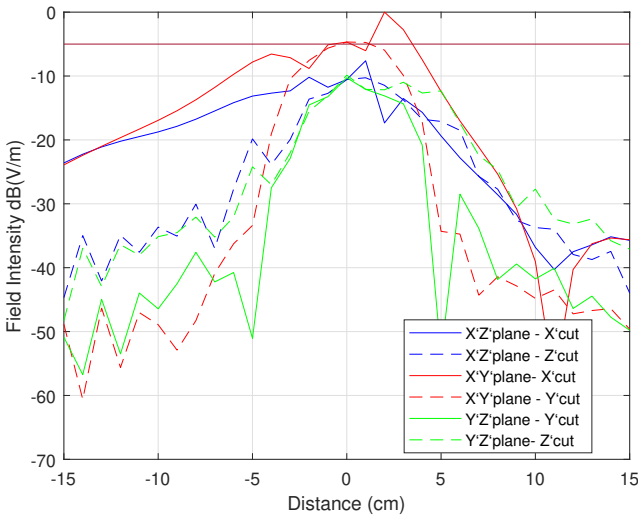

Figure 5.20: 2D E-fields at the Test Zone

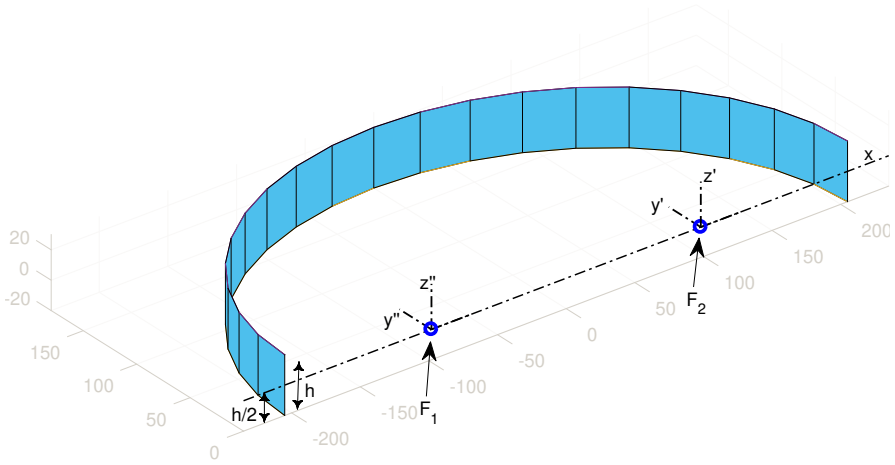

Figure 5.21: Side Elliptical Cylinder reflector (Dimensions in cm)

The dimensions of the semi-major axis and the semi-minor axis remain the same as per the ERR reflector. The height of the reflector was calculated such that the test zone had the right dimensions, as stated in the 3GPP recommendations [17].

5.5.2 Angles of Departure and Arrival

The azimuth angles of departure are given by the angles that delimit the shape of the reflector, as only half of the ellipse is being considered the azimuth angles of departure (AAoD) are all the values of $\psi \in [0, \pi]$.

The azimuth angles of arrival of the ECR are computed as follows: Given that the i-th reflection point $P_i(x_i, y_i, z_i)$ on the surface of the reflector is known, the AAoA α_i of any incident

ray at F_2 is given by equation 5.11, and illustrated in Fig. 5.22

$$\alpha_i = \cos^{-1}\left(\frac{(F_2 - P_i)\cdot(F_2 - O)}{|F_2 - P_i||F_2 - O|}\right) \tag{5.11}$$

One of the advantages of using an ellipse is that the system is fully bidirectional, which means that the DUT and the feeder can be placed in any of the focal points. For the previous calculation it was considered that the feeder was be placed at F_1, but if the order is inverted and the feeder was placed in F_1 the the AAoA are given by equation 5.12. Theoretically the range of AAoA would be $0 \geq \alpha \geq 180$ degrees.

$$\alpha_i = \cos^{-1}\left(\frac{(F_1 - P_i)\cdot(F_1 - O)}{|F_1 - P_i||F_1 - O|}\right) \tag{5.12}$$

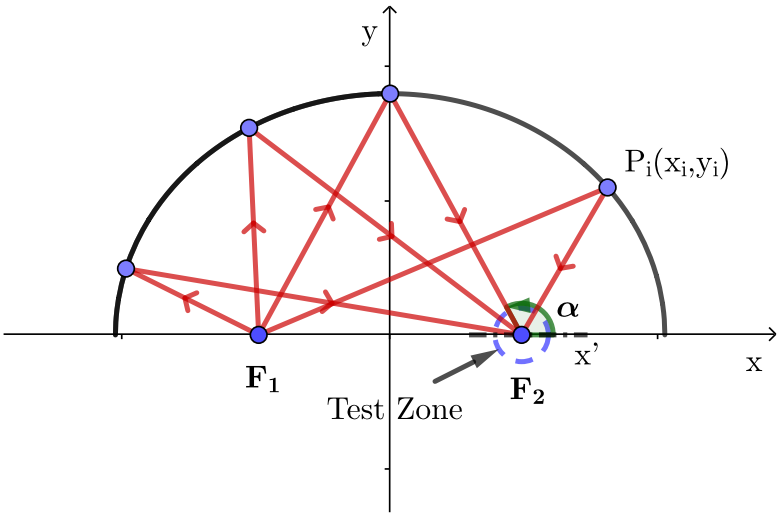

Figure 5.22: Top view of Elliptical Cylinder Reflector - Azimuth AoA

In order to generate signals that arrive to the DUT in 3D, multiple elliptical cylinder reflectors were needed. Considering the fact that in real scenarios the signals will arrive to the device from angles smaller than 60 degrees in elevation, thus for this test method it was considered having three reflectors in total. The first in the azimuth plane and the other two elevated 30 and 60 degrees respectively. The rotation was realized around the x-axis. Fig. 5.23 illustrates the idea, where only the centre lines of the reflectors are shown. The Point P is placed in at the 30 degrees. A ray being launched from F2 to F1 is depicted by the red lines. The angles of arrival in the elevation plane are represented by β which are measured from the xy-plane towards the z'-axis. Given that the i-th reflection point $P_i(x_i, y_i, z_i)$ is known, the EAoA β_i of any incident ray at F_1 can be calculated as follows:

1. Calculate the projection point $Pproj_i$ of P_i onto the xy-plane given by equation (5.6)
2. Calculate β_i

(5.13) $$\beta_i = \cos^{-1}\left(\frac{(F_1 - Pproj_i)\cdot(F_1 - P_i)}{|F_1 - Pproj_i||F_1 - P_i|}\right)$$

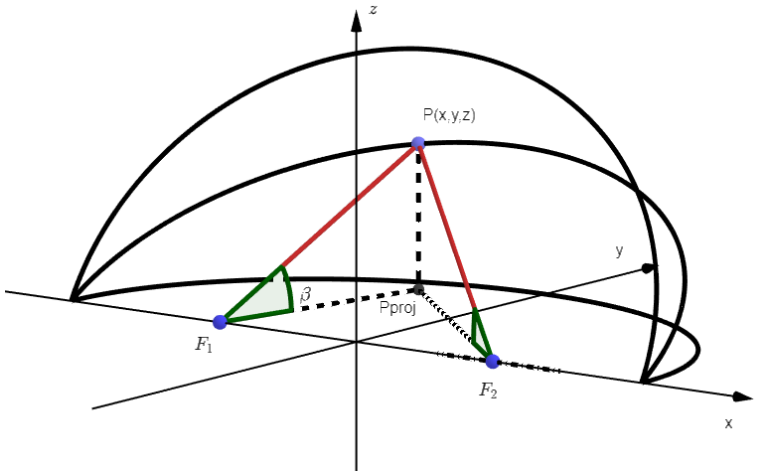

Figure 5.23: Elevation AoA

Theoretically the range of EAoA for the reflector elevated 30 degrees would be from $0 \geq \beta \geq 30$ degrees, and for the reflector elevated 60 degrees the range of EAoA is $0 \geq \beta \geq 60$ degrees. For the reflector located in the azimuth plane the EAoA would be 0 degrees.

5.5.3 Angular Mapping between AAoA and DAoA

To perform tests of the prototype it is required to know beforehand the mathematical expression that relate the azimuth angles of departure with the azimuth and elevation angles of arrival, because at these angles the maximum power transfer should occur.

The equations that relate the AAoD with the AAoA for each elevation angle (0, 30 and 60 degrees) are given by fifth-order polynomials (equation 5.14) with different coefficient.

(5.14) $$f(\xi) = p1 * \xi^5 + p2 * \xi^4 + p3 * \xi^3 + p4\xi^2 + p5\xi + p6$$

The p_i coefficients of equation 5.14 with 95% confidence bounds are listed below:

Similarly, the angular correspondence between the azimuth angles of departure with the elevation angles of departure can be found by a sinusoidal equation such as 5.15

(5.15) $$f(\xi) = a1 * sin(b1 * \xi + c1)$$

The a_1, b_1 and c_1 coefficients of with 95% confidence bounds for the reflectors elevated 30 and 60 degrees are listed below:

Table 5.1: Mapping of Angles of Arrival and Departure Elev 0 deg

Coeff	0 deg	30 deg	60 deg
p_1	0.36	-1.189	-8.368
p_2	03.87	0.071	-16.88
p_3	13.24	15.070	25.11
p_4	20.87	29.830	68.37
p_5	38.69	41.140	47.17
p_6	50.58	45.970	28.08

Table 5.2: Mapping of Angles of Arrival and Departure Elev 0 deg

Coeff	30 deg	60 deg
a_1	30.530	59.03
b_1	0.921	0.941
c_1	1.903	1.912

For the case of the relation between the azimuth angles of departure and the elevation angles of arrival, the distribution that better describes this relation is a Fourier model with three terms, as given by 5.16

$$f(\xi) = a0 + a1 * cos(\xi * w) + b1 * sin(\xi * w) + a2 * cos(2 * \xi * w) + b2 * sin(2 * \xi * w) + a3 * cos(3 * \xi * w) + b3 * sin(3 * \xi * w) \tag{5.16}$$

The coefficients of equation with 95% confidence bounds corresponding to the reflectors elevated 30 and 60 degrees are listed below:

Table 5.3: Mapping of Angles of Arrival and Departure Elev 0 deg

Coeff	30 deg	60 deg
a_0	-86.82	-17.05
a_1	61.19	-23.91
a_2	149.70	77.24
a_3	41.74	43.49
a_4	-63.41	-2.42
a_5	-16.50	-3.92
a_6	-0.1846	-11.54
w	0.01508	0.020

Figure. 5.24, shows the all the angular relations previously described. The horizontal axis corresponds to the azimuth angles of departure and the vertical axis corresponds to the angles of departure and arrival in azimuth and elevation. These relations will be used later to measure the peak power at each point to validate the construction of the ECR prototype.

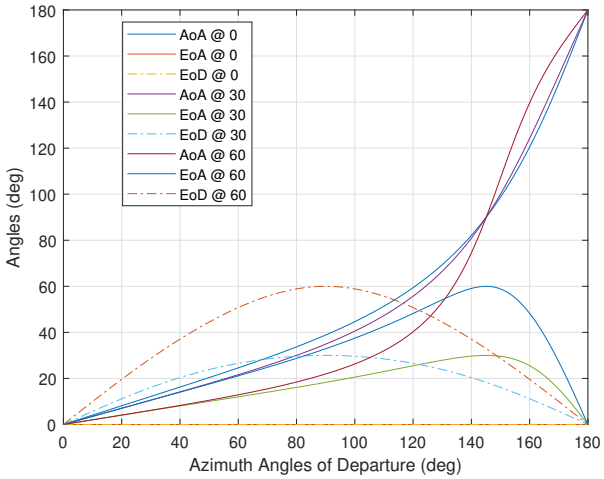

Figure 5.24: Mapping of AAoA and AAoD used to automate the simulations and test of the prototype.

5.5.4 Test Zone of ECR method

Unlike the case of the ERR where all the rays converge towards a single point from any look direction in azimuth and elevation and the test zone in terms of geometric optics is theoretically a point as was demonstrated above, the ECR distributes the energy of the reflected signal in a different way especially in the elevation plane or XZ-plane.

If a perfect isotropic source illuminates the ECR reflector from one of the focal points (e.g. F1), theoretically all the rays or energy of the signal will converge towards a single point at the other focal point (e.g. F2) as depicted in Fig. 5.25 in the azimuth plane (XY-plane). However, this is not ideal, because the DUT would receive a pseudo-isotropical signal if placed at the focal point F_2. It is important to recall that real signals being transmitted by a base station will have narrow beam widths and will arrive from random directions. Therefore, to emulate this, the feeder antenna of the OTA test method must be a directional antenna which radiates and receives greater power in a specific direction. To illustrate this Fig. 5.26 shows a signal with a limited beamwidth illuminating the ECR reflector. It is possible to observe that all the rays in the azimuth plane converge at the other focal point and then it starts spreading again as expected. The blue circle around F_2 represents the test zone.

The fact that all the rays converge towards one point means that the reflected signal concentrates the signal at the focal point, which is not desirable because the beamwidth does not spread sufficiently to create the desired test zone volume in the azimuth plane. It is important to recall that the test system should emulate a far-field signal whose radiated power intensity continuously spreads as it propagates in free space generating plane waves.

On the other hand, the cylindrical shape of the reflector has the advantage that in the elevation plane (XZ-plane) the energy is spread. In terms of GO one can say that the rays diverge

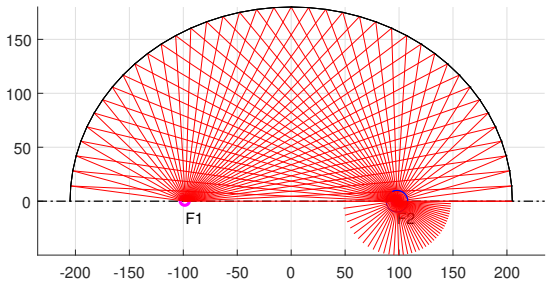

Figure 5.25: Signal distribution with a isotropic source in the azimuth plane (Dimensions in cm)

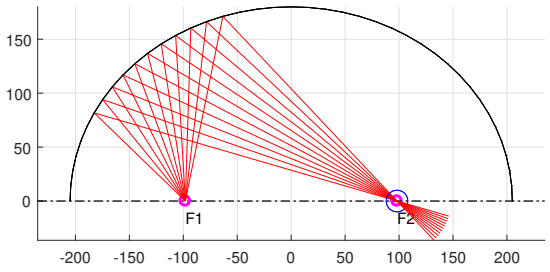

Figure 5.26: Signal distribution with a Directive source in the azimuth plane (Dimensions in cm)

from the centre of the reflector in opposite directions as shown in Fig. 5.27. Two examples of signals with azimuth angles of departure of 90 and 130 degrees are shown. At the DUT focal point there is a black square plane of 40 cm of edge which contains other blue square of 20 cm of edge. The latter represents desired TZ size and the former allows to observe how far the rays spread beyond the desired TZ area. The results of the simulations show that the original beamwidth of the illuminating signal converge in the azimuth plane and diverge in the vertical plane. The distribution of the rays at the TZ plane is represented by the green dots, which creates a very thin vertical area. This area varies depending on the angle of departure. The higher the angle of departure the smaller this area becomes. For example, the AAoD of 10 degrees the covered area is approximately of 5 cm × 40 cm (XY plane × XZ-plane) and for an AAoD of 155 degrees the area covered was 5 cm × 30 cm. Therefore, in terms of geometric optics the estimated waist width was

5 cm, and the height covered would be from 30 cm to 40 cm. It is important to notice that in order to avoid direct transmission from the feeder to the DUT or blockage from the DUT the lowest AAoD must be 10 degrees and the maximum should be 150 degrees.

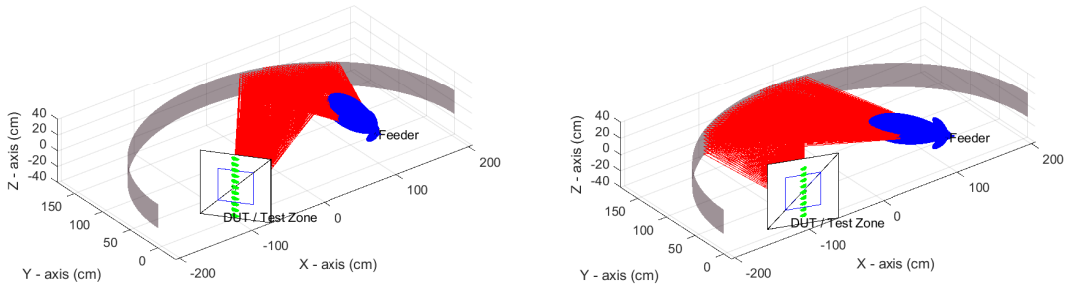

(a) EAoD: 0 deg, AAoD: 90 degrees

(b) EAoD: 0 deg, AAoD: 130 deg

Figure 5.27: Distribution of energy along the Test Zone Area for the ECR positioned on the azimuth plane

The total path distance travelled by each ray that intersects the TZ square for 10 different azimuth angles of departure were recorded. The box plot diagram shown in Fig. 5.28 summarizes the distribution for each AAoD. It can be seen that the median distance for all the iterations is very close to 410.1 cm (magenta line). In the ideal case of an ellipsoid the expected total distance should have been 410 cm (twice the length of the semi-major axis). Also, is noticeable that the higher the angle of departure the larger the range becomes. The smallest range is at AAoD of 34 degrees which is 0.7 cm and the largest range is seen when AAoD is 180 of 1.28 cm. The interquartile range of the 5 first iterations is very similar of approximately 0.20 cm which increases to approximately 0.30 cm for the last 4 AAoDs. For a 28 GHz signal it can be seen that the total path difference for the smallest AAoD equates to a 20% of a wavelength an for the AAoD of 180 it is 20% larger than a wavelength.

Similar simulations were performed for the reflectors elevated 30 and 60 degrees around the x-axis. Two examples of the distribution of the reflected rays resultant of the reflector are shown in Fig. 5.29 and Fig. 5.30. One can observe that for both cases the area formed by the intersecting point at the TZ square has a certain inclination which varies depending on the AAoD and the EAoD. Which means that the electric field would arrive illuminate the DUT diagonally. When the reflector is elevated 30 degrees it can be seen that the illuminated TZ (green dot) form angle just under 40 degrees with respect to the vertical axis. And for the highest reflector the inclination angle of the illuminated TZ it varies between 45 and 55 degrees.

Similar to the scenario where the reflector was placed on the azimuth plane, the box diagrams for the reflectors elevated 30 and 60 degrees are shown in Fig. 5.31 and Fig. 5.32. For both cases it can be seen that the median distance travelled is 410.2 cm. The interquartile ranges are show

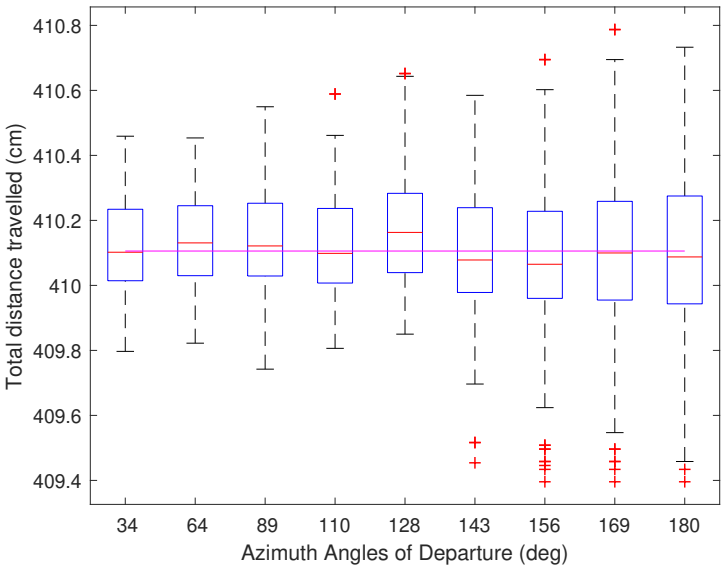

Figure 5.28: Comparison of distance travelled by each ray from different azimuth angles of departure of the ECR positioned on the azimuth plane

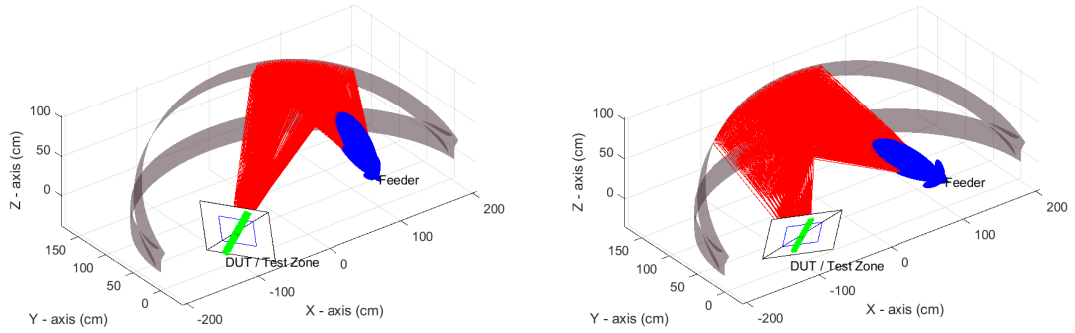

(a) EoD: 30 degrees, AAoD: 90 degrees

(b) EoD: 24 degrees, AAoD: 130 degrees

Figure 5.29: Distribution of energy along the Test Zone Area for the ECR elevated 30 degrees

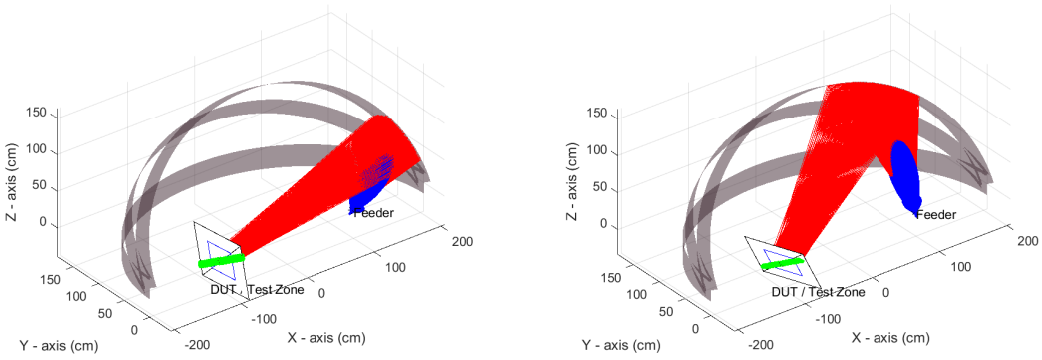

(a) EoD: 29 degrees, AAoD: 20 degrees

(b) EoD: 60 degrees, AAoD: 90 degrees

Figure 5.30: Distribution of energy along the Test Zone Area for the ECR elevated 60 degrees

minimum variations for each one of the elevations analysed, for 30 degrees elevation it is around 0.3 cm and for 60 degrees it is around 0.5 cm, which means that there is a larger dispersion at the highest elevation. The largest total distance range of rays from the two reflectors is approximately 1.4 cm (without consideration of the outlier points), which is 0.2 cm larger than the ECR placed in the azimuth plane.

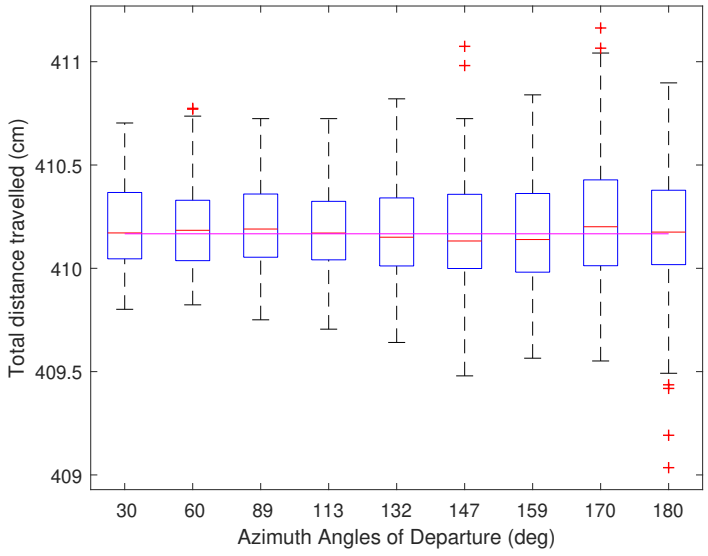

Figure 5.31: Comparison of distance travelled by each ray from different azimuth angles of departure of the ECR elevated 30 degrees

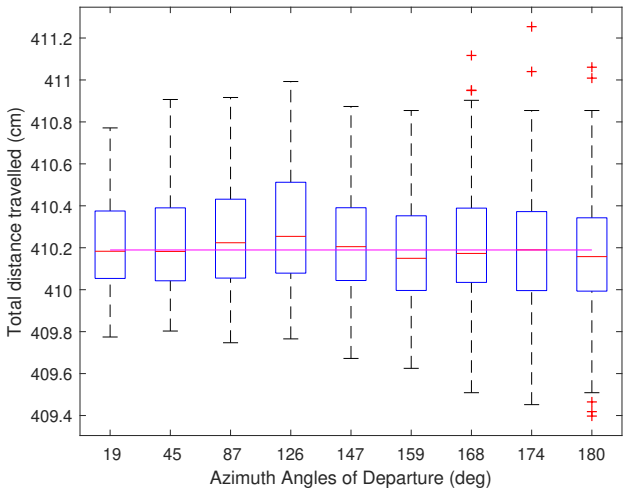

Figure 5.32: Comparison of distance travelled by each ray from different azimuth angles of departure of the ECR elevated 60 degrees

5.5.4.1 Distribution of E-Fields in the test zone volume

Similarly, to the case of the ellipsoid reflector the estimation of the size of the TZ for the ECR was based on the spatial distribution of the scattered E-fields evaluated over the $X''-Y''$, $X''-Z''$, and $Y''-Z''$ planes. The size of the evaluation planes was 30 cm × 30 cm. Also, to reduce the interference produced by the line of sight fields of the back and side lobes of the feeder antenna a plane with perfect absorber characteristics was placed at the origin of the global coordinate system depicted in Fig. 5.33. Additionally, the simulations were done with only one reflector at a time, therefore signals produced by reflections from the adjacent reflectors where not considered. Two signals with random angles of departures illuminating each reflector are discussed below.

Distribution of E-Fields of ECR placed on azimuth plane

In the first case the elliptical cylinder reflector was located on the azimuth plane, and the feeder antenna was pointed to an azimuth angle of departure of 90 degrees and elevation of 0 degrees. The azimuth angle of arrival was approximately 39 degrees. The fields distribution is shown in Fig. 5.34. The top left plot shows all the evaluation planes overlapped. The direction of arrival of the signal can be observed easily in the $X''-Y''$ plane. In this plane it can also be observed that contribution from other angles are also present inside the test zone area that correspond to the side lobes of the feeder antenna. In the vertical planes $X''-Z''$ and $Y''-Z''$ (upper and bottom right plots) it can be seen that the reflected signal was spread even beyond the targeted test zone size (20 cm x 20cm x 20 cm) as was also predicted by the ray tracing algorithm. It is worth mentioning that the feeder antenna was transmitting with vertical polarisation, meaning parallel to the Z-axis, and the fields shown in the individual planes correspond to the Ez-fields,

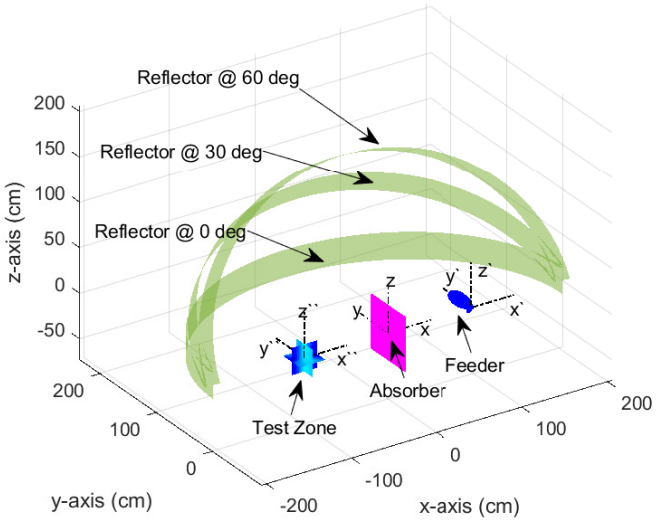

Figure 5.33: Setup for the evaluation of E-fields at the Test Zone of the ECR method

the other components of the E-field were not taken into account as their contribution to the total scattered field was negligible. Which means that the ECR reflector maintains the polarity of the incident fields. For comparison, the plot on the upper left corner with the three orthogonal planes shows the total E-fields.

A cut through of the evaluation planes where they intersect to each other is shown in Fig. 5.35. One can observe the waist width of the signal is of approximately 10 cm, given by the Y''-cuts line. As the signal arrive diagonally to the test zone volume the X''-cuts show that the levels of the E-field inside the test zone do not decay so rapidly, and also reveal that the highest pick is offset 2.5 degrees from the centre of the TZ. In the Z''-cuts one can observe the distribution of the signal in the vertical direction. The ripple of the signal in this cut is within a range of ±0.3dB. Therefore, in this case the objective of having a larger test zone in the vertical plane was correctly achieved.

The second case corresponds to a signal transmitted with azimuth AoD of 140 degrees, which corresponds to an AoA of 89 degrees. Figure. 5.36 shown the distribution of the E-field. One can observe that the waist width is narrower than the previous analysis, and here is of approximately 5 cm. In the $X'' - Y''$ plane one can observe the angle of arrival of the signal, but again more scattered fields also arrive from other directions, although with lower Field Intensity levels. In the vertical planes it can be seen that the signal was spread along the positive and negative Z''-axis. Because the signal is arriving perpendicular to the $X'' - Z''$ plane then the bottom right plot shows that the E-fields are distributed more uniformly in the $Y'' - Z''$ plane.

The 2D plot of the cuts where the planes intersect shown in Fig. 5.37, exhibit that inside the test zone in the Z''-axis direction the ripples of the signal are in the range of ±0.3 dB.

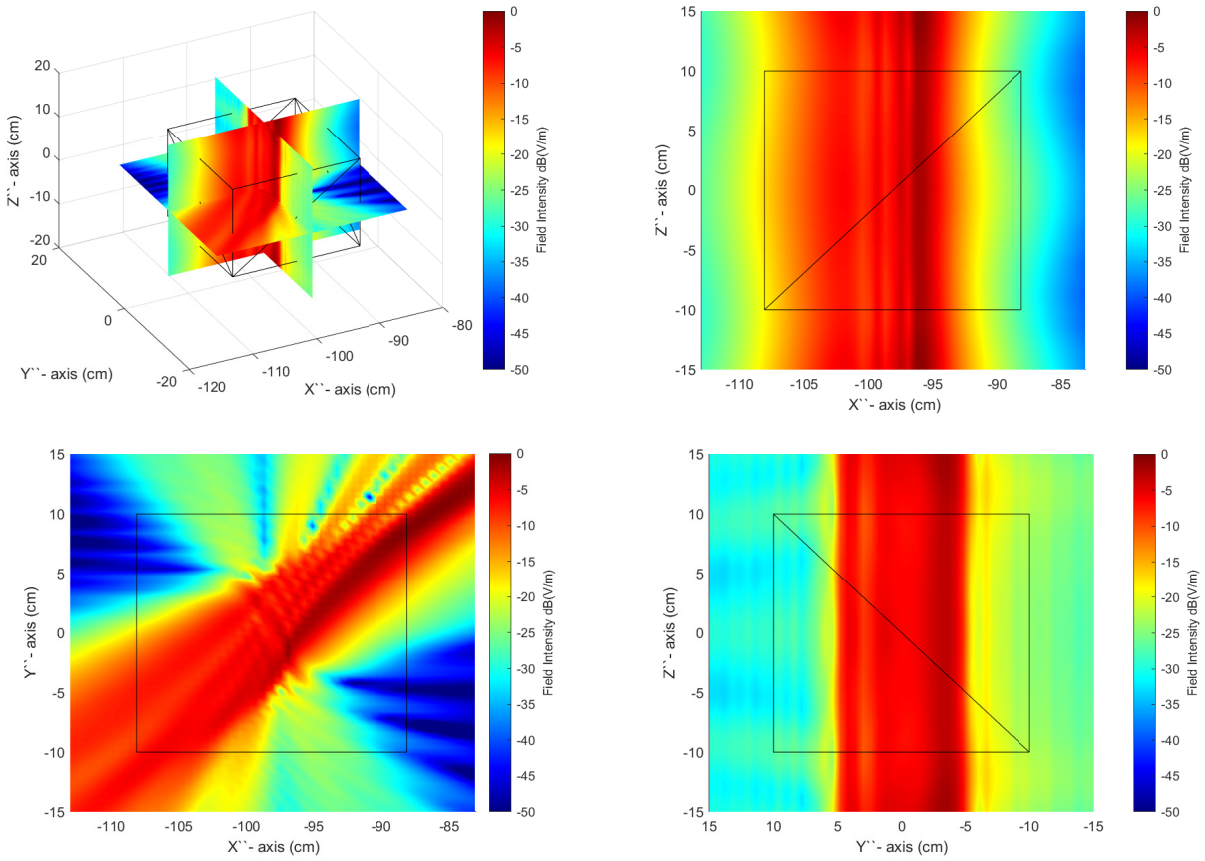

Figure 5.34: Distribution of scattered field at the Test Zone from a signal pointed to AAoD = 90 degrees and EAoD = 0 degrees (Field Intensity normalised to 0 dB)

Furthermore, one can observe that the waist width of the signal is very narrow in the X''-axis cut. The Y''-axis cut show that in the range of -5 to 5 cm inside the TZ there is a very small ripple of the fields. With these simulations one can say that the attainable TZ size that this reflector could create would have a width between 5 cm and 10 cm, the height is larger than 20 cm and the length would be also larger than cm. Which is still smaller than the desired size of 20 cm × 20 cm × 20 cm.

Distribution of E-Fields of ECR elevated 30 degrees

In this section the distribution of the E-fields scattered by the reflector is elevated 30 degrees are analysed. The azimuth angle of departure of the feeder was 90 degrees as in the first case analysed of the previous reflector and the elevation angle of departure was 30 degrees as it coincides with the elevation of the reflector.

The azimuth angle of arrival of the reflected signal theoretically should be 35 degrees but in the $X'' - Y''$ plane shown in the bottom left plot of Fig. 5.38 it can be seen that the highest

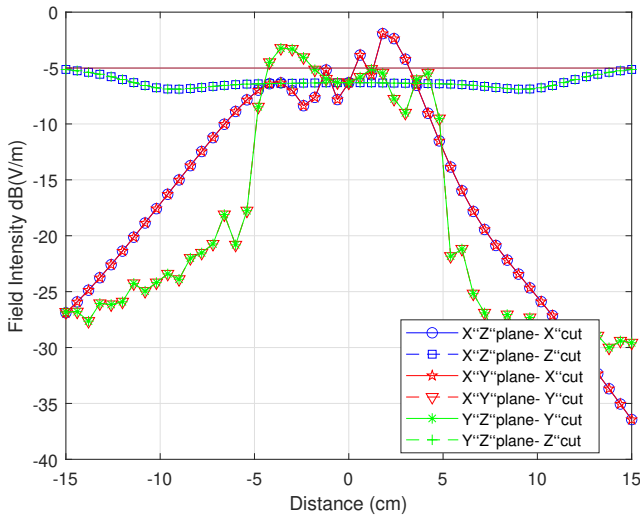

Figure 5.35: 2D E-fields at the Test Zone reflector at azimuth plane (Field Intensity normalised to 0 dB)

power arrive with an angle of approximately 45 degree with respect to the $X''-$axis. Compared to its pair plot in Fig. 5.34 one can observe that there is approximately additional 5 degrees of deviation from the theoretical angle of arrival. According to the simulations with the ray tracing tool it was expected that the signal in the vertical planes $X''-Z''$ and $Y''-Z''$ would be tilted approximately 40 degrees with respect to the $Z''-$axis, and is precisely what is depicted in the two right plots of Fig. 5.38.

At the intersection lines of the evaluation planes shown in Fig. 5.39 one can observe that the beam waist width is practically the same as in the first case analysed of 10 cm. The major difference is the distribution of the fields in the Z''-cuts because before the ripple of the fields was very small inside the TZ area because the signal spread along the Z''-axis, whereas now the fields fluctuate between -2.5 dB and -10 dB (inside the distance range of interest between -10 and 10 cm shown in Fig. 5.39 on the horizontal axis). However, this was expected as now the signal arrive to the TZ diagonally.

Distribution of E-Fields of ECR elevated 60 degrees

The last case analysed in this chapter is a signal with an azimuth angle of departure of 90 degrees and 60 degrees in elevation, that illuminates the reflector also elevated 60 degrees. This case would be a direct comparison with the azimuth reflector and 30 degrees elevated reflector previously discussed. The theoretical angles of arrival in azimuth is 22 degrees and 33 degrees in elevation. The ray tracing simulation in Fig. 5.30b, give us a rough idea of how the fields should be distributed at the TZ which helps to associate the behaviour shown here in Fig. 5.40. It can be seen in the bottom right plot how the signal spread due to the cylindrical shape of the reflector that originally was parallel to the $Z''-$axis now has an inclination of around 55 degrees with

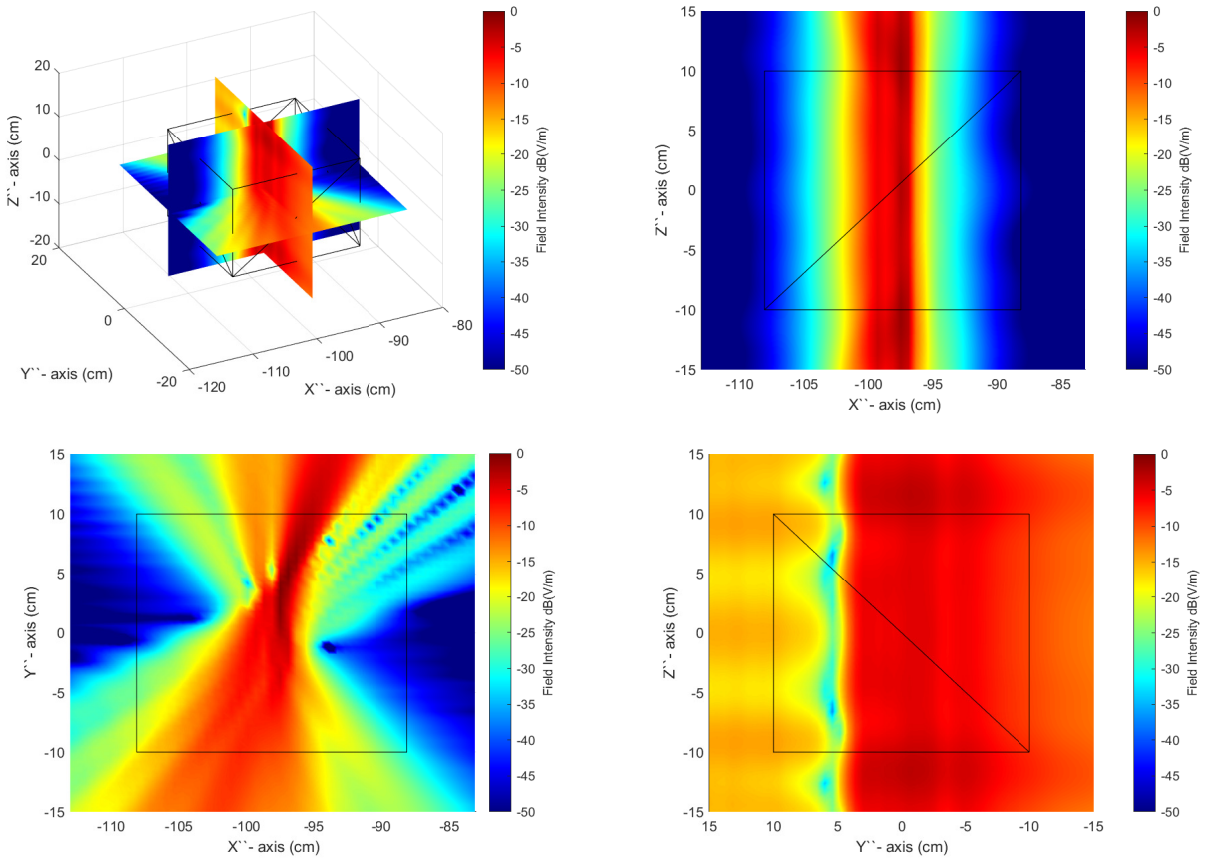

Figure 5.36: Distribution of scattered field at the Test Zone from a signal pointed to AAoD = 130 degrees and EAoD = 0 degrees (Field Intensity normalised to 0 dB)

respect to the Z''−axis. The waist width is still similar to the other two cases of about 10 cm.

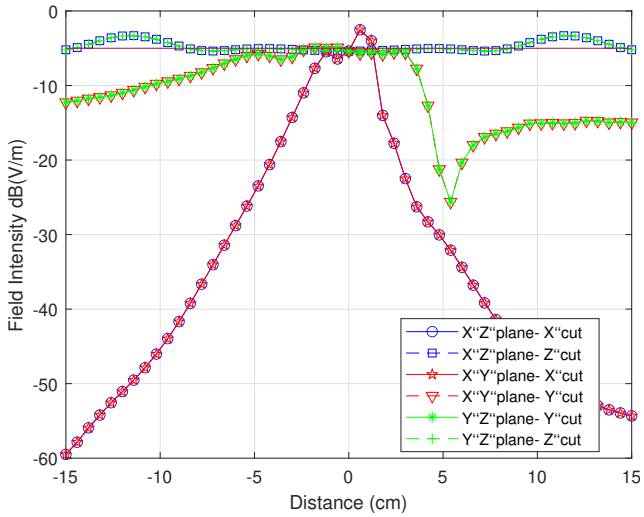

Figure 5.37: 2D E-fields at the Test Zone reflector at azimuth plane (Field Intensity normalised to 0 dB)

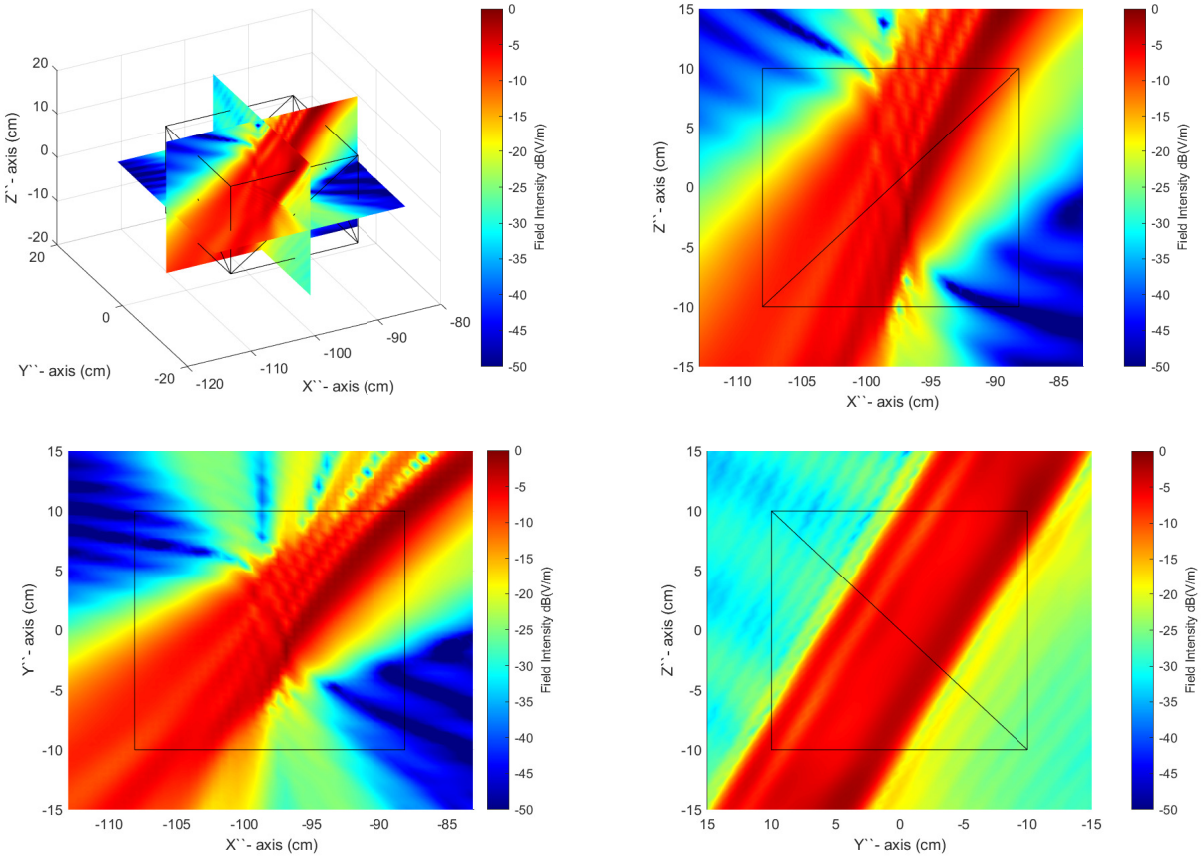

Figure 5.38: Distribution of scattered field at the Test Zone from a signal pointed to AAoD = 90 degrees and EAoD = 30 degrees (Field Intensity normalised to 0 dB)

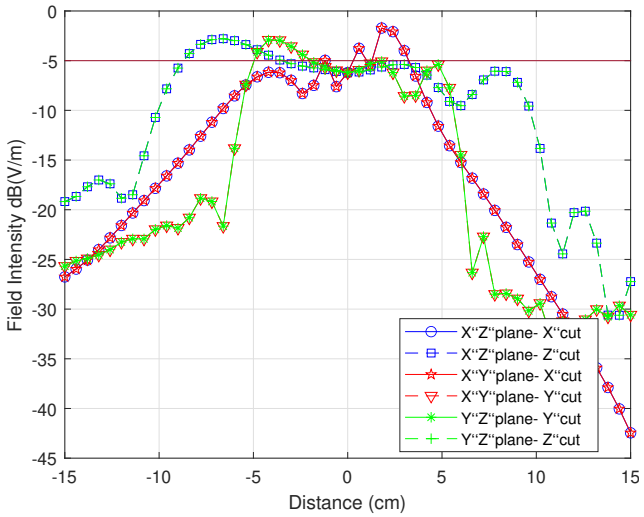

Figure 5.39: 2D E-fields at the Test Zone from reflector elevated 30 degrees (Field Intensity normalised to 0 dB)

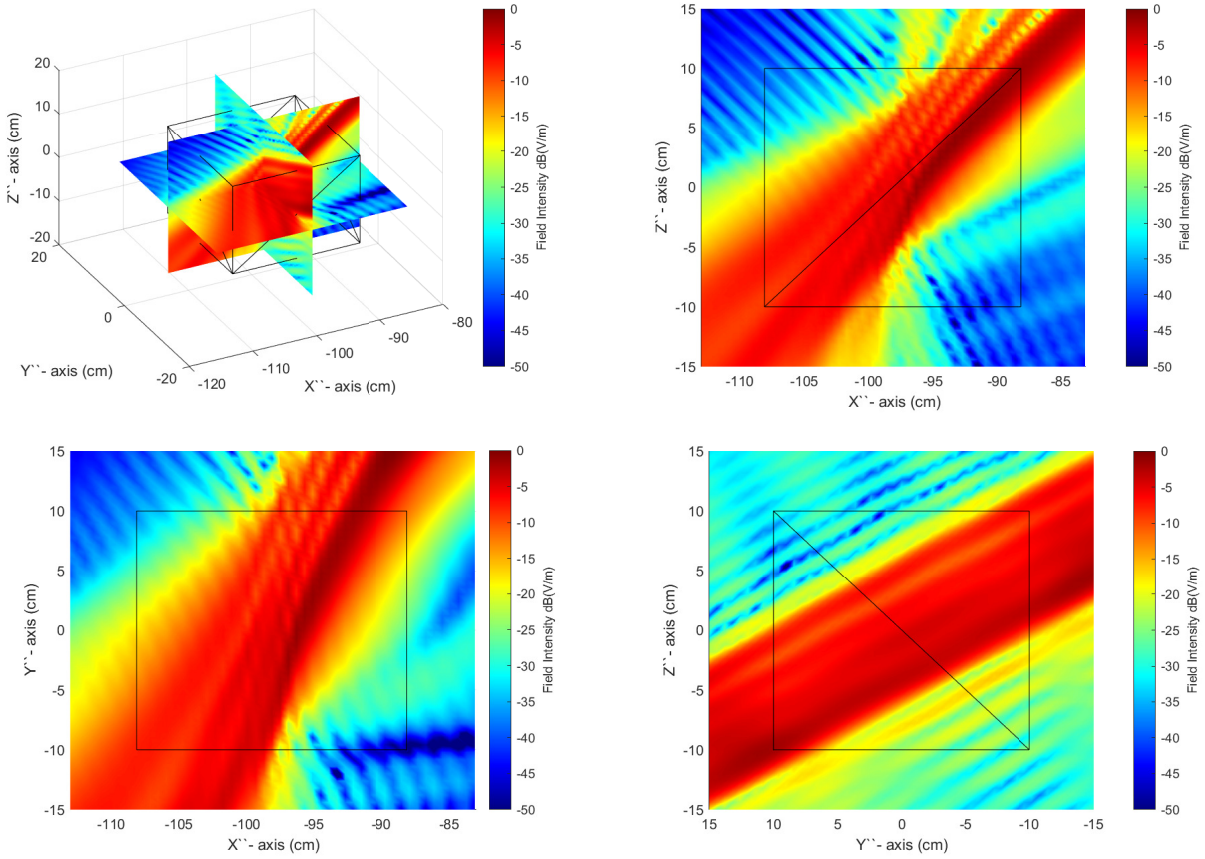

Figure 5.40: Distribution of scattered field at the Test Zone from a signal pointed to AAoD = 90 degrees and EAoD = 60 degrees (Field Intensity normalised to 0 dB)

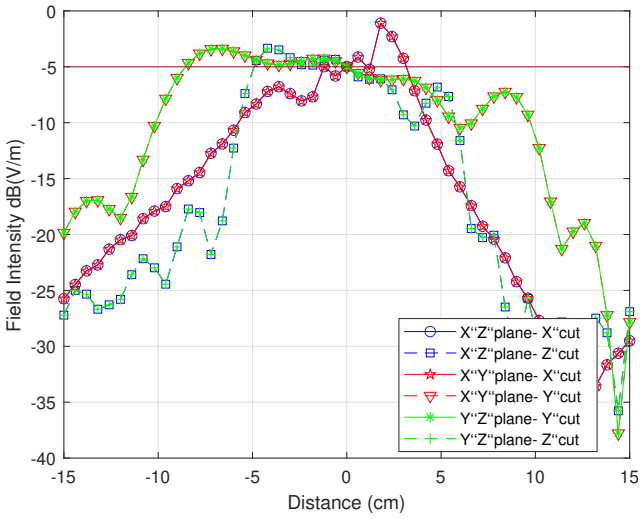

Figure 5.41: 2D E-fields at the Test Zone from reflector elevated 60 degrees (Field Intensity normalised to 0 dB)

5.6 Conclusions

In this chapter two possible candidate methods the Ellipsoid of Revolution Reflector (ERR), the Elliptical Cylinder Reflector (ECR) were analysed. These candidates share some similarities such as, both are based in the reflective properties of the ellipse, and more importantly they can create signals that can illuminate the device under test in a 3D space.

Each one of the candidates is able to create different kind of signal apertures. The ERR focus the signals at the other focal point creating a very small TZ volume, that would not be ideal to test devices such as smartphones or tablets. The estimated realizable size of the TZ volume would be of approximately 5 cubic centimetres.

Two orientations of the ellipsoid reflector were considered seeking to increase the number of angles that could be created. The Front ERR could create azimuth AoA's in the range of 28 to 143.79 degrees. On the other hand, the range of azimuth AoA that the side reflector could generate was from 0 to 180 degrees. Therefore, the latter configuration was the best option, thus it became the basis for the design and analysis of the ECR and in the next chapter the discrete plane reflector (DPR) methods.

The test method with a set of three elliptical cylinder reflectors partially increased the size of the test zone in one plane, and in the orthogonal plane the signal remained as narrow as was the case of the ERR. The height of the reflector was calculated such that the reflected signals at the angles of departure above 150 degrees spread sufficiently to illuminate DUT in the vertical plane such that it complies with the diameter of the TZ suggested by the 3GPP.

From the analysis of the spatial distribution of E-field at the TZ it was possible to visually and numerically through the simulation observe the advantages of the ECR reflectors over the ERR reflectors, as the former allow the scattered fields to diverge and create a larger more uniformly illumination in the test zone. Additionally, it helped to complement and validate the result obtained with the self-developed ray tracing algorithm. Furthermore, one important feature to highlight is that the ECR method does not alter the polarization of the transmitted signal which was demonstrated when looked at the vertical component of the scattered signal individually and the total scattered field.

Theoretically, the range of azimuth AoA that the side reflector could generate was from 0 to 180 degrees and the EAoA varied from 0 to 60 degrees depending the elevation given to the reflector. A possible advantage of the elliptical cylinder reflectors is that it could create signals that can alter their angles of arrival continuously, this feature may be desired for some test cases, but the drawback is the fields inside of the TZ are not uniformly distributed inside the volume, because the reflected signal will always have a small aperture in one of the planes caused by the converging signals produced by the elliptical shape.

CHAPTER 6

5G OTA TEST METHOD BASED ON DISCRETE PLANE REFLECTORS (DPR)

6.1 Introduction

The analysis of the OTA test method with ECR reflectors in Chapter 5 has shown that it would be possible to create a test zone larger than that observed from the ellipsoid reflector, however this is not sufficiently large to comply with the targeted test zone size of 20 cm by 20 cm by 20 cm. Therefore, to overcome this constraint, a final OTA test architecture was envisioned and is described in this chapter. The method is based on a set of discrete plane reflectors distributed along a part-ellipsoid shape.

The main difference with the other two test methods is that this method does not make use of large continuous surfaces, but instead a series of discrete reflectors distributed in an ellipsoidal shape, thereby creating a 3D spatially addressable space. This will support the real-time emulation of the spatial dynamic mmWave channel and performance characterisation of the DUT. A schematic of the proposed mmWave OTA test method is given in Fig. 6.1. It shows three sets of reflectors, the first are positioned on the azimuth plane (0 degrees elevation) and are label as "Reflectors @ 0 deg". The second set of reflectors are elevated 30 degrees and the third set of reflectors are elevated 60 degrees.

The TZ produced by this system can accommodate devices up to 20 cm x 20 cm. The system is also tolerant to the positioning of the array panels within the DUT, as it is expected that the devices will include multiple arrays panels to achieve sufficient spherical coverage. The number of independent simultaneous transmitting signals is given by the specifications of the feeder array antenna and the number of available RF ports.

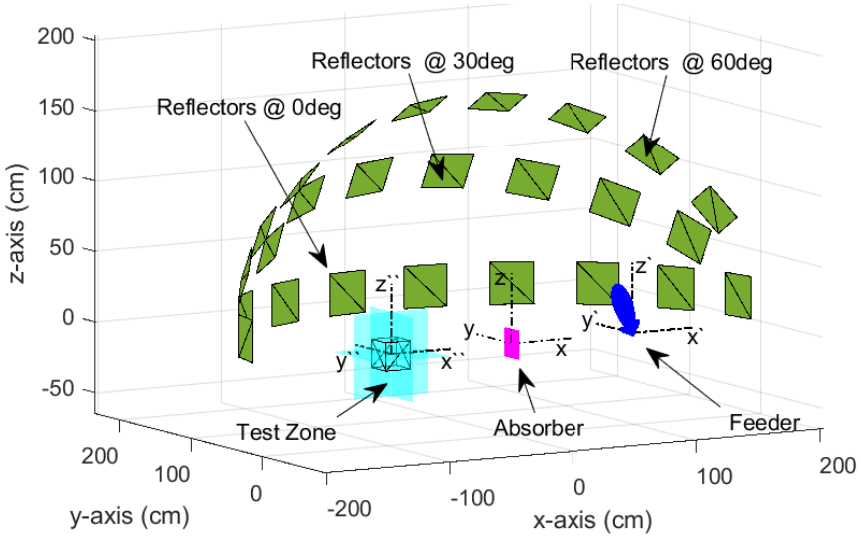

Figure 6.1: Discrete OTA test method setup

6.2 Design of the discrete plane reflectors

The dimensions of the base ellipse are 205 cm x 180 cm (semi-major axis x semi-minor axis) which are similar to the ECR and ERR methods. Each reflector is a square flat surface of edge length 30 cm such that the beamwidth of the reflected signal is large enough to cover the target TZ size and approximate a far-field signal from all angles of arrival.

As previously stated, the method is based on a series of plane reflectors distributed in a part-ellipsoid shape. Recall that the ellipse is a curve surrounding two focal points (F1 and F2), such that for every point P on the curve the sum of its distances to the focal points is constant. The ellipse can be mathematically described by (6.1)

$$x = a\cos\alpha, \quad y = b\sin\alpha, \quad z = h \tag{6.1}$$

Where, $\alpha \in [0, 2\pi)$; x, y, and z are the coordinates in the space of a point $P(x, y, z)$, a is the length of the semi-major axis, b is the length the semi-minor axis, and $h = 0$ is the height, in . It is assumed that the ellipse is centred at the origin $O(0, 0, 0)$ of the Cartesian coordinate system.

For the case under consideration, only half of the ellipse is used, and further segmented into $s = 20$ parts. For this, the set of α angles required is given by (6.2)

$$\alpha_i = \frac{1:2:s}{s}\pi, \quad i = \{1, 2, \cdots, s/2\} \tag{6.2}$$

For every angle α_i a point $P_i(x_i, y_i, z_i)$ is create with (6.1), and the normal vectors to the ellipse $\boldsymbol{n_i} = [n_{xi}, n_{y_i}, n_{zi}]$ at each point P_i is calculated with the gradient of the function with

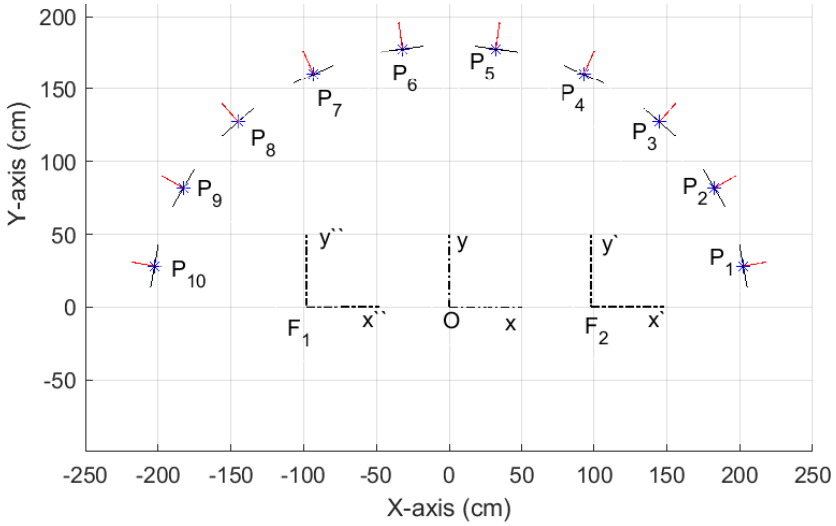

Figure 6.2: Discrete OTA coordinate systems and reflector identification (Dimensions in cm)

eq(6.3). The point and normal vector are shown in in Fig.6.2 with blue asterisk and red arrow respectively.

$$n_{xi} = b\cos(\alpha_i), \quad n_{y_i} = b\sin(\alpha_i), \quad n_{zi} = 0 \tag{6.3}$$

Next a plane parallel to the $YZ-$plane was created with a height $h = 30$ cm and a width $w = 30$ cm. This plane was realized by defining four vertices points: $Q_1 = (0, w/2, h/2)$, $Q_2 = (0, -w/2, h/2)$, $Q_3 = (0, -w/2, -h/2)$, and $Q_4 = (0, w/2, -h/2)$. This plane was replicated 10 times. Each one of the planes was rotate such that they were orthogonal to each corresponding $\boldsymbol{n_i}$ normal vectors. The rotated angle was obtained from $\sigma_i = \tan^{-1}(ny_i/nx_i)$.

After each plane with the corresponding orientation was translated so that their centroids coincided with each P_i point, depicted in Fig.6.3

Finally, to obtain a 3D structure identical copies of the reflectors were created by rotating the vertices points Q_j of the reflectors at 0 degrees and angle δ that could be 30 or 60 degrees in the Euclidean space around the X-axis. This was done by multiplying each point with the rotation matrix $\boldsymbol{R}_x(\delta)$ as given in (6.4), thus one obtains a part-ellipsoid 3D structure as illustrated in Fig. 6.1.

$$\boldsymbol{R_x} = \begin{bmatrix} 1 & 0 & 0 \\ 0 & \cos\delta & -\sin\delta \\ 0 & \sin\delta & \cos\delta \end{bmatrix} \tag{6.4}$$

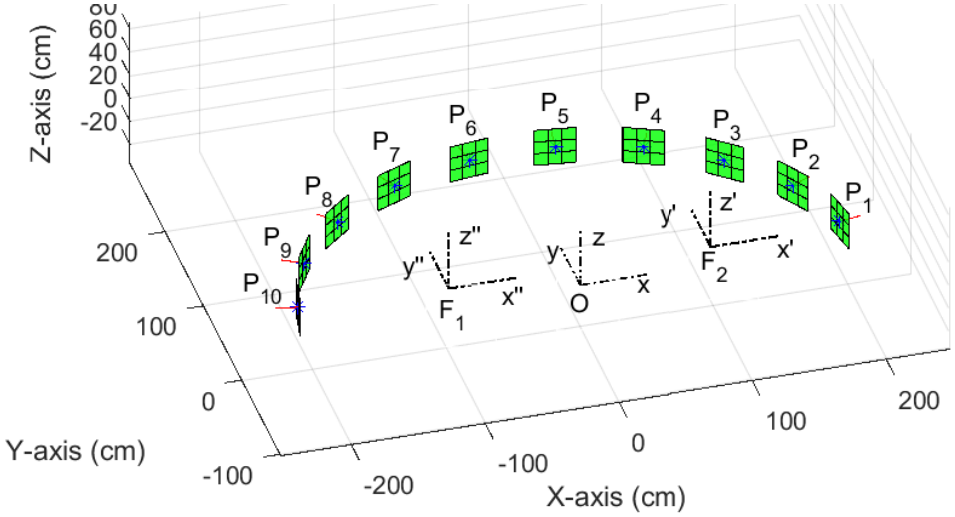

Figure 6.3: Discrete plane reflectors located at P_i points

6.3 Angles of Arrival and Departure

Contrary to the other two methods ERR and ECR analysed before, this method only has a finite number of angles of departure and arrival given by the number of reflectors used. The centroid points P_i (where i is the number of reflector) of each individual reflector is the reference where beam peak of the feeder antenna would be pointed. The computation of the angles of departure and arrival in azimuth and elevation follow the same logic as the case of the ERR, therefore the formulas were not repeated here. The theoretical angular mappings between angles of departure and arrival in azimuth and elevation for the reflectors with elevation 0 degrees are given in Table 6.1. It can be seen that the range of azimuth AoA of the signals illuminating the DUT in the azimuth plane is between 5 and 165 degrees. And the elevation angles are always 0 degrees. The angles of departure and arrival can be directly interchanged depending on the arrangement of the DUT and feeder, as they can be placed in any of the focal points without the results being affected.

For the reflectors elevated 30 degrees it can be seen in Table. 6.2 that the minimum azimuth AoA is 4.6 degrees and the maximum is 166 degrees. The EAoA increase from 2.7 degrees up to 29.9 degrees at reflector 7 and later the EAoA decay to 7.5 degrees again.

For the reflectors elevated 60 degrees it can be seen in Table. 6.3 that the minimum azimuth AoA is 2.6 degrees and the maximum is 172.4 degrees. The EAoA of reflector 1 is 4.6 degrees. The highest angle of arrival comes from reflector 7 being this 59.9 degrees, and the last EAoA is 13 degrees from reflector 10.

Table 6.1: Mapping of Angles of Arrival and Departure of reflectors elevated 0 deg

Reflector	AoD	AoA	EoD	EoA
No	0 deg	0 deg	0 deg	0 deg
1	15.1	5.4	0.0	0.0
2	44.0	16.2	0.0	0.0
3	69.8	27.6	0.0	0.0
4	91.8	39.9	0.0	0.0
5	110.4	53.8	0.0	0.0
6	126.2	69.7	0.0	0.0
7	140.1	88.2	0.0	0.0
8	152.4	110.2	0.0	0.0
9	163.8	135.9	0.0	0.0
10	174.7	164.9	0.0	0.0

Table 6.2: Mapping of Angles of Arrival and Departure of reflectors elevated 30 deg

Reflector	AoD	AoA	EoD	EoA
No	30 deg	30 deg	30 deg	30 deg
1	13.2	4.6	7.5	2.7
2	39.9	14.1	20.3	8.0
3	66.9	24.4	27.9	13.4
4	92.1	35.9	29.9	18.7
5	113.2	49.8	27.9	23.8
6	130.2	66.8	23.8	27.9
7	144.0	87.9	18.7	29.9
8	155.6	113.0	13.4	27.9
9	165.9	140.1	8.0	20.3
10	175.4	166.0	2.7	7.5

6.4 Test Zone of the Discrete Plane Reflector method

It is necessary to determine the dimensions of the TZ where the DUT will be tested. Contrary to parabolic reflectors [81] that collimate signals and effectively minimize the spread of them as they propagate; plane reflectors used in this method produce signals that continuously diverge the reflected signal while propagating similar to how signals propagate in free space. Additionally, a plane reflector does not produce any magnification or focusing of the scattered signal, thus it only would act as a mirror redirecting the incoming signal to another location in space. In the DPR method the individual reflectors follow a part-ellipsoid shape, and as the feeder antenna is placed at one of the focal points the distribution of the reflected signals at the TZ is not uniform for all the reflectors, because it depends on the location and size of the discrete reflectors.

The effective aperture of the signal at the TZ varies depending on the azimuth and elevation angles of departure, size and shape of the reflector, and the radiation pattern of the feeder antenna. To illustrated this in terms of geometric optics, Fig. 6.4 shows two signals. The first

Table 6.3: Mapping of Angles of Arrival and Departure of reflectors elevated 60 deg

Reflector	AoD	AoA	EoD	EoA
No	60 deg	60 deg	60 deg	60 deg
1	7.9	2.6	13.0	4.6
2	25.8	8.3	37.0	14.0
3	53.6	14.6	54.4	23.7
4	93.6	22.7	59.9	33.8
5	126.6	34.3	54.3	44.3
6	145.7	53.3	44.3	54.3
7	157.2	86.4	33.8	59.9
8	165.3	126.4	23.7	54.4
9	171.7	154.2	14.0	37.0
10	177.3	172.4	4.6	13.0

one is pointing to reflector 8. According to the reflection law, it is possible to virtually mirror the source point $F1$ across the imaginary line extended from the reflector, forming the point $F1'$. It is shown that the beam aperture of the incident signal is smaller than the reflector, thus the reflected signal maintains its original aperture denoted by angle ψ. The second signal is pointing to reflector 4. $F1''$ is the mirrored source point which also has the same aperture ψ. Due to the larger distance between $F1$ and reflector 4 the signal (doted arrows) is wider than the reflector, which makes the reflector a spatial filter. The part of the signal impinging the reflector is denoted by the solid lines. Since only a portion of the signal is reflected, the effective aperture of signal at $F2$ from reflector 8 (segment J-Q) is larger than the signal from reflector 4 (segment M-N). Numerically, it was found that the smallest effective aperture will be 23 cm from the reflector closest to the DUT, and the maximum effective aperture is 107 cm for reflector closest to the feeder antenna. Due to these variations the TZ is considered to be only the region inside the circle with a diameter of 20 cm where all the reflected signals are expected to have similar RF conditions, and not the whole effective aperture of the reflected signals. A 20 cm TZ is consistent with the latest recommendations of 3GPP that the quiet zone for smartphones shall be considered a sphere with radius of R = 10 cm [17]. Although Fig. 6.4 shows the distribution of the signals in the horizontal plane (XY-plane), the same applies for the vertical plane (XZ-plane), as the reflector are square shapes.

6.4.1 Ray path lengths and spatial distribution

Some examples of how the reflected rays are distributed from the reflectors 2, 4, 6, and 8 are compared in Fig. 6.5 in terms of GO. It can be seen that the scattered signal from reflector 2 (Fig. 6.5a) diverges in both azimuth and elevation planes and completely illuminates test zone square (inscribed small square) and also illuminates a larger square plane of 40 cm of edge length. As the azimuth angles of departure increase, the area that the rays intersecting with the TZ

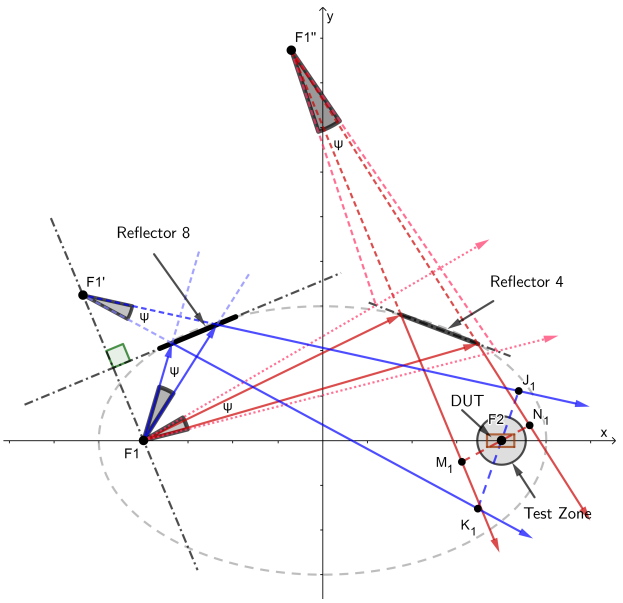

Figure 6.4: 2D example of effective aperture of reflected signals

plane reduces. For example, for the case of reflector 6 (Fig. 6.5c) the area illuminated at the TZ is approximately 23 cm × 23 cm. The illumination area continues to decrease up to reflector 10 that would produce an illuminating area of 20 cm × 20 cm, which is the minimum desired area that this method was designed to realise.

From the simulations it is also noticeable that undesired signals are scattered from adjacent reflectors to the targeted reflector. For example (Fig. 6.5c) illustrates this, as it shows that the targeted reflector was reflector 6, and most of the rays are reflected from this, but also some rays from reflector 7 are also being reflected reaching the TZ area. For the case of reflector 8 (Fig. 6.5d) undesired reflected rays from both of its adjacent reflectors also reach the TZ area. For these two cases the rays reflecting from the adjacent reflectors come from the main beam of the feeder antenna, which means that will have power levels comparable to the desired signal that will corrupt the uniformity of the fields inside the test zone. In Subsection 7.3.2.3 these interferences are further analysed. Additionally, from these simulations it was found that the reflector 1 to 5 do not experience interference produced by the other nearby reflectors caused from the main beam.

The distribution of the total path lengths of the rays travelled from the feeder to the TZ plane from each reflector are shown in Fig. 6.6. It can be seen that the median distance for reflectors 1 to 6 is 410.24 cm, which is only 0.24 cm larger than the path length expected in the case of a perfect ellipsoid. The median distance for the last 4 reflectors was affected because rays with larger or smaller travel distances coming from adjacent reflectors are also present within the TZ plane. For the case of reflector 6 additional rays only from reflector 7 appear, hence, it can be seen rays with larger distances. For the cases of reflectors 7 to 9 reflectors rays arriving from both adjacent reflectors are seen, therefore, larger dispersion of the total path lengths compared

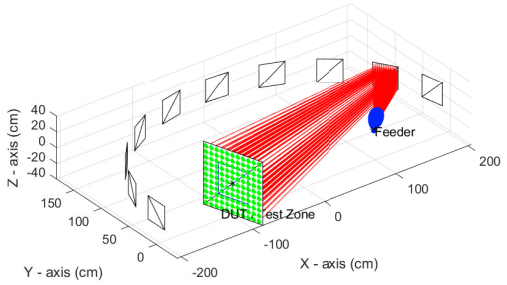

(a) Reflector 2, EAoD: 0 deg, AAoD: 44 deg

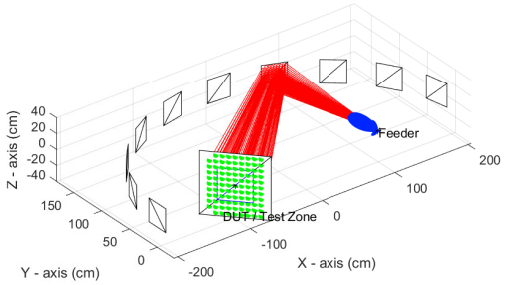

(b) Reflector 4, EAoD: 0 deg, AAoD: 91 degrees

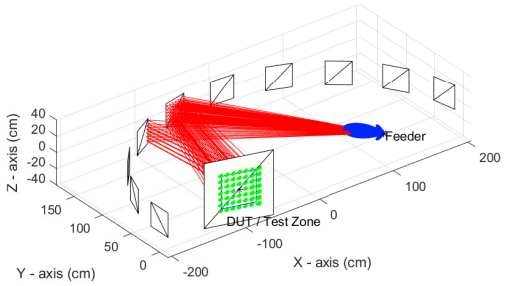

(c) Reflector 6, EAoD: 0 deg, AAoD: 126 deg

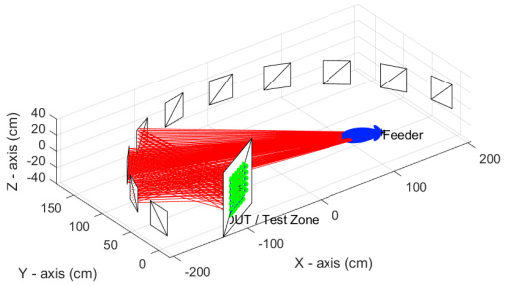

(d) Reflector 8, EAoD: 0 deg, AAoD: 152 deg

Figure 6.5: Distribution of energy along the Test Zone Area for reflectors positioned on the azimuth plane

to the expected median of 410 cm are observed.

If the adjacent reflectors that create interference in the TZ are not taken into account, then the distribution of the total path lengths of the rays in the TZ plane for the different reflectors are shown in Fig. 6.7. It can be seen that the minimum length of the ray paths arriving at the test zone form the different angles of departure is the ideal distance of 410 cm and the maximum length is 410.5. The distance difference with the largest ray paths is 0.5 cm, which is smaller than half wavelength at 28 GHz. Additionally, it was observed that the median ray path length was 410.25 cm.

Similar simulations were performed for the discrete reflectors elevated 30 and 60 degrees. Figure 6.8 show the results of four tests, as was expected, the reflected rays fully cover the TZ plane from any angle of departure. The distribution of the total path lengths of the rays for all the reflectors are shown in Fig. 6.9, where can be seen that the total lengths of the rays experienced grater variations compared to the cases of the reflectors placed on the azimuth plane. However, the median total distance for all the cases shown a minimum variation as all of them remained

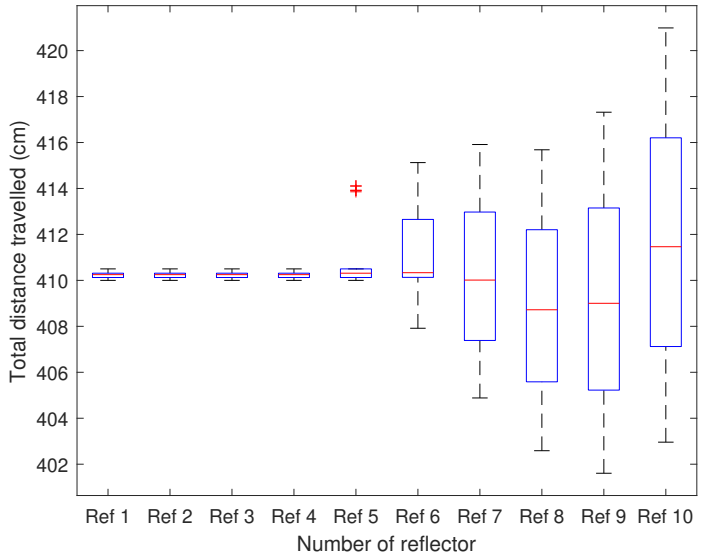

Figure 6.6: Statistical distribution of the total path lengths of the rays at the test zone plane per reflector including interfering rays

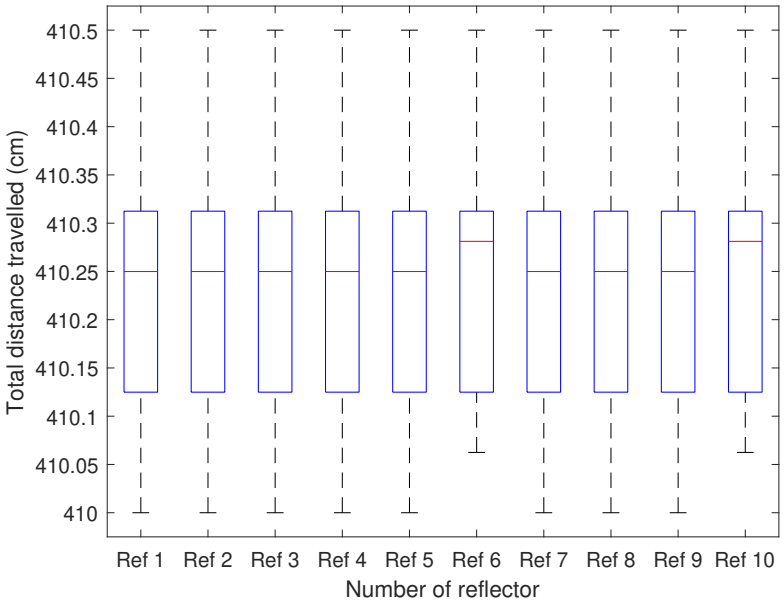

Figure 6.7: Statistical distribution of the total path lengths of the rays at the test zone plane per reflector without interfering rays

below the 410.3 cm, which is very similar to the non-elevated reflectors. The range of the total distances for all the cases remained below 410.6 cm with the exemption of reflector 2 that the range was higher with one ray having a length larger than 410.8 cm.

When the reflectors were elevated 60 degrees around the x-axis, according to the simulations a similar (Fig. 6.10) behaviour was seen when compared to the other two cases of 0 and 30

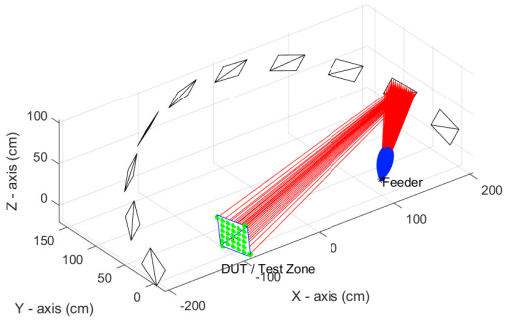

(a) Reflector 2, EAoD: 20 deg, AAoD: 40 deg

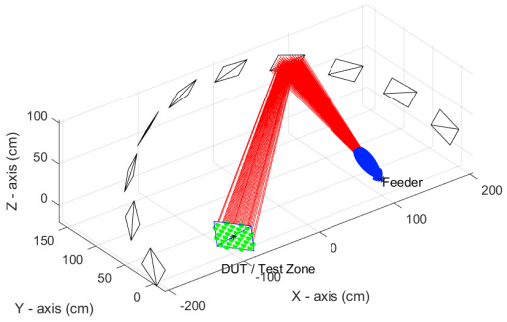

(b) Reflector 4, EAoD: 30 deg, AAoD: 93 degrees

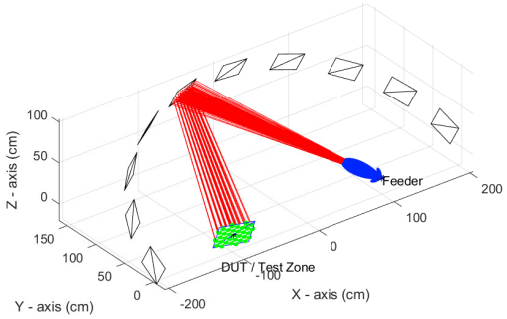

(c) Reflector 6, EAoD: 23 deg, AAoD: 130 deg

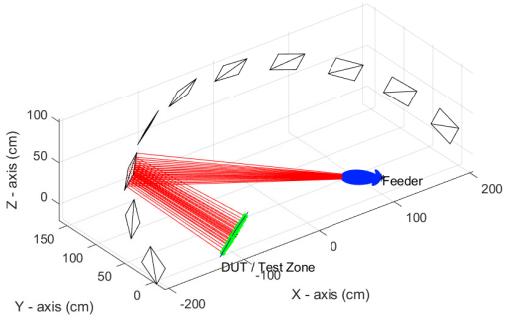

(d) Reflector 8, EAoD: 13 deg, AAoD: 156 deg

Figure 6.8: Distribution of energy along the Test Zone Area for reflectors elevated 30 degrees

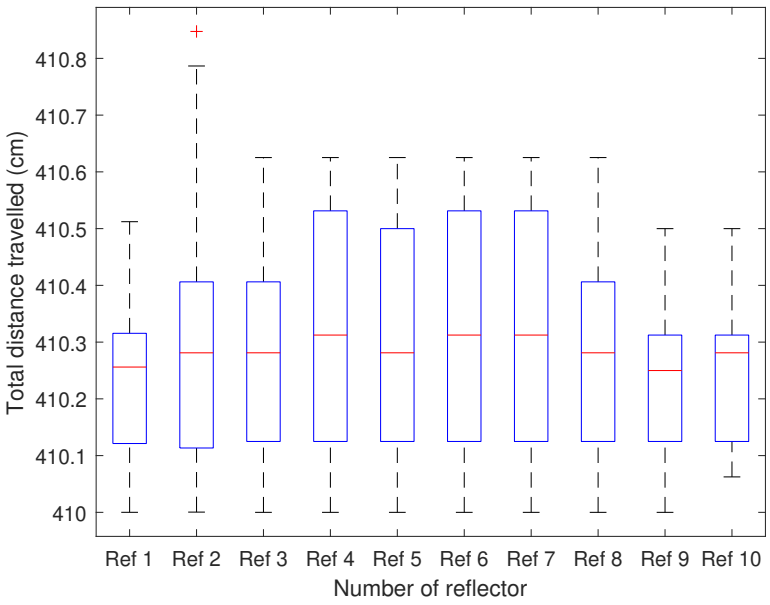

Figure 6.9: Statistical distribution of ray path lengths per reflector when elevated 30 degrees without interferers

degrees. The spatial distribution of the reflected rays fully cover the desired test zone plane. The median distance travelled by the rays was approximately 410.27 cm. The range of total distances was between 410 cm and 410.8 cm only for the reflectors 2 and 5. However, for the other cases the range remained withing 410 and 410.6 cm which is similar to the best case when the reflectors are placed in the azimuth plane (see Fig. 6.11).

Knowing the total distances travelled by the rays from the different reflectors positioned at different heights give a coarse idea that the amplitude levels of the scattered signals at the test zone plane will have certain uniformity as the distances are very close to the ideal theoretical case of 410 cm. As a quick reference with the worst case that is a total distance of 410.8 cm the additional free space path loss that this ray would experience at 28 GHz would be less than 0.1 dB. The analysis of the distribution of field and phases is further extended below.

‘

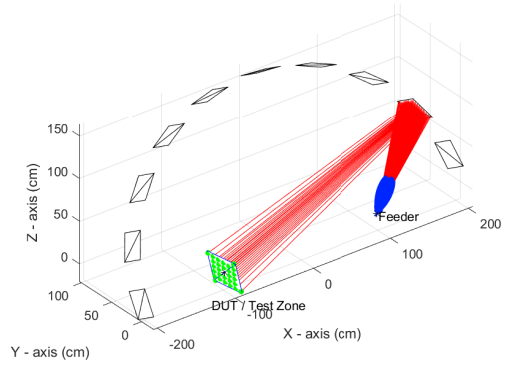

(a) Reflector 2, EAoD: 37 deg, AAoD: 26 deg

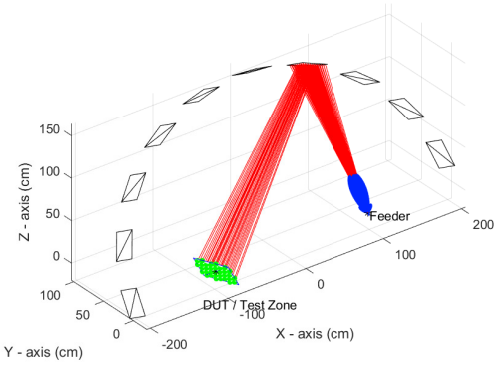

(b) Reflector 4, EAoD: 60 deg, AAoD: 94 deg

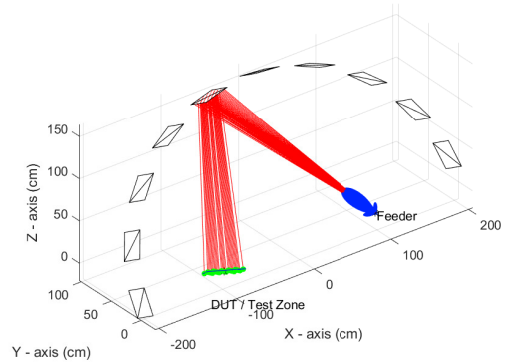

(c) Reflector 6, EAoD: 44 deg, AAoD: 146 deg

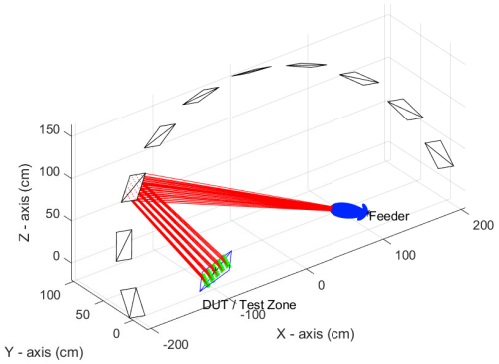

(d) Reflector 8, EAoD: 14 deg, AAoD: 165 deg

Figure 6.10: Distribution of energy along the Test Zone Area for reflectors elevated 60 degrees

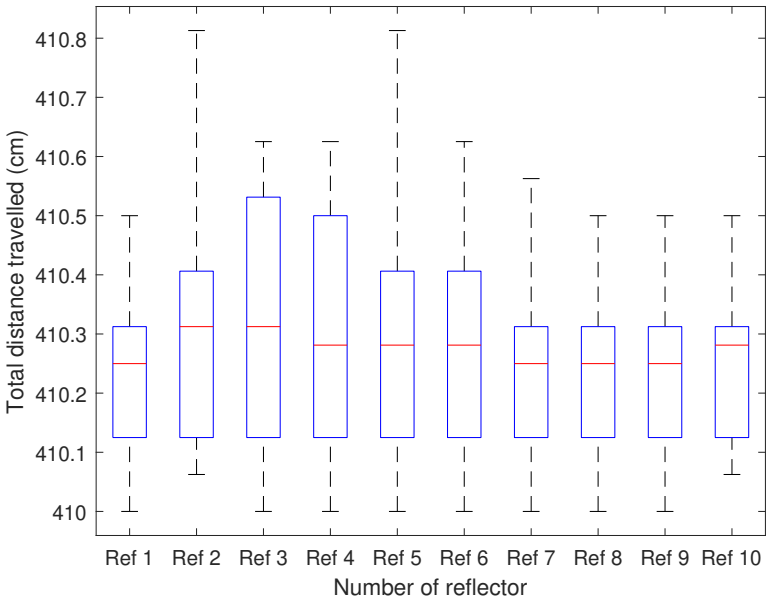

Figure 6.11: Statistical distribution of ray path lengths per reflector when elevated 60 degrees without interferers

6.4.2 Analysis of distribution of fields inside of the test zone

The ray tracing simulations helped to gain a good intuition of the behaviour of the reflected signals and the expected size of the test zone that each reflector generates. However, it is also important to study the distribution the fields at the test zone similarly to what was done for the ECR and ERR methods. According to the ray tracing simulations, it is expected that the energy spreads more evenly in both the azimuth and elevation planes compared to the other two methods.

6.4.2.1 Analysis of reflectors placed on the horizontal plane

For the analysis of the distribution of the fields inside the test zone the same reflectors 2, 4, 6, and 8 as above were considered as they give a good insight of the overall characteristics of the test zone realised by the DPR test method.

Figure 6.12 compares the distribution of the fields inside of the TZ from the different reflectors. It is important to recall that the TZ is considered to be the volume circumscribed by the cube with black edges. The Fig. 6.12a, 6.12b, 6.12c, and 6.12d clearly show on the $X''Y''-$ planes the angles of arrival of the signals scattered from the reflectors (approximately 16 deg, 40 deg, 70 deg, and 110 deg respectively). Further, it can be observed that depending on the reflector the fields are distributed differently, for example it can be seen that the signal illuminating the TZ from reflector 2 spread the most when compared to the other reflectors as there are fields with intensity above 25 dB outside of the TZ, and the signals from Reflector 8 spread the least. This was also shown before with the ray tracing tool in Fig. 6.5. Additionally, it can be seen that the fields are not completely evenly distributed inside of the test zone. However, it can be immediately noticed that there has been a big improvement compared to the ECR and ERR test methods as these showed variations of the power density larger than 60 dB inside of the TZ volume, whereas, for the case of the flat reflectors the worst case showed a field intensity difference of maximum 5 dB (see Fig. 6.13).

The discrete plane reflectors method could be considered as an indirect (quasi) far-field test apparatus, because the DUT is not looking (being illuminated) directly to the feeder antenna, as is the case of the compact antenna test range method described in Subsection 3.5.2. Consequently, the characteristics of the test zone produced by each reflector were evaluated in a similar way as a compact antenna test range (described in Subsection 3.7.6). The parameters considered were the amplitude taper, amplitude ripple and phase ripple. Let's recall that the amplitude taper is measured as the variation of a second-degree polynomial function, which is obtained by means of a least squares best fit through the amplitude data over a cut through the test zone in dB. The amplitude ripple is measured by determining the variation of the amplitude about the second degree polynomial fit also expressed in dB. And the phase ripple is the deviation from a best fit straight line over the test zone expressed in degrees. The amplitude taper and amplitude ripple

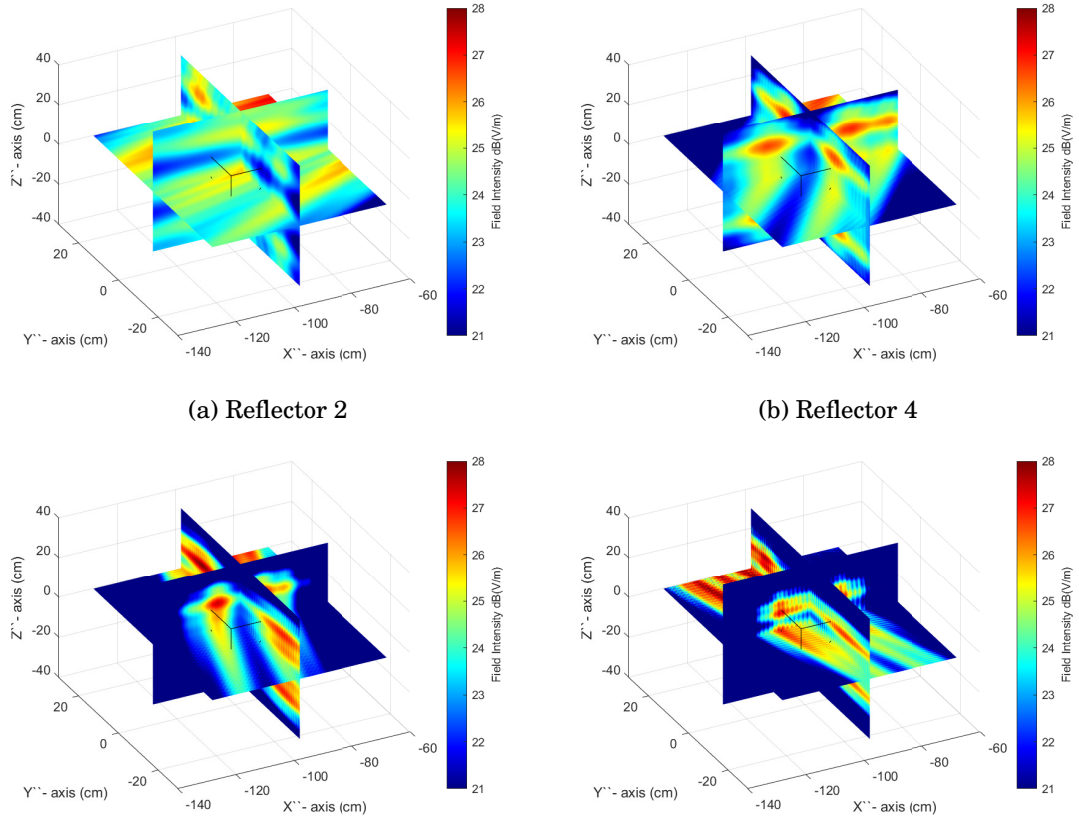

(a) Reflector 2

(b) Reflector 4

(c) Reflector 6

(d) Reflector 8

Figure 6.12: Distribution of E-fields inside of the test zone when the reflectors are placed at the azimuth plane

inside the TZ volume were evaluated on the intersection lines where the planes intersect, which actually coincide with the local coordinate system of the F_1 focal point (X'', Y'', Z'').

The aforementioned improvement of the uniformity of the signals inside the test zone volume is depicted in Fig. 6.13. The region of interest is within the range -10 cm to 10 cm in the horizontal axis of the individual plots as this is the region inside the test zone volume. The field intensity at the centre of the TZ cube (F_1 focal point) varies depending on the reflector. Reflector 2 shows the largest power of approximately 25.5 dB and Reflector 6 the least power of approximately 22 dB. The amplitude taper and amplitude ripples of the reflectors 2, 4, 6 and 8 are summarized in Table.6.4. Recalling, the definition of the quiet zone of a compact antenna test range detailed in Subsection 3.7.6, the target amplitude taper is 1 dB and the amplitude ripple is ±0.5 dB. For the worst case of the flat reflectors analysed here reflector 8 has an amplitude taper of 2.3 dB and 2.5 dB in the $X''-$cut and $Y''-$cut respectively. The maximum amplitude ripple is produced by reflector 6 in the $X''-$cut of ±3 dB. Although, overall most of the amplitude taper and ripples of the reflectors under analysis showed higher values than the specifications of a compact antenna

test range system, it is important to remember that this OTA test method is not intended to replace the CATR system therefore a compromise in the purity of the levels inside of the test zone could be acceptable because the idea of this test method is to become a complementary system that allows to test the performance of the device in its final form factor creating multiple signals that illuminate the DUT from different directions in the 3D space and is not intended to characterise the radiation properties of the antennas alone.

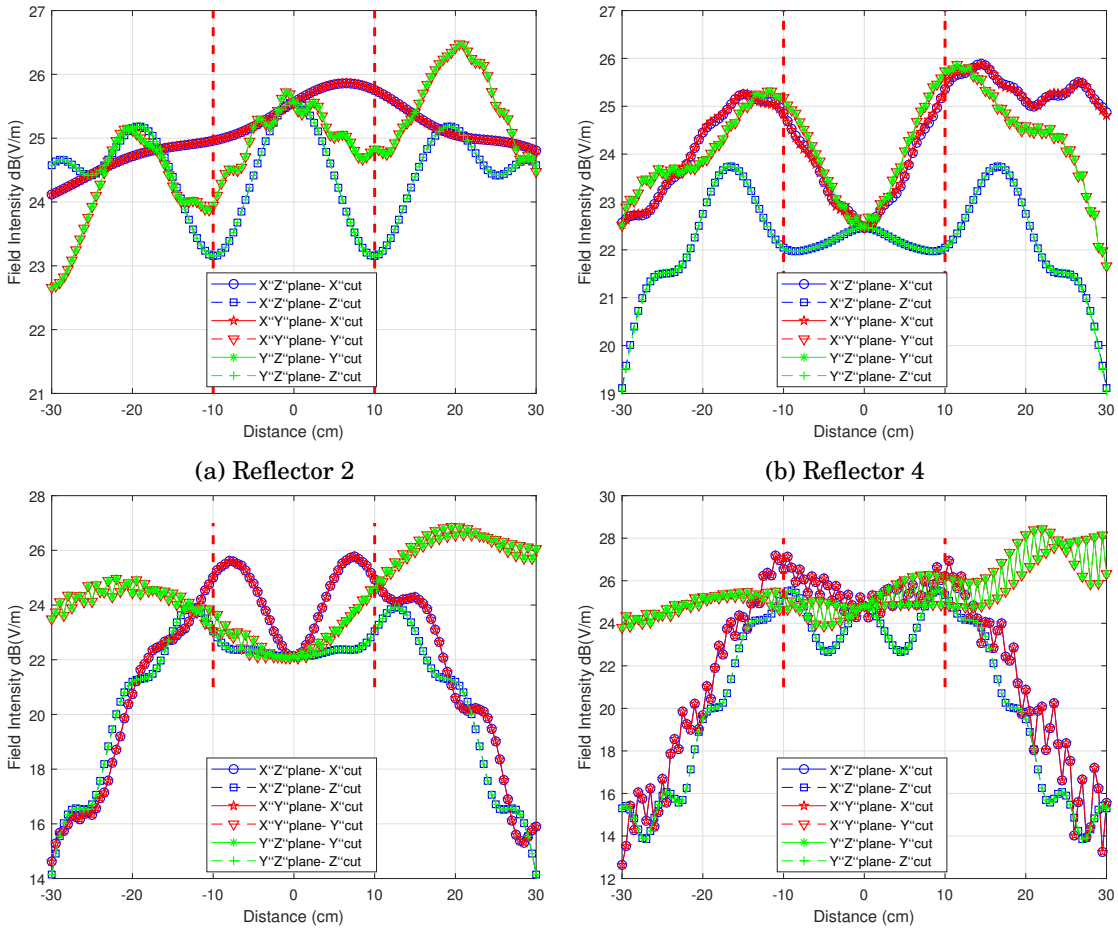

(a) Reflector 2

(b) Reflector 4

(c) Reflector 6

(d) Reflector 8

Figure 6.13: Amplitude ripple within the test zone when the reflectors are located at the azimuth plane

6.4.2.2 Analysis of amplitude and phase ripple inside the test zone at a plane transverse to the reflected signals

In Subsection 6.4.1 a plane transverse to the direction of arrival of the reflected signals from the different reflectors was used to shown the distribution of total path lengths of the rays, and the analysis of amplitudes and phases of the signals was pending which is continued here. The size of the plane where the fields were analysed was of 60 cm by 60 cm (see Fig. 6.14a, Fig. 6.15a,

Reflector	$X''-$cut		$Y''-$cut		$Z''-$cut	
	Ampl. Taper (dB)	Ampl. Ripple (dB)	Ampl. Taper (dB)	Ampl. Ripple (dB)	Ampl. Taper (dB)	Ampl. Ripple (dB)
Ref 2 - 0 deg	1.6	±0.4	2.1	±0.9	0.9	±1.27
Ref 4 - 0 deg	0.5	±1.8	0.3	±2.1	0.1	±0.76
Ref 6 - 0 deg	1.9	±3.0	1.1	±1.3	1.3	±1.45
Ref 8 - 0 deg	2.3	±2.2	2.5	±0.7	1.9	±1.93

Table 6.4: Summary of the parameters of the test zone from reflectors elevated 0 degrees

Fig. 6.16a, and Fig. 6.17a). The area of interest corresponding to the test zone plane is considered between the marks of -10 cm and 10 cm in both horizontal and vertical axis. A larger analysis area was used because it helps to understand better the behaviour of the reflected signals inside and outside of the test zone and how they change from the different reflectors.

The parameters of the test zone produced by the reflected signals from reflector 2 are shown in 6.14. The top figures show the distribution of the fields and the phases, and the bottom figures illustrate the cut through of the fields and phases plots at the horizontal and vertical axis as shown by the dashed lines of Fig. 6.14a and Fig. 6.14b respectively. The largest amplitude level is seen outside of the test zone at -20 cm in the $X''-$axis and 0 cm in the $Z''-$axis. As was expected from the ray tracing simulation (see Fig. 6.5a) the reflected signal spread in azimuth and vertical planes well outside of the desired test zone. It can also be seen that there is a certain periodicity of the field intensity as it can be observed 3 strong peaks every 20 cm in the horizontal and vertical axis. Inside of the desired test zone area shown inside the red dashed lines in Fig. 6.14c it can be seen that the amplitude taper of the horizontal cut is approximately 0.6 dB and the vertical cut is 0.1 dB. The amplitude ripples with respect to the corresponding quadratic fit lines (black dashed lines) inside the TZ plane were ±0.8 dB for the horizontal cut and ±1.3 dB for the vertical cut. With respect to the phases it can be seen that the largest deviations from the linear fit lines are present at the boundaries of the test zones shown in Fig. 6.14c is of approximately 87 deg. However, the phase difference between the phase centre of the test zone area and the boundary was 53 degrees for both axial cuts.

The parameters of the test zone produced by the reflector 4 are shown in 6.15. Once again as predicted by the ray tracing algorithm the reflected signals cover a smaller region as shown in Fig. 6.15a. The largest amplitude levels are mirrored about the vertical and horizontal axis. However, these 4 high peaks are located outside the desired test zone. In Fig. 6.15c it can be seen that the amplitude taper of the horizontal cut is approximately 0.5 dB and the amplitude taper of the vertical cut was approximately 0.2 dB. The amplitude ripples with respect to the corresponding quadratic fit lines (black dashed lines) inside the TZ plane are ±2.7 dB and ±0.7 dB for the horizontal and vertical cuts respectively. With regards to the phases distribution it can be seen that the largest deviations from the linear fit lines are present at the boundaries of the test

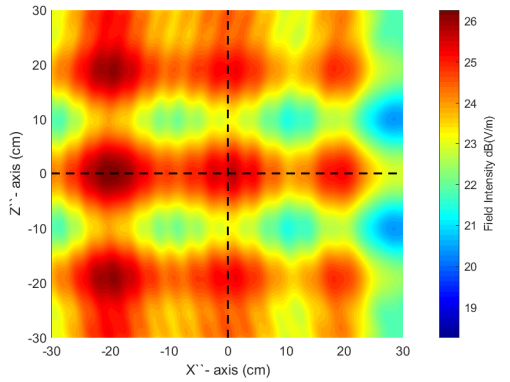

(a) Reflector 2 - Field Distribution

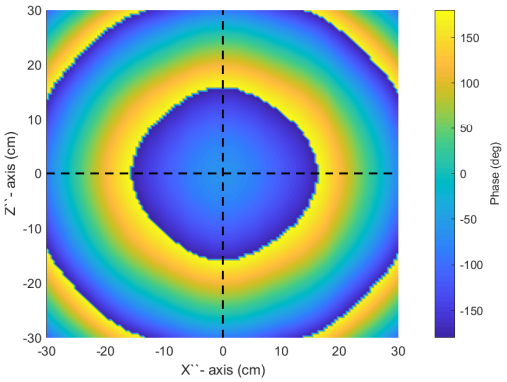

(b) Reflector 2 - Phase Distribution

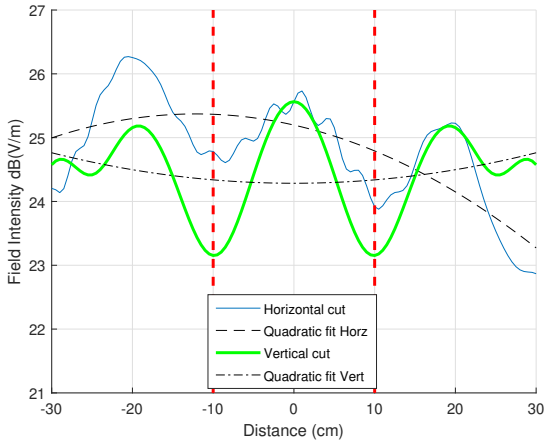

(c) Reflector 2 - Amplitude taper and ripple

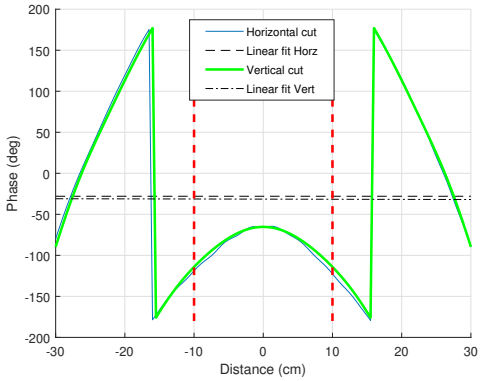

(d) Reflector 2 - Phase ripple

Figure 6.14: Evaluation of amplitude taper, amplitude ripple and phase ripple of reflector 2, when sample points are oriented orthogonal to the angle of arrival of the signal

zone shown in Fig. 6.15c and are of approximately 90 deg. However, the phase difference between the phase centre of the test zone area and the boundary was 45 degrees for both horizontal cut, and 59 degrees for the vertical cut.

The parameters of the test zone produced by the reflector 6 are shown in 6.16. The region covered by the strongest field levels have reduced spatially even more compared to reflector 2 and reflector 4 as shown in Fig. 6.16a. The largest amplitude levels are also mirrored about the vertical and horizontal axis. However, these 4 high peaks are still located outside the desired test zone. In Fig. 6.16c it can be seen that the amplitude taper of the horizontal cut is approximately 1.3 dB and the amplitude taper of the vertical cut was approximately 0.9 dB. The amplitude ripples with respect to the corresponding quadratic fit lines (black dashed lines) inside the TZ plane were ±3 dB and ±1.5 dB for the horizontal and vertical cuts respectively. Interestingly, it can be seen that field intensity distribution of the vertical cut is becoming flatter, compared to the previous reflectors and the fields in the horizontal cut are showing larger variations. With regards to the phases distribution it can be seen that the largest deviations from the linear fit

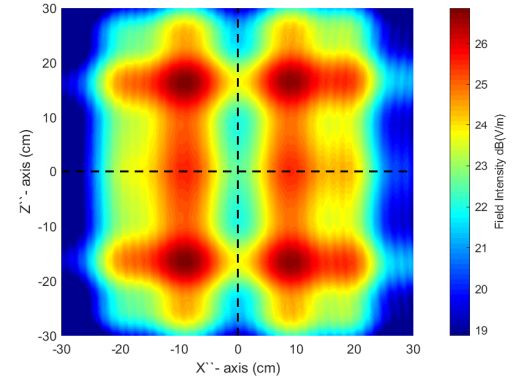

(a) Reflector 4 - Field Distribution

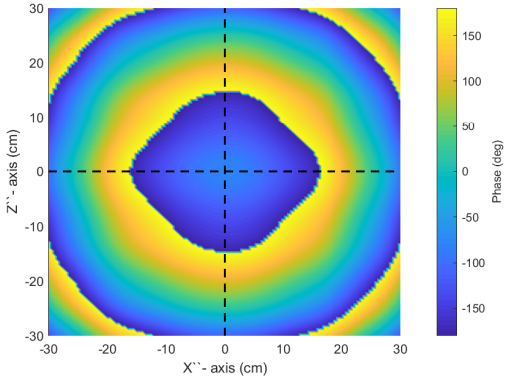

(b) Reflector 4 - Phase Distribution

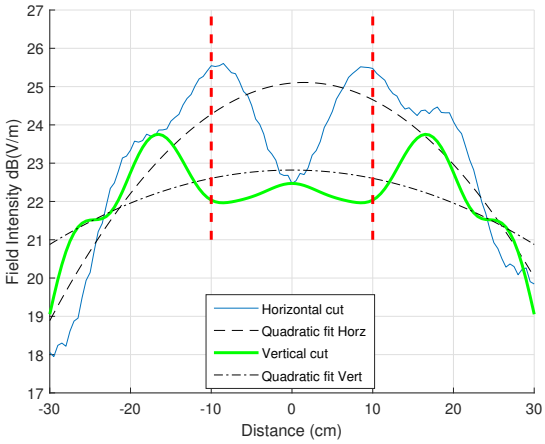

(c) Reflector 4 - Amplitude taper and ripple

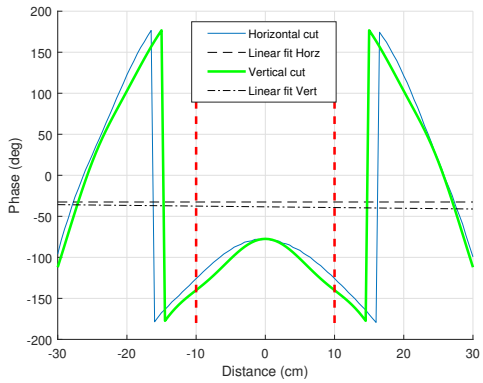

(d) Reflector 4 - Phase Distribution

Figure 6.15: Evaluation of amplitude taper, amplitude ripple and phase ripple of reflector 4, when sample points are oriented orthogonal to the angle of arrival of the signal

lines were seen at the phase centre of the test zone shown in Fig. 6.16c and are of approximately 86 deg for the horizontal cut and 66 degrees for the vertical cut. Also, the phases distributions differ the most between the cuts. The vertical cut shows a narrower distribution.

The parameters of the test zone produced by the reflector 8 are shown in 6.17. The region covered by the strongest field levels is the smallest of all reflector analysed shown in Fig. 6.17a. The largest amplitude levels are also mirrored about the vertical and horizontal axis but this time are located exactly at the boundary of the desired test zone. In Fig. 6.17c it can be seen that the amplitude taper of the horizontal cut is approximately 1.7 dB and the amplitude taper of the vertical cut was approximately 1.4 dB. The amplitude ripples with respect to the corresponding quadratic fit lines (black dashed lines) inside the TZ plane were ±1.9 dB and ±2.2 dB for the horizontal and vertical cuts respectively. Interestingly, it can be seen that field intensity distribution of the horizontal cut shows small ripples along the curvature, that started to show in reflector 6, however here it is more pronounced. On the other hand, the fields distribution in the vertical do not show such small ripples. Regarding the phases distribution it can be seen that

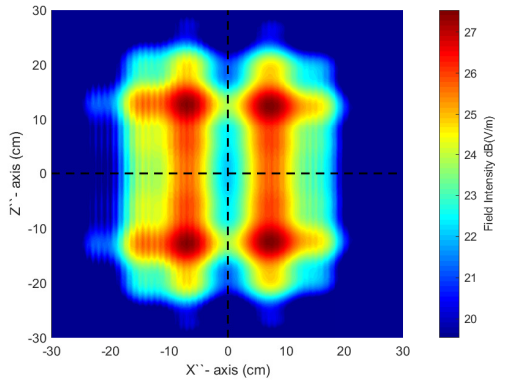

(a) Reflector 6 - Field Distribution

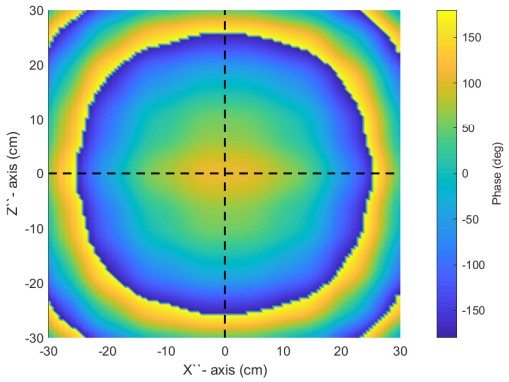

(b) Reflector 6 - Phase Distribution

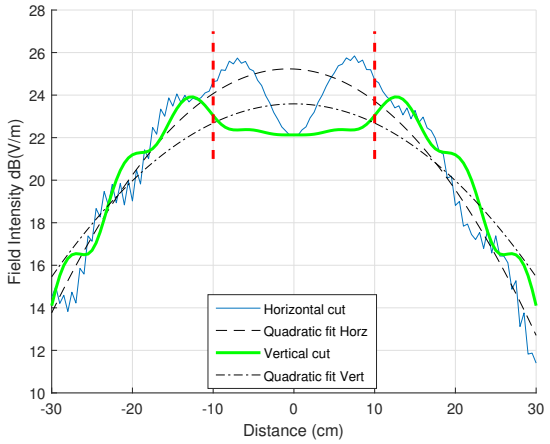

(c) Reflector 6 - Amplitude taper and ripple

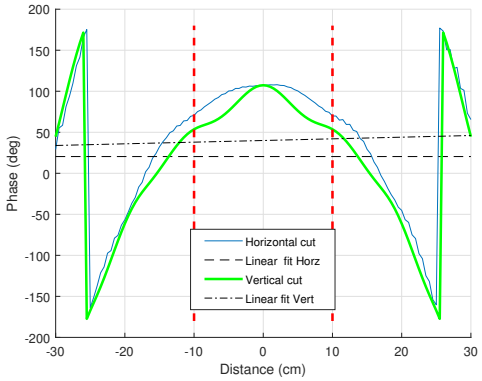

(d) Reflector 6 - Phase ripple

Figure 6.16: Evaluation of amplitude taper, amplitude ripple and phase ripple of reflector 6, when sample points are oriented orthogonal to the angle of arrival of the signal

both profiles are again similar to each other as was the case from reflector 2 shown in Fig. 6.17c. The largest deviation from the linear fit lines was observed at the +10cm boundary of the test zone in the vertical cut approximately 62 degrees for the horizontal cut and 40 degrees for the horizontal cut.

To summarise it was observed that the minimum amplitude taper was produced by reflector 2 which was smaller than 0.1 dB and the largest was seen from reflector 8 of 1.7 dB, and this increased with the number of reflector or with the angle of departure. However, the amplitude ripples didn't show and increasing trend with respect to the angle of departure. The maximum amplitude ripple was seen from reflector 6 of ±3 dB in the horizontal cut and the smallest was seen from reflector 4 in the vertical cut of ±0.7. The phase ripple for all the cases showed high deviation from the linear fit line being the maximum 90 degrees from reflector 4 and the minimum 40 degrees from reflector 8. However, the phase difference between the phase centre of the test zone plane and the boundaries of it, were significantly smaller, for example for reflector 6 in the horizontal cut showed a difference of 31 degrees and the largest was 60 degrees again from

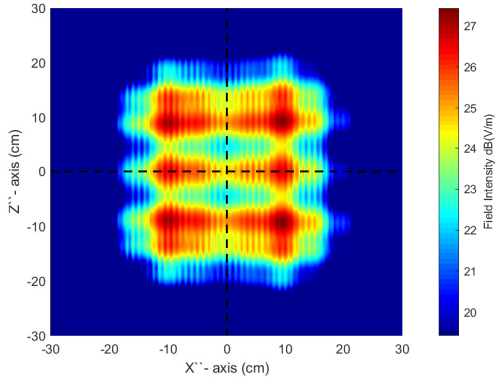

(a) Reflector 8 - Field Distribution

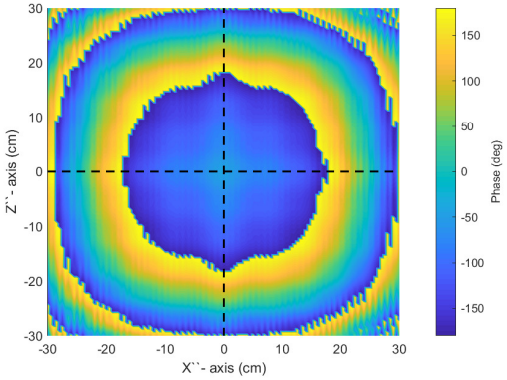

(b) Reflector 8 - Phase Distribution

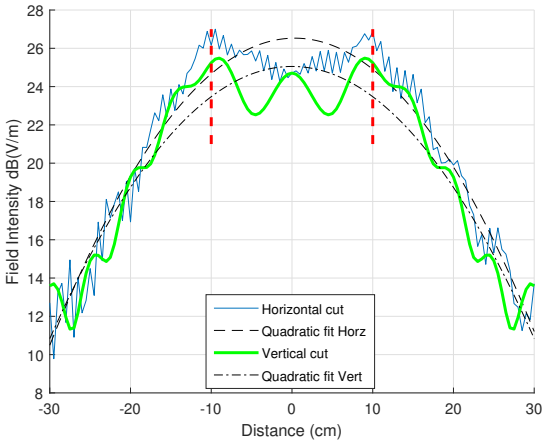

(c) Reflector 8 - Amplitude taper and ripple

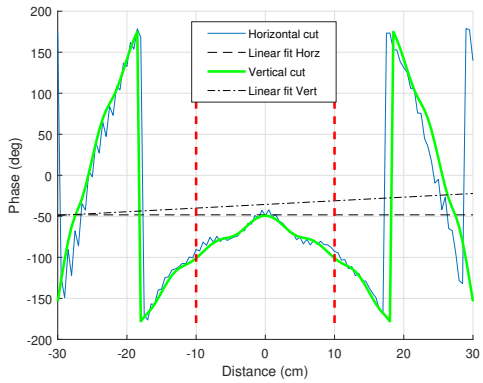

(d) Reflector 8 - Phase ripple

Figure 6.17: Evaluation of amplitude taper, amplitude ripple and phase ripple of reflector 8, when sample points are oriented orthogonal to the angle of arrival of the signal

reflector 6.

6.4.2.3 Analysis of reflectors elevated 30 and 60 degrees

For the analysis of the set of reflectors elevated 30 and 60 degrees, reflectors 3 and 7 were considered as the samples of each set. The plots (a) and (b) in Fig. 6.18 correspond to the reflectors elevated 30 degrees and plots (c) and (d) correspond to the reflectors elevated 60 degrees. One can visually appreciate how the reflected signals illuminate the test zone from the corresponding angles in elevation and in azimuth. The fields arriving from the reflectors elevated 60 degrees show a steeper slope than the 30 degrees reflectors.

The absolute power at the centre of the TZ cube (F_1 focal point) of both reflectors 3 is approximately 23.6 dB, whereas of the reflectors 7 is 22.5 dB, therefore there is a 1 dB difference for both set of reflectors. The amplitude taper and amplitude ripples of the reflectors 3 and 7 elevated 30 and 60 degrees are summarized in Table.6.5. Similar to the reflector placed at the

Reflector	$X''-$cut		$Y''-$cut		$Z''-$cut	
	Ampl. Taper (dB)	Ampl. Ripple (dB)	Ampl. Taper (dB)	Ampl. Ripple (dB)	Ampl. Taper (dB)	Ampl. Ripple (dB)
Ref 3 - 30 deg	0.4	±0.5	0.1	±0.4	0.8	±1.1
Ref 7 - 30 deg	2.2	±3.2	0.6	±0.9	1.3	±1.5
Ref 3 - 60 deg	0.9	±0.4	1.1	±1.2	0.2	±0.6
Ref 7 - 60 deg	2.5	±3.2	1.3	±1.4	0.6	±0.9

Table 6.5: Summary of the parameters of the test zone from reflectors elevated 30 and 60 degrees

azimuth plane in elevation the values here are above the ideal case of a CATR. Therefore, one can conclude that independently of position in elevation of the reflectors the amplitude taper and ripple will be higher than the ideal case. The maximum amplitude taper here was produced by reflector 7 elevated 60 degrees of 2.5 dB and also has the highest amplitude ripple of ±3.2dB

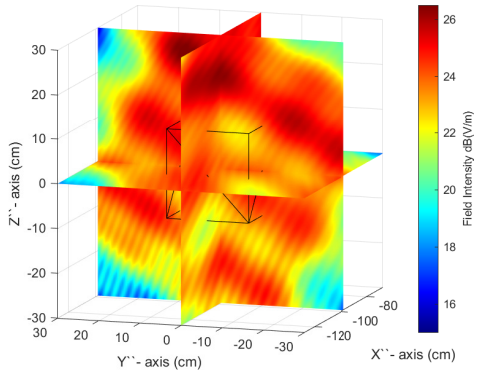

(a) Reflector 3 - Elevated 30 deg

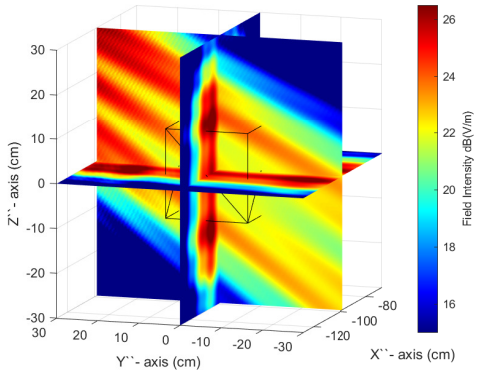

(b) Reflector 7 - Elevated 30 deg

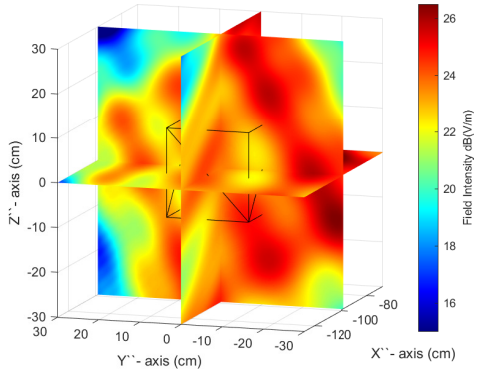

(c) Reflector 3 - Elevated 60 deg

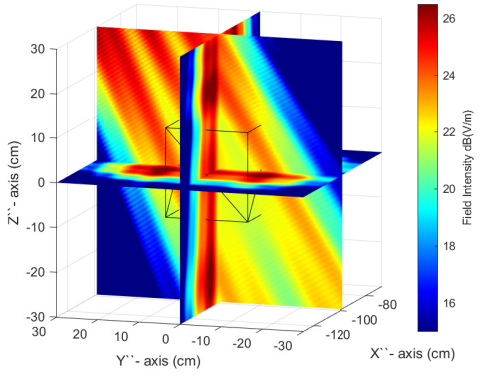

(d) Reflector 7 - Elevated 60 deg

Figure 6.18: Distribution of E-fields within the test zone when the reflectors are elevated 30 and 60 degrees

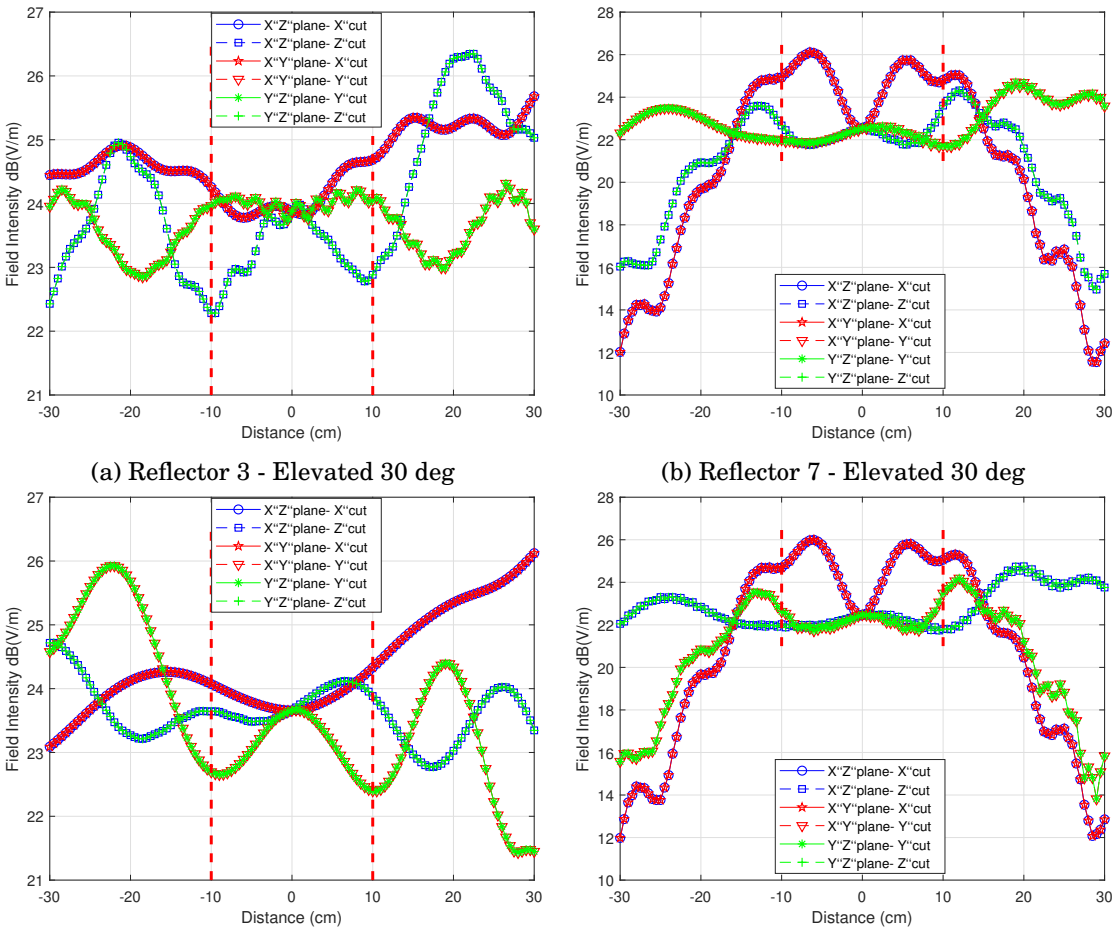

(a) Reflector 3 - Elevated 30 deg

(b) Reflector 7 - Elevated 30 deg

(c) Reflector 3 - Elevated 60 deg

(d) Reflector 7 - Elevated 60 deg

Figure 6.19: Amplitude ripple within the test zone when the reflectors are elevated 30 and 60 degrees.

6.4.3 Sensitivity of the system when transmission source is off focus

One of the main components of the OTA test method is the feeder antenna, which as stated before is expected to be a phased array antenna with multiple independent sub arrays. During the development of this research project, it was possible to use a commercially available phased array antenna to test the DPR prototype and will be fully described in the following chapter. Thus, the physical dimensions of this antenna array were used here to determine the sensitivity of the test method when the feeder antenna is offset from the focal point. The phase antenna was an array of 256 antenna elements operating in the band of 26 to 30 GHz. Approximately, the dimensions of the antenna front end were 8 cm × 8 cm. The 256 antenna elements were sub divided in four equal sub arrays of 64 elements each. The centroid point Pc_n of each sub array was approximately located 2.5 cm away from the focal point diagonally, as illustrated in Fig. 6.20. The centroid of the whole array was placed at the focal point. Therefore, some simulations offsetting the transmitter antenna were performed to determine how this affect the characteristics of the TZ.

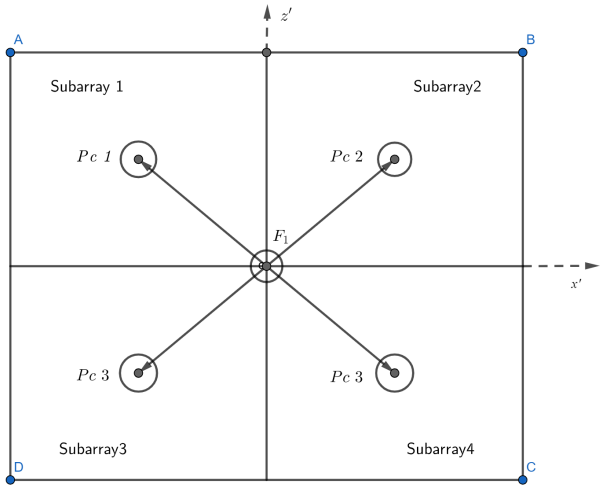

Figure 6.20: Illustration of antenna array Anokiwave AWA-0142-IK

Two scenarios were considered and the results from reflectors 3 and 7 are analysed. For the first scenario the feeder antenna was moved to the Pc_1 inside of sub array 1 and on the second scenario the feeder antenna was placed at Pc_4 inside of sub array 4. Due to symmetry of the location of the sub arrays the other two sub arrays 2 and 3 are not shown here but showed a similar trend.

6.4.3.1 Test zone sensitivity from reflector 3 elevated 30 degrees

Figure 6.21 allows to visually compare the two scenarios specified above. The first column of plots (subplots a, d ,g, j and m) corresponds to the ideal case when the feeder antenna is located a focal point. The second column and third column to the feeder moved to Pc_1 and Pc_4 respectively. The

first row (subplots a, b, and c) show an overview of the TZ with the three intersecting planes. The second row (subplot d, e, and f) belong to the $Y''Z''-$plane. On these plots one can observe how the distribution of the fields changed position. Taking as a reference the area with the highest power one can see that when the antenna is at Pc_1 this section moved down along the $Z''-$axis by 2 cm, and the opposite occurred for the other case. The third row depict the $X''Y''-$plane or azimuth plane and one can observe that the area with highest power are opposite to each other. The fourth row shows the $X''Z''-$plane or elevation plane, where it is also possible to see how the fields changed.

Although, visually one can see that the inner fields vary from the ideal case, the range of these variation is very small, because the overall range of the amplitude ripple of the signals increased maximum by 0.5 dB. This is clearly shown in Fig. 6.21n and Fig. 6.21o when compared Fig. 6.21m.

6.4.3.2 Analysis of sensitivity of the test zone from reflector 7 elevated 60 degrees

The same simulations as for reflector 3 were performed in order to determine the fields distribution illuminating the TZ that were scattered reflector 7 depicted in Fig. 6.22. The matrix of plots follows the same organization as of the plots and subplots specified above.

At a first look at the individual evaluation planes it is difficult to visually detect the differences in the field's distribution inside the TZ. The most visually notorious change occur in the $X''Y''-$plane or azimuth plane, at can be seen that the area with the highest power level at Pc_4 appears at the 9 cm mark in the $Y''-$-axis, Pc_1 it is located at the -10 cm mark in the same axis. In the elevation plane ($X''Z''-$plane) it is possible to observe that the centre of the area with highest power was shifted to 1 cm to -2 cm mark in the $Z''-$-axis comparing the ideal case with the Pc_1 case, and for the Pc_4 it moved to +3 cm.

The 2D cut lines from Fig. 6.21m, Fig. 6.21n and Fig. 6.21o more clearly show that the overall amplitude range variation is negligible between the three cases under evaluation as it remained between 22.5 dB to 26.5 dB. Furthermore, one can observe that the individual trends of the amplitude ripples of each cut show very little differences that could be neglected.

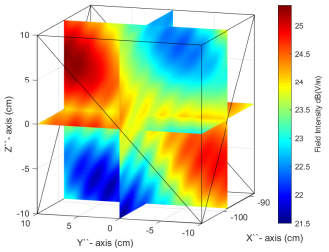

(a) Reflector 3 at F_1

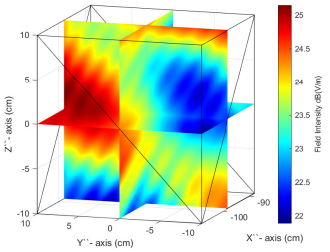

(b) Reflector 3 at PC1

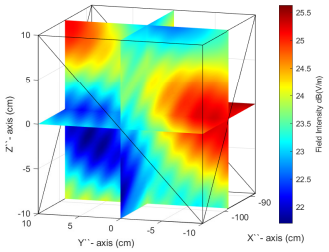

(c) Reflector 3 at PC4

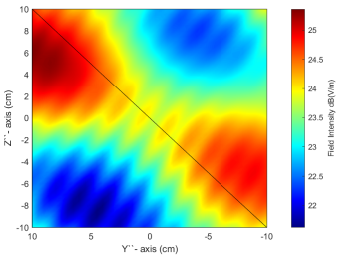

(d) $Y''Z''-$plane at F_1

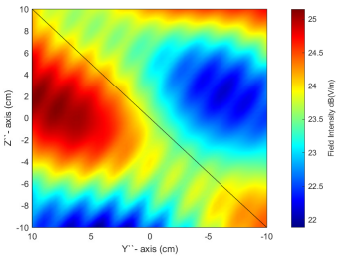

(e) $Y''Z''-$plane at PC1

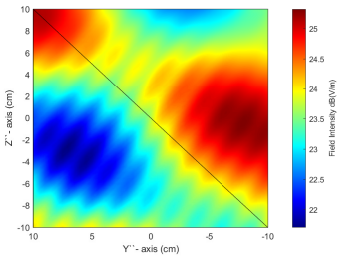

(f) $Y''Z''-$plane at PC4

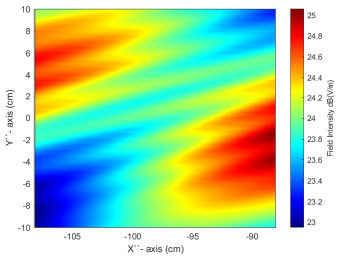

(g) $X''Y''-$plane at F_1

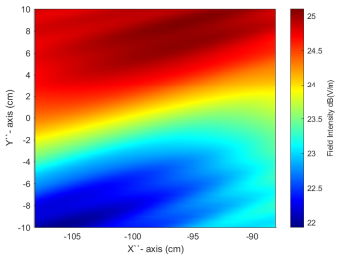

(h) $X''Y''-$plane at PC1

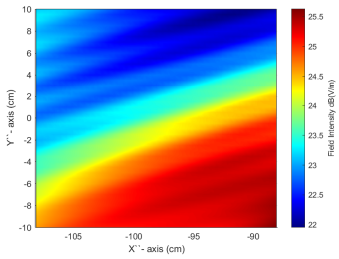

(i) $X''Y''-$plane at PC4

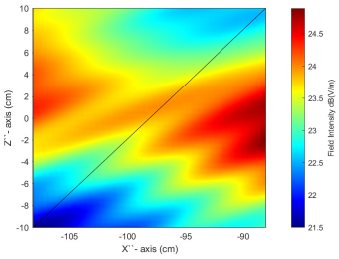

(j) $X''Z''-$plane at F_1

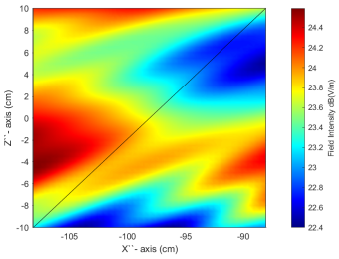

(k) $X''Z''-$plane at PC1

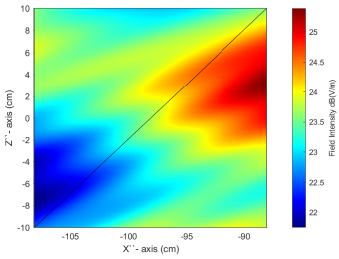

(l) $X''Z''-$plane at PC4

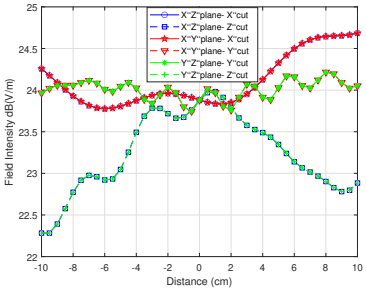

(m) Amplitude ripple at F_1

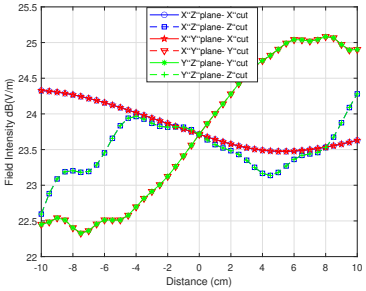

(n) Amplitude ripple at PC1

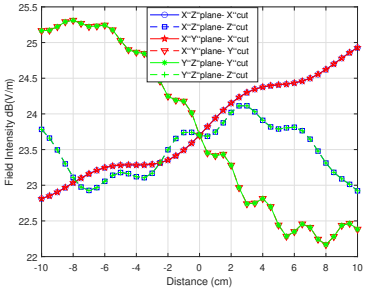

(o) Amplitude ripple at PC4

Figure 6.21: Sensitivity of TZ from reflector 3 elevated 30 degrees

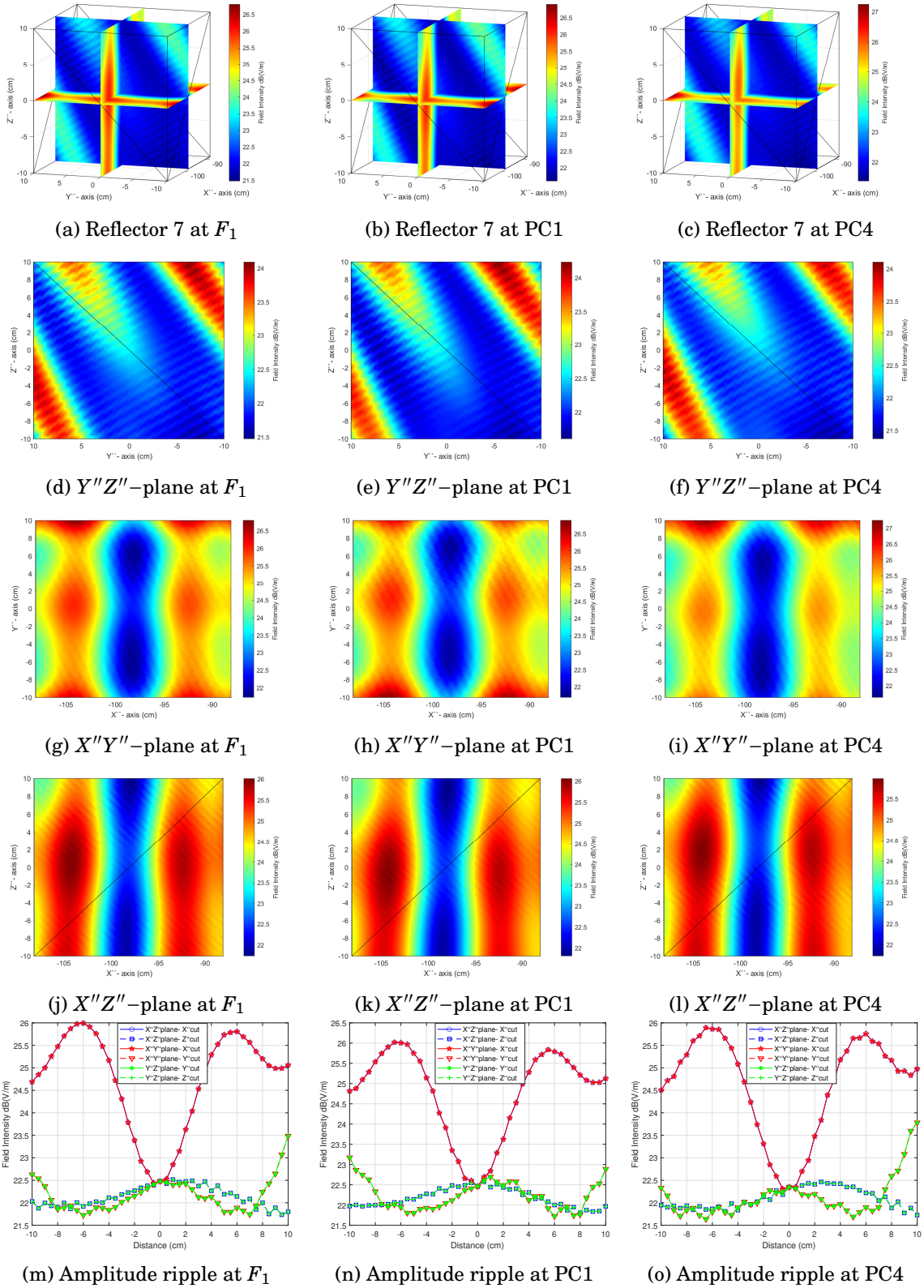

(a) Reflector 7 at F_1 (b) Reflector 7 at PC1 (c) Reflector 7 at PC4

(d) $Y''Z''-$plane at F_1 (e) $Y''Z''-$plane at PC1 (f) $Y''Z''-$plane at PC4

(g) $X''Y''-$plane at F_1 (h) $X''Y''-$plane at PC1 (i) $X''Y''-$plane at PC4

(j) $X''Z''-$plane at F_1 (k) $X''Z''-$plane at PC1 (l) $X''Z''-$plane at PC4

(m) Amplitude ripple at F_1 (n) Amplitude ripple at PC1 (o) Amplitude ripple at PC4

Figure 6.22: Sensitivity of TZ from reflector 7 elevated 60 degrees

6.5 Conclusions

In this chapter the design criterion and analysis of the test zone produced by the Discrete Plane Reflector (DPR) test method was discussed. This candidate test method is also based on the concepts of an ellipse and takes advantage of its reflective properties, which allow to generate multiple signals with different directions of arrival that illuminate a device under test in a 3D space from a single point or feeder. In order to create a three-dimensional space multiple flat square reflectors were positioned following a part-ellipsoid shape.

The main difference with the previous test methods analysed is that the flat reflector of the DPR test method diverged the incident signal upon reflection in both the azimuth and elevation planes. With the ray tracing tool, it was possible to see that although the rays representing the scattered signals diverged the path lengths were not significantly larger from the theoretical case of a perfect ellipse within the desired test zone area. For the test zone a plane oriented orthogonal to the theoretical direction of arrival was considered. Theoretically, the path length of the rays reflected from a perfect ellipse should have been 410 cm and according to the simulations the maximum path length in the test zone plane obtained was 410.5 cm, which means that the amplitude of the signals should not vary considerably.

Based on the ray tracing simulations it was also observed that the adjacent reflectors to the targeted one may become a source of interference at the TZ which is an important consideration that should be taken into account and should be evaluated with the prototypes to determine the degree interference that they cause at the test zone, and requires to think on way to mitigate this issue.

Based on simulations it was possible to estimate the realizable size of the TZ volume which would be of approximately 20 cm x 20 cm x 20 cm (width x length x height), as was the target size suggested by the 3GPP in [55] and defined in Subsection 3.7.6. Inside this volume it was demonstrated by simulations that the estimated that the maximum amplitude taper would be of approximately 2.5 dB and the maximum ripple should be approximately ±3.2 dB. It is important to note that these results were obtained under ideal conditions without interfering adjacent reflectors. Also, it was not taken into consideration undesired reflections produced by the structure that holds the reflectors or reflections inside the test chamber.

The sensitivity of the system was also evaluated, in order to determine the ability of the method to cope with the signal source being located away from the focal point, as it would be the case if the feeder antenna is realized with a phased arrays antenna with independent sub arrays and independent RF ports. The results of the simulations showed that the overall amplitude ripple range does not vary significantly if the feeder is moved approximately 2.5 cm away from the focal point diagonally, and the reflected signals still covered the full TZ area from all the reflectors. Therefore, one can say that the DPR setup has a low sensitivity to displacing the feeder antenna within a short distance from the focal point.

When compared to the ERR and ECR test methods the Discrete Plane Reflectors test method

is the best option to generate test zone volume with sufficient aperture in both azimuth and elevation planes, such that real-life like test scenarios to test the performance of devices can be created. This solution would be a cost - effective solution compared with current over the air test methods because manufacturing flat reflectors is much less expensive than given a specific curvature to any material.

It is important to emphasise this OTA test method is not intended to replace the CATR system. The idea of this test method is to become a complementary system that allows to test the performance of the device in its final form factor creating multiple signals that illuminate the DUT from different directions in the 3D space and is not intended to characterise the radiation properties of the antennas.

CHAPTER 7

PROTOTYPING OF 5G OVER THE AIR TEST METHOD

7.1 Introduction

To verify the viability of the proposed architectures for mmWave OTA testing and to measure the achieved TZ size of the system, two prototypes were implemented, an elliptical cylinder reflector (see Fig. 7.4), and a set of plane discrete reflectors (see Fig. 7.19). The performance of the candidate systems was ascertained by measuring the angular response and the dimension and stability of the TZ. Further details follow.

7.2 Testing and Characterization of Elliptical Cylinder Reflector

7.2.1 Implementation

Here only a section of the ECR was constructed and evaluated. The dimensions of the reflector were identical to the theoretical test case (see chapter 5), the semi-major axis 205 cm, semi-minor axis 180 cm and height 40 cm. The reflective surface was built from a sheet of plastic, which was coated with aluminium tape as shown in Fig. 7.1 and Fig. 7.2. To give the adequate curvature to the reflector's surface the sheet of plastic was glued to a set of acrylic formers. These formers were small sections of approximately 60 cm long of the ellipse, which were laser cut of a 10 mm thick acrylic sheet and joined together to achieve the full length of the desired quarter section of the ellipse. Figure 7.3 shows the design of the two pairs of six formers and the associated assembly. It is important to discuss the construction and assembly methodology of the reflector as it was found during characterisation that this introduced multiple sources for errors that in

hindsight can be minimised if the formers would have been a continuous structure. The final prototype fully assembled is shown in Fig. 7.4.

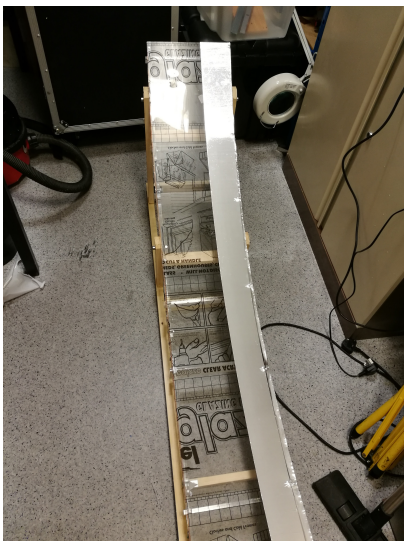

Figure 7.1: Coating reflector surface with aluminium tape

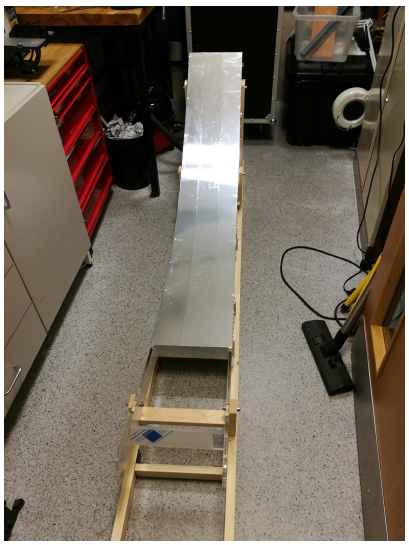

Figure 7.2: Assembly of reflective surface to acrylic formers

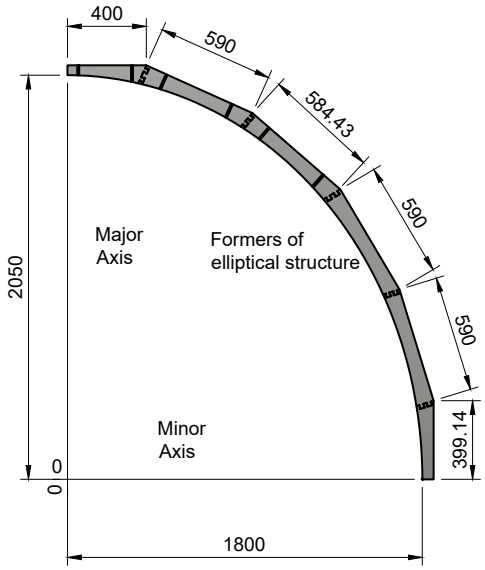

Figure 7.3: Acrylic former of the elliptical cylinder reflector

7.2.2 Characterisation

As mentioned above the prototype was constructed out of several small sub structures which in turn could have caused deviations of the desired elliptical curvature. Thus, it was necessary

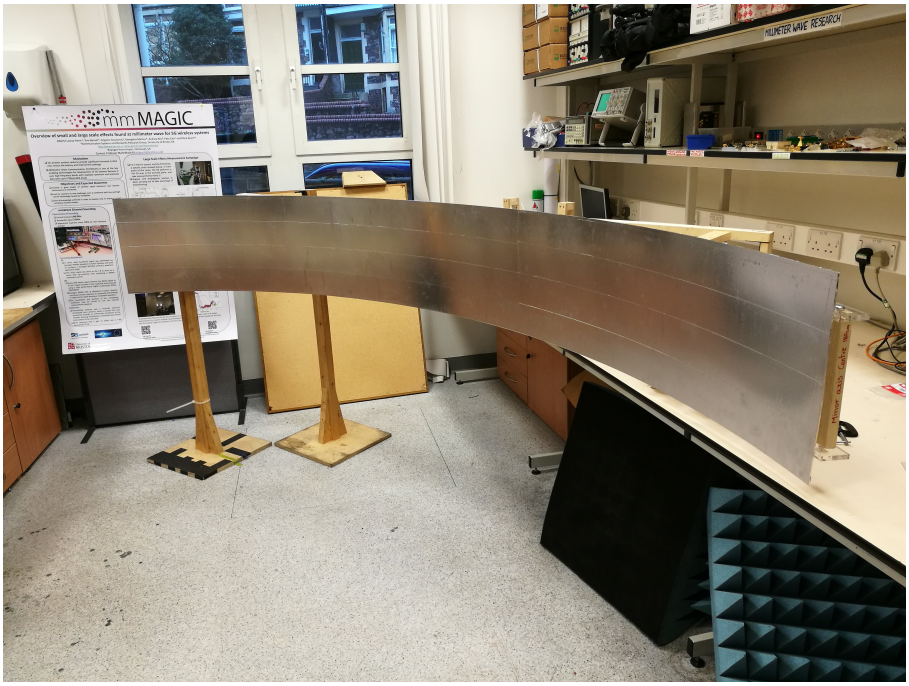

Figure 7.4: Final prototype of elliptical cylinder reflector

to characterise the ECR reflector to determine if the desired geometrical shape and spatial reflection properties were attained. The characterisation was carried out by means of recording the amplitude and phase of the reflected signal as a function of the angles of arrival (AoA) produced by signals transmitted with different angles of departure (AoD). The test setup was placed inside of an anechoic chamber. This measurement set-up consisted of the ECR, two dual-polarised Flann horn antennas (model DP241-AB), used to transmit and receive the signals, which represented the feeder antenna (FA) and the device under test. A pair of motorised position controllers were used to adjust the antenna orientation, and a vector network analyser (VNA) was used to measure the scattering parameters S21 at 26 GHz (corresponding to the UK mmWave pioneer band). A block diagram of the test setup is shown in Fig. 7.5.

7.2.2.1 Link budget of the measurement

The expected link budget of the system was calculated in order to compare it with the practical measurements, since this accounts for all the losses and gains from the transmitter to the receiver as well as losses at the point of reflection. The link budget equation based on the Friis equation expressed in logarithms is given by eq. 7.1

$$P_{Rx} = P_{Tx} + G_{Tx} - L_{Tx} - FSPL + G_{Rx} - L_{Rx} \tag{7.1}$$

Where P_{Rx} is the Received Power in dBm, P_{Tx} is the Transmitted Power : 0 dBm, G_{Tx} and

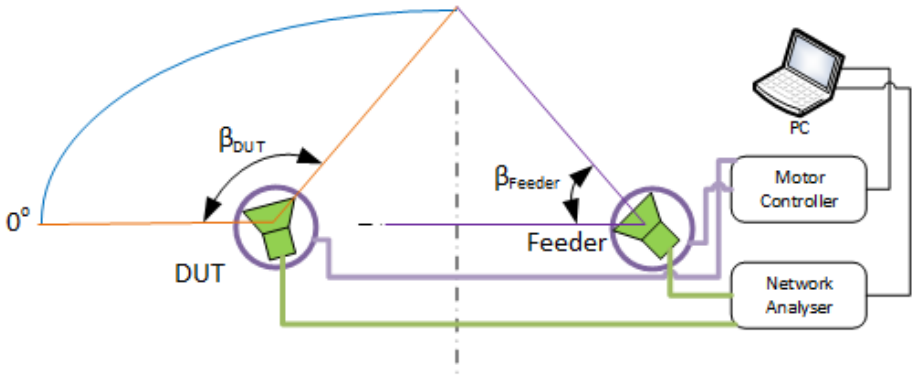

Figure 7.5: Block diagram of setup to characterise the ECR curvature

G_{Tx} are the gain of the antennas: 21 dBi, FSPL is the Free Space Path Loss in dB, L_{Tx} and L_{Rx} are the losses due to cables, connector, etc. These loses were measured with the VNA and are approximately 8 dB per link end. Figure. 7.6 shows the expected received power at various distances. Considering the dimensions of the system, the minimum distances between the two test antennas was 2 metres, which is the distance in LOS of the antennas, thus theoretically the expected received power was -39 dBm. On the other hand, the distance that the signal will travel from one antenna to the other after reflecting from the reflector was 4.1 metres, thus it was expected to receive -46 dBm along the full curvature.

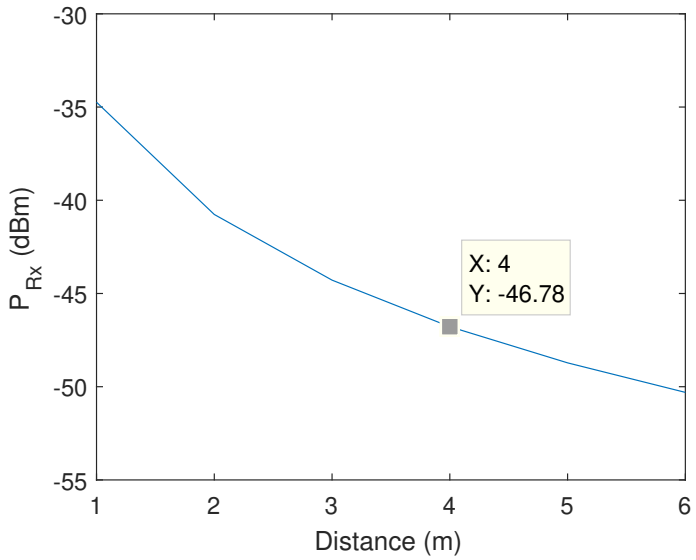

Figure 7.6: Estimated received power of the system (application of Frii's equation and measured power levels and losses)

7.2.2.2 Characterisation of the reflector

The test setup used to measure the characteristics of the reflector in the anechoic chamber is show in Fig. 7.7. The configuration was detailed in the block diagram of Fig. 7.5. A human machine interface was developed in MATLAB to control both the Newport 3-Axis motor controller ESP301, and the VNA. A triggering signal each half degree angle of departure was sent from the motor controller to the VNA which captured the complex S-21 transmission coefficients (amplitude and phase). The angles of arrival were calculated with the equation 5.14 explained in subsection 5.5.3, where the maximum power transfer should have occurred. Thus, measuring the peak power at each point allows to validate the construction of the ECR prototype. Each sample was averaged over 120 instantaneous captures. The range of angles of departure of the feeder antenna were from $0^o < \beta_{Feeder} < 60^o$, and the range of angles of arrival of the DUT were from $0^o < \beta_{DUT} < 120^o$.

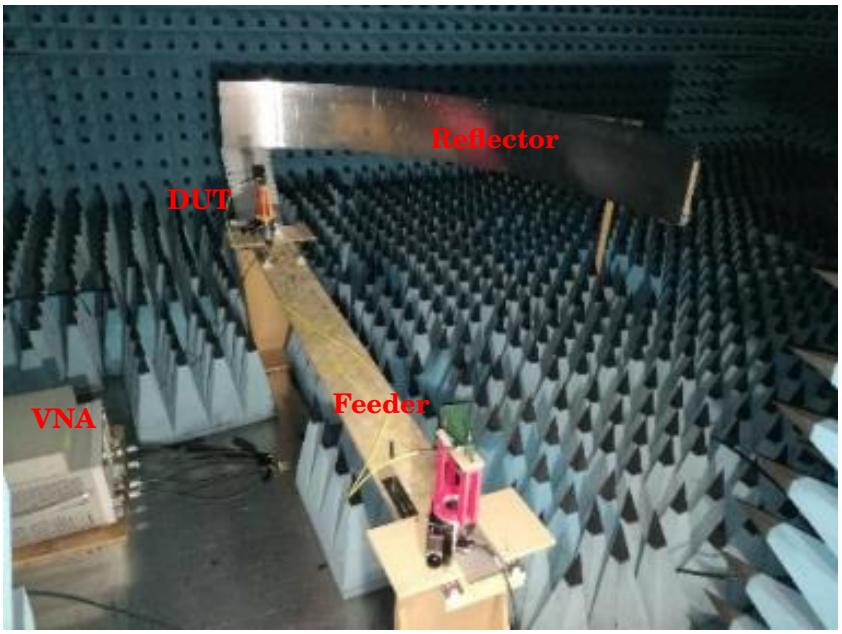

Figure 7.7: ECR prototype under evaluation within an anechoic chamber. The chamber measures 8m x 4.5m x 5m. The prototype was installed along the width of the chamber.

The recorded magnitudes of the reflected signals measured along the reflector expressed in logarithmic scale (dB) are shown in Fig. 7.8. There are two lines in the chart. The top line (blue colour) shows the magnitude with both antennas in horizontal polarisation (H-H) and the bottom line (orange colour) shows the magnitude with the antennas in vertical polarisation (V-V). The H-H line shows the power levels increase from -48 dB to -44dB which correspond the angles of arrival from 0 to 14 degrees. The levels in this region are lower due to the shadowing produce by the DUT antenna, because feeder antenna and DUT antenna are positioned on the X-axis of the ellipse. Between 14 to 100 degrees, the levels fluctuated in the range of -42 dB to -44 dB,

apart from a big null between 73 and 87 degrees where the signal level dropped 3 dB compared to the mean levels received at the other AoA. This sudden variation in power was caused by an imperfection in the surface that provoked the signal to scatter in an unwanted direction. For the case of V-V polarisation it is observed that the power levels follow a similar trend as the H-H line. However, it can be seen that on average there is approximately a 4 dB difference with its orthogonal counterpart. The median power in the region of 7 to 70 degrees is approximately -47 dB with a standard deviation of 1 dB. The median power level in H-H was -43 dB with a standard deviation of 1 dB in the same region. The large null is also present in V-V but is more pronounced showing a difference in received levels larger than 8 dB.

These results allow one to conclude that for most of the length of the reflector the desired elliptical curvature was accomplished, since the tests with different polarisations show similar trends. Moreover, it can be seen that the signal in V-V polarisation is more sensitive to surface imperfections hence the greater fluctuations of the power levels. The nulls appear in both measurements at the same angles of arrival, which indicates that there is a construction default of the reflector, that deviates the reflected signals from the focal point, although physically the surface of the reflector appeared to be correct by visual inspection. This null was located where two of the small sections of the acrylic formers joined together which were the critical points during the implementation of the reflector, because due to the spacing created by the laser beam the curvature could have been affected.

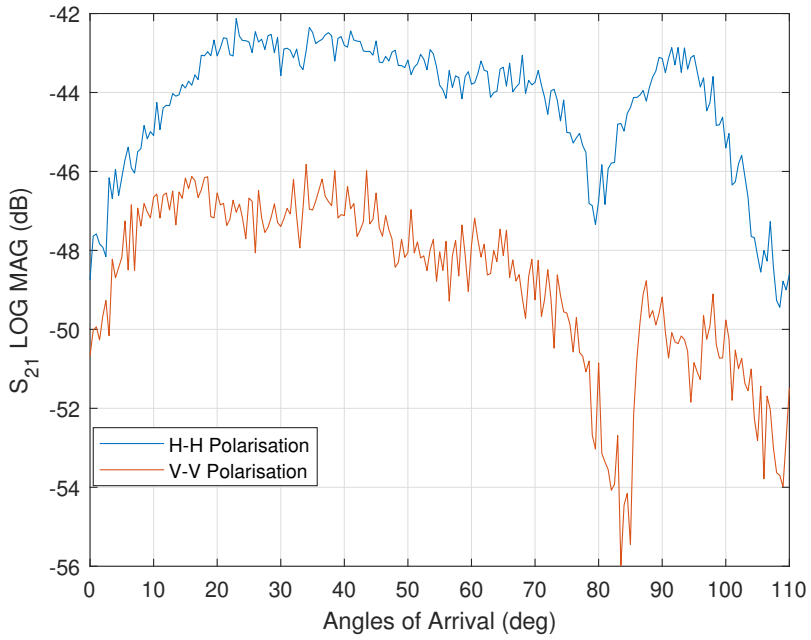

Figure 7.8: Characterisation of the curvature of the reflector ECR

7.2.3 Angular Measurements

According to the hypothesis raised in the theoretical analysis in the previous chapters, the system should be capable to generate independent signals with different angles of arrival, and ideally the reflected signal should resemble a far field signal, such that the DUT can be tested as if it was being illuminated by a real signal. In order to determine if the reflected signals achieved these conditions a set of angular measurements were carried out. The tests were performed as follows: (i) The feeder was fixed at a particular angle of departure, (ii) the DUT antenna was rotated as if it would be scanning the entire length of the reflector. (iii) Once completed the feeder moved to the next AoD. The initial AoD was 10 degrees, and the DUT antenna scanned the AoA from 0 degrees to 120 degrees. The S-21 parameter were recorded with the network analyser at one-degree increments. This process was repeated for AoD up to 60 degrees in 5 degrees increments. The test setup used to perform the angular measurements was the same show previously in Fig. 7.7. With this test it was expected to capture the amplitude power pattern (graph of the spatial variation of the power density along a constant radius [56]) of the horn antenna in 2D, which, in turn, would indicate that the measurements were made in the far-field zone.

The results of the measurements corresponding to the angles of arrival with the antennas horizontally polarised are depicted in the linear plot shown in Fig. 7.9. To facilitate the comparison between the different measurements all the patterns were normalised to its maximum value. It can be observed that for each AoD, the main beam of the radiation pattern points at a particular AoA.

The difference between theoretical and measured AoA values as a function of AoD is given in Table 7.1. The angle of arrival was considered to be given by the beam-peak angle of the DUT antenna pattern. The median error between them is approximately 6 degrees. These results indicate that this reflector can effectively generate multiple signals with different AoA as was expected from the simulations. The probable sources of the errors were misalignment of the feeder antenna, and non-uniformities of the reflector given the construction method and simplicity of alignment.

In Fig. 7.9, it is also possible to observe that the beamwidth and shape of the measured antenna patterns changes in each AoA. The main lobe becomes narrower as the AoA increases. For AoA up to 70 degrees the mean HPBW was 25 degrees which is more than double of the original HPBW of the horn antenna. Whereas, for higher AoA it can be seen that the radiation patterns are even narrower approaching the 15 degrees, which is much closer to the original beamwidth of 12 degrees. In can be seen that at around 93 degrees two patterns are overlapping and cannot be distinguished one from the other. Analytically, these signals should have arrived at 91 and 99 degrees respectively. The reason for this overlapping is because the FA was illuminating the part of the reflector that had a deformation as was previously shown in Fig. 7.8. The same is true for the two following patterns corresponding to the AoAs of 107 and 111 degrees. However, it is interesting to notice that the radiation patterns have a more similar shape than the original

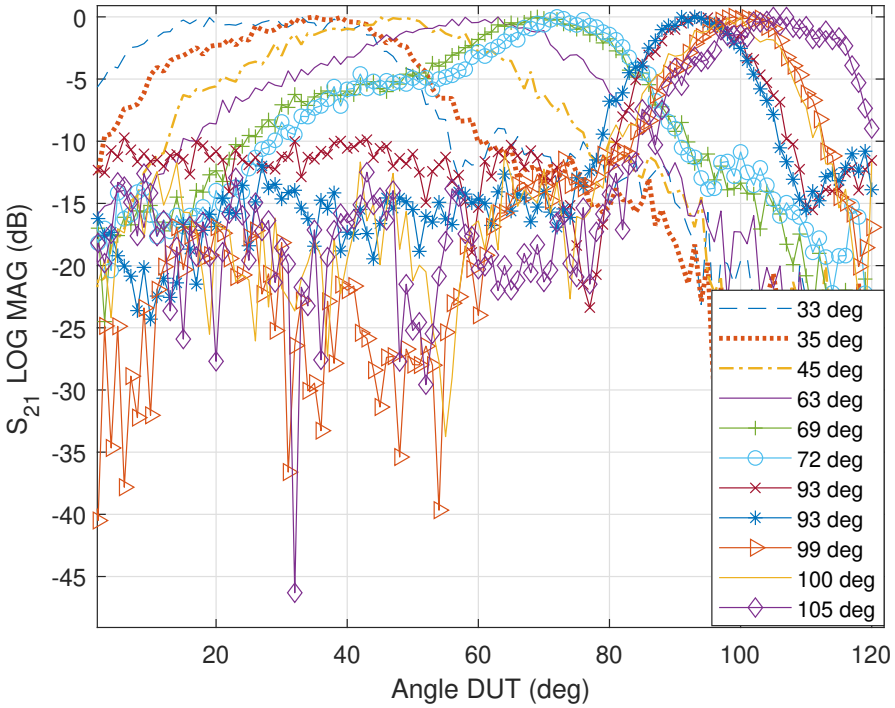

Figure 7.9: Angles of Arrival with test antennas in horizontal polarisation for ECR

Table 7.1: Angular correspondence and error for ECR

AoD (deg)	AoA Theoretical (deg)	AoA Measured (deg)	Error (deg)
10	28	33	-4
15	41	36	5
20	53	45	8
25	64	63	1
30	74	70	4
35	83	72	11
40	91	93	-2
45	99	95	4
50	107	99	6
55	111	100	11
60	116	107	11

pattern of the horn antenna. This can be seen with greater detail in the polar plot of Fig. 7.11b. The directivity of the different patters was also calculated. For the AoA above 70 degrees the directivity was around 21 dBi, which is practically the same as to the horn antenna measured in ideal conditions in the far field region.

On the other hand, for all the cases of AoA of up to 70 degrees the calculated directivities were in the range of 17 to 19 dBi, which is approximately 3dB lower than the measured in ideal conditions. The possible reasons for the less directive, wider beam patterns at lower AoA, is that due to the shape of the elliptical reflector the reflected signals are concentrating the power at the focal point, as was expected analytically, and as result they magnify the gain of the side lobes of the DUT antenna. This can be observed in Fig. 7.10a, 7.10b and 7.11a where the original antenna pattern of the horn antenna was overlaid with the test measurements. It can also be assumed that the ripple seen in the measurement of the radiation patterns was produced due to the irregularities in the surface of the reflector, such as air bubbles, lumps, scratches, etc of this prototype due to its simple and quick manufacture. As previously mentioned in theory if a far field signals is achieved after reflection it would have been be possible to measure the pattern of the DUT antenna, however when compared with the ideal antenna pattern of the horn antennas it is possible to see that it is not possible to distinguish the main and side lobes, which means that the measurement was not done in the far field zone.

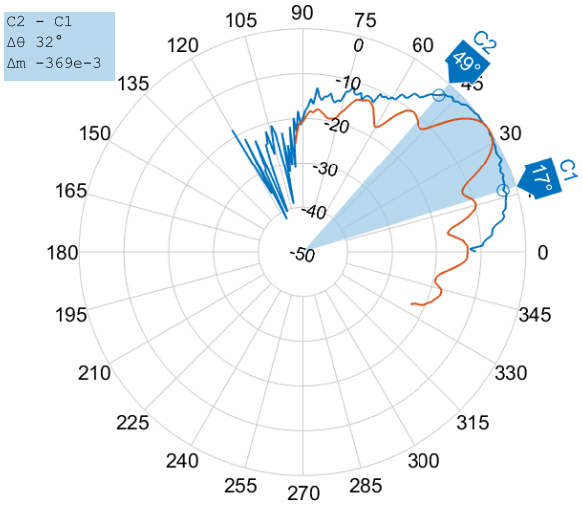

(a) Angles of Arrival 35 degrees

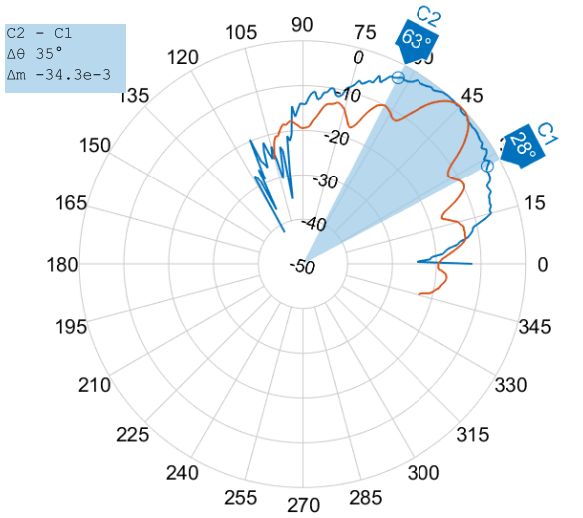

(b) Angle of Arrival 45 degrees

Figure 7.10: Comparison of radiation patterns original vs measured from ECR at AoA 35 and 45 degrees

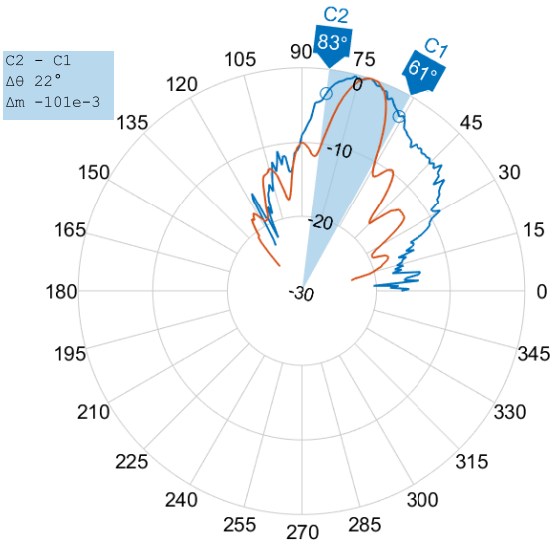

(a) Angles of Arrival 72 degrees

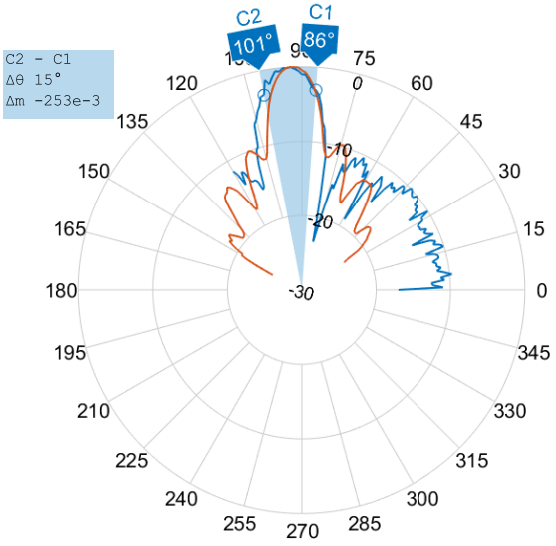

(b) Angle of Arrival 93 degrees

Figure 7.11: Comparison of radiation patterns original vs measured from ECR at AoA 72 and 93 degrees

7.2.4 Planar Characterization

To validate the quality of the TZ a planar measurement technique was used. It comprised of two linear actuators placed orthogonally to each other, such that the scanning surface was a plane, allowing measurement of the effective area of the TZ . The dimensions of the scanning plane were 20 cm height by 20 cm length. The tangential electromagnetic fields of the signals coming from the reflectors were sensed by the Rx antenna, where the amplitude and phase parameters were captured in a matrix of M x N elements which were equidistant. The distance between sample points were $d = \lambda/4$, where λ is the wavelength of the tested frequency. As the test frequency was 26 GHz, then the distance between each sample point was $d = 0.29$ cm. Fig. 7.12 illustrates the sampling points distribution. The centre of the coordinate x' and z' was located at the focal point.

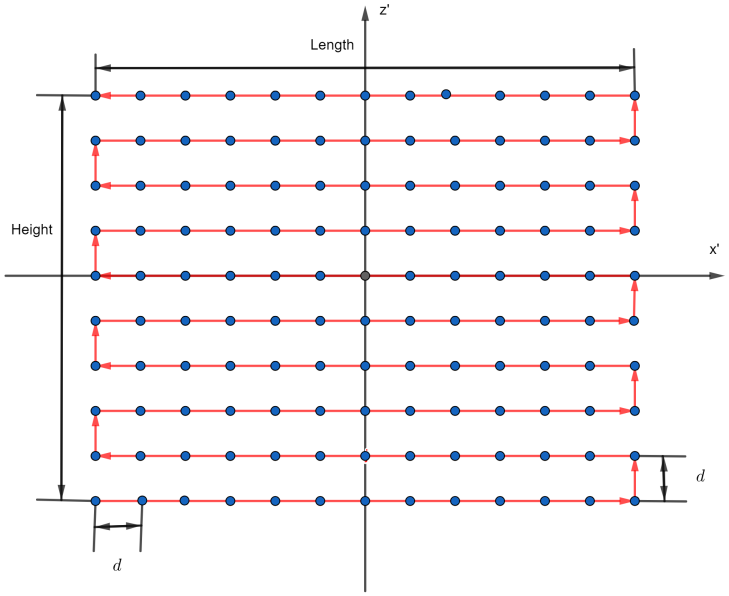

Figure 7.12: Planar measurements sampling points

The setup used to measure the TZ is show in Fig. 7.13. The DUT antenna mounted in the planar positioner was rotated towards the corresponding angle of arrivals which were previously shown, such that the aperture of the antenna would be facing directly towards the corresponding AoA, and then the plane was scanned. The feeder was fixed at the other focal point at some particular angles of departure. This procedure was used to measure the TZ of the signals in the azimuth plane and elevated 30 degrees in the elevation plane, as shown in Fig. 7.13.

The planar measurements were performed at two angles of arrival 33 and 70 with the reflector placed on the horizontal plane, and at 45 degrees when the reflector was elevated to 30 degrees. These angles were chosen to avoid the section of the reflector that showed a deviation in the curvature as explained in subsection 7.2.2.2. According to the simulations it was expected that the TZ area would be very narrow in the horizontal plane, and very broad in the vertical plane. The scanning area was limited to 20 cm x 20 cm, so it was expected to have constant power gain in an

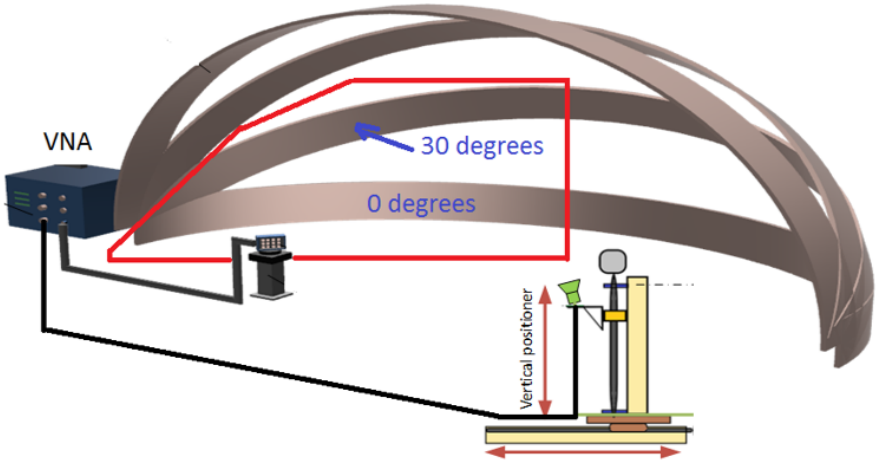

Figure 7.13: Planar measurements setup

area of approximately 5 cm x 20 cm. To have a general idea of the how the power was distributed at the respective AoAs, Fig. 7.14 shows the empirical cumulative distribution function (ECDF) of the three measurements. It can be observed that the three measurements have similar dynamic ranges higher than 45 dB and the median power was around 24 dB. These results demonstrate that the signals fluctuate significantly within the measured area. The median power is extremely low, since ideally the desired fluctuation within the TZ should be within a 3dB margin.

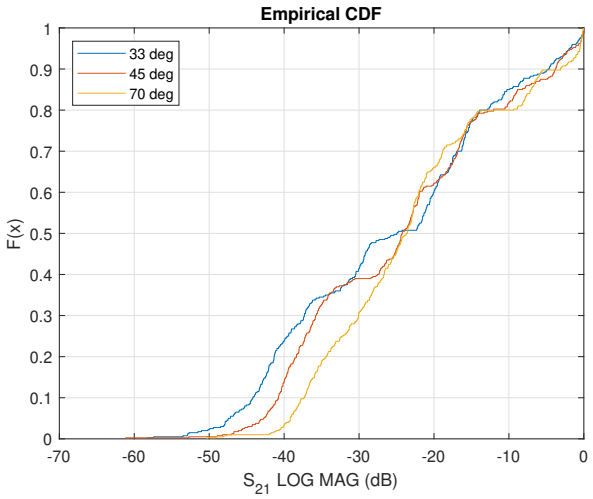

Figure 7.14: CDF of the whole plane from planar measurements setup

Individually the results of the measurements at the different AoA in azimuth and elevation are shown in Fig. 7.15, Fig. 7.16 and Fig. 7.17 respectively. Two areas have been marked with dashed lines. The red line indicates the desired TZ area of 20 cm x 20 cm in which the signal should fluctuate in a 3dB range, and the blue rectangle shows the effective TZ area achieved where the power approaches this desired condition. It can be seen that the TZ area is of approximately 2

cm x 20 cm for the three cases. Which clearly indicates that the signal is spreading in the vertical plane as was expected in the simulations and converged in the horizontal plane. Furthermore, the figures show a steep gradient of the signals at both sides of the centre of the TZ , because the power rapidly decays within the measured area. It is also noticeable that the results from the elevated reflector show greater variability than the ones in the horizontal plane. These results could be attributed to the difficulty in exactly position the reflector and alignment of the probe antennas, because it was only a quarter of an ellipse.

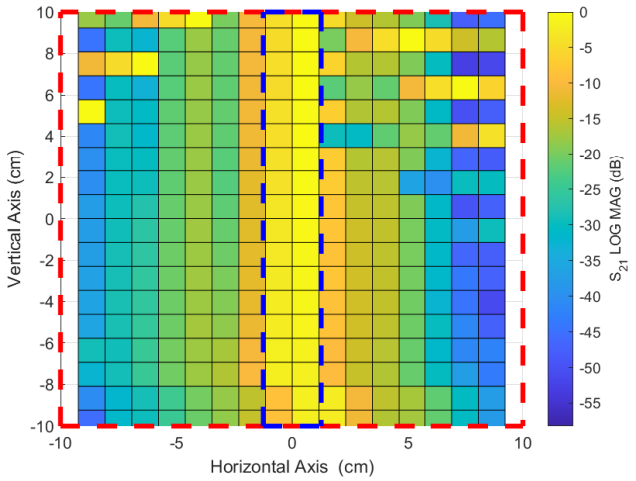

Figure 7.15: Planar measurements at AoA of 33 deg and 0 deg elevation.

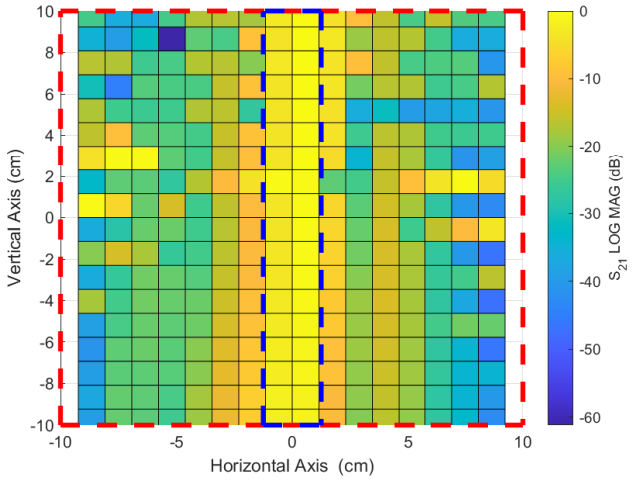

Figure 7.16: Planar measurements at AoA of 70 deg and 0 deg elevation

The ECDF of the effective TZ area within the blue dashed lines is shown in Fig. 7.18. It can be seen that the median received power of the signals is approximately 3 dB and the greatest fluctuation is -9 dB. For the first measurement at AoA of 33 degrees 65 percent of the signal is in

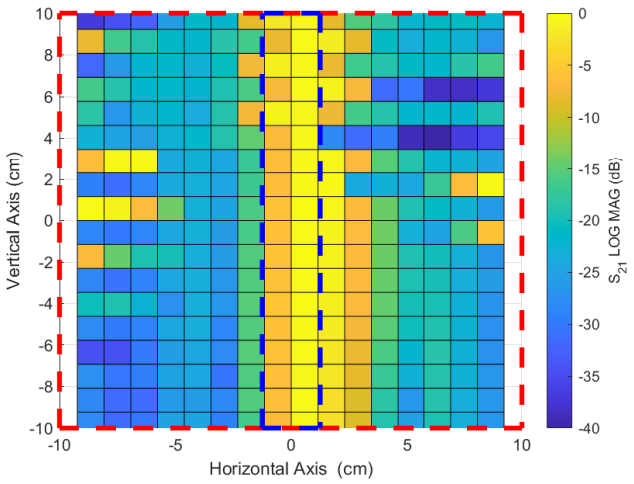

Figure 7.17: Planar measurements at AoA of 45 deg and 30 deg elevation

the 3dB range, for AoA 70 degrees 60 per cent of the signal is inside this range and 72 per cent of the signal for the elevated case.

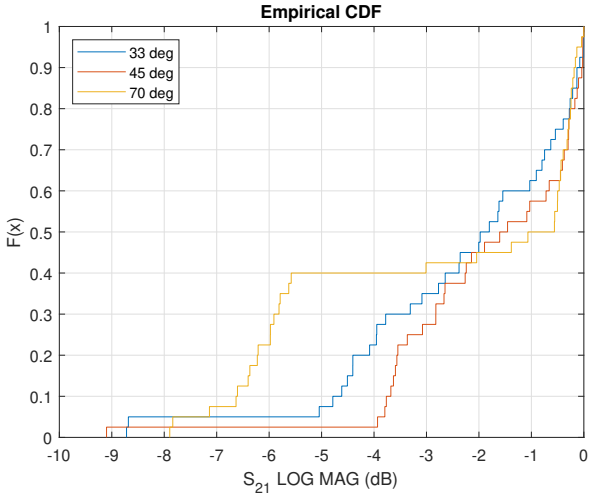

Figure 7.18: ECDF of the Test Zone from planar measurements setup

To summarize, this prototype helped to demonstrate that with an elliptical cylinder reflector configuration it is possible to generate the following scenarios and features:

1. Multiple signals with different angles of arrival in the azimuth and elevation planes as expected from the simulations.

2. The test signals can be scanned continuously along the extent of the reflector, creating continuously evolving angles of arrival at the DUT.

3. The cylindrical shape enlarges the beamwidth of the signal (or the TZ volume) the in one plane (in this case the vertical plane).

4. The effective TZ size is sufficiently large to test small antennas with an antenna diagonal of maximum 5 cm.

The drawback of this test system is that the TZ is not sufficiently large to test the performance of device of the size of a smartphone in a "black box" sense (see subsection 3.8), but as mention above can be used to test the performance of parts of the device if the position of the antennas is known and their phase centre is positioned at the focal point.

7.3 Testing and Characterization of Discrete Plane Reflectors

7.3.1 Implementation

Building on the analysis in chapter 6 and the concept of the DPR a prototype consisting of two sets of plane reflectors was constructed. Each set had seven flat reflectors. One set of reflectors was located in the horizontal plane and the other set was elevated 30 degrees. The dimensions of the base ellipse used to distribute the plane reflectors were similar to the one stated in the theoretical analysis (see chapter 5) and the ECR reflector. The semi-major axis was 205 cm and the semi-minor axis was 180 cm. Each reflector was a flat square surface of 30 cm of edge. The material of the reflective surfaces was flame retardant FR-4. To give the adequate position and angle to the reflectors a former similar to the ECR case was designed in small sections of 60 cm long, which were laser cut of a 10 mm thick plywood sheet and joined together to achieve the full length of half of the ellipse. Similar to the ECR case, the construction and assembling methodology of the reflector was not perfect which led to some errors that will be described and discussed in this section. The final prototype fully assembled is shown in Fig. 7.19. The difference with respect to the ECR prototype is that for DPR the feeder antenna an Anokiwave [14] characteristics will be explained bellow. On the other focal point, the Flann horn antenna (model DP241-AB) was used.

7.3.1.1 Characteristics of the Anokiwave phase antenna array

The Anokiwave AWA-0142-IK phase array antenna covers the band 24.25 to 27.5 GHz [18]. This operates as a 256-element single beam device, or as 4 x 64-element independent sub-arrays. Each sub-array has an independent RF feed port known as J7, J8, J9 and J10 ports. Additionally, each sub-array can independently steer the beam in a $\pm 60^o$ conical scan volume centred at boresight. The nominal HPBW of the sub-arrays was 20 degrees, and the diagonal length of each sub-array was 5.7 cm. Figure 7.20 shows the antenna array and illustrates how the sub-arrays were localized.

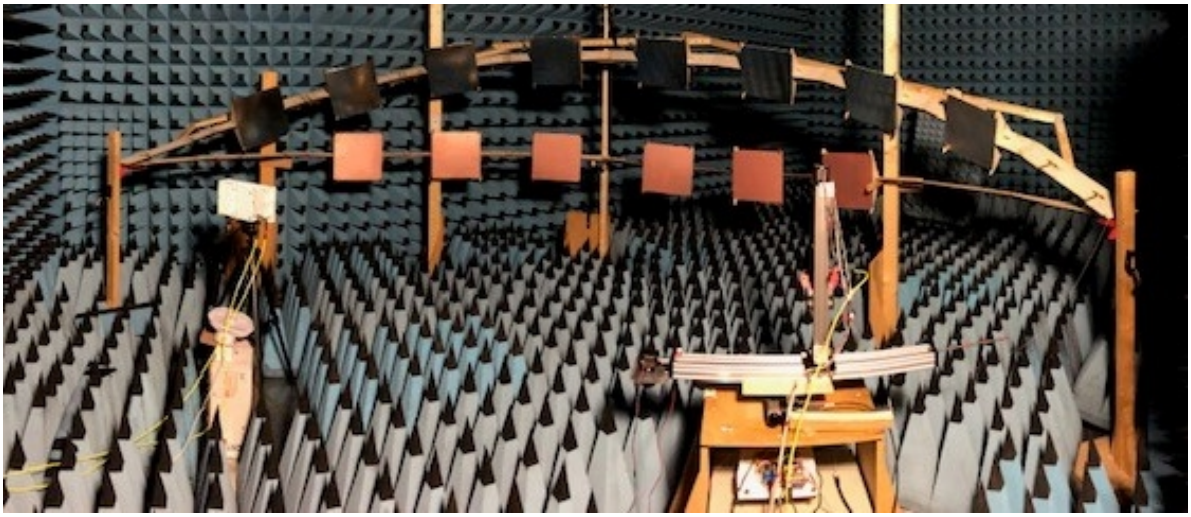

Figure 7.19: Discrete OTA test apparatus in Bristol's anechoic chamber

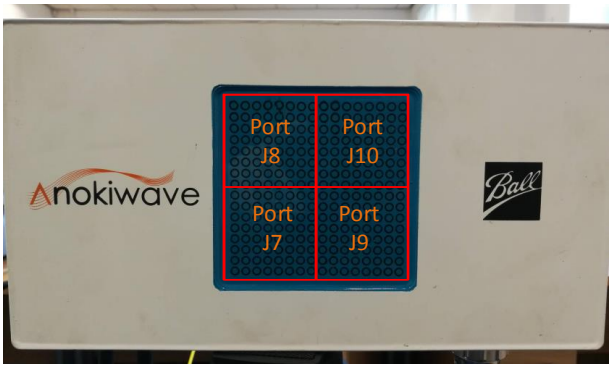

Figure 7.20: Anokiwave AWA-0142-IK phase array, with sub-arrays identified and labelled.

To understand the response of the discrete reflectors it was necessary to measure the radiation characteristics of the array antenna at different angles since these will illuminate the discrete reflectors and the patterns may vary depending on the angle of departure. The radiation patterns were measured in the anechoic chamber. The patterns were measured by steering the beam every 10 degrees in the range from 0 to 60 degrees in azimuth plane. As the array is square, and the distribution of the antenna elements is symmetrical it was assumed that the patterns are mirrored on the negative angles. The array was set in receiver mode, 64 elements and two different beam modes were evaluated, the uniform illumination and side lobes tapering. Uniform illumination provides the same amplitude stimulus to each antenna element. The side lobes tapering provides a 25 dB side lobe level Taylor taper. The beam taper settings are hardcoded into the firmware of the antenna. The distance between the transmitter and receiver was 4 metres. The setup used to measure the antenna patterns in the anechoic chamber is show in Fig. 7.21a

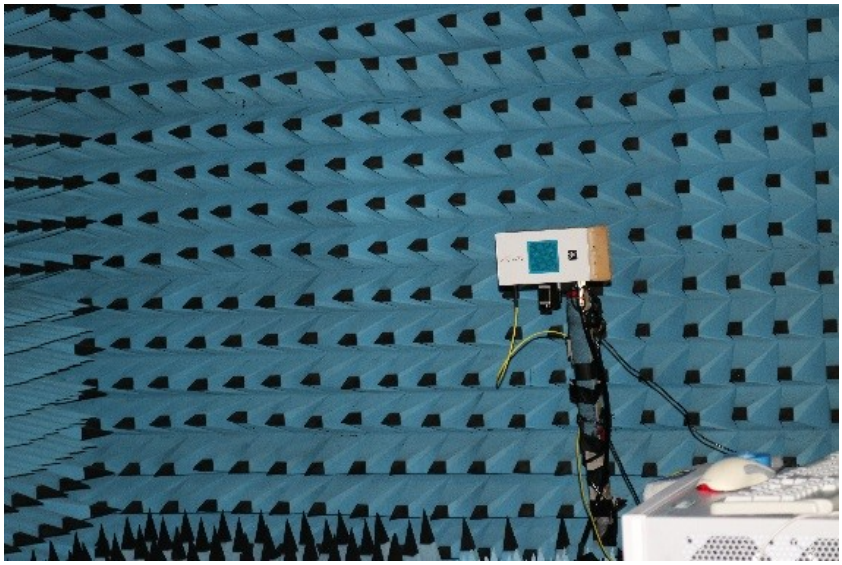

(a) Anokiwave array inside anechoic chamber

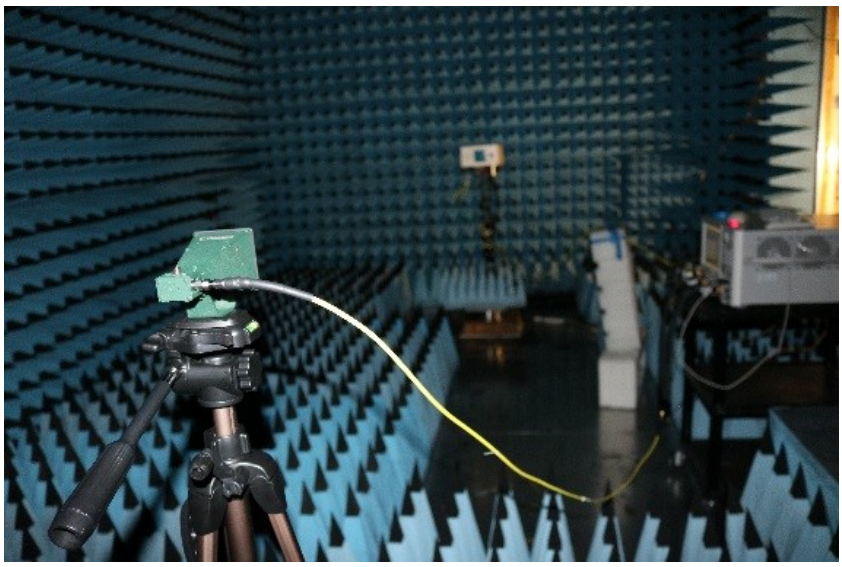

(b) Setup to measure the radiation pattern of the array antenna

Figure 7.21: Radiation pattern measurement setup in anechoic chamber

In Fig. 7.22 it is shown the measured radiation patterns when the antenna array was set in uniform illumination mode. The antenna parameter such as peak pointing angle, half power beamwidth, and first side lobes pointing angles and levels are summarized in Table 7.2. According to the data captured it is possible to see that there is a good agreement between the theoretical steering angles and the measured angles between 0 to 50 degrees. The major difference is seen at 60 degrees because the beam peak point is approximately 7 degrees away from the expected location. Further, the greater received power level was measured at boresight, and the lowest beam peak level is about 2 dB at 60 degrees. It is also shown that the HPBW increases as the

Table 7.2: Characteristics array patterns Uniform illumination mode

Theoretical angle (deg)	Measured angle (deg)	Rx'ed Power Level (dBm)	HPBW (deg)	Left Side Lobes angles (deg)	Right Side Lobe angles (deg)	Left Side lobe power (dBm)	Right Side lobe power (dBm)
0	1	-41.8	16	-23	27	-55.5	-54.8
10	9	-42.4	16	-15	37	-54.9	-57.0
20	22	-42.5	17	-3	50	-55.7	-55.4
30	29	-42.5	19	4	64	-54.3	-56.9
40	40	-42.5	18	-43/13	81	-55.2	-59.9
50	47	-42.6	23	17	96	-55.9	-86.4
60	53	-44.1	25	26	143	-54.4	-70.5

beam is steered away from 0 degrees, starting at 16 degrees to 25 degrees. With respect to the first side lobes, the ones on the left on average are 12.5 dB below the beam peaks, whereas at the right side these are on average 14.46 dB below, except for the last two beams (50 and 60 degrees) whose side lobes are well below 25 dB.

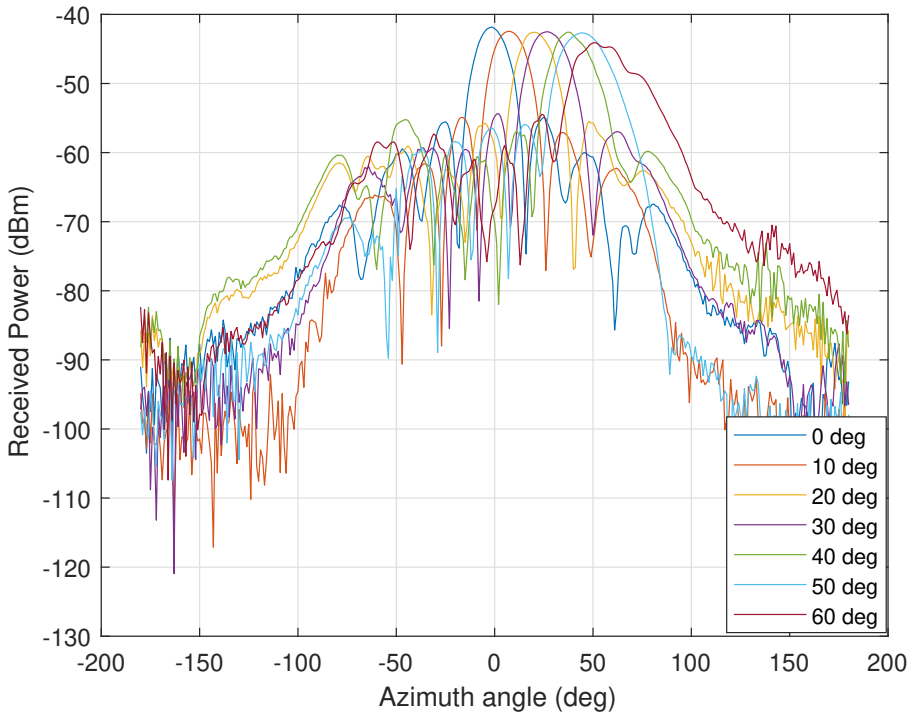

Figure 7.22: Antenna pattern with Uniform phase weighting from 0 to 60 degrees

On the other hand, Fig. 7.23 shows the antenna patterns measured with the array configured in "Side lobes tapering mode". Similar to the uniform illumination mode the antenna patterns

were measured every 10 degrees in the range from 0 to 60 degrees in azimuth plane. For this case, only the negative beam angles were measured assuming symmetry of the 64 elements array for the positive steering angles. The parameters of the antenna patterns per steering angle are summarised in Table 7.3. It is possible to observe that there is a good agreement of the theoretical and measured beam pointing angles apart of 60 degrees, which differs the most. The received power levels are also consistent throughout the different beam steering angles the difference between boresight and 60 degrees is approximately 1.8 dB. The HPBW of all the beams in this mode are broader than in uniform mode. The first side lobes in both the positive and negative angles of the patterns compared with the main lobes on average are 20 dB below. At 40 and 60 degrees it is possible to see that there exist two side lobes that are stronger than the first ones.

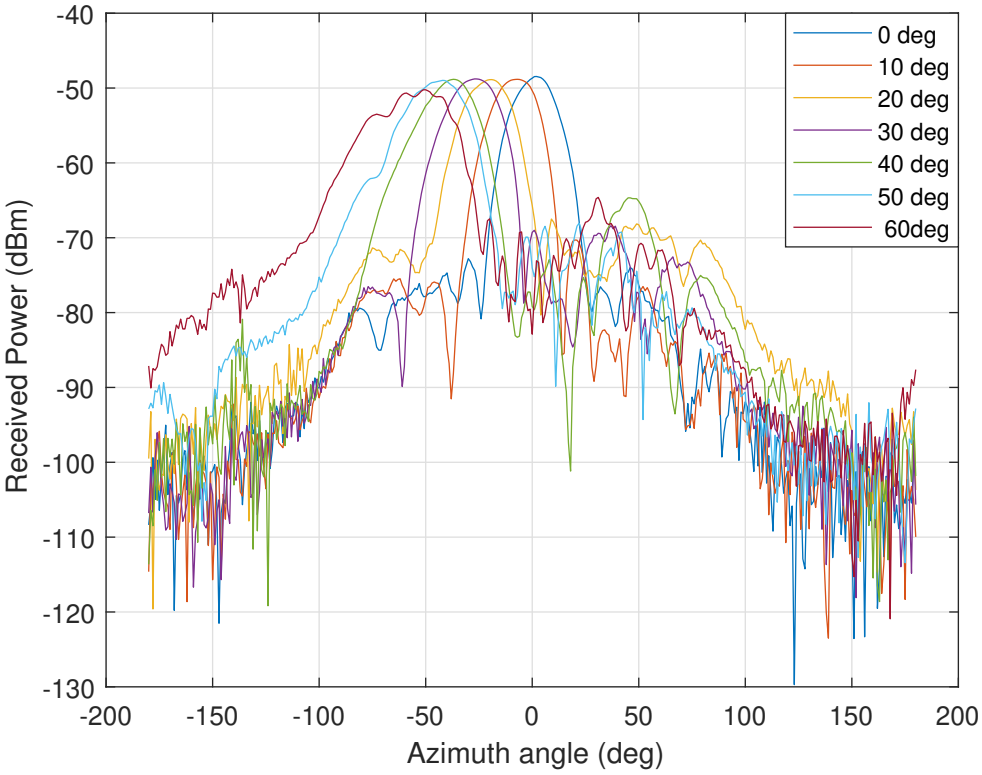

Figure 7.23: Antenna pattern with Low sidelobe phase weighting from 0 to 60 degrees

7.3.2 Characterisation

To characterise the DPR setup, the forward scattering parameters were measured with a 4-port Vector Network Analyzer. This allowed to perform two measurements with different sub-arrays simultaneously. The antenna array was used as transmitter and was located at one focal point and at the other focal point was placed a horn antenna used as a receiver. The latter was mounted on a positioning setup that consisted of two linear actuators providing two degrees of freedom in

Table 7.3: Characteristics array patterns Low side lobes

Theoretical angle (deg)	Measured angle (deg)	Peak Power Level (dBm)	HPBW (deg)	Left Side Lobes angles (deg)	Right Side Lobe angles (deg)	Left Side lobe power (dBm)	Right Side lobe power (dBm)
0	0	-48.4	19	-32	44	-72.8	-73.9
-10	-9	-48.8	21	-48	19	-75.9	-70.3
-20	-21	-48.8	21	-63	7	-71.7	-67.5
-30	-29	-48.7	23	-79	-1	-76.5	-69
-40	-39	-48.8	21	-138	6/46	-80.8	-72.9/-64.7
-50	-44	-48.9	26	-102	-4	-75.2	-69.9
-60	-53	-50.2	28	-143	-22/29	-74.2	-67.48/-64.6

vertical and horizontal positioning. This assembly was then located on top of a rotating table. A block diagram of the test setup is shown in Fig. 7.24. It is important to note that the geometric centre of the antenna array was placed at the focal point, which meant that the centre of the transmitting sub-arrays was about 2.5 cm diagonally away of the focal point (see Fig. 6.20).

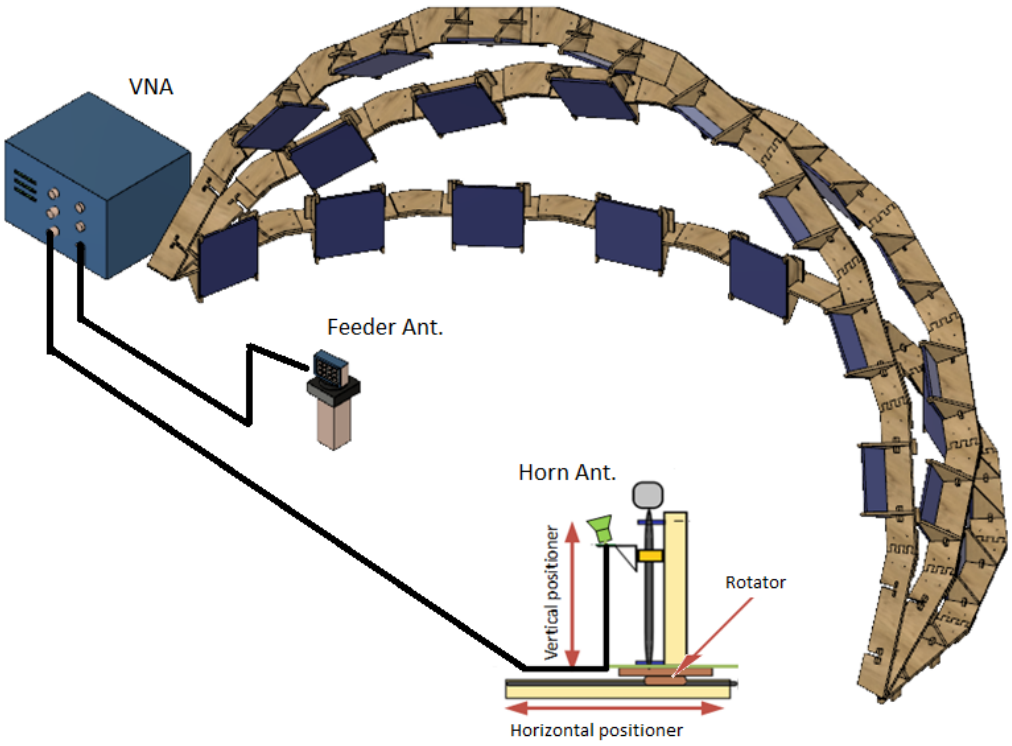

Figure 7.24: Block diagram of the setup to characterise the DPR system

7.3.2.1 Angles of Arrival with Anokiwave Antenna Array

In order to demonstrate that the discrete flat reflectors can illuminate the DUT with different angles of arrival as was expected from the numerical simulations, the following tests were performed: The feeder antenna array was fixed parallel to the major axis at focal point F1. The beam from sub-array J8 was pointed towards one of the reflectors according to the theoretical angles of departure detailed in Table 7.4, then the DUT antenna was rotated scanning the system from 50 to 180 degrees. Once the angular measurement was completed the beam was steered towards the next reflector and the scanning process repeated once again. The samples were captured at one-degree increments. With this configuration and due to the limited conical scan volume of ±60 degrees of the Anokiwave array not all the reflectors could be used. Out of the theoretical ten reflectors that each set of reflectors was designed to have only seven could be tested. It was not possible to use reflectors number 1, 2 and 10 because the AoD needed to illuminate them in terms of the Anokiwave angle (theta, phi) would have been (84, 180), (73, 180) and (74,0) degrees respectively, which was no possible due to the limitation of the maximum steerable angle to ±60 degrees.

To clarify how the angular mapping works, let's consider that reflector 3 will be used. According to Table 7.4 to illuminate reflector 3 the feeder antenna needs to point a beam with an AoD of 27 degrees, to do this it is necessary to configure the Anokiwave array to point the beam 62 degrees in theta and 180 degrees in phi. The expected angle of arrival for this case would be 70 degrees. The active antenna uses standard physics definition of spherical coordinates. Phi (ϕ)=0 is aligned with the x-axis (azimuth) and phi = 90 is aligned with the z-axis (elevation). Theta (θ)=0 is orthogonal to the face of the antenna. A graphical representation viewed from the rear of the array of the beams pointed direction Q towards Phi= 135 degrees and Theta = 45 degrees is seen in Fig. 7.25.

The results of the tests are shown in Fig. 7.26, which shows the antenna patterns of the horn antenna measured with the signals being reflected from each reflector individually. The power was normalized to the maximum received power of each pattern to facilitate the comparison between all the reflectors. Visually it is possible to see that the discrete reflectors can create multiple signals that arrive at the DUT with different angles of arrival as expected. In the last column of Table 7.4 the measured angles of arrival given by the beam pointing angle are listed. If compared with the theoretical angles of arrival in the same Table 7.4 it is possible to see that the difference between them for all the seven reflectors is less than 2 degrees. These differences can be attributed to some factors, amongst them are the inaccuracies of the system during construction, and the offset location of the sub-arrays with respect to the focal point. The latter will be analysed further in the following subsections.

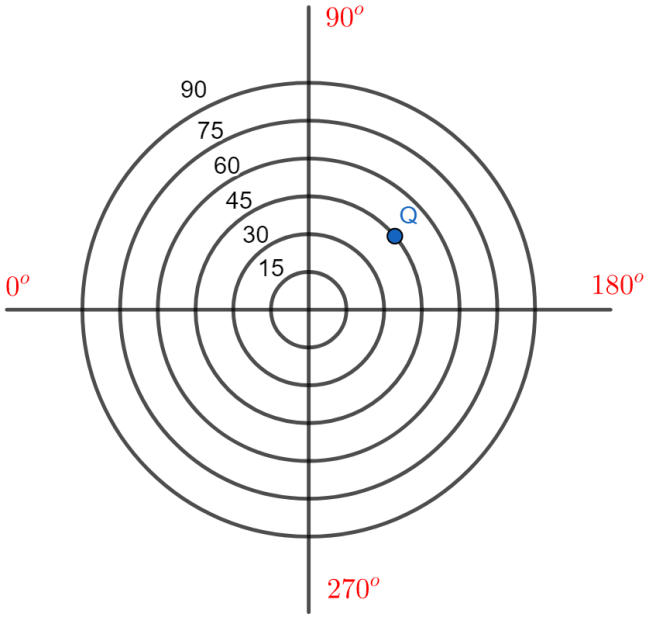

Figure 7.25: Pointing diagrams viewed from the rear of the array, showing a beam steered towards point Q($\phi = 135^o$,$\theta = 45^o$)

Table 7.4: Summary of AoD and AoA, and mapping to Anokiwave available angles

Reflector Number	**Theoretical AoD (deg)**	**Theoretical AoA (deg)**	**Anokiwave Theta Angle (deg)**	**Anokiwave Phi Angle (deg)**	**Measured AoA (deg)**
1	5	15	84	180	N/A
2	16	44	73	180	N/A
3	27	69	62	180	70
4	39	92	50	180	91
5	53	110	36	180	109
6	69	126	20	180	126
7	88	140	02	180	138
8	110	152	19	0	151
9	135	163	45	0	162
10	165	174	74	0	N/A

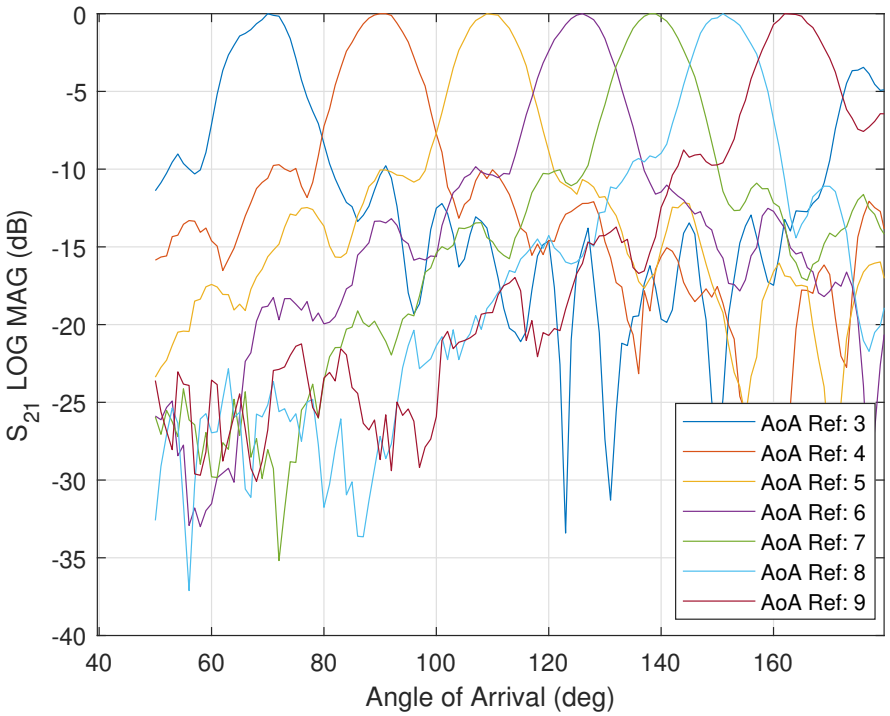

Figure 7.26: Angles of Arrival measured from DPR in the azimuth plane

7.3.2.2 Analysis of Angles of Arrival generated by the different sub-arrays

In this subsection it is analysed how the sub-arrays being offset from the focal point affect the angles of arrival of the signals, and compares how the antenna patterns of the horn antenna vary with respect to the ideal case which is being measured in ideal conditions such as in the far field region. To do this, angular tests similar to the once performed in subsection 7.3.2.1 were carried out but utilizing three sub-arrays J7, J8 and J10. J7 and J8 are place vertically aligned and J8 and J10 are horizontally aligned, thus parallel and vertical positioning can be evaluated. The angular tests performed provided two-dimensional antenna patterns cuts of the horn antenna. These were compared with the ideal case shown in Fig. 4.6, shifted to the beam pointing angle of each measurement. The analysis was done by comparing beamwidth and beam pointing angle of the main beam region. The patterns were normalized to the peak of the main beams of each measurement. Additionally, the three antenna patterns were compared against the original pattern using pattern subtraction [82, 83]. Each reflector response was analysed individually.

Reflector Number 3

In Fig. 7.27a four patterns were overlaid, the original pattern was shifted towards the expected angle of arrival, which for this case was 70 degrees and is shown with circled marks. The other

three patterns from the sub-arrays J7, J8 and J10 are shown in colours blue, orange and yellow respectively. It can be seen that the patterns follow a similar trend than the original pattern. The HPBW of the original pattern was 14 degrees, whereas the HPBW of J7 was 12 degrees, and J8 and J10's was 13 degrees. Thus, for all the three cases the beamwidth is smaller by 2 degrees and 1 degree respectively. On the other hand, the beam pointing angle of the three ports was 70 degrees which is the same as theoretically expected.

The discrepancies between each one of the patterns measured with the signals from the different sub-array compared with the original signal every angle is shown in Fig. 7.27b, where can be seen within the HPBW range the largest difference is about 2.5 dB at 77 degrees seen with port J7. Port J8 has the least discrepancies being less than 1 dB in the same HPBW. For J7 and J8 the maximum fluctuations are in the range of ±3dB region and outside of the HPBW. The pattern of the sub-array J10 had larger fluctuations than the other two of up to 5dB.

Reflector Number 6

The angles of arrival measured with the sub-arrays J7, J8 and J10 were 126 degrees which are practically the same as the expected, shown in Fig. 7.28a. The HPBWs captured from J7 and J8 and J10 were 13 degrees which is 1 degree less than the original pattern. The discrepancies between the sub-array patterns compared with the original signal every angle is shown in Fig. 7.28b. Here, can be observed that patterns measured using Reflector 6 show variations that are within the range of ±2.1dB for all the angles between 109 and 144 degrees. Within the HPBW range the fluctuation of the three patterns are even lower of about ±1dB.

Reflector Number 9

As shown in Fig. 7.29a the angles of arrival of the sub-arrays J7, J8 were 162 degrees which are offset by approximately 1.8 degrees below the expected AoA. The AoA captured with sub-array J10 was closer to the theoretical expected AoA with a difference around 0.8 degrees. The HPBW of J7 and J8 was 14 degrees and 13 degrees for J10. The discrepancies between the sub-array patterns compared with the original signal every angle is shown in Fig. 7.29b. It can be observed that within the HPBW angular range the fluctuation of the three patterns are in the range of ±1dB. The variations around the null regions are the highest. However, the worst case is seen around 175 to 179 degrees for the sub-arrays J7 and J8. With J10 the measured antenna pattern is closer to the original of the three patterns evaluated ones.

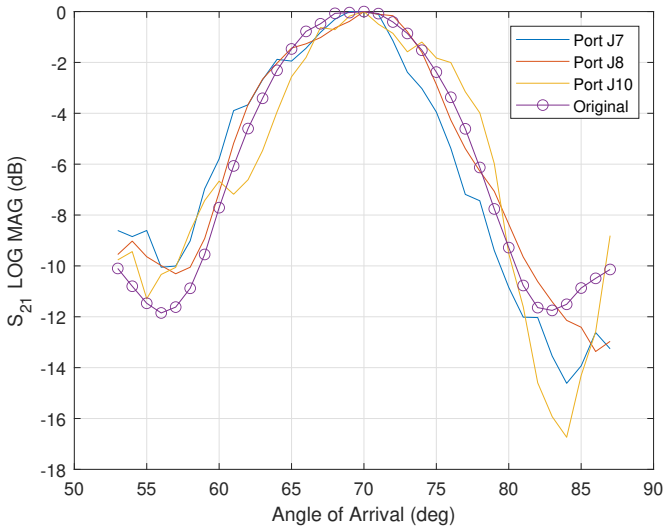

(a) Angles of Arrival from Reflector 3 illuminated from J7, J8 and J10 sub-arrays.

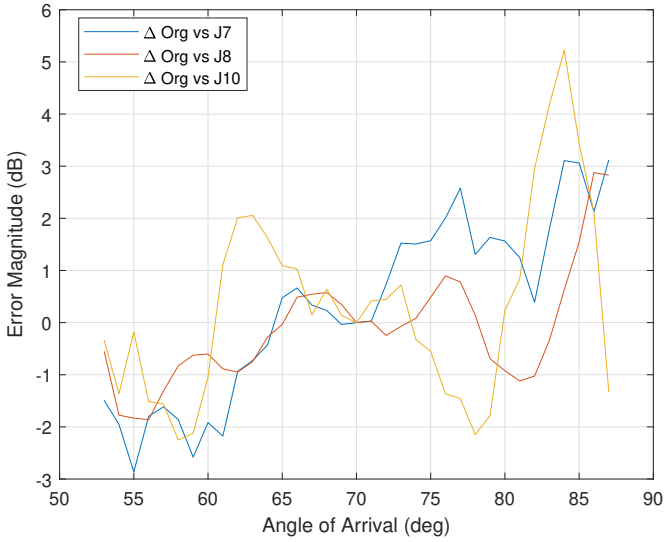

(b) Comparison of J7, J8 and J10 patterns with original by pattern subtraction from Reflector 3.

Figure 7.27: AoA Reflector 3.

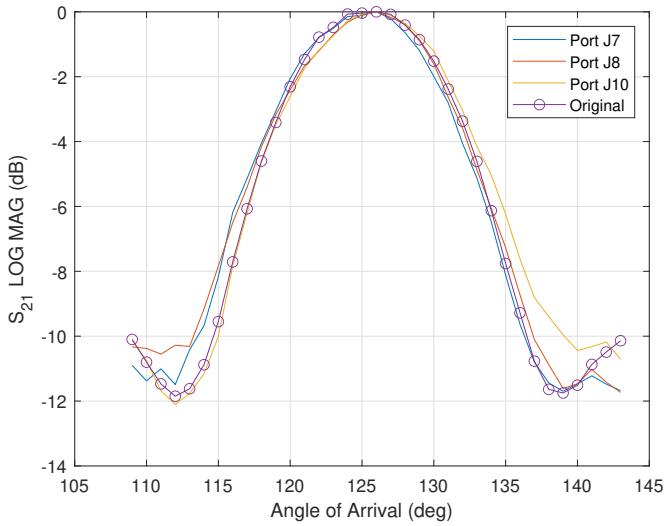

(a) Angles of Arrival from Reflector 6 illuminated from J7, J8 and J10 sub-arrays.

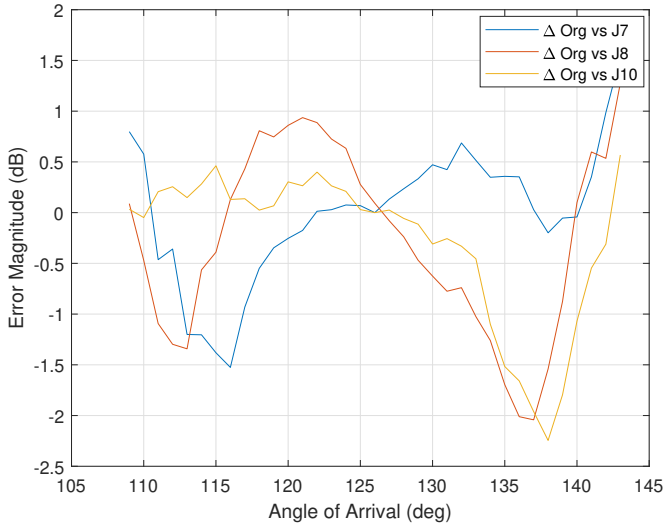

(b) Comparison of J7, J8 and J10 patterns with original by pattern subtraction from Reflector 6.

Figure 7.28: AoA Reflector 6.

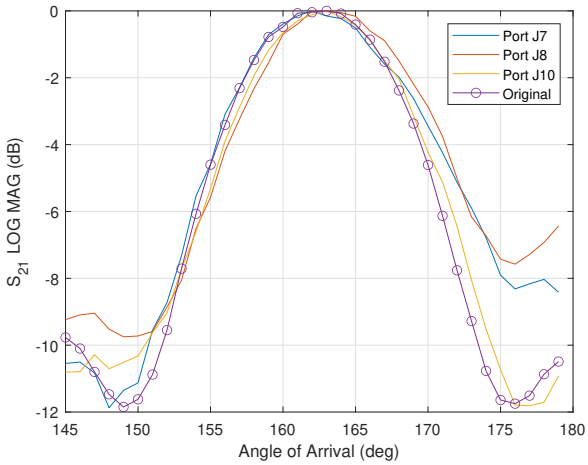

(a) Angles of Arrival from Reflector 9 illuminated from J7, J8 and J10 sub-arrays.

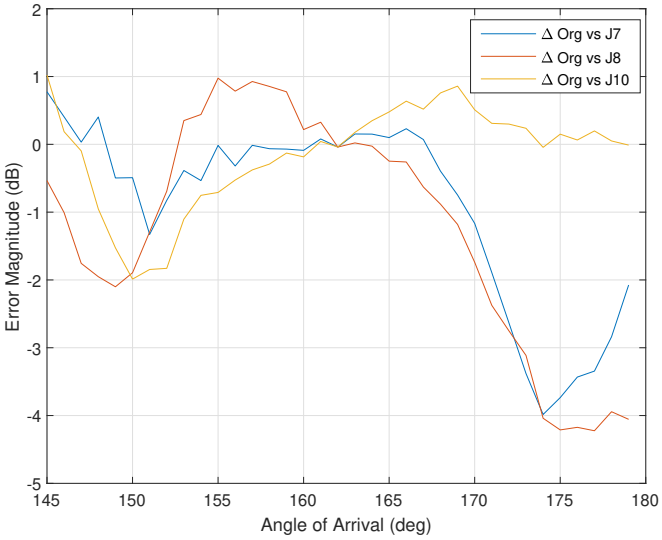

(b) Comparison of J7, J8 and J10 patterns with original by pattern subtraction from Reflector 9.

Figure 7.29: AoA Reflector 9.

7.3.2.3 Interference caused by adjacent reflectors

In the theoretical analysis was shown that due to the positioning of the discrete reflectors and the diverging nature of the signals propagated from the FA, some of the energy intended to reflect from a specific reflector will unwantedly also reflect from adjacent reflectors. These undesired reflections will cause some interference inside the TZ. In this section, it was evaluated how these interfering signals affect the TZ. To evaluate this, angular measurements similar to the last two previous subsections were performed capturing the antenna pattern of the horn antenna. The difference was that in this case all the discrete reflectors were in their corresponding position, and not only the targeted one. The analysis was done by comparing the antenna pattern of the horn antenna measured with only one reflector as the base line with the antenna pattern captured with all the reflectors being in their intended place. Furthermore, two transmission modes of the Anokiwave array were used, the uniform and the side lobes tapering in order to determine if having different antenna patterns from the transmitter side, affects the reading of the horn antenna patterns. As it was shown in subsection 7.3.2.2 the three patterns measured from all the different sub-arrays were pretty similar when measured with only one reflector, therefore, here only the sub-array J7 was used to perform these tests and the pattern obtained was compared to the one measured when a single reflector was in place. Every reflector is analysed below individually.

Interference analysis of Reflector Number 3

Figure 7.30a presents the radiation patterns of the horn antenna with only reflector 3 (which will be called the original pattern) in position in red colour and the radiation pattern of the horn antenna with all the reflectors in blue (which will be called the evaluated pattern). This patterns were measured with the active antenna configured in Uniform mode. The first five strongest lobes are identified with numerical labels, which are ordered according to the radiation strength of each one, being 1 the highest peak and 5 the lowest. For both cases it is seen that there exist two main beams for the original pattern these are pointing to 70 and 176 degrees, and for the evaluated the point angles are 72 and 174 degrees. The lobe seen at 174 and 176 degrees respectively is due to the fact that some of the energy in LOS with the array antenna is received by the side lobes of the horn antenna. The radiation intensity of side lobes 3, 4 and 5 are a between 2 and 6 dB higher than the original signal respectively, which indicates that undesired signals are being reflected from the other reflectors with angles of arrival of 144, 132 and 95 degrees.

When selecting the low side lobe mode of the Anokiwave array, the beam becomes wider and has a lower gain. Fig. 7.30a shows the differences between the original and the evaluated radiation patterns. Once again two main lobes are seen pointing to similar angles than with the uniform transmission mode. The side lobes of the evaluated signal appear to be higher than the original as well, but more localized, because in the previous case it can be seen that the overall levels of the smaller side lobes are higher than the original. Whereas, for this case the side lobes

3, 4 and 5 look more like individual smaller beams. The angles that these beams are pointing are 108, 143 and 94 degrees, which could be considered the AoA of interfering signals. These angles correspond reflectors 4,5 and 6.

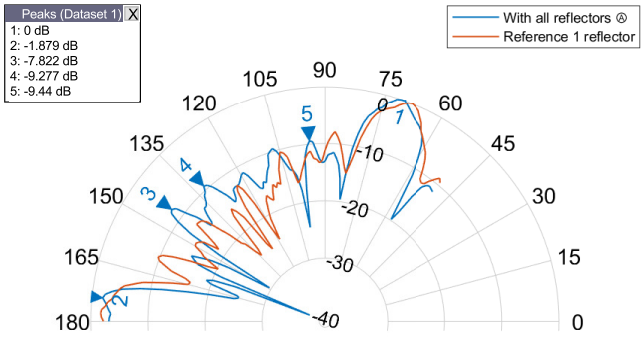

(a) Interference caused by Reflectors 4,5,6,7,8 and 9 when Reflector 3 was the target reflector illuminated with the Uniform mode.

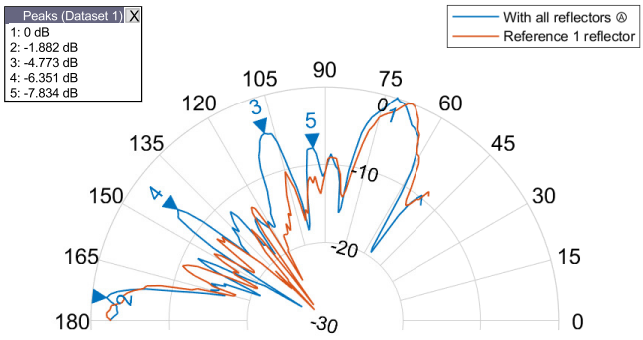

(b) Interference caused by Reflectors 4,5,6,7,8 and 9 when Reflector 3 was the target reflector illuminated with the Side lobe tapering mode.

Figure 7.30: Interference analysis Reflector 3.

Interference analysis of Reflector Number 5

For this case the expected angle of arrival of the signal was 110 degrees, as shown in Fig. 7.31a, and Fig. 7.31b by the radiation patterns in red of the original pattern. For the uniform mode the main beam pointing angle of the evaluated pattern is 107 degrees, being 3 degrees misaligned

from the theoretical angle. Two strong side lobes are observed coming from 89 and 140 degrees, whose radiating intensities are 5 and 6 dB below the peak. These interfering signals correspond to reflectors 4 and 6 respectively. A similar scenario is seen with side lobe tapering mode, were the angles of arrival of the main and interfering signals are the same as well as the power levels. Other two side lobes are observed but are below -10 dB, however, are approximately 7 and 10 dB stronger than the power levels of the original pattern at the corresponding angles.

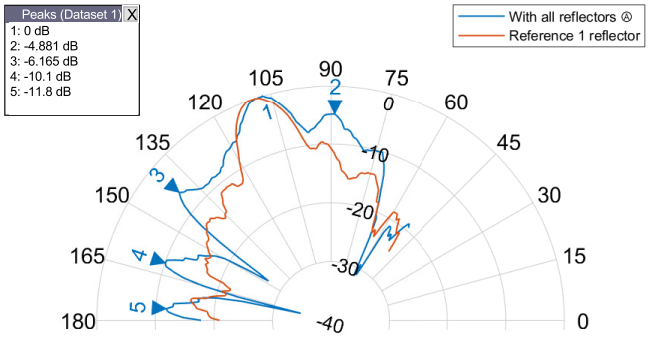

(a) Interference caused by Reflectors 3,4,6,7,8 and 9 when Reflector 5 was the target reflector illuminated with the Uniform mode.

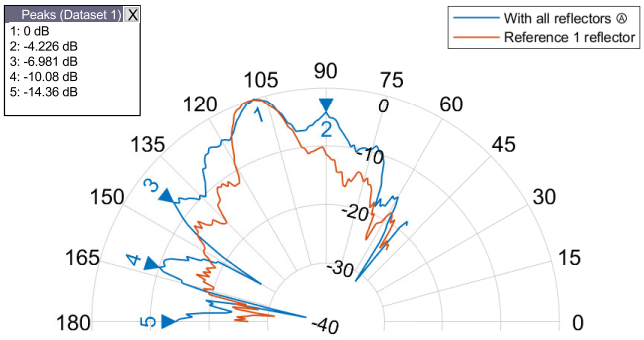

(b) Interference caused by Reflectors 3,4,6,7,8 and 9 when Reflector 5 was the target reflector illuminated with the Side lobe tapering mode.

Figure 7.31: Interference analysis Reflector 5.

Interference analysis of Reflector Number 9

Reflector 9 is physically the closes reflector to the feeder active antenna. When individually measured the radiation pattern of the horn antenna, the HPBW of the antenna was 13 degrees, which is shown in both Fig. 7.32a, and Fig. 7.32b. Additionally, it showed a first side lobe at approximately 180 degrees whose power level was only 7 dB below from the maximum. The secondary side lobes were below -10 dB. A similar behaviour is seen by the evaluated pattern when the reflector 9 is illuminated with low side lobes mode. However, with the other transmission mode, it is possible to observe secondary side lobes appearing at 124, 71, 147 and 107 degrees with power level a little over the -10 dB mark reaching up to -7dB. These angles of arrival correspond to reflectors 6,3, 8 and 5 respectively. Which indicates that for this case using a low side lobe antenna to illuminate the reflector would be more beneficial to avoid unwanted signal arriving from adjacent reflectors.

7.3.3 Angles of Arrival for 30 degrees elevation reflectors

It is required that the system can emulate 3D spatial environment, and in chapter 6, it was detailed the procedure used to design such structure. In this subsection, the results of the angular measurements of the reflectors elevated to 30 degrees were analysed. The test setup was previously shown in Fig. 7.19. The reference to measure the desired angle of elevation was the centre of the ellipse, thus the 30 degrees were measured from the y-axis or the semi minor axis towards the ceiling of the anechoic chamber. The test consisted as per the previous cases in measuring a section of the radiation pattern of the horn antenna. Two simultaneous measurements using the reflect signal transmitted by the sub-arrays J7 and J10 which are diagonally positioned in the Anokiwave array (see Fig.7.20) were captured. The boresight of the horn antenna was mechanically steered in the azimuth and elevation planes to adequately point towards the incident reflected signal. By measuring with two different sub-arrays, it was possible to compare if the angles of arrival of the signals will deviate from the theoretical expected AoA in azimuth. Furthermore, it allows to determine if there are noticeable differences between patterns when the signals are received at different angle in elevation. For these test the reflector number 3 was not considered because as it was previously described the theta and phi angles of the Anokiwave antenna needed to be 2 degrees over its maximum limit ±60 degrees (see Table 7.4 in order to steer the beam towards this reflector and after several attempts to make this work, the radiation pattern of the antenna under test was unrecognisable. Therefore, only reflectors 4 to 9 will be analysed. It is word mentioning that the measurements were performed with individual reflector, to avoid interfering signals from other reflector corrupting the data.

Figure 7.33a shows the 6 radiation patterns measured while the illumination signal was generated by sub-array J7 with the respective azimuth angles of arrival. These angles were also summarized in Table 7.5. If compared with the theoretical AAoA, it can be seen that the greatest deviation was seen by reflector 5 which is misaligned approximately 4 degrees, whereas for the

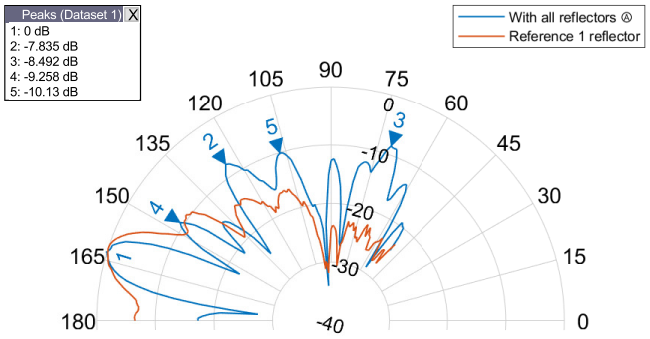

(a) Interference caused by Reflectors 3,4,5,6,7 and 8 when Reflector 9 was the target reflector illuminated with the Uniform mode.

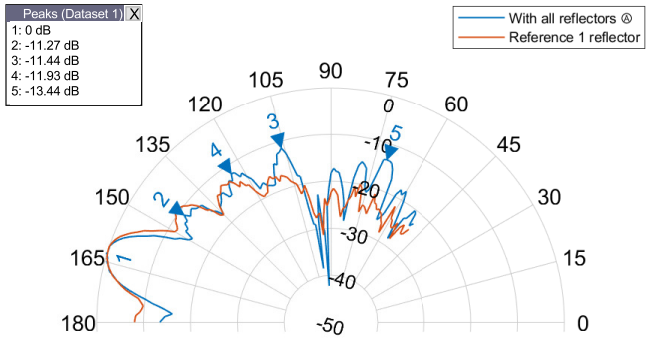

(b) Interference caused by Reflectors 3,4,5,6,7 and 8 when Reflector 3 was the target reflector illuminated with the Side lobe tapering mode.

Figure 7.32: Interference analysis Reflector 9.

other reflectors the miss alignments are less than 2 degrees. Similar conditions were measured when illuminating the reflectors with the sub-array J10 shown in Fig. 7.33b. The AAoA were close to the expected angles with a maximum misalignment of around 3 degrees from Reflector 8, and that were also summarized in Table 7.5.

7.3.4 Validation of the Test Zone

As for the case for the elliptical cylinder reflector, the same planar measurement technique was used here for the discrete plane reflectors setup, in order to determine the size of the TZ area. The

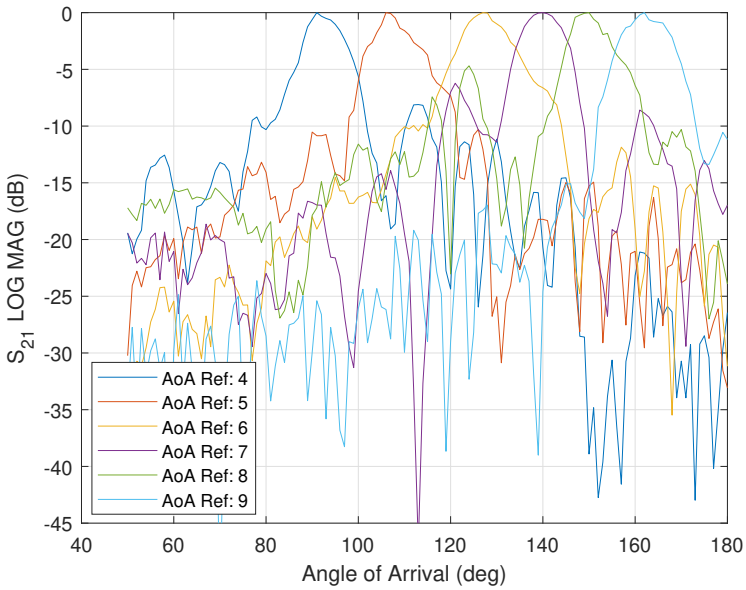

(a) Azimuth angles of arrival with sub-array J7

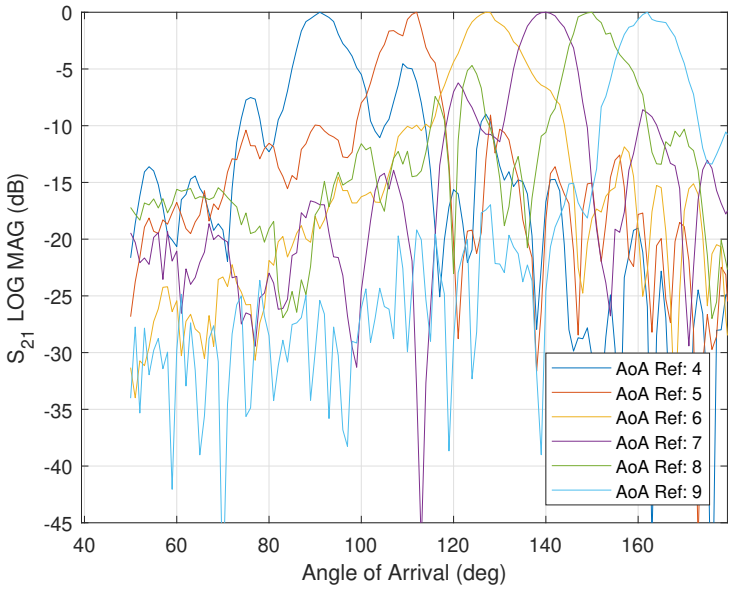

(b) Azimuth angles of arrival with sub-array J10

Figure 7.33: Azimuth angles of arrival measured with reflectors elevated 30 degrees

measurement setup shown in Fig. 7.24 for these tests was improved enlarging the travel distance of the linear actuators, thus the dimensions of the scanning plane surface was approximately of 40 cm height by 40 cm length. The scattered signals coming from each individual plane reflector were sensed by the horn antenna. The sampled points were stored in a matrix of M x N elements, where M = N = 40, which gives a total of 1600 sampling points per reflector. The sampling points

Table 7.5: Summary of AoD and AoA in azimuth and elevation

Reflector Number	**Theoretical AAoD (deg)**	**Theoretical AAoA (deg)**	**Theoretical EAoD (deg)**	**Theoretical EAoA (deg)**	**Measured AAoA J7 - J10**
1	5.3	15.3	2.7	7.6	N/A
2	16.1	44.4	8.0	20.4	N/A
3	27.5	70.3	13.4	28.0	N/A
4	39.8	92.2	18.7	30.0	91 - 92
5	53.5	110.7	23.8	27.9	106 - 112
6	69.3	126.5	27.9	23.8	127 - 127
7	87.8	140.2	30.0	18.8	140 - 138
8	109.7	152.5	28.1	13.4	150 - 149
9	135.6	163.8	20.6	8.0	162 - 165
10	164.7	174.7	7.6	2.7	N/A

were captured at equidistant points. The distance between samples was $d = \lambda$, where λ is the wavelength of the tested frequency. As the test frequency was 26 GHz, then the distance was $d = 1.15$ cm. Fig. 7.12 illustrates the sampling points distribution. The centre of the coordinate x' and z' was located at the focal point.

The horizontal linear actuator was rotated to the corresponding angle of arrival such that aperture of the receiving horn antenna would be facing directly towards the centre of the reflector under test. Thus, the scattered signals from the reflector where captured inside the scanning plane. The beam of the Anokiwave phased antenna array was electronically steered towards the centre of the reflectors according to the corresponding angle of departure. This procedure was used to measure the TZ from the reflectors located in the azimuth plane.

Reference measurement: Transmitter and Receiver in line of sight

In order to have a reference frame to compare the results of the reflected signals, planar measurements of the antenna array in LOS at distance of 4 m between the transmitter (Anokiwave antenna array) and the receiver (horn antenna) were carried out. The uniform transmission mode was used throughout the tests. Figure. 7.34a shows the distribution of the fields inside the scanning area. The magnitudes of the fields were normalized to the maximum value and expressed in logarithmic scale within the scanning plane. It can be seen that the amplitude power range was about 3.8 dB, the mean was -1.27 dB and the standard deviation was about 0.58 dB. The phase distribution expressed in degrees is shown in Fig. 7.34b.

The amplitude parameters of the test zone extracted from the horizontal axis cut through are shown in Fig. 7.35a. It can be seen that the amplitude taper was less than 1.5 dB, the amplitude ripple was in the range of ±0.5dB and the phase ripple was in the order of ±55 deg, shown in Fig. 7.36a. On the other hand, the results of the vertical axis cut through are shown in Fig. 7.35b.

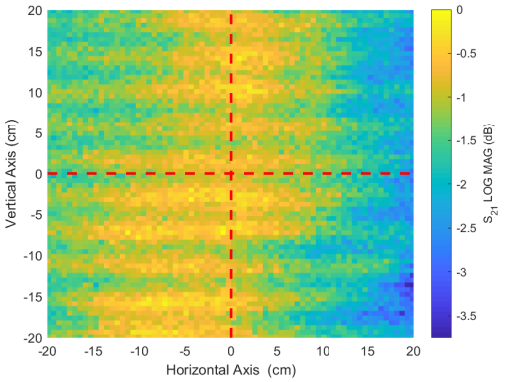

(a) Distribution of the signal inside scanning plane with uniform transmission mode in LOS

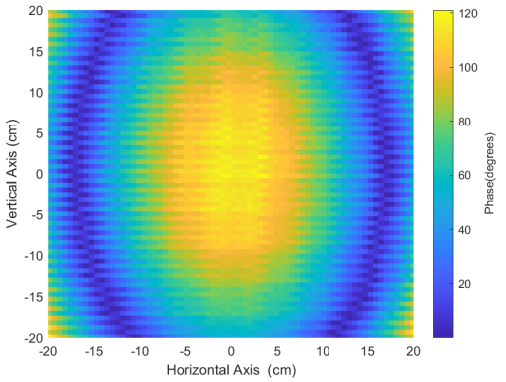

(b) Distribution of the phases inside scanning plane with uniform transmission mode in LOS.

Figure 7.34: Distribution of the signal inside the scanning plane (40 cm x 40 cm) transmitted directly from the feeder antenna set in uniform transmission mode

The amplitude taper was less than 0.2 dB, the amplitude ripple was in the range of ±0.5dB and the phase ripple was in the order of ±40 deg, shown in Fig. 7.36b. These results show that at a distance of 4 m between the transmitter and receiver the test zone would be in a quasi far field region as the amplitude distribution in the horizontal axis is only 0.5 dB above the specs described in subsection 3.7.6, which means that is uniformly distributed. However, the phase difference between the centre of the scanning area and the edge are greater than 22.5 degrees (as described in subsection 3.2), and the phase ripple showed a much larger variation than the specs which would be expected to have a phase ripple of ±5 degrees.

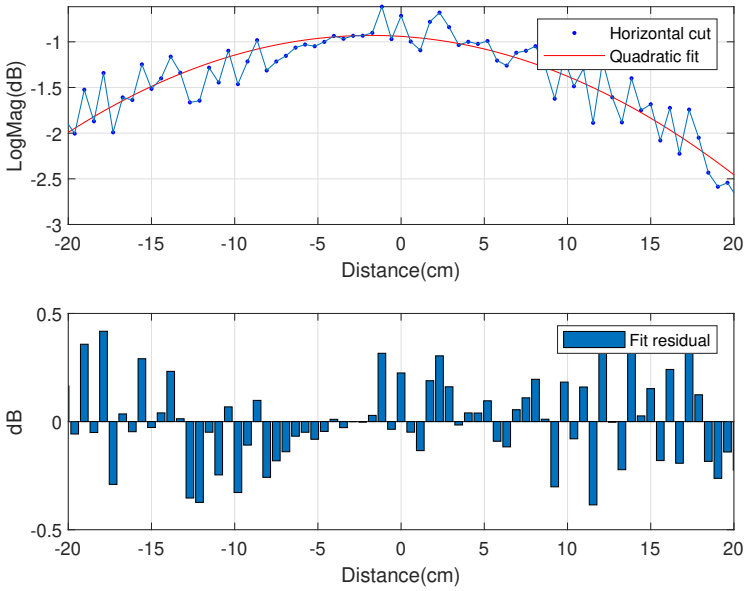

(a) Specification of amplitude taper and ripple of the TZ along the horizontal axis

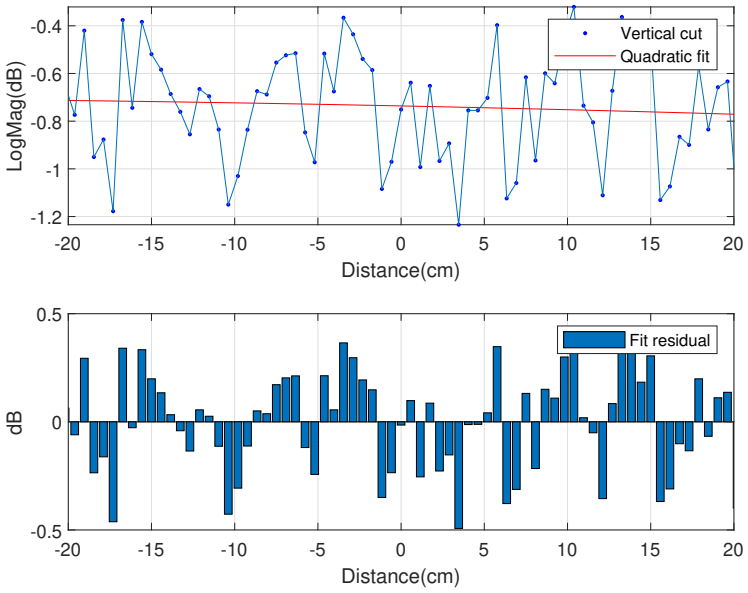

(b) Specification of amplitude taper and ripple of the TZ along the vertical axis

Figure 7.35: Specification of TZ of the LOS signal in terms of amplitude taper and amplitude ripple.

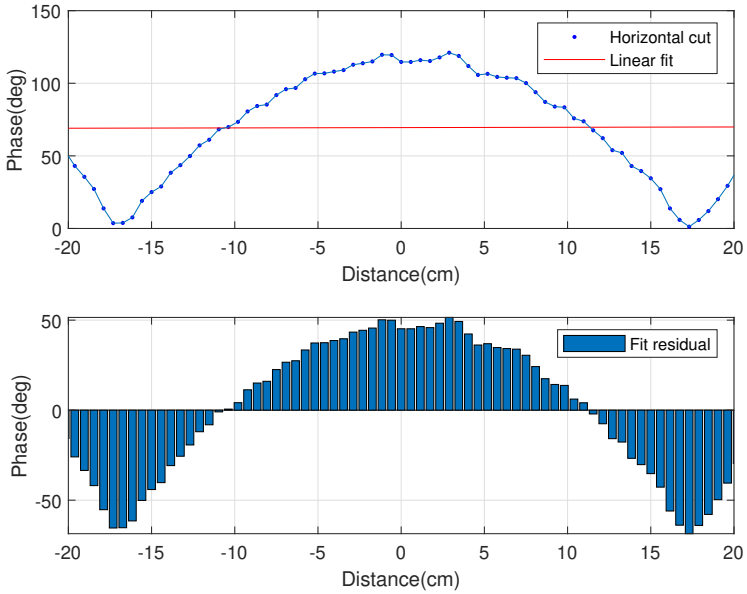

(a) Specification of phase ripple of the TZ along the horizontal axis

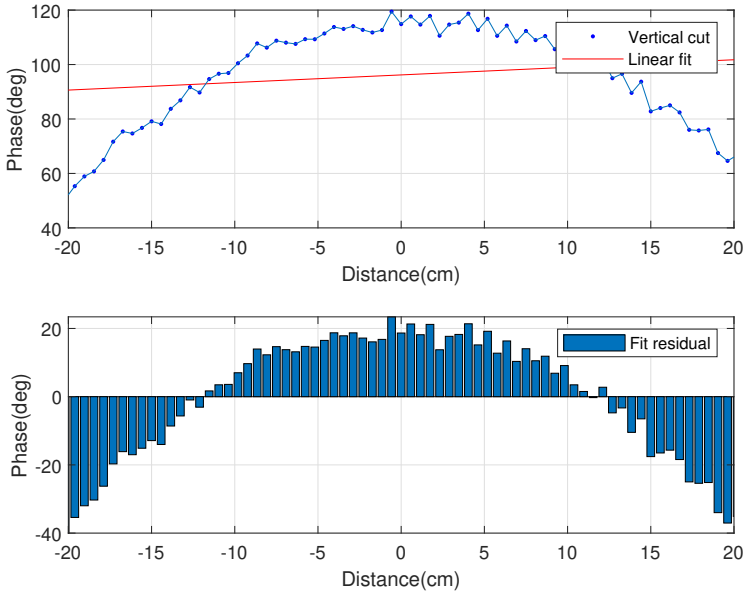

(b) Specification of phase ripple of the TZ along the vertical axis

Figure 7.36: Specification of the phase ripple of the LOS signal

Analysis of distribution of fields inside the scanning area from the reflectors

For the analysis of the TZ generated by each reflector two sub-arrays J7 and J10 were used from the Anokiwave phased antenna array to illuminate each reflector, in order to compare if due to their location (physical phase centre of the sub-arrays) being away from the focal point could potentially affected the characteristics of the TZ area, as was explained in subsection 6.4.3. However, to facilitate the analysis of the test zone only the result from sub-array 7 will be shown here and the results from sub-array J10 are shown in appendix B.

Figures 7.37 and 7.38 show the distribution of the fields captured from each reflector as well as the phase distributions from sub-array J7. Each sub figure shows a red dashed square which represents the targeted size of the test zone of 20 cm by 20 cm. The figures 7.37a, 7.37c, 7.37e, 7.37g, 7.38a, 7.38c, and 7.38e show that the desired test zone areas are not precisely located at the centre of the horizontal and vertical axis of the scanning plane as was the case of the simulations (see chapter 6). Reflectors 3, 8 and 9 show the largest displacements of the TZ in the horizontal axis, being these 10 cm, 10 cm and 5 cm respectively. The displacements of the TZs were produce due to a deviation of the frame that held the reflectors. For all the reflectors it is also possible to see that the strongest signals are not located at the centre of the TZ as would be the case if a parabolic reflector was used. Similar distributions were observed in the simulations showed in chapter 6. Further when compared to the ideal case of the LOS signal shown in Fig. 7.34a, it can be seen that the range of the magnitude levels measured in the scanning area are much larger after the signal is reflected. For the ideal case the range was about 3.5 dB whereas here the levels varied up to 20 dB inside the scanning plane. However, through the calculation of the cumulative distribution function it was found that 80% of the levels of the scattered signals from all the reflector only varied up to 8 dB. The lower levels basically correspond to sampled points at the boundaries of the scanning plane. Further, Figures 7.37b,7.37b,7.37d,7.37f,7.37h,7.38b,7.38d, and 7.38f show the distribution of the phases from each reflector, where it can be observed the progression depending on the angle of arrival which indicate that the signals are arriving in an oblique angle compared with the ideal case shown in Fig. 7.34b

Interestingly, it is also possible to see that in the vertical axis the measured levels are highly constant for all the reflectors, whereas in the horizontal axis there are greater fluctuations. Hence, although the objective was to achieve a TZ of only 20 x 20 cm with these results it can be observed that in the vertical axis the TZ is at least twice the size of what was expected.

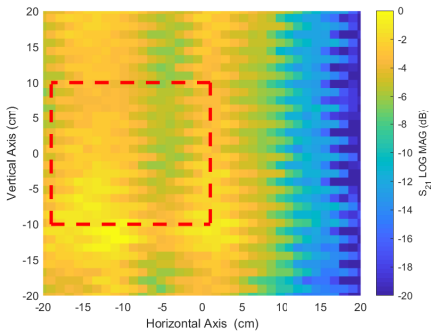

(a) Reflector 3 magnitude distribution

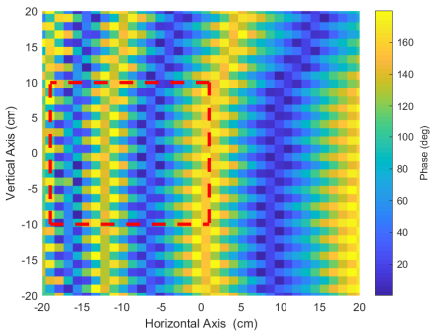

(b) Reflector 3 phase distribution

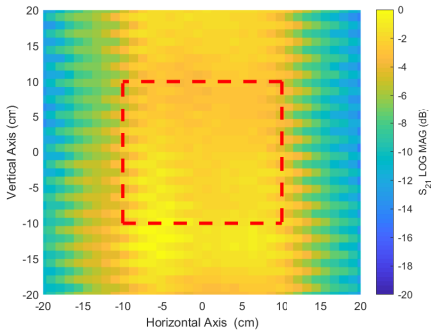

(c) Reflector 4 magnitude distribution

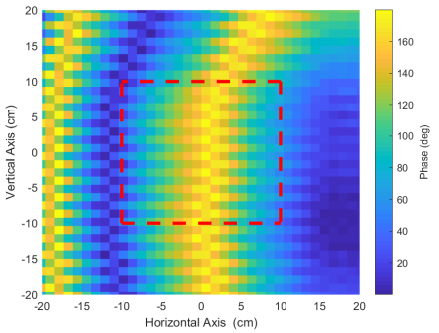

(d) Reflector 4 phase distribution

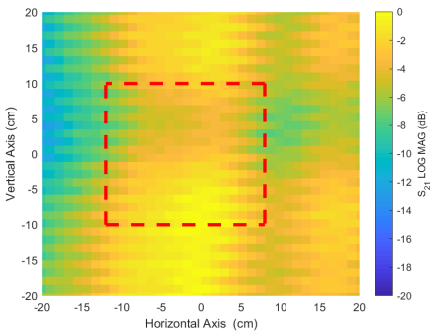

(e) Reflector 5 magnitude distribution

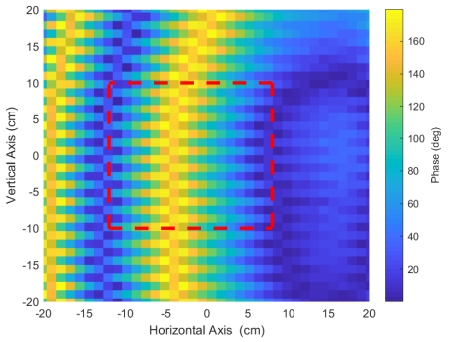

(f) Reflector 5 phase distribution

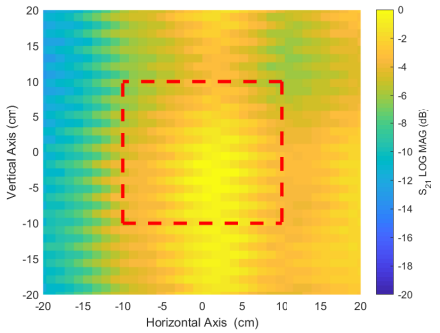

(g) Reflector 6 magnitude distribution

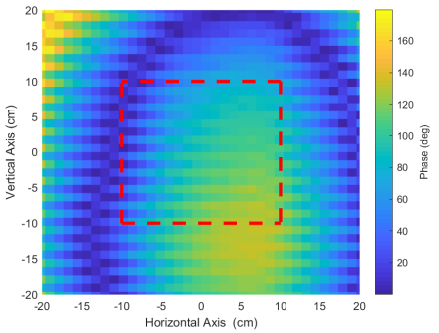

(h) Reflector 6 phase distribution

Figure 7.37: Distribution of fields inside the scanning plane when the reflectors were illuminated by sub-array J7

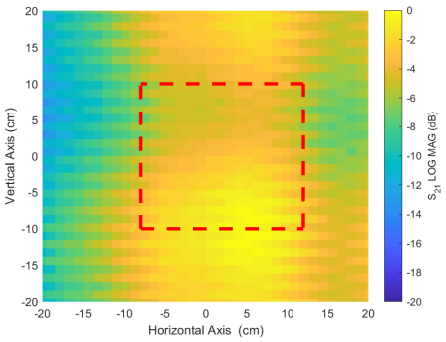

(a) Reflector 7 magnitude distribution

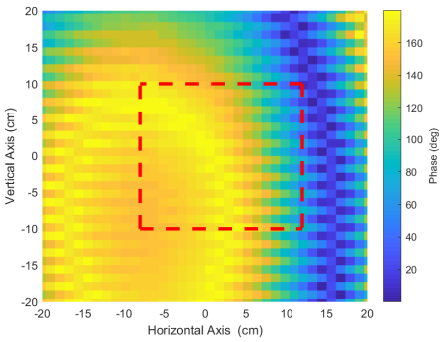

(b) Reflector 7 phase distribution

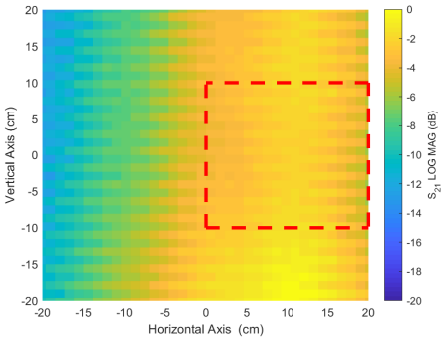

(c) Reflector 8 magnitude distribution

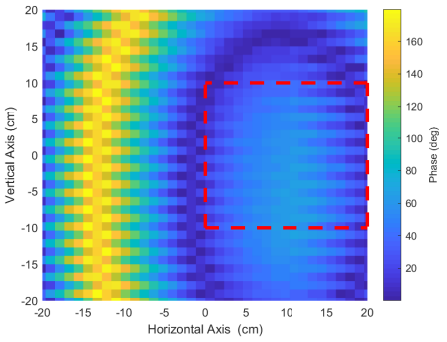

(d) Reflector 8 phase distribution

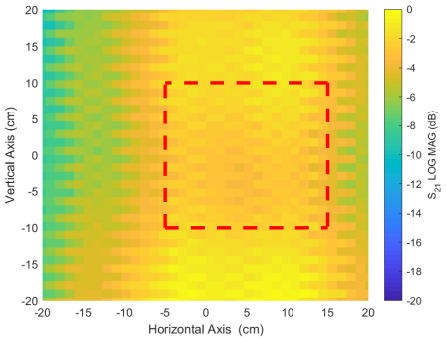

(e) Reflector 9 magnitude distribution

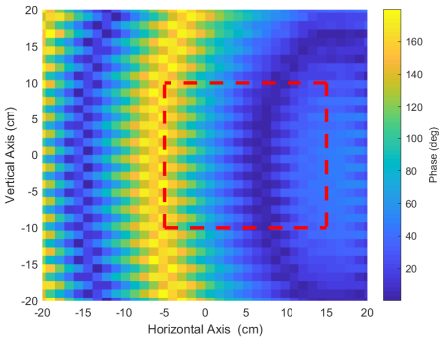

(f) Reflector 9 phase distribution

Figure 7.38: Distribution of fields inside the scanning plane when the reflectors were illuminated by sub-array J7

Analysis of parameters inside the test zone from the reflectors

As mentioned above, in order to determine the characteristics of the test zone attained from each reflector, parameters such as: the amplitude taper, amplitude ripple and phase ripple were calculated and are summarized in Table. 7.6. The parameters were evaluated also by a cut through of the horizontal and vertical axis of each TZ. The procedure adopted to compute these parameters was similar to the one described above for the LOS signal and in subsection 3.7.6. Remind that the parameters of the TZ from the LOS signal obtained were: amplitude taper less than 1.5 dB, amplitude ripple less than ±0.5 dB and phase ripple less than ±55 degrees. It is important to note that the results shown in Table. 7.6 only correspond to the data inside the desired test zone (inside the red dashed squares inside Fig. 7.37, and Fig. 7.38) not over the whole scanning plane.

The results from the horizontal axis cut showed that Reflector 4 produced the largest amplitude tapper of 5 dB when illuminated by sub-array J7; however, reflectors 5, 6, and 7 also show high amplitude tappers above 4 dB when illuminated by sub-arrays J7. Reflectors 3, 8, and 9 are the ones that approximate the most to the ideal case shown by the reference measurement in subsection 7.3.4 as they differ by maximum 1 dB. Interestingly, these 3 reflectors are located closer to the focal points were the transmitter and receiver antennas were placed. It is also possible to observe that amplitude taper levels of reflectors 4 and 6 differ when they were illuminated from sub-arrays J7 and J10, by 3 dB and 1.8 dB respectively. The reflector 9 being the closes to the receiving antenna showed the smallest amplitude taper falling within the desired range below 1 dB. With respect to the amplitude ripple, that only reflectors 4 and 5 are within the desired range of ±0.5 dB, all the other reflectors show a higher ripple being the worst case reflector 9.

The reflectors 3 and 5 exhibit a phase ripple similar to the reference signal about ±55 degrees. The largest difference in phase ripple depending on the sub-array illuminating the same reflector is seen from reflectors 4 and 7 which were approximately 28 degrees and 41 degrees respectively. For all the other cases the difference was below 3 degrees between sub-arrays.

Above it was observed that the distribution of the fields inside the whole scanning plane along the direction of the vertical axis appeared to be more uniform than the horizontal direction. This is corroborated in Table. 7.6, by the distribution of the amplitude taper in the vertical axis of the majority of the reflectors. Apart from the case of reflector 5 the amplitude taper of all the reflector is less than 4 dB. However, on average the amplitude taper in the horizontal and vertical axis are very similar 2.9 dB and 2.7 dB respectively. Also, on average the amplitude ripple in the vertical axis is below ±0.9 dB, being reflectors 5, 6 and 8 all illuminated by sub-array J10 that are outside of this range. Interestingly, the phase ripple in the vertical axis of all reflectors are below ±33.1 degrees.

The interested reader can look at all the graphs from where the information above was extracted in appendix B.

Reflector / sub-array	Horizontal Axis			Vertical Axis		
	Ampl. Taper (dB)	**Ampl. Ripple (dB)**	**Phase Ripple (deg)**	**Amp. Taper (dB)**	**Ampl. Ripple (dB)**	**Phase Ripple (deg)**
Ref 3 - J7	2.0	±1.0	±54.5	1.9	±0.6	±18.0
Ref 3 - J10	2.0	±0.9	±51.5	1.5	±0.5	±16.6
Ref 4 - J7	5.0	±0.5	±37.8	0.9	±0.2	±14.3
Ref 4 - J10	1.9	±0.5	±65.6	2.9	±0.6	±13.1
Ref 5 - J7	4.3	±0.5	±54.4	4.8	±0.9	±14.1
Ref 5 - J10	4.7	±0.5	±50.6	5.0	±1.1	±17.4
Ref 6 - J7	4.3	±0.9	±27.1	3.6	±0.8	±09.1
Ref 6- J10	2.5	±2.1	±27.0	1.8	±1.9	±09.1
Ref 7 - J7	4.7	±0.7	±91.6	4.0	±1.2	±19.7
Ref 7 - J10	4.6	±1.2	±50.6	0.8	±0.5	±12.4
Ref 8 - J7	2.3	±1.2	±74.3	2.3	±0.5	±17.0
Ref 8 - J10	1.0	±1.7	±74.0	2.9	±1.5	±17.0
Ref 9 - J7	0.2	±2.8	±92.0	3.0	±0.7	±33.1
Ref 9 - J10	0.4	±2.7	±92.0	2.3	±0.6	±33.1

Table 7.6: Summary of specifications of test zone measured from each reflector placed in the azimuth plane

7.4 Conclusions

In this chapter a description of the implementation and characterisation of the novel mmWave OTA test methods prototypes based on ECR and DPR was given. In order to characterise both systems mainly two setups were used, one to perform angular measurements and the second one to perform planar measurement. The former was used to validate the concept of the systems being capable to generate different angles of arrival in azimuth and elevation planes, and the latter used to determine the quality and size of the TZ.

The results of the angular measurements clearly shown that both the ECR and DPR test systems can conveniently generate multiple signals with different AoA in both azimuth and elevation planes using these simple architectures. The measured angles of arrival of the DPR method when the reflectors where placed at the azimuth plane matched very closely with the theoretically calculated angles. The largest difference was seen from reflector 7 that differed only by 2.19 degrees. When the reflectors were elevated 30 degrees also minimal differences were found between measured and theoretical angles (see Table. 7.5).

There was good agreement of the simulation and measurements regarding the distribution of the fields in the vertical plane inside the TZ area of the ECR method. The simulations predicted a TZ in the range of 5 to 10 cm in width and 20 cm or above in height, and the measurements (limited to 20 cm in both axis) showed that the magnitude levels (in dB) had a uniform distribution over an area of 2 cm width by 20 cm height, which indicates that the attained width of the signals in practice was smaller than the predicted. This TZ area would not be sufficiently big to test the performance of smartphones in its final form factor or any other larger device. However, potentially this system could be used for testing smaller devices or independent antenna modules implemented in a device. The main advantage of this system is that it can generate continuous angles of arrival if those were required for conformance testing of the devices.

The prototype of the DPR method was evaluated using a state-of-the-art mmWave antenna array technology (from Anokiwave) that acted as the feed antenna, that allowed the emulation of 3D spatially independent signals from a single device avoiding the need for mechanical actuation as the beams were steered electronically. This device is of great importance for this test method as helps to prove the viability of the proposed test method as this kind of devices are already commercially available.

The validation of the test zone was performed through the use of a planar measurement technique. The results were evaluated against an ideal scenario where the feeder antenna and the probe antenna were placed in line of sight and the characteristics of the test zone were extracted by calculating the typical parameters of the test zone (corresponding to a Compact antenna test range method (3.7.6)) which are the amplitude taper, amplitude ripple and phase ripple, and also against the simulation results obtained in chapter 6. The simulation showed that the maximum amplitude tapper was of approximately 2.5 dB and the maximum ripple was of approximately ±3.2 dB, which were the worst-case scenarios. The ideal case in line of sight

showed an amplitude taper of less than 1.5 dB, the amplitude ripple was in the range of ±0.5 dB and the phase ripple was in the order of ±55 deg. The measurements showed that for the worst case the amplitude taper was 5 dB, the amplitude ripple was approximately ±2.8 dB, and the phase ripple was ±92. Evidently, the measurements showed that the distribution of the signals inside the test zone experienced higher variations; however, it is important to notice that during real many factor can influence the results such as:

1. The antennas being offset from the focal points.
2. The reflectors are not perfectly placed at the desired points.
3. Irregularities in the reflector surface.
4. Undesired reflection produced inside the test chamber can degrade the quality of the test zone.

In summary, it was demonstrated both theoretically and experimentally that the ECR and DPR OTA test methods could be potential candidates for testing RRM and demodulation requirements of 5G mmWave mobile devices in dynamic spatial environments and could be proposed to be included as one of the test methods within the Release 16 study item on testability at 3GPP [17] which will consider dynamic spatial environments. The attained test zone size was of 20 cm x 20 cm x 20 cm. The average the amplitude taper inside the test volume was 2.6 dB and the ripple ±1.2, and the worst cases were the amplitude taper was 5 dB, the amplitude ripple was approximately ±2.8 dB, and the phase ripple was ±92.

CHAPTER 8

CONCLUSIONS AND RECOMMENDATIONS

The fifth generation of mobile communications 5G New Radio, will deliver multi-gigabit data rates and low latency communications required to cope with the ever-increasing number of connected devices as well as the demand of data-driven applications and services. Among the envisioned use cases of 5G are: enhanced Mobile Broadband intended to deliver high data rates, massive Machine Type Communications with a focus to connect large number of devices to one base station and Ultra-Reliable and Low Latency Communications where devices rely on very low latency to perform their tasks [84].

5G NR will make use of the newly available spectrum at millimetre wave frequencies and massive MIMO technology in order to support the need for high peak data rates and high network capacity. It has been shown in literature (described in Chapter 2) that the propagation conditions at these frequencies are more challenging compared to sub 6 GHz bands. Some of these engineering challenges are listed below:

1. Millimetre waves suffer from higher path loss e.g. at a distance of 100 m a 38 GHz signal experiences approximately 26 dB more attenuation in free-space than a 2 GHz signal.

2. The spatial propagation environment can be described in terms of a small number of clusters available (up to 6) with narrow angular spread in the order of 3 degrees, which means that the energy is more directional.

3. The line of sight probability decreases exponentially with the distance e.g. at a 100 m there is only 20% probability in Urban Micro scenarios.

4. High signal blockage by human body, trees, streets furniture, etc., for instances it has been measured that the penetration of the signals through the human body experience losses between 20 and 40 dB (see Chapter 2).

All these factors degrade the signal to noise ratio levels at the receiver end; therefore, it is essential to use highly directive active antenna arrays to increase the gain (beam focusing) to compensate for the additional path loss. Further, active antenna arrays allow the implementation of beamforming techniques which are key features to track the signals that are highly dynamic in both spatial and temporal domains in order to maintain reliable connections. Due to the small wavelengths of mmWave frequencies and high losses the level of integration of the active antenna arrays with the radio frequency circuitry will increase significantly. Consequently, testing ports at the mobile devices will no longer exist eliminating the possibility to test the mobile devices with conducted methods. Therefore, the only way to test the performance of the devices will be through OTA testing methods.

Testing 5G NR FR2 user equipment over the air presents new challenges, such as:

1. To achieve spherical coverage the UE requires multiple active antenna array modules, and each one of these must be characterised independently and in bundle.

2. Depending on the position of the antenna modules the antenna pattern will change; therefore, there is no constant antenna pattern anymore.

3. There would be different transmitting and receiving antenna arrays.

4. The phase centre of antenna modules under test are unknown as they will change from device to device and from vendor to vendor; therefore, it becomes a black box testing.

5. Beamforming and beam management must be characterised, in order to evaluate the capability of the devices to acquire and tracking of signals.

6. Besides common antenna parameters, the demodulation performance and radio resource management (RRM) requirements in 3D spatially dynamic narrow beamwidth environments (spatial agility) with multiple angles of arrival simulation will be essential.

Therefore, OTA testing methods are necessary in order to characterise the way the antenna facet with the beamformer and its algorithms are performing. In order to do so, the OTA testing methods must be capable to mimic the behaviour of UEs in 3D real-world situations.

The existing well-known OTA methods such as the Multi Probe Anechoic Chamber, the Reverberation Chamber and the Radiation Two Stage method theoretically could be adapted to work at mmWave frequencies. However, they present some challenges and limitations such as:

1. To adapt the quiet zone of the MPAC method to create the ideal test conditions, the number of probe antennas must be extended depending on the frequency and size of the device under test, for example to have a test zone diameter of 15 cm at 2.4 GHz only 8 probes are needed, whereas, for a 30 GHz test system the number of probes would be approximately of 96 (subsection 3.4.1,[60]).

2. To create 3D spatial scenarios also more rings of antennas are required which not only increase the technical difficulty but exponentially increases the costs of implementation of the system, which could make the system prohibitive for some devices manufactures and test houses.

3. The RC conceptually cannot create directional signals as will be the case of how mmWave frequencies will propagate in real scenarios. One way to achieve narrower signals could be by coating the walls of the chamber with absorbers and leaving other spaces uncovered. However, this configuration is changing the essence of the reverberation environment.

4. The RTS method could be employed to test the beam characteristics of the devices but only for static conditions which would be an important limitation.

5. The Direct far field method would be the ideal method as true far-field signals would illuminate the device under test. However, due to the small wavelengths at mmWave frequencies the so called Fraunhofer distance would be too large (e.g. for a 15 cm DUT the far-field distances at 2.4 GHz is 36 cm, at 30 GHz the distance is 4.5 m and at 60 GHz the distance is 9 m), which means that large test chambers are required which again are costly to implement.

6. The indirect far field method reduces the size of the test chamber but has the same limitations as the RTS method, as this cannot generate multiple dynamic signals.

7. The patented state of the art methods based on elliptical reflectors were mainly intended to extract the radiation characteristics of the devices, however, due to the geometry of the reflectors the test zone area that these methods could realise would not be sufficiently big for 5G NR FR2 devices.

In conclusion, the MPAC method technically would be the most suitable candidate to test 5G NR FR2 devices; however, it demands investing in expensive test equipment and most likely in new and bigger anechoic chambers which could be prohibitive to new and small companies and research institutes that are working around this topic. On the other hand, the other methods mostly could be used to perform only static tests. Consequently, the main contribution of this thesis was to develop a test method that would be able to complement what the other systems were lacking which is recreation of 3D spatially dynamic environments to evaluate the performance of 5G NR FR2 devices together with the active antenna arrays modules. Which directly implies enabling the possibility to test beamforming, beam steering algorithms, beam management, radio resource management, and demodulation parameters. Additionally, addresses the economical side because building the proposed infrastructure with discrete reflectors is not so expensive.

The approach taken by the author of this thesis to address the need to create multiple signals with different angles of arrival was to exploit the reflecting properties of the ellipse since any signal being generated from one focal point would pass through the other focal point.

By using an elliptical shape as a base, also allowed to eliminate the need to have mechanically moving elements in the test system, as opposed to all the other test methods that heavily rely on mechanically rotating positioners. The main limitation of mechanical moving parts is that they cannot be moved as quickly as an electronic based device such as active antenna arrays and this would not allow to realistically emulate the dynamics of a real mmWave frequency channel. Also, calibration and repeatably with mechanical moving elements is a complex task to achieve and maintain.

The greatest limitation of an ellipsoidal reflector (described in chapter 5) is its inherent characteristic to focus all the energy at a single point or small volume, meaning that the test zone would be very small, therefore, it is was not possible to specify a size of the test zone. The test zone was evaluated by capturing the distribution of the total scattered electric field inside a cube volume of 20 cm × 20 cm × 20 cm (Fig 5.20). It was observed that the amplitude of the fields varied significantly inside this volume. The range of fluctuation was of about 60 dB inside the test zone (Fig. 5.21). The largest amplitude level of the reflected signal was focus around the focal point (Fig. 5.19 and Fig. 5.21). Although, the fluctuation of the amplitude level of the E-fields were very large it was possible to distinguish that the illuminating signals had different angles of arrival at the test zone (Fig. 5.18 and Fig. 5.19).

The evolution of this test method was to use three elliptical cylinder reflectors (section 5.5) placed at different elevations. The advantage of this method over the ellipsoid reflector was that the reflected signal spreads in one plane, distributing the amplitude levels of the scattered fields more uniformly in one plane. However, the drawback was that in the orthogonal plane the signal still converged at the focal point. The simulations showed that the E-field levels were more uniformly distributed in the X-Y plane for about 10 cm (Fig. 5.36 and 5.40). In the vertical plane it reached the desired 20 cm with a ripple of ±1dB (Fig 5.36 and 5.38). The overall fluctuation within the test zone volume improved, as they reduced to a range of 30 dB. On the other hand, it was possible to see that the scattered signals illuminated the test zone from different angles of arrival in both azimuth and elevation planes (Fig. 5.35, Fig. 5.37 and Fig. 5.39).

As a final step in the development of the proposed over the air test method a set of discrete plane reflectors distributed following a part-ellipsoid shape (Chapter 6). Such a structure facilitated a controllable expansion of the test zone from what initially was a “pin-point” like test zone generated by the ellipsoid reflector, or the “extended strip” like produced by the elliptical cylinder reflectors to an appropriately sized test zone area commensurate with the practical size of the active RF components within 5G millimetre wave terminals and access point technology. According to the simulations in subsection 6.4.2 overall amplitude ripple of the E-field inside the test zone in the worst case was approximately ±3.2dB and the amplitude taper was approximately 2.5dB, which are a huge improvement compared with previous methods and this was independently of the angle of arrival in azimuth and elevation (Fig. 6.13 and Fig. 6.15).

The simulation results of the sensitivity analysis of the discrete plane reflector test method

6.4.3 showed that the amplitude tapper and ripple of the electric fields inside the test zone volume did not change largely when compared with the ideal case when the feeder antenna is placed at the focal point (Fig. 6.17 and 6.18)

The characterisation of the prototypes consisted mainly in measuring the ability of the test methods to create different angles of arrival and measuring the amplitude taper and ripple of the scattered fields at the test zone. For the case of the ECR (section 7.2.4) it was possible to observe that indeed it is possible to differentiate signals arriving from different angles (Fig. 7.10 and 7.11). However, with this method it was not possible to accurately reconstruct the beam pattern of the horn antenna that emulated the DUT (Fig. 7.10 and 7.11). The amplitude ripple of the ECR was evaluated with a planar measurement methodology and as was expected from the simulations a narrow beamwidth in the centre of the test zone was seen in the azimuth plane and on the vertical plane the signals spread more uniformly (Fig. 7.15 and Fig. 7.16).

Contrary to the ECR with the DPR it was possible to reconstruct the beam pattern more accurately, especially the main lobe of the test horn antenna. Additionally, with this it was also easier to determine the angle of arrival of the signals (Fig. 7.26). The maximum angular error of the angle of arrival was of approximately 1.7 degrees for the reflector 5 placed in the azimuth plane. In the reflectors evaluate elevated 30 degrees larger error were observed (Table 7.5). This can be attributed to the fact that the supporting structure of the reflectors was not rigid enough and tended to flex in the middle, which caused the reflectors to be slightly off from their ideal position. The effects that adjacent reflectors caused to the overall desired signal was evaluated. It was possible to observe undesired signals in the form of high-level side lobes (Fig. 7.30 and 7.31).

Lastly, the planar measurements were performed for the reflectors placed on the azimuth plane. It was observed a larger amplitude taper compared to simulation results of Chapter 6 as the measured amplitude taper in the worst case was 2.5 dB higher than the simulations. The amplitude ripple for the worst case was similar to the simulations, the difference was smaller than $\pm$1dB. The differences in the distribution of the fields inside the test zone measured compared to the simulated can be attributed to multiple factors, such as:

1. Undesired reflections from the anechoic chamber
2. Undesired reflections from the supporting structure
3. Diffraction from the sharp edges of the reflectors
4. Undesired reflections from test equipment placed inside the test chamber
5. Misalignment of the feeder and probe antennas
6. Inaccuracies of the linear actuators
7. Misalignment of reflectors due to methodology used to construct the supporting structure.

8. Irregularities on the surface of the reflector

To conclude, one can argue that although the proposed test methods are conceptually simple approaches, the discrete plane reflectors architecture is novel and feasible way to overcome the some challenges for testing the performance of 5G NR FR2 mobile devices that require to control the beam pattern of their multiple active antenna arrays in a 3D spatially dynamic environment. The Test Zone size achieved was of the 20 cm by 20 cm by 20 cm, realized from plane reflector of 30 cm by 30 cm and a base elliptical shape with a semi-major axis of 205 cm and a semi-minor axis of 180 cm.

8.1 Final Remarks and Future Work

The previous generations of wireless technologies use over-the-air measurements for a small subset of tests and measurement performance assessments. For the new millimetre wave applications and devices such as the 5G NR FR2, virtually all measurements need to be performed over the air. This creates a need for different approaches to the traditional time and cost-intensive measurement approaches for a new market, with significant volume of device types and applications.

The proposed test method is a low cost and low complexity solution capable to generate multiple independent signals from a single source device using a multi-port active antenna array. Other test methods require a large number of probe antennas to replicate this characteristic plus all the expensive hardware needed to implement and control these probes (e.g. Base line measurement setup specified in technical report 3GPP TR 38.810 described in Chapter 3)

The discrete plane reflector test method is expected to be of considerable interest to device vendors (RF chipsets & steerable antenna arrays), handset and CPE vendors, base station/radio head vendors and wireless network operators as expensive field trials can be avoided for link and tracking performance optimisation. Additionally, this has relevance to mobile wireless modem designers, those who make mobile devices from smartphones to connected vehicles, those to make the mobile wireless infrastructure.

The system has an additional potential to measure reflectivity of various materials as well as characterise the impact of materials upon beamforming functionality and link performance. Different kinds of test scenarios and greater control of the reflected signals can be created using metamaterials whose reflective properties can be dynamically controlled. This becomes even more important given the move of the industry for much more mainstream use of millimetre wave technology as a mobile wireless access technology.

Depending on the building material and shape given to the discrete reflectors different test scenarios can be created going beyond the common test capabilities of existing OTA test methods.

At the end of this research project, there are still some open questions that need to be investigated and addressed in order to improve the quality of the test zone, some of them are listed below:

- There is a need to determine all the elements that cause undesired reflections inside the test chamber in order to reduce the amplitude ripple inside the test zone. For this it would be required to firstly characterize the anechoic chamber empty. Secondly, it would be required to characterize the chamber with the frame structure that supports the reflectors. Thirdly, characterize the reflections with the complete setup, thus, it would be possible to de-embed the effects of the chamber and fixtures.
- As it was shown in Chapter 7, adjacent reflectors create undesired reflections from certain angles, therefore, it would be convenient to optimize either the shape and/or the size of the reflectors. Moreover, it could be beneficial to design and manufacture active surfaces base on metamaterials that could change their electromagnetic properties in order to have a better control of the test signals. The desirable states of these surfaces could be twofold:
  1. Reflect and absorb
  2. Reflect and transmit
- Conduct further Test zone fidelity and sensitivity analysis, determine manufacturing tolerances of the holding frame and installation accuracy after the reflectors are optimized.
- As this is a completely new approach to evaluate the performance of 5G devices compared to the other well-known testing method, it would be important to validate its functionality with real 5G NR FR2 devices together with a base station emulator and a channel emulator.
- Moreover, it would be important to determine what trade-offs can be made when testing the devices in its final form factor in terms of the quality of the test zone.
- Introduction of the concept to the corresponding 3GPP work group that discusses about the OTA test methods, such that the proposed method here can be taken into consideration.

The analysis, design and characterization of the DPR method prototype analysed above was done at 26 GHz. However, if the reflectors are realized with metallic surface, then the same system could be used at frequencies up to 60 GHz. However, the higher the frequency the larger the path loss of the signals would be; thus, to make use of this method for higher frequencies it would be required to reduce the overall size of base ellipse, such that the total path length that the signal has to travel would be shorter. But consequently, other mechanisms to achieve a large enough test zone size would be required, and also take into account and carefully analysed the coupling between the feeder antenna, the DUT and reflectors.

References

[1] International Telecommunications Union, "IMT Vision Framework and overall objectives of the future development of IMT for 2020 and beyond," *Recommendation ITU–R M2083–0*, pp. 14–16, 2015.

[2] T. L. Marzetta, G. Caire, M. Debbah, I. Chih-Lin, and S. K. Mohammed, "Special issue on massive mimo," *Journal of Communications and Networks*, vol. 15, pp. 333–337, Aug 2013.

[3] Z. Pi and F. Khan, "An introduction to millimeter-wave mobile broadband systems," *IEEE Communications Magazine*, vol. 49, pp. 101–107, June 2011.

[4] T. G. Pelham, D. Reyes, M. Beach, E. Mellios, and M. Rumney, "Non-intrusive characterization of 60ghz antenna array, using packet measurements," in *12th European Conference on Antennas and Propagation (EuCAP 2018)*, pp. 1–3, 2018.

[5] 3GPP TS34.114, "User Equipment (UE) / Mobile Station (MS) Over The Air (OTA) antenna performance;Conformance testing," *Technical Specification Group Radio Access Network*, vol. V12.2.0, pp. 1–150, 2016.

[6] Y. Jing, Z. Wen, H. Kong, S. Duffy, and M. Rumney, "Two-stage over the air (ota) test method for mimo device performance evaluation," in *2011 IEEE International Symposium on Antennas and Propagation (APSURSI)*, pp. 71–74, July 2011.

[7] P. Kyösti, W. Fan, and J. Kyrolainen, "Assessing measurement distances for OTA testing of massive MIMO base station at 28 GHZ," *in 2017 11th European Conference on Antennas and Propagation (EUCAP)*, pp. 3679–3683, 2017.

[8] Y. Jing, M. Rumney, H. Kong, and Z. Wen, "Overview of 5g ue ota performance test challenges and methods," in *2018 IEEE MTT-S International Wireless Symposium (IWS)*, pp. 1–4, May 2018.

[9] R. Wang, X. Wu, Y. Yang, S. Zhu, X. Zhao, and Z. Liu, "5g ota testing: Challenges and standardization progress," in *2018 IEEE Asia-Pacific Conference on Antennas and Propagation (APCAP)*, pp. 469–470, Aug 2018.

[10] CTIA V3.7, “Test plan for wireless device over-the-air performance,” 2017.

[11] 3GPP TS37.977, “Universal Terrestrial Radio Access (UTRA) and Evolved Universal Terrestrial Radio Access (E–UTRA); Verification of radiated multi-antenna reception performance of User Equipment (UE),” *Technical Specification Group Radio Access Network*, vol. V14.5.0, 2017.

[12] T. S. Rappaport, Y. Xing, G. R. MacCartney, A. F. Molisch, E. Mellios, and J. Zhang, “Overview of millimeter wave communications for fifth-generation (5g) wireless networks,Äîwith a focus on propagation models,” *IEEE Transactions on Antennas and Propagation*, vol. 65, pp. 6213–6230, Dec 2017.

[13] M. Gapeyenko, A. Samuylov, M. Gerasimenko, D. Moltchanov, S. Singh, E. Aryafar, S. Yeh, N. Himayat, S. Andreev, and Y. Koucheryavy, “Analysis of human-body blockage in urban millimeter-wave cellular communications,” in *2016 IEEE International Conference on Communications (ICC)*, pp. 1–7, May 2016.

[14] Anokiwave Inc, “28 GHz Active Array Antenna Enables Rapid 5G Prototyping.” `http://microwavejournal.com/articles/28100-ghz-active-array-antenna-enables-rapid-5g-prototyping`, 2017.
[Online; accessed 23-March-2019].

[15] Keysight Technologies, “OTA Test for Millimeter-Wave 5G NR Devices and Systems.” `http://literature.cdn.keysight.com/litweb/pdf/5992-2600EN.pdf`, 2018.
[Online; accessed 23-March-2019].

[16] D. Reyes, M. Beach, E. Mellios, J. Haine, and M. Rumney, “Over-the-air test method for 5g mmwave devices with beamforming capabilities,” in *2018 IEEE Globecom Workshops (GC Wkshps)*, pp. 1–6, Dec 2018.

[17] 3GPP TR38.810, “Technical Specification Group Radio Access Network; Study on test methods for New Radio; (Release 15).”

[18] Anokiwave Inc., “Introduction to all silicon mmwave 5g arrays.” `https://www.anokiwave.com`, 2019.
[Online; accessed 13-August-2020].

[19] D. Reyes, M. Beach, M. Rumney, J. Haine, and E. Mellios, “Novel over-the-air test method for 5g millimetre wave devices, based on elliptical cylinder reflectors,” in *2019 IEEE 90th Vehicular Technology Conference (VTC2019-Fall)*, pp. 1–6, 2019.

[20] 3GPP TS23.002, “Technical specification group services and system aspects;network architecture (release 12),” *3rd Generation Partnership Project*, vol. V12.3.0, 2013.

[21] S. Lien, S. Hung, D. Deng, and Y. J. Wang, "Efficient ultra-reliable and low latency communications and massive machine-type communications in 5g new radio," in *GLOBECOM 2017 - 2017 IEEE Global Communications Conference*, pp. 1–7, Dec 2017.

[22] GSMA Intelligence, "Understanding 5G: Perspectives on future technological advancements in mobile." https://www.gsmaintelligence.com/research/?file=141208-5g.pdf&download, 2014.
[Online; accessed 25-March-2019].

[23] 3GPP TR 38.901, "5g; study on channel model for frequencies from 0.5 to 100 ghz," *Technical Report ETSI*, vol. 15.0.0 Release 15, pp. 1–94, 2016.

[24] Aalto University, Nokia, ATT, NTT DOCOMO, BUPT, New York University,CMCC, Qualcomm,Ericsson, Samsung,Huawei, University of Bristol, INTEL, University of Southern California, KT Corporation, "5G Channel Model for bands up to 100 GHz." http://www.5gworkshops.com/5G%20channel%20model%20for%20bands%20up%20to%20100%20GHz%20-%20Second%20revisioin.pdf, 2016.

[25] I. F. H. Hertz, "Quasi deterministic radio channel generator user manual and documentation." http://quadriga-channel-model.de/wp-content/uploads/2016/09/quadriga_documentation_v1.4.8-571.pdf, 2016.

[26] Katsuyuki Haneda (Aalto), Sinh L. H. Nguyen (Aalto), Aki Karttunen (Aalto), Jan Järveläinen (Aalto), Aliou Bamba (CEA), Raffaele D,ÄôErrico (CEA), Jonas Medbo (EAB), Fabian Undi (HHI), Stephan Jaeckel (HHI), Naveed Iqbal and (HWDU), Jian Luo (HWDU), Marcin Rybakowski (NOKIA), Cheikh Diakhate (Orange), Jean-Marc Conrat (Orange), Alexander Naehring (R&S), Shangbin Wu (SRUK), Angelos Goulianos (UniBris), Evangelos Mellios (UniBris), "Measurement results and final mmmagic channel models." https://bscw.5g-mmmagic.eu/pub/bscw.cgi/d202656/mmMAGIC_D2-2.pdf, 2017.

[27] G. M. S. Sun and T. Rappaport, "A novel millimeter-wave channel simulator and applications for 5g wireless communications," *IEEE International Conference on Communications (ICC)*, 2017.

[28] T. S. R. Mathew K. Samimi, "Characterization of the 28 ghz millimeter-wave dense urban channel for future 5g mobile cellular." http://wireless.engineering.nyu.edu/static-homepage/tech-reports/Characterization-of-the-28-GHz-Millimeter-Wave.pdf, 2014.

[29] Vuokko Nurmela, Aki Karttunen; AnttiRoivainen, Leszek Raschkowski, Tetsuro Ima, Jan Järveläinen, Jonas Medbo,Jaakko Vihriälä,Juha Meinilä, Katsuyuki Haneda,Veikko Hovinen, Juha Ylitalo, Nobutaka Omaki,Katsutoshi Kusume,Pekka Kyösti, Tommi

Jämsä,Aki Hekkala, Richard Weiler,Michael Peter, "Metis channel models d1.4." https://www.metis2020.com/wp-content/uploads/METIS_D1.4_v3.pdf, 2015.

[30] R. J. Weiler, M. Peter, W. Keusgen, A. Maltsev, I. Karls, A. Pudeyev, I. Bolotin, I. Siaud, and A.-M. Ulmer-Moll, "Quasi-deterministic millimeter-wave channel models in miweba," *EURASIP Journal on Wireless Communications and Networking*, vol. 2016, no. 1, p. 84, 2016.

[31] S. Sun, T. S. Rappaport, T. A. Thomas, A. Ghosh, H. C. Nguyen, I. Z. Kovacs, I. Rodriguez, O. Koymen, and A. Partyka, "Investigation of prediction accuracy, sensitivity, and parameter stability of large-scale propagation path loss models for 5g wireless communications," *IEEE Transactions on Vehicular Technology*, vol. 65, pp. 2843–2860, May 2016.

[32] T. S. Rappaport, S. Sun, and M. Shafi, "Investigation and comparison of 3gpp and nyusim channel models for 5g wireless communications," in *2017 IEEE 86th Vehicular Technology Conference (VTC-Fall)*, pp. 1–5, 2017.

[33] S. Deng, G. R. MacCartney, and T. S. Rappaport, "Indoor and outdoor 5g diffraction measurements and models at 10, 20, and 26 ghz," in *2016 IEEE Global Communications Conference (GLOBECOM)*, pp. 1–7, Dec 2016.

[34] S. Sun, T. S. Rappaport, M. Shafi, P. Tang, J. Zhang, and P. J. Smith, "Propagation models and performance evaluation for 5g millimeter-wave bands," *IEEE Transactions on Vehicular Technology*, vol. 67, pp. 8422–8439, Sep. 2018.

[35] T. S. Rappaport, S. Sun, and M. Shafi, "Investigation and comparison of 3gpp and nyusim channel models for 5g wireless communications," 2017.

[36] M. K. Samimi and T. S. Rappaport, "3-d millimeter-wave statistical channel model for 5g wireless system design," *IEEE Transactions on Microwave Theory and Techniques*, vol. 64, pp. 2207–2225, July 2016.

[37] M.Samimi and T. Rappaport, "Local multipath model parameters for generating 5g millimeter-wave 3gpp-like channel impulse response," in *2016 10th European Conference on Antennas and Propagation (EuCAP)*, pp. 1–5, April 2016.

[38] 3GPP TR25.914, "Measurements of Radio Performances for UMTS Terminals in Speech Mode."

[39] S. Rajagopal, S. Abu-Surra, and M. Malmirchegini, "Channel feasibility for outdoor non-line-of-sight mmwave mobile communication," in *2012 IEEE Vehicular Technology Conference (VTC Fall)*, pp. 1–6, Sep. 2012.

[40] T. Wu, T. S. Rappaport, and C. M. Collins, "The human body and millimeter-wave wireless communication systems: Interactions and implications," in *2015 IEEE International Conference on Communications (ICC)*, pp. 2423–2429, June 2015.

[41] K. Zhao, J. Helander, Z. Ying, D. Sjoberg, M. Gustafsson, and S. He, "mmwave phased array in mobile terminal for 5g mobile system with consideration of hand effect," in *2015 IEEE 81st Vehicular Technology Conference (VTC Spring)*, pp. 1–4, May 2015.

[42] International Commission on Non-Ionizing Radiation Protection, "Guidelines for limiting exposure to time-varying electric, magnetic, and electromagnetic fields (up to 300 ghz).," in *health physics 74 (4):494-522*, 1998.

[43] D. Colombi, B. Thors, and C. Tkörnevik, "Implications of emf exposure limits on output power levels for 5g devices above 6 ghz," *IEEE Antennas and Wireless Propagation Letters*, vol. 14, pp. 1247–1249, 2015.

[44] J. Litva and T. Kwokyeung, *Digital beamforming in wireless communications*. Boston: Artech House, 1996.

[45] J. D. Kraus and R. J. Marhefka, *Antennas For All Applications*. McGraw-Hill„ 2003.

[46] M. Kottkamp, A. Pandey, D. Raddino, A. Roessler, and R. Stuhlfauth, *5G New Radio Fundamentals, procedures, testing aspects*. Rohde and Schwarz, 2019.

[47] O. E. Ayach, S. Rajagopal, S. Abu-Surra, Z. Pi, and R. W. Heath, "Spatially sparse precoding in millimeter wave mimo systems," *IEEE Transactions on Wireless Communications*, vol. 13, pp. 1499–1513, March 2014.

[48] F. Sohrabi and W. Yu, "Hybrid digital and analog beamforming design for large-scale antenna arrays," *IEEE Journal of Selected Topics in Signal Processing*, vol. 10, pp. 501–513, April 2016.

[49] 3GPP TR 21.915, "Digital cellular telecommunications system (phase 2+) (gsm);universal mobile telecommunications system (umts);lte; 5g," *Technical Report ETSI*, vol. 15.0.0 Release 15, pp. 1–94, 2019.

[50] M. Webb, D. Gibbins, and M. Beach, "Slot antenna performance and signal quality in a smartphone prototype," *IEEE Antennas and Wireless Propagation Letters*, vol. 9, pp. 1053–1056, 2010.

[51] M. Rumney, *LTE and the Evolution to 4G Wireless: Design and Measurement Challenges*. Wiley Publishing, 2013.

[52] C. Lötbäck, "Extending the frequency range of reverberation chamber to millimeter waves for 5g over-the-air testing," in *2017 11th European Conference on Antennas and Propagation (EUCAP)*, pp. 3012–3016, March 2017.

[53] A. Skärbratt, J. Äsberg, and C. Orlenius, "Over-the-air performance testing of wireless terminals by data throughput measurements in reverberation chamber," in *Proceedings of the 5th European Conference on Antennas and Propagation (EUCAP)*, pp. 615–619, April 2011.

[54] I. Carton Llorente, W. Fan, and G. F. Pedersen, "Mimo ota testing in small multiprobe anechoic chamber setups," *IEEE Antennas and Wireless Propagation Letters*, vol. 15, pp. 1167–1170, 2016.

[55] 3GPP RP-1904160, "Work Flow (WF) on NR MIMO OTA," 2019.

[56] C. A. Balanis, *Antenna theory: analysis and design*. Wiley-Interscience, 2005.

[57] W. Fan, G. F. Pedersen, P. Kyösti, A. Hekkala, T. Jämsä, and M. Gustafsson, "Recent advances on ota testing for 5g antenna systems in multi-probe anechoic chamber setups," in *2017 Sixth Asia-Pacific Conference on Antennas and Propagation (APCAP)*, pp. 1–3, Oct 2017.

[58] M. Rumney, "Testing 5g: Time to throw away the cables," *Microwave Journal*, 2016.

[59] T. Laitinen, P. Kyösti, J. Nuutinen, and P. Vainikainen, "On the number of ota antenna elements for plane-wave synthesis in a mimo-ota test system involving a circular antenna array," in *Proceedings of the Fourth European Conference on Antennas and Propagation*, pp. 1–5, April 2010.

[60] Pekka Kyösti, Tommi Jämsä, Jukka-Pekka Nuutinen, "Channel modelling for multiprobe over-the-air mimo testing," *International Journal of Antennas and Propagation*, vol. 2012, p. 11, 2012.

[61] P. Kyösti, L. Hentilä, W. Fan, J. Lehtomäki, and M. Latva-Aho, "On radiated performance evaluation of massive mimo devices in multiprobe anechoic chamber ota setups," *IEEE Transactions on Antennas and Propagation*, vol. 66, pp. 5485–5497, Oct 2018.

[62] 3GPP TS37.842, "TSG RAN E–UTRA and UTRA; radio frequency (RF) requirement background for Active Antenna System (AAS) base station (BS)," *Technical Specification Group Radio Access Network*, vol. V13.2.0, 2017.

[63] Rohde and Schwarz, "R & S showcases gold standard test solution for radiation measurements on 5G devices," *Microwave Journal*, 2018.

[64] Keysight Technologies, "R5-1708557 applicability of CATR to tx testing, 3GPP TSG-RAN WG4 meeting 84," 2017.

[65] 3GPP TR38.133, "Technical Specification Group Radio Access Network;New Radio(NR); Requirements for support of radio resource management (Release 15)."

[66] W. Fan, P. Kyösti, M. Rumney, X. Chen, and G. F. Pedersen, "Over-the-air radiated testing of millimeter-wave beam-steerable devices in a cost-effective measurement setup," *IEEE Communications Magazine*, vol. 56, pp. 64–71, July 2018.

[67] The Howland Company, "Reflective ellipsoid chamber." `https://patentimages.storage.googleapis.com/30/ff/1e/36d9388ec940a1/US20140327586A1.pdf`, 2014.
US Patent US 2014/0327586 A1.

[68] Intel Corporation., "Millimeter-wave reflector antenna system and methods for communicating using millimeter-wave signals," 2013.
US Patent US8395558 B2.

[69] Rohde and Schwarz, "Over the air test systems and method for testing a device under test." `https://patentscope.wipo.int/search/en/detail.jsf?docId=US242625187&tab=NATIONALBIBLIO`, 2013.
US Patent US20190162780.

[70] 3GPP TS 38.101-2, "5g; nr; user equipment (ue) radio transmission and reception; part 2: Range 2 standalone, release 15," *Technical Specification Group Radio Access Network*, vol. V15.2.0, pp. 1–150, 2018.

[71] C. Parini, S. Gregson, J. McCormick, and D. Rensburg, *Theory and Practice of Modern Antenna Range Measurements*.
IET, 2014.

[72] C. S. Gregson, "Examination of the effect of common catr quiet zone specifications on antenna pattern measurement uncertainties (lapc 2017)," *Loughborough Antennas and Propagation Conference*, 2017.

[73] C. D. McNamara and J. Malherbe, *Introduction to The Uniform Geometrical Theory of Diffraction*.
Artech House Inc, 1990.

[74] R. G. Kouyoumjian, "Asymptotic high-frequency methods," *Proceedings of the IEEE*, vol. 53, no. 8, pp. 864–876, 1965.

[75] W. Strasser and H.-P. Seidel, *Theory and Practice of Geometric Modeling*.
Springer Science & Business Media„ 2012.

[76] T. Möller and B. Trumbore, “Fast, minimum storage ray-triangle intersection,” in *Journal of Graphics Tools*, vol. 2, p. 21,Äì28, 1997.

[77] A. Harish and M. Sachidananda, *Antennas and Wave Propagation*.
Oxford University Press, 2007.

[78] V. Mahajan, *Fundamentals of Geometrical Optics*.
SPIE PRESS, 2014.

[79] H. Chou, L.Kuo, H.Chou, K. Hung, and P. Nepa, “Realistic implementation of ellipsoidal reflector antennas to produce near,Äêfield focused patterns,” *Radio Science*, 2011.

[80] N. Mattiucci, M. Bloemer, N. Aközbek, and G. D‘Aguanno, “Impedance matched thin metamaterials make metals absorbing,” *Scientific Reports*, Nov 2013.

[81] Dau-Chyrh Chang, Chao-Hsiang Liao, and Chih-Chun Wu, “Compact antenna test range without reflector edge treatment and rf anechoic chamber,” *IEEE Antennas and Propagation Magazine*, vol. 46, pp. 27–37, Aug 2004.

[82] A. C. Newell and G. E. Hindman, “Antenna pattern comparison using pattern subtraction and statistical analysis,” *Proceedings of the 5th European Conference on Antennas and Propagation (EUCAP)*, 2011.

[83] D. W. Hess, “Historical background on the use of equivalent stray signal in comparison of antenna patterns,” in *Proceedings of the 5th European Conference on Antennas and Propagation (EUCAP)*, 2011.

[84] 5GPPP 5G Infrastructure Association, “5g vision;the 5g infrastructure public private partnership: the next generation of communication networks and services..” `https://5g-ppp.eu/wp-content/uploads/2015/02/5G-Vision-Brochure-v1.pdf`.
[Accessed: 2020-09-06].

APPENDIX A

Ray Launching algorithm

The ray-tracing algorithm firstly launches primary rays with a certain direction of departure in azimuth and elevation. Secondly, every object of the testing environment is checked to see if it intersects with any of them. If a particular ray does not intersect an object on its way it is discarded. If it does intersect with an object, the direction of reflection is calculated and a secondary ray launched, and the process repeats but this time the intersection with the receiver plane is checked. If it does than the total and partial distances travelled by the rays are calculated, similarly the angles of arrival of each ray. The intersection point is stored and used to calculate the test zone size. An implementation of the algorithm in pseudocode is shown below:

Algorithm 1 Ray Tracing Algorithm

Calculate Antenna Pattern points **A**
Calculate Reflector's Vertices points **Q**
Define Azimuth Angle Departure β in range $[0, \pi]$
Define Elevation Angle Departure γ in range $[0, \pi/2]$
Rotate each A points according to β and γ
for $i = 1$ **to** total number of ray **do**
    Find rays direction $l_{F_1A} = A - F_1$
    Calculate intersection between rays and reflectors with ray to triangle algorithm
    if Ray intersection = True **then**
        Calculate direction of reflection vector **d**
        Store Intersection point W
    else
        Discard ray
    end if
    Calculate Intersection Points of rays with TZ plane
    if Ray intersection = True **then**
        Store Intersection point I
    else
        Discard ray
    end if
    Calculate Distance D_1 from F_1 to W
    Calculate Distance D_2 from W to I
    Calculate Total Ray Length $D_{total} = D_1 + D_2$
    Calculate Azimuth Angle of Arrival AoA
    Calculate Elevation Angle of Arrival AoE
    Calculate Intersection Point P_{Rx}
    Plot ray
end for

Algorithm 2 Feeder Antenna Pattern Positioning

$A = [A_x, A_y, A_z]$ Antenna pattern pts
$dF = \sqrt{a^2 - b^2}^T$
$F_1 = [-dF, 0, 0]^T$ Feeder focal point
β = Define Azimuth Angle Departure in range $[0, \pi]$
γ = Define Elevation Angle Departure in range $[0, \pi/2]$
Rot Calculation of rotation matrix
for $i = 1:1:length(A_x)$ **do**
    for $j = 1:1:length(A_x)$ **do**
        $g = (Rot * [A_x(i,j); A_y(i,j); A_z(i,j)]) + F_1$ Rotation of Ant. pts and translation to F1
        $Ar_x(i,j) = g(1)$ Storing x - components
        $Ar_y(i,j) = g(2)$ Storing y - components
        $Ar_z(i,j) = g(3)$ Storing y - components
    end for
end for

Algorithm 3 Triangle to Ray Intersection Algorithm

Define $\epsilon_r t = 0.000001$
Find vectors for two edges sharing vertex S_1
$\mathbf{Edge}_1 = \mathbf{S}_2 - \mathbf{S}_1$
$\mathbf{Edge}_2 = \mathbf{S}_3 - \mathbf{S}_1$
Calculate determinant also used to calculate U parameter
$\mathbf{VectP} = \mathbf{D} \times \mathbf{Edge}_2$
$\det = \mathbf{Edge}_1 \cdot \mathbf{VectP}$
if ($\det < \epsilon_r t$) **then** If determinant is near zero ray lies in plane of triangle
    Break
end if
Calculate distance from S_1 to ray origin
$\mathbf{VectT}_1 = \mathbf{O} - \mathbf{S}_1$
Calculate U parameter and test bounds
$\mathbf{U} = \mathbf{VectT} \cdot \mathbf{VectP}$
if ($\mathbf{U} < 0.0 || U > det$) **then**
    Break
end if
Calculate V parameter and test bounds
$\mathbf{VectQ} = \mathbf{VectT} \times \mathbf{Edge}_1$
$\mathbf{V} = \mathbf{D} \cdot \mathbf{VectQ}$
if ($\mathbf{V} < 0.0 || U > U + V > det$) **then**
    Break
end if
Calculate t, scale parameters, ray intersects triangle
$\mathbf{T} = \mathbf{Edge}_2 \cdot \mathbf{VectQ}$
$t = T * (1/\det)$
$u = U * (1/\det)$
$v = V * (1/\det)$

APPENDIX B

Analysis of Angles of Arrival generated by the different sub-arrays

Reflector Number 4

As can be seen in Fig. 1a the angles of arrival of the three sub-arrays are 91 degrees which are offset by approximately 1.2 degree below the expected AoA. The HPBW with sub-array J7 was 13 degrees and 14 degrees with sub-arrays J8 and J10. The discrepancies between the sub-array patterns compared with the original signal every angle is shown in Fig. 1b. Here, can be observed that patterns measured using Reflector 4 vary less then when compared to Reflector 3, because the range power levels are within ±2dB for all the angles between 75 and 107 degrees. Within the HPBW range the fluctuation of the three patterns are even lower of about ±0.75dB, which indicates that the antenna patterns measured from the sub-arrays are closer to the original pattern. The largest differences are seen around the first null region and first side lobe.

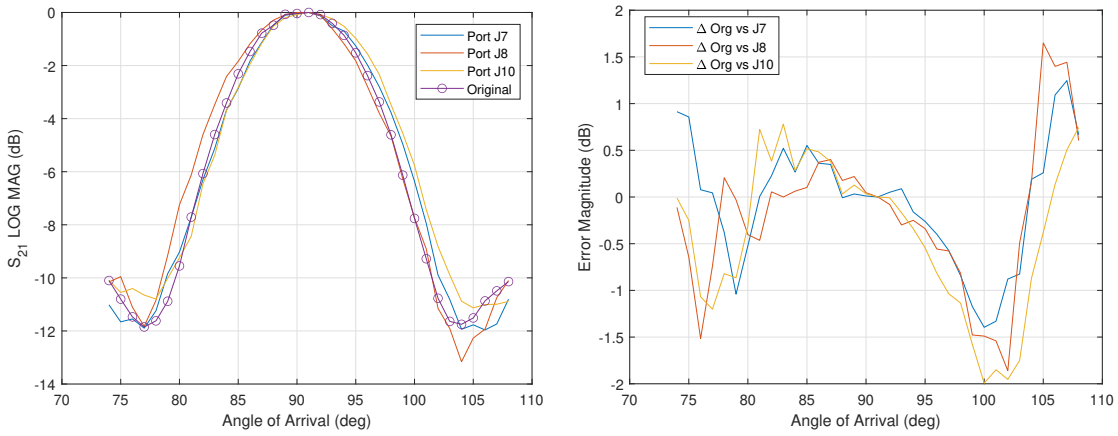

(a) Angles of Arrival from Reflector 4 illuminated from J7, J8 and J10 sub-arrays.

(b) Comparison of J7, J8 and J10 patterns with original by pattern subtraction from Reflector 4.

Figure 1: AoA Reflector 4.

Reflector Number 5

The angles of arrival of the sub-arrays J7, J8 and J10 were 109 degrees which are approximately 1.7 degrees below the expected AoA, which is shown in Fig. 2a. The HPBW of the horn antenna measured from J7 and J8 was 14 degrees and 12 degrees with sub-array J10. The discrepancies between the sub-array patterns compared with the original signal every angle is shown in Fig. 2b. The J10 pattern is the most stable one with variation in the range of 1.3 to -2.1 dB for all evaluated angles. For the three cases the greatest difference is located around 95 degrees and 122 degrees which correspond to the null regions. Within the HPBW range the fluctuation of the three patterns are even lower of about ±1.5dB.

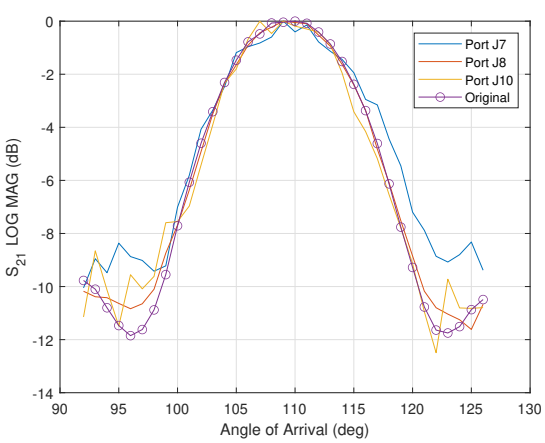

(a) Angles of Arrival from Reflector 5 illuminated from J7, J8 and J10 sub-arrays.

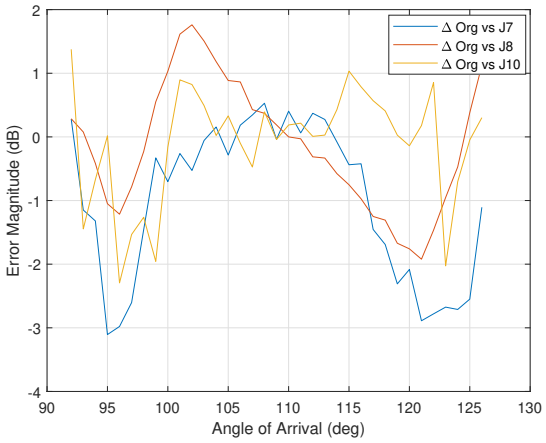

(b) Comparison of J7, J8 and J10 patterns with original by pattern subtraction from Reflector 5.

Figure 2: AoA Reflector 5.

Reflector Number 7

Figure 3a shows the angles of arrival captured from the sub-arrays J7, J8 were 140 degrees which are offset approximately by 2.1 degrees below the expected AoA, whereas with J10 was 138 degrees which the closest to the expected. The HPBWs from all sub-arrays J7 and J8 and J10 were 14 degrees which match with the original pattern. The discrepancies between the sub-array patterns compared with the original signal every angle is shown in Fig. 3b. Within the HPBW angle range the fluctuation of the three patterns are between ±0.3dB, which is the lowest of all the measurements. As the other cases analysed, the greatest difference is around the null region. J8 is the worst case with a difference close to 2dB. Between angles 122 and 152 degrees the discrepancies lay between ±1dB.

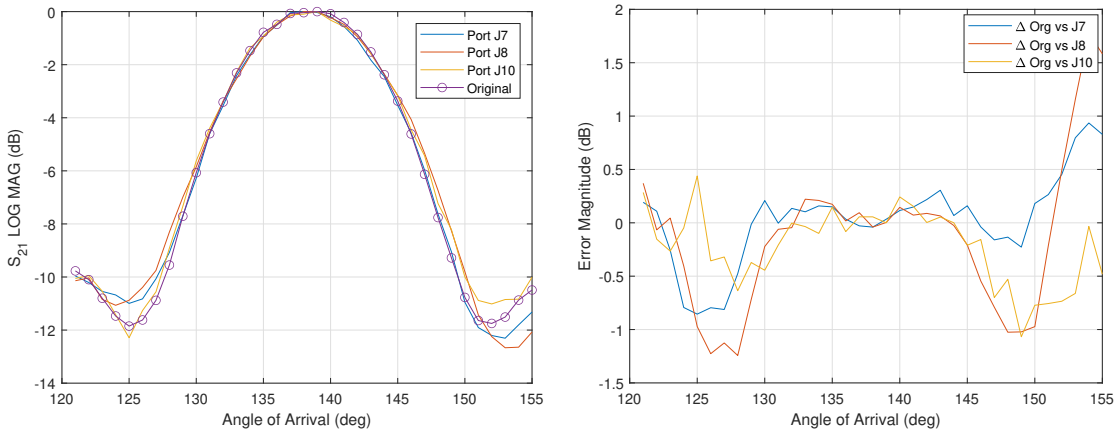

(a) Angles of Arrival from Reflector 7 illuminated from J7, J8 and J10 sub-arrays.

(b) Comparison of J7, J8 and J10 patterns with original by pattern subtraction from Reflector 7.

Figure 3: AoA Reflector 7.

Reflector Number 8

As can be seen in Fig. 4a the angles of arrival from the sub-arrays J7, J8 were 151 degrees which is around 1.4 degrees away from the expected AoA and with J10 the AoA was 152 degrees that is similar to the expected angle. The HPBW of J7 coincided with the original pattern, whereas with J8 and J10 the HPBW was 13 degrees. The discrepancies between the sub-array patterns compared with the original signal every angle is shown in Fig. 4b. It can be observed that within the HPBW angular range the fluctuation of the three patterns are in the range of ±1dB. In the whole range of angles analysed the maximum variations are in the range of ±3dB. As per the other reflectors analysed the greater difference are observed around the null region.

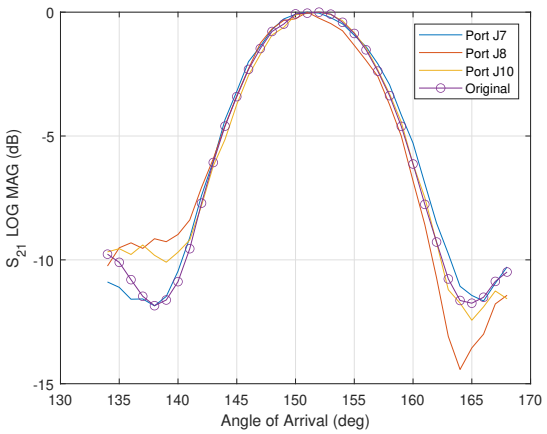

(a) Angles of Arrival from Reflector 8 illuminated from J7, J8 and J10 sub-arrays.

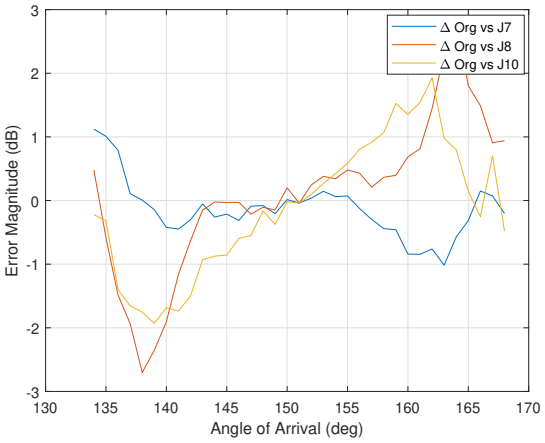

(b) Comparison of J7, J8 and J10 patterns with original by pattern subtraction from Reflector 8.

Figure 4: AoA Reflector 8.

Interference caused by adjacent reflectors

Interference analysis of Reflector Number 4

As specified in Table 7.4 the expected angle of arrival from reflector 4 was 92 degrees. However, in Fig 5a where the original and evaluated radiation patterns are shown for uniform illumination it can be seen that the original pattern in red has only one main lobe pointing towards 90 degrees, and the level of its side lobes are everywhere below -10 dB. Whereas, the evaluated pattern three main lobes. The strongest beam is pointing to 109 degrees, the second strongest is point to 92 degrees, which is the desired angle of arrival, but the power level is 2.5 dB below the first lobe. The third strongest beam is only 3.1 dB dB below the first beam and is pointing to 73 degrees, hence it could be considered that these three strong lobes actually form part of a unique beam with a half power beamwidth of 35 degrees. This is comprehensible if compared to the simulations where it is shown that the transmitted signal should also be reflected from reflectors 3, 4 and 5 although the intended reflector was only reflector 4. The angles of the strongest beams previously described directly coincide with the adjacent reflectors. A similar situation is seen if the FA is set to transmit in low side lobe mode, depicted in Fig 5b. Where three main lobes pointing towards the angles 108, 91 and 71 degrees are seen, which correspond to reflectors 5,4 and 3 respectively. A fourth side lobe is seen in both cases at 144 degrees which is 7 dB below the main lobe that corresponds to a less strong signal coming from reflector 7.

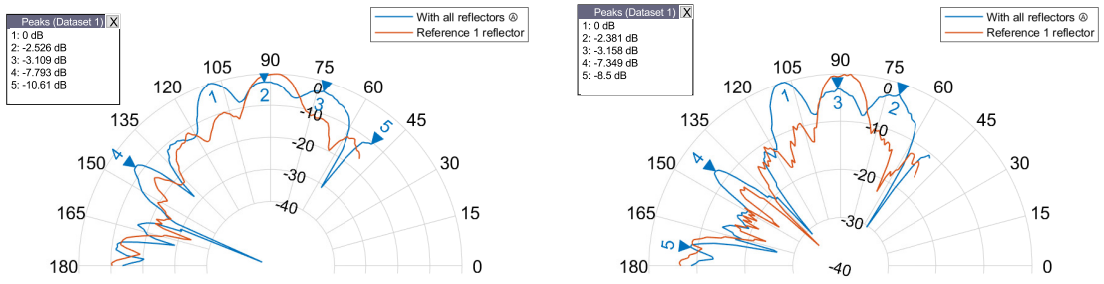

(a) Interference caused by Reflectors 3,5,6,7,8 and 9 when Reflector 4 was the target reflector illuminated with the Uniform mode.

(b) Interference caused by Reflectors 3,5,6,7,8 and 9 when Reflector 4 was the target reflector illuminated with the Side lobe tapering mode.

Figure 5: Interference analysis Reflector 4.

Interference analysis of Reflector Number 6

When reflector 6 is illuminated the expected angle of arrival is 126 degrees and this is precisely the AoA achieved when only the reflector under consideration was used, which is shown in Fig. 6a and in Fig. 6b by the radiation patterns in colour red. Opposite to what was seen with reflectors 3, 4 and 5, with reflector 6 in the evaluated pattern only exists one main lobe which is pointing to 125 degrees, which is very close to the theoretical AoA. On the other hand, the side lobes of the evaluated signal follow a similar trend than the original signal. Overall, all the secondary lobe levels of the evaluated pattern are everywhere below -10dB, as is the case of the original signal for the uniform mode case. With the low side lobes mode illuminating reflector 6 a side lobe at 107 degrees is observed which is 5 dB down from the maximum. Other than this the secondary lobes also remain below -10 dB. No strong interferers are seen in this case which agrees with the simulations previously detailed.

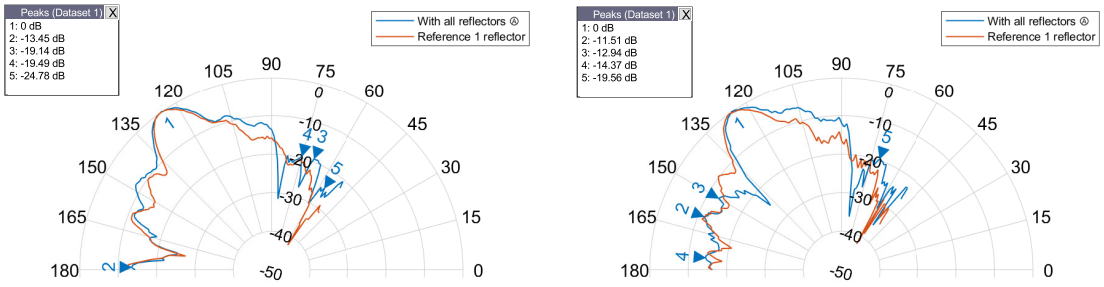

(a) Interference caused by Reflectors 3,4,5,7,8 and 9 when Reflector 6 was the target reflector illuminated with the Uniform mode.

(b) Interference caused by Reflectors 3,4,5,7,8 and 9 when Reflector 6 was the target reflector illuminated with the Side lobe tapering mode.

Figure 6: Interference analysis Reflector 6.

Interference analysis of Reflector Number 7 and 8

The analysis of the reflectors 7 and 8 have been united because they are very similar to each other, because the evaluated radiation patterns are almost identical to the original signals for both transmission modes uniform and low side lobes. Additionally, the main beams pointed exactly to the same angles measured with the original patterns and the secondary side lobes for all cases remain under -10 dB. These characteristics can be observed in figures 7a, 7b, 8a, and 8b. Overall can be said that the adjacent reflector does not affect the signal seen by the DUT.

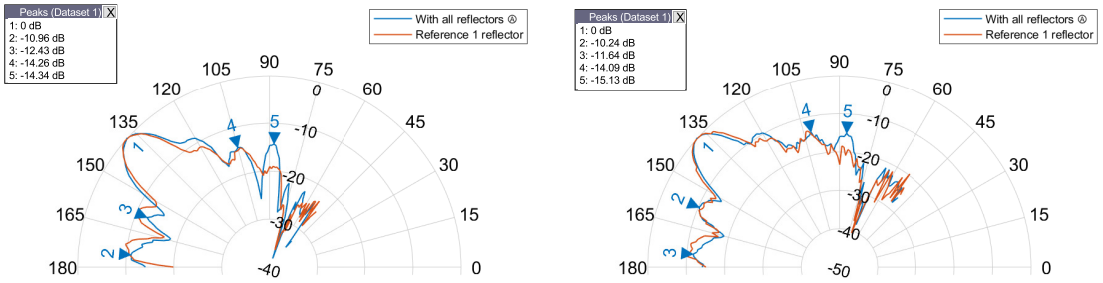

(a) Interference caused by Reflectors 3,4,5,6,8 and 9 when Reflector 7 was the target reflector illuminated with the Uniform mode.

(b) Interference caused by Reflectors 3,4,5,6,8 and 9 when Reflector 7 was the target reflector illuminated with the Side lobe tapering mode.

Figure 7: Interference analysis Reflector 7.

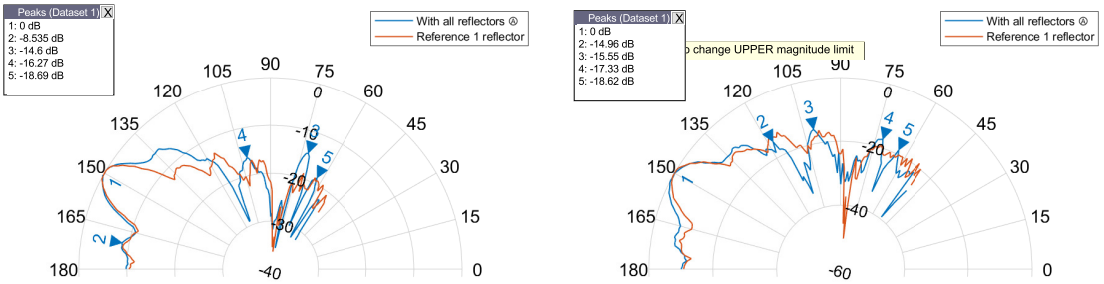

(a) Interference caused by Reflectors 3,4,5,6,7 and 9 when Reflector 8 was the target reflector illuminated with the Uniform mode.

(b) Interference caused by Reflectors 3,4,5,6,7 and 9 when Reflector 8 was the target reflector illuminated with the Side lobe tapering mode.

Figure 8: Interference analysis Reflector 8.

Validation of the Test Zone

Analysis of distribution of fields inside the scanning area from the reflectors

For the analysis of the TZ generated by each reflector two sub-arrays J7 and J10 were used from the Anokiwave phased antenna array to illuminate each reflector, in order to compare if due to their location (physical phase centre of the sub-arrays) being away from the focal point could potentially affected the characteristics of the TZ area, as was explained in subsection 6.4.3. Here the result from sub-array J10 are shown. Figures 9 and 10 show the distribution of the fields captured from each reflector as well as the phase distributions from sub-array J10. Each sub figure shows a red dashed square which represents the targeted size of the test zone of 20 cm by 20 cm. The figures 9a, 9c, 9e, 9g, 10a, 10c, and 10e show that the desired test zone areas are not precisely located at the center of the horizontal and vertical axis of the scanning plane as was the case of the simulations (see chapter 6).

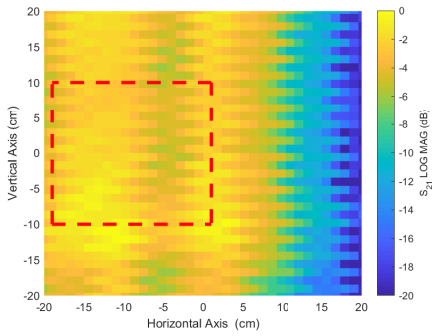

(a) Reflector 3 magnitude distribution

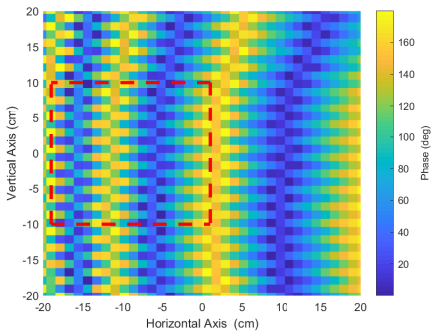

(b) Reflector 3 phase distribution

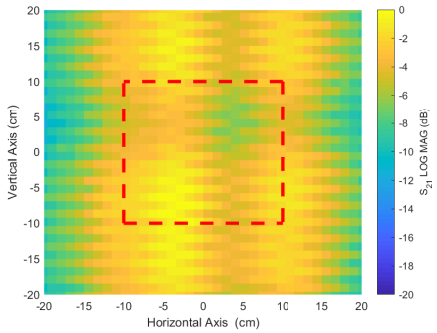

(c) Reflector 4 magnitude distribution

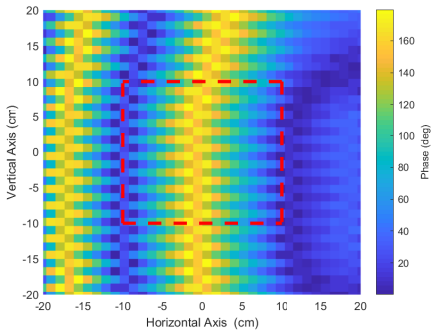

(d) Reflector 4 phase distribution

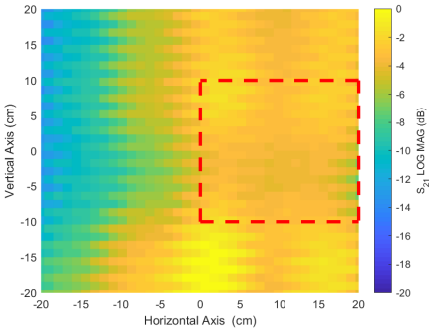

(e) Reflector 5 magnitude distribution

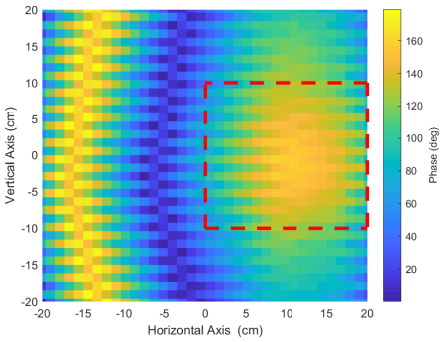

(f) Reflector 5 phase distribution

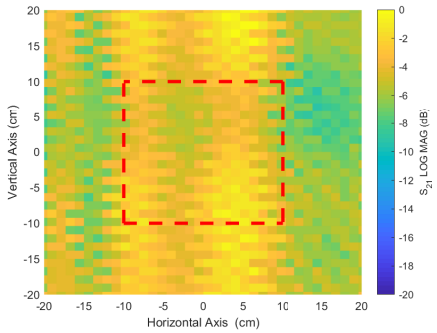

(g) Reflector 6 magnitude distribution

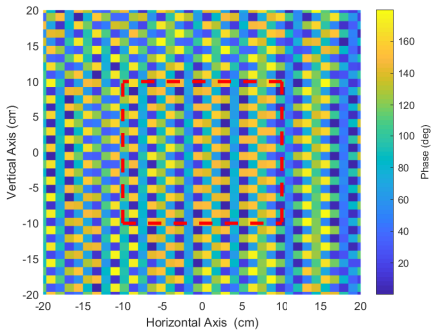

(h) Reflector 6 phase distribution

Figure 9: Distribution of fields inside the scanning plane when the reflectors were illuminated by sub-array J10

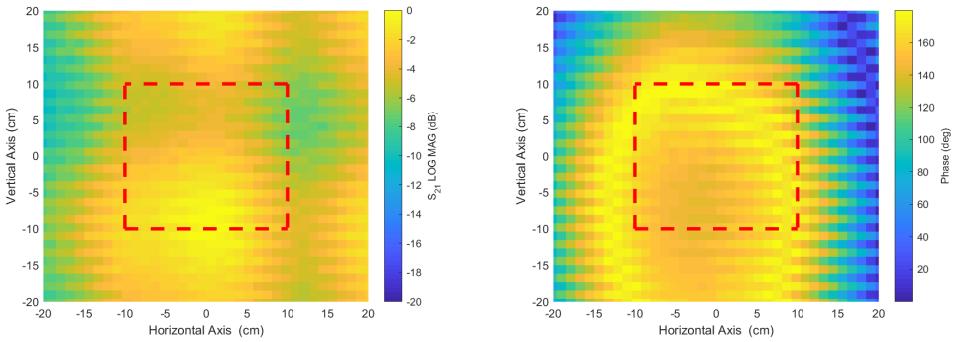

(a) Reflector 7 magnitude distribution

(b) Reflector 7 phase distribution

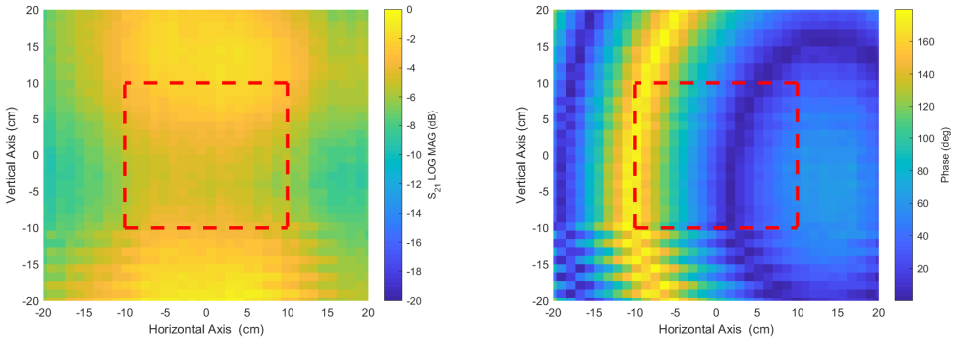

(c) Reflector 8 magnitude distribution

(d) Reflector 8 phase distribution

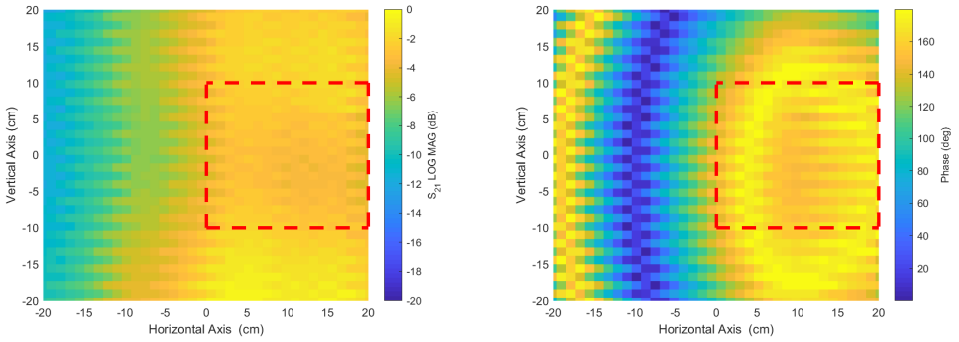

(e) Reflector 9 magnitude distribution

(f) Reflector 9 phase distribution

Figure 10: Distribution of fields inside the scanning plane when the reflectors were illuminated by sub-array J10

Reflector Number 3

The analysis of each reflector was divided in two parts, the first part refers to the raw data of the plane measurements normalized to the highest power. And the second part focus in more detail in the TZ area. Thus, in Fig. 11a the power from each sub-array is depicted. The sub-array J7 is represented by the blue line and the sub-array J10 the orange line. The two signals look very similar, with subtle differences in power, but for the most very similar. The ECDF of these signals shown in Fig. 11b shows that they follow a similar pattern as was expected looking at the raw data plot. The range of J10 was around 28 dB which is approximately 7 dB smaller than J10 which indicates smaller variations of the signal. However, the median power of J7 is approximately -7.6 dB which is only about 0.6 dB smaller than its counterpart.

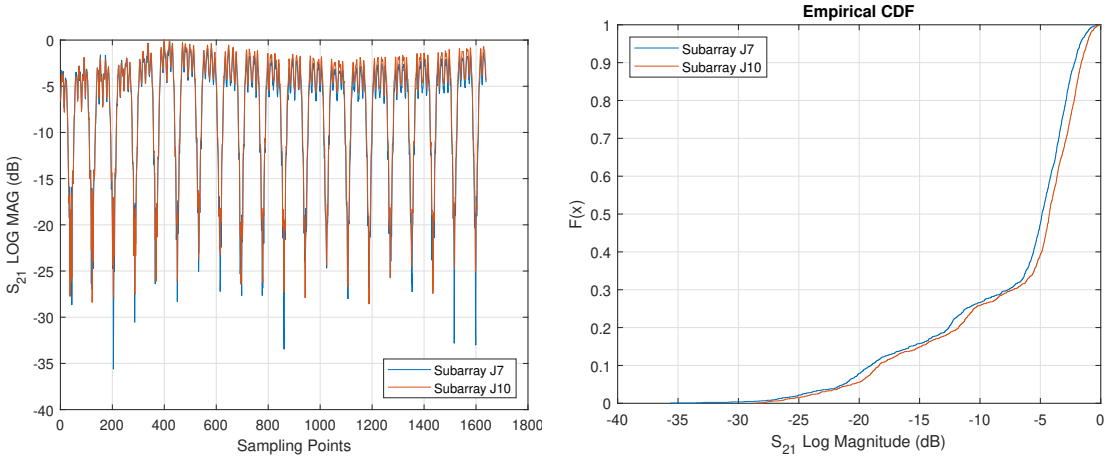

(a) Distribution of the signal in the measured plane.

(b) Distribution of the signal in the measured plane.

Figure 11: Reflector 3 distribution of the power in the plane with the Uniform transmission mode

The distribution of the signals over the scanning plane when illuminated from sub-array J7 is shown in Fig. 12a and from sub-array J10 is shown in Fig. 12b. Visually their distributions looked very similar. Looking deeply into the TZ area Fig. 13 shows in an ECDF plot that the range is of 8 dB. The median powers of the sub-arrays are 3.5 and 2.6 respectively. The standard variations of both are approximately 1.4 dB.

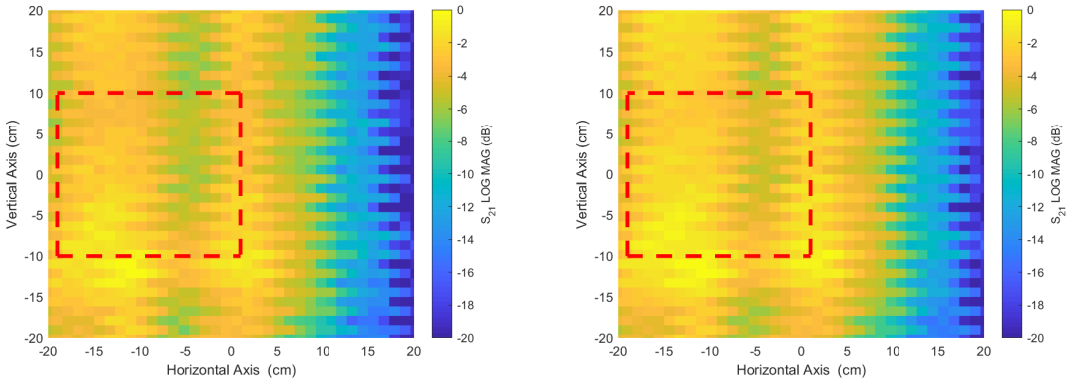

(a) Distribution of the signal in the measured plane J7.

(b) Distribution of the signal in the measured plane J10

Figure 12: Reflector 3 distribution of the power in the plane with the Uniform transmission mode

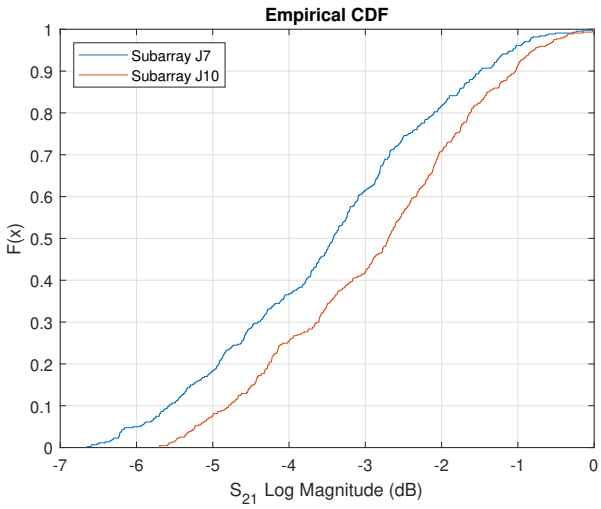

Figure 13: ECDF of the Test Zone from Reflector 3

Reflector Number 4

Figure 14a shows the normalized magnitude (in dB) from sub-arrays J7 and J10. The former is represented by the blue line and the latter is represented by the orange line. In this case the two signals show different trends above the 800 sampling points if compared one two one. The ECDF of these signals shown in Fig. 14b shows with greater detail the differences between the signals that are more notorious below -4 dB. There is approximately a 5 dB difference in the range of the signals, where the sub-array J10 is the smallest with 14 dB. The median power of J7 is approximately -6.2 dB and -5.2 dB for J10. The standard deviation are 4.4 dB and 3.3 dB respectively.

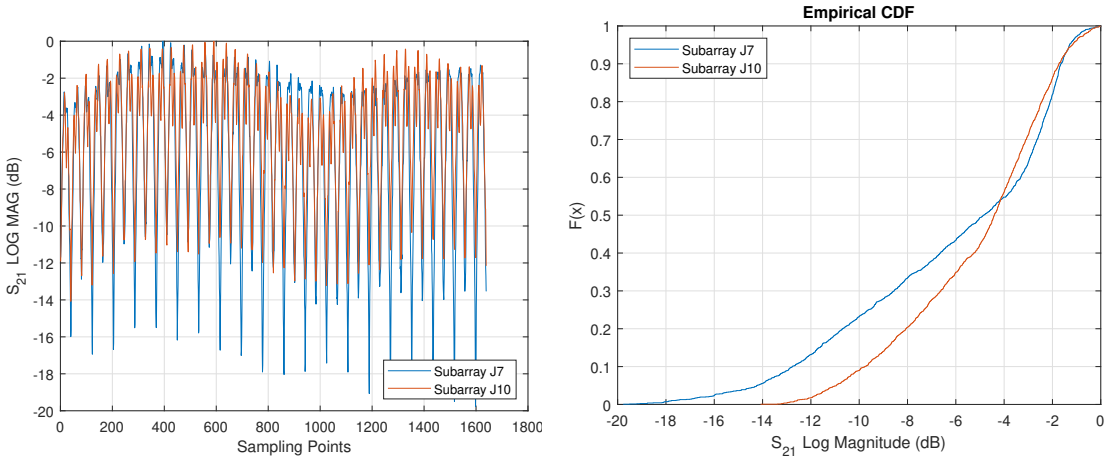

(a) Distribution of the signal in the measured plane.

(b) Distribution of the signal in the measured plane.

Figure 14: Reflector 4 distribution of the power in the plane with the Uniform transmission mode

The distribution of the signals over the scanning plane when illuminated from sub-array J7 is shown in Fig. 15a and from sub-array J10 is shown in Fig. 15b. In the latter it is possible to observe that around the centre of the TZ area (from 0 to 5 in the horizontal axis and from 0 to 10 cm in the vertical axis) there is a greater variation of the signal produced by the sub-array J10, than J7. The ECDF plot of both TZs area shown in Fig. 16 allows to observe that the range is of 8 dB. The median power of both sub-arrays inside the TZ area is approximately 3 dB. As the reflector 3, the standard deviation of both sub-arrays is approximately 1.4 dB.

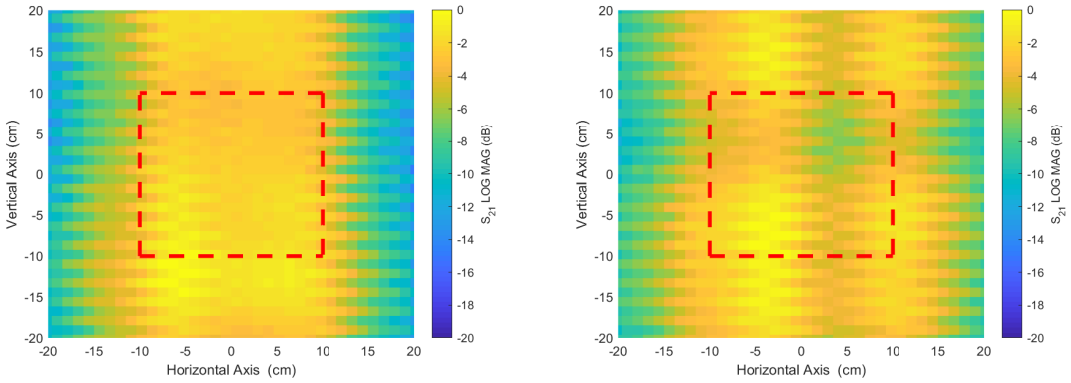

(a) Distribution of the signal in the measured plane J7.

(b) Distribution of the signal in the measured plane J10

Figure 15: Reflector 4 distribution of the power in the plane with the Uniform transmission mode

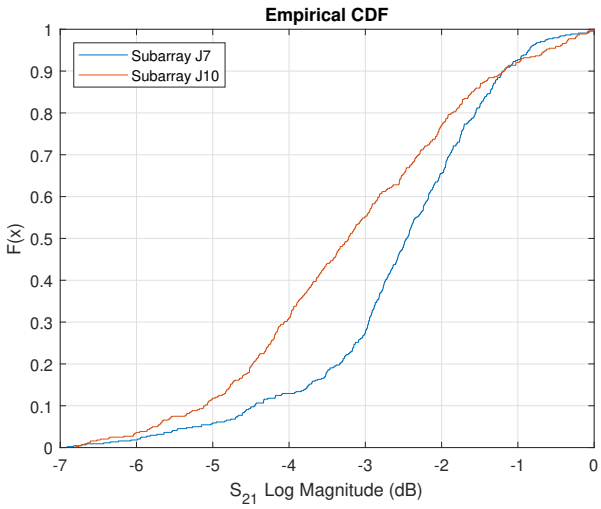

Figure 16: ECDF of the Test Zone from Reflector 4

Reflector Number 5

The normalized magnitude (in dB) from sub-arrays J7 and J10 are shown in Fig 17a, which are represented by the blue and orange lines respectively. The highest point of J7 was captured at sample point 100 and for J10 it is at sample point 224. The ECDF of these signals is shown in Fig. 17b. From 0 to 4 dB the two curves follow a similar trend. At around the -4dB mark the two CDFs cross each other and greater differences in the trend are noticed. The median power of J7 is approximately -4.6 dB and -5.2 dB for J10. The standard deviation are 2.8 dB and 3.3 dB respectively. Contrasting the previous two reflectors the median power has also reduced, especially for the case of J7, which means that the signal presents smaller fluctuations within the whole test area.

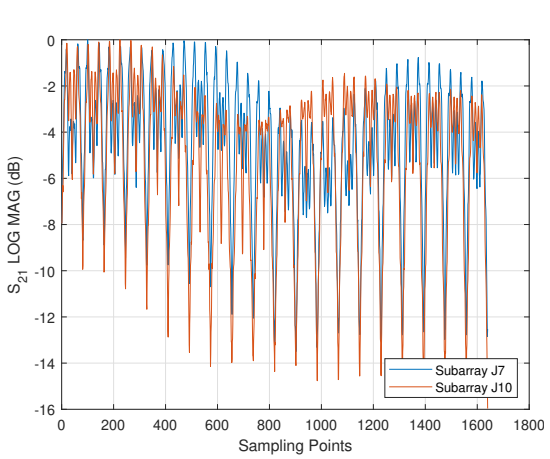

(a) Distribution of the signal in the measured plane.

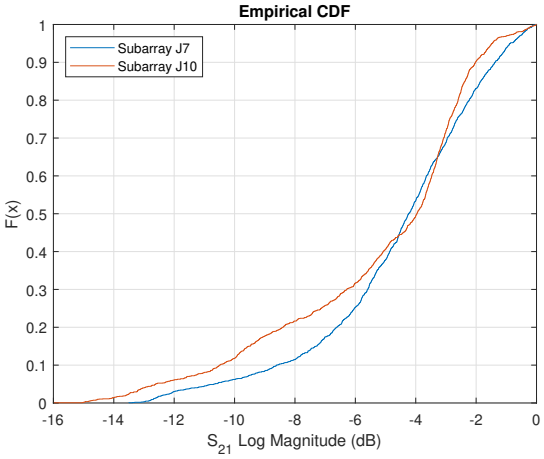

(b) Distribution of the signal in the measured plane.

Figure 17: Reflector 5 distribution of the power in the plane with the Uniform transmission mode

The distribution of the signals over the scanning plane when illuminated from sub-array J7 is shown in Fig. 18a and from sub-array J10 is shown in Fig. 18b. It can be observed that J10 has a more stable received signal in both axes vertical and horizontal within the TZ area. As expected from the sampling points graphs it is possible to observe that around the centre of the TZ area the power dropped a 3 dB. For the case of J10 it can be seen that TZ is not centred around the of the horizontal axis, but it was shifted approximately 10 cm to the right. The ECDF plot of both TZ areas shown in Fig. 19 shows that the magnitude (in dB) range within the TZ area are 8 dB and 10 dB for J7 and J10 respectively. The median powers inside the TZ area are approximately -3.1 dB and -3.8 dB. The standard deviation of both sub-arrays slightly increased compared to reflectors 3 and 4, and for these cases are approximately 1.8 and 2 dB.

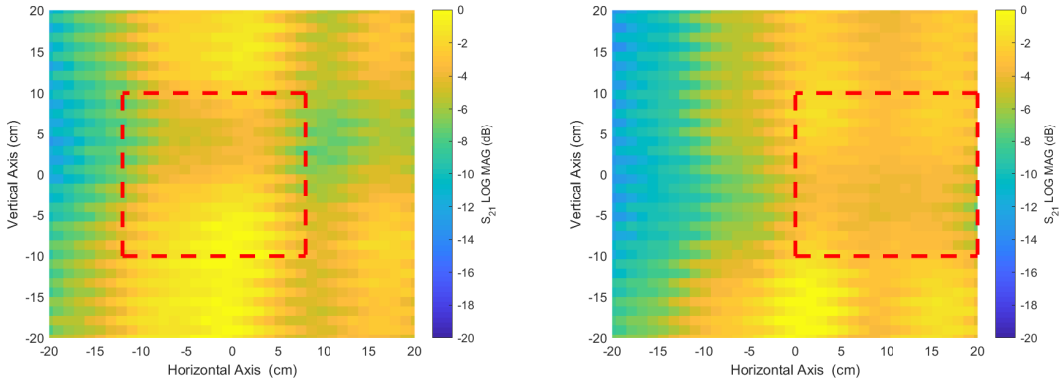

(a) Distribution of the signal in the measured plane J7.

(b) Distribution of the signal in the measured plane J10

Figure 18: Reflector 5 distribution of the power in the plane with the Uniform transmission mode

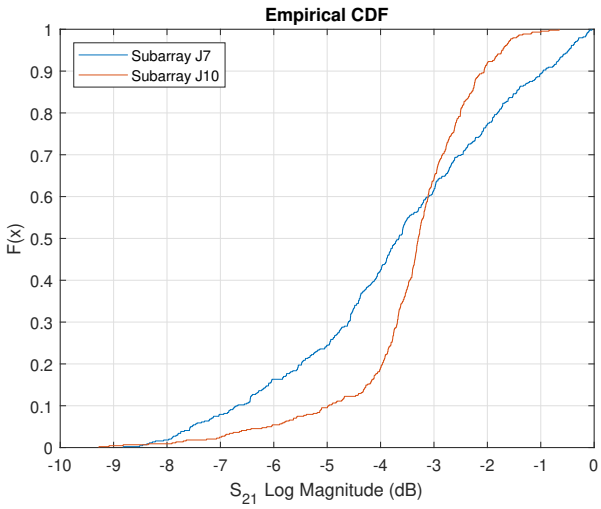

Figure 19: ECDF of the Test Zone from Reflector 5

Reflector Number 6

The normalized received power from sub-arrays J7 and J10 are shown in Fig 20a, which are represented by the blue and orange lines respectively. The highest point of J7 was captured at sample point 677 and for J10 it is at sample point 1451. The ECDF of the signals in Fig. 20b shows that the range of J7 is approximately 15 dB and 10 dB for J10. The two ECDF's follow a relatively similar trend up to -6 dB. The median power of J7 is approximately -4.9 dB and -4.5 dB for J10 measured across the whole plane. The standard deviation are 3.2 dB and 1.9 dB respectively. According to the statistics the signal from J10 presents smaller fluctuations compared to J7.

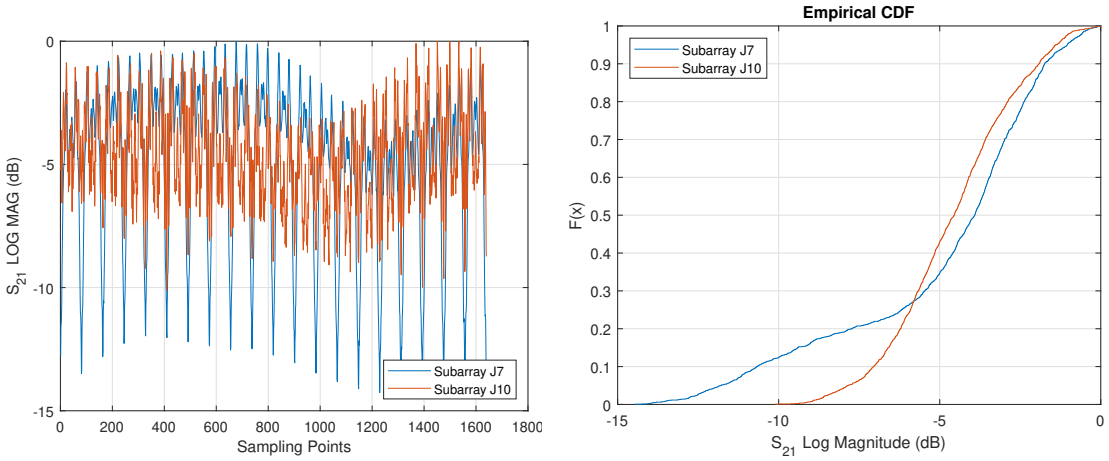

(a) Distribution of the signal in the measured plane.

(b) Distribution of the signal in the measured plane.

Figure 20: Reflector 6 distribution of the power in the plane with the Uniform transmission mode

The distribution of the signals over the scanning plane when illuminated from sub-array J7 is shown in Fig. 21a and from sub-array J10 is shown in Fig. 21b. It can be observed that J10 has a more stable received signal in both axes vertical and horizontal within the TZ area and across the whole area measured, which was also observed by a steeper ECDF in Fig. 20b. For the case of J10 it is possible to observe that around the centre of the TZ area the power dropped a couple of dB's. Whereas the signal from J7 shows greater variations above the 5 cm mark in the vertical axis. Both TZ are centred around the horizontal axis. The ECDF plot of both TZ areas shown in Fig. 22 shows that the magnitude (in dB) range within the TZ area differ only by 1 dB. Additionally, the median powers inside the TZ area for both cases was approximately -3.4 dB. The standard deviation of both sub-arrays is approximately 1.7 dB.

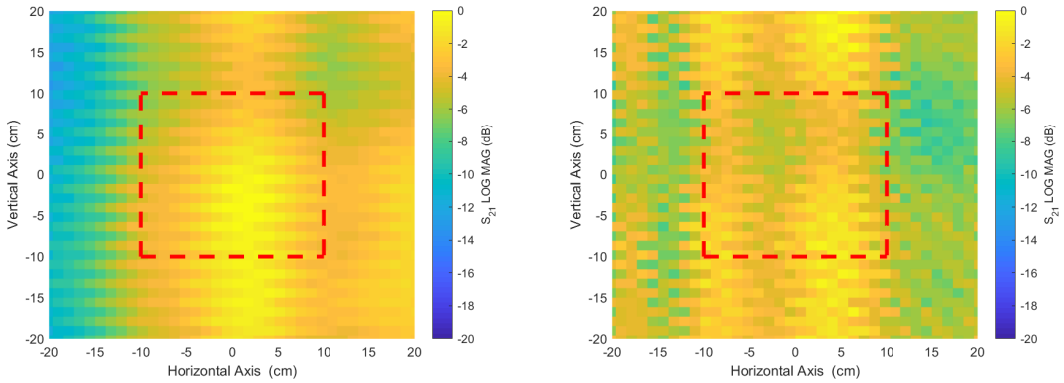

(a) Distribution of the signal in the measured plane J7.

(b) Distribution of the signal in the measured plane J10

Figure 21: Reflector 6 distribution of the power in the plane with the Uniform transmission mode

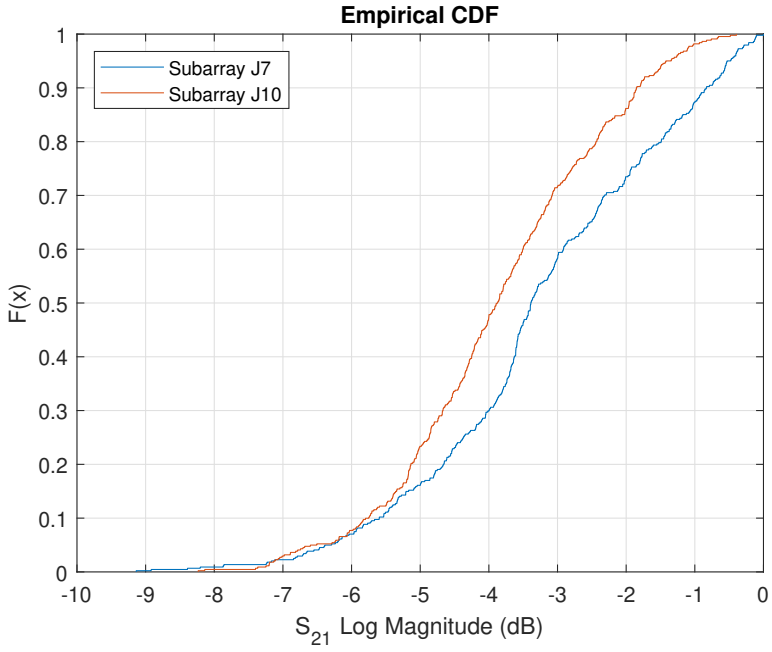

Figure 22: ECDF of the Test Zone from Reflector 6

Reflector Number 7

The normalized magnitude (in dB) from sub-arrays J7 and J10 follow a similar trend along the whole measured plane which is shown in Fig 23a. The blue corresponds to sub-array 7 and the orange lines to sub-array J10. The highest point of J7 was captured at sample point 436 and for J10 at sample point 471. The ECDF of the signals in Fig. 23b shows that the range of J7 is approximately 14.7 dB and 11.6 dB for J10. The two CDF's follow a relatively similar trend. The median power of J7 is approximately -5.1 dB and -4.2 dB for J10 measured across the whole plane. The standard deviation are 3.2 dB and 2.3 dB respectively. According to the statistics the signal from J10 presents smaller fluctuations compared to J7.

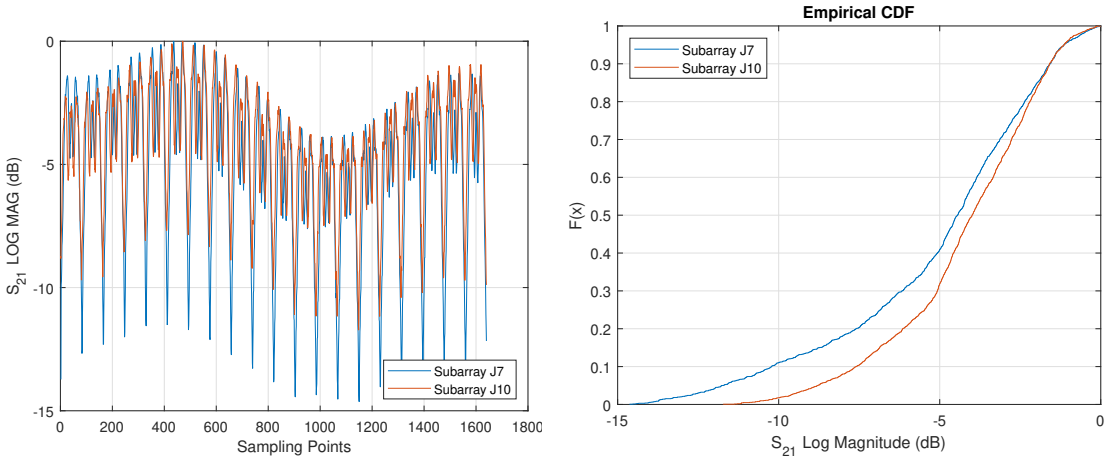

(a) Distribution of the signal in the measured plane.

(b) Distribution of the signal in the measured plane.

Figure 23: Reflector 7 distribution of the power in the plane with the Uniform transmission mode

The distribution of the signals over the scanning plane when illuminated from sub-array J7 is shown in Fig. 24a and from sub-array J10 is shown in Fig. 24b. It can be observed that J10 has a more stable received signal in both axes vertical and horizontal within the TZ area and across the whole area measured, which was also observed by a steeper CDF in Fig. 23b. For the case of J7 it is seen that the area where the signal has greater power and is more stable has shifted about 3 cm to the right, and the opposite happened to J10 that the signal shifted to the left, thus the TZ are not perfectly aligned at the centre of the 0 mark of the horizontal axis. It is possible to observe that around the centre of the TZ area the power dropped 7 dB. Similar to the other reflectors there is a shape like a waist above the 2 cm mark in the vertical axis, where the power is reduced in both cases. The ECDF chart of both TZ areas illustrated in Fig. 25 shows that the magnitude (in dB) range within the TZ area differ only by 1 dB. Additionally, the median powers inside the TZ area for J7 and J10 was approximately -3.4 dB and -3.2 dB respectively. The standard deviations of were approximately 2.3 and 1.5 dB.

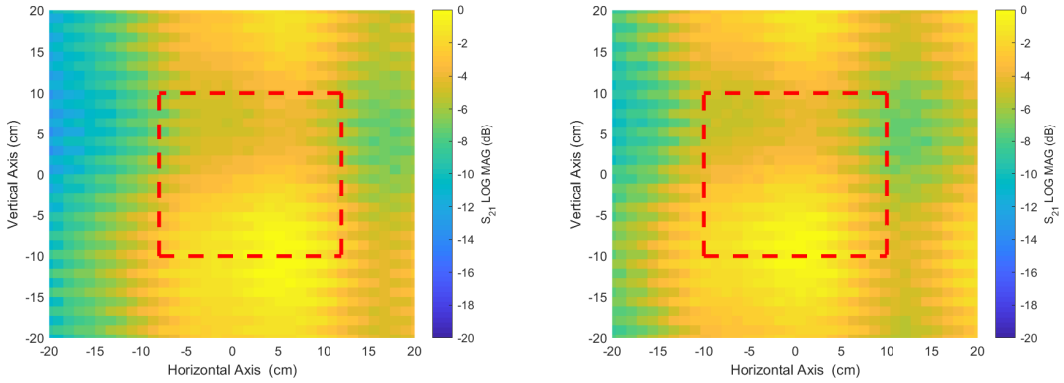

(a) Distribution of the signal in the measured plane J7.

(b) Distribution of the signal in the measured plane J10

Figure 24: Reflector 7 distribution of the power in the plane with the Uniform transmission mode

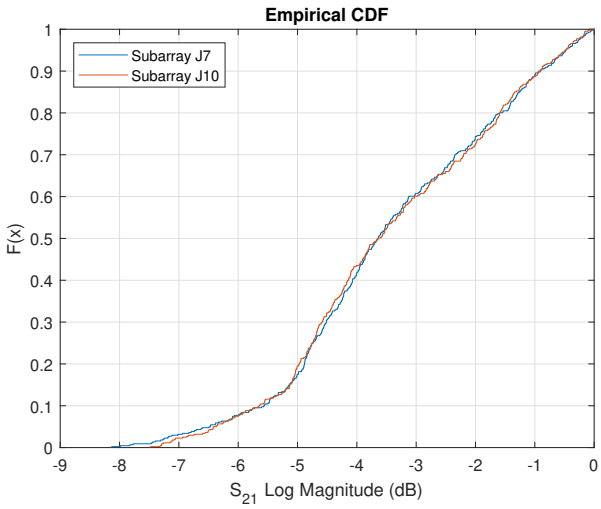

Figure 25: ECDF of the Test Zone from Reflector 7

Reflector Number 8

The normalized magnitude (in dB) from sub-arrays J7 and J10 does not follow a similar trend along the whole measured plane which is shown in Fig 26a. The blue corresponds to sub-array 7 and the orange lines to sub-array J10. The highest point of J7 was captured at sample point 436 and for J10 at sample point 471. The ECDF of the signals in Fig. 26b shows that the range of J7 is approximately 13.5 dB and 11.0 dB for J10. The two CDF's follow a relatively similar trend. The median power of J7 is approximately -5.4 dB and -4.9 dB for J10 measured across the whole plane. The standard deviation are 3.4 dB and 2.2 dB respectively. According to the statistics the signal from J10 presents smaller fluctuations compared to J7.

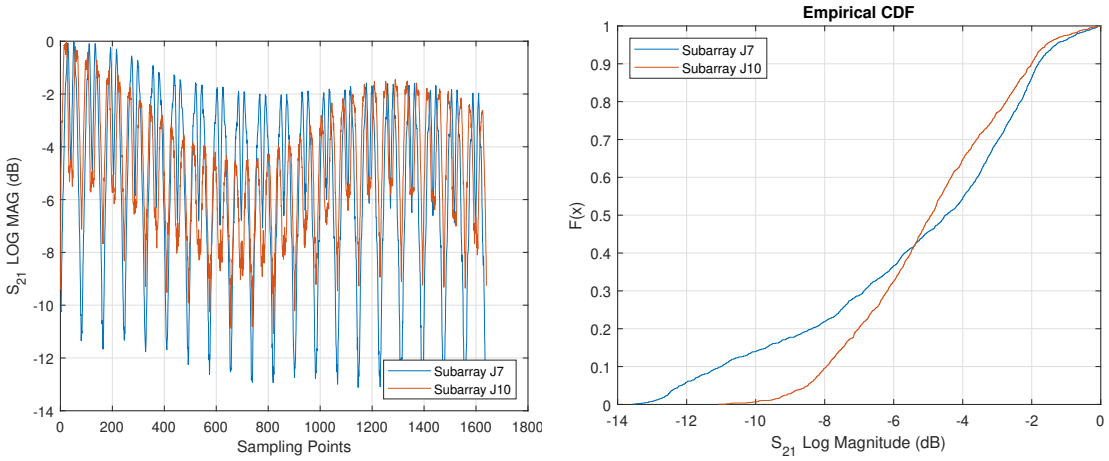

(a) Distribution of the signal in the measured plane.

(b) Distribution of the signal in the measured plane.

Figure 26: Reflector 8 distribution of the power in the plane with the Uniform transmission mode

The distribution of the signals over the scanning plane when illuminated from sub-array J7 is shown in Fig. 27a and from sub-array J10 is shown in Fig. 27b. It can be observed that J10 has a more stable received signal in both axes vertical and horizontal within the TZ area and across the whole area measured, which was also observed by a steeper CDF in Fig. 26b. For the case of J7 it is seen that the area where the signal has greater power and is more stable has shifted about 10 cm to the right, whereas J10 has not shifted thus the TZ are aligned at the centre of the 0 mark of the horizontal axis. It is possible to observe that around the centre of the TZ area the power dropped a 4 dB. Similar to the other reflectors there is a shape like a waist above the -2 cm mark in the vertical axis, where the power is reduced in both cases. The ECDF chart of both TZ areas illustrated in Fig. 28 shows that the magnitude (in dB) range within the TZ area differ around 2.5 dB, with J7 9.52 dB. Additionally, the median powers inside the TZ area for J7 and J10 was approximately -4.1 dB and -3.3 dB respectively. The standard deviations of were approximately 2.1 and 1.4 dB.

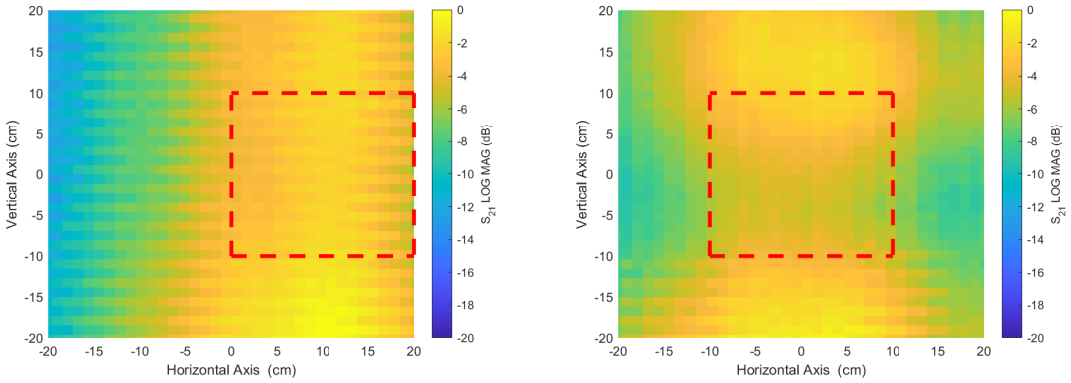

(a) Distribution of the signal in the measured plane J7.

(b) Distribution of the signal in the measured plane J10

Figure 27: Reflector 8 distribution of the power in the plane with the Uniform transmission mode

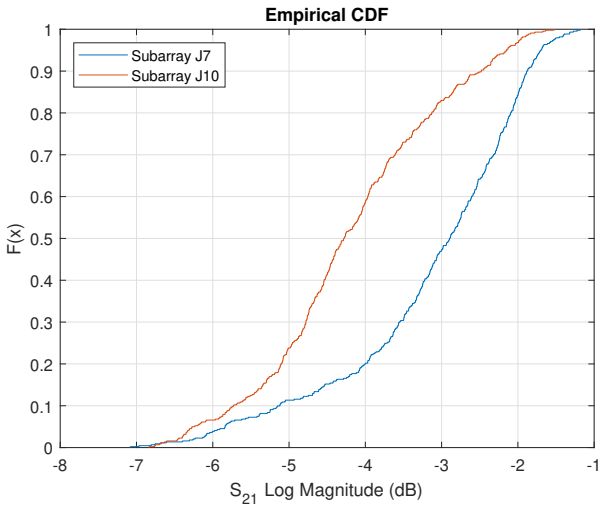

Figure 28: ECDF of the Test Zone from Reflector 8

Reflector Number 9

The normalized magnitude (in dB) from sub-arrays J7 and J10 follow a similar trend along the whole measured plane which is shown in Fig 29a. The blue corresponds to sub-array 7 and the orange lines to sub-array J10. The highest point of J7 was captured at sample point 52 and for J10 at sample point 23. The ECDF of the signals in Fig. 29b shows that the magnitude (in dB) range of J7 is approximately 11 dB and 13 dB for J10. The two ECDF's follow a relatively similar trend. The median power of J7 is approximately -3.9 dB and -4.9 dB for J10 measured across the whole plane. The standard deviation are 2.27 dB and 3.02 dB respectively. According to the statistics the signal from J7 presents smaller fluctuations compared to J10.

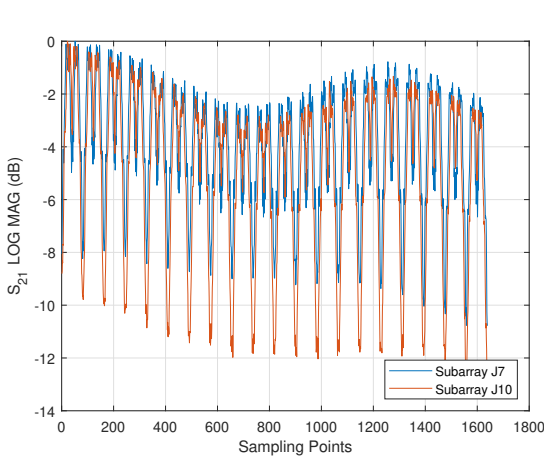

(a) Distribution of the signal in the measured plane.

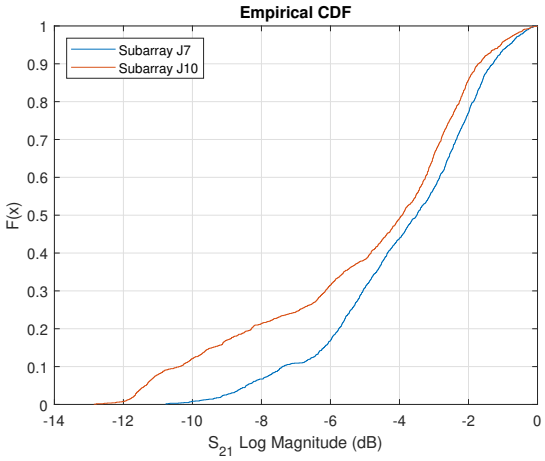

(b) Distribution of the signal in the measured plane.

Figure 29: Reflector 9 distribution of the power in the plane with the Uniform transmission mode

The distribution of the signals over the scanning plane when illuminated from sub-array J7 is shown in Fig. 30a and from sub-array J10 is shown in Fig. 30b. For the case of J7 it is seen that the area where the signal has greater power and is more stable has shifted about 5 cm to the right, and J10 shifted 10 cm to the left, thus the TZ are not perfectly aligned at the centre of the 0 mark of the horizontal axis. It is possible to observe that around the centre of the TZ area the power dropped 3 dB. Similar to the other reflectors there is a shape like a waist above the 0 cm mark in the vertical axis, where the power is reduced in both cases. The ECDF chart of both TZ areas illustrated in Fig. 31 shows that the magnitude (in dB) range within the TZ area differ only by 0.6 dB, J7 has the highest of approximately 6.6. Additionally, the median powers inside the TZ area for J7 and J10 was approximately -3.4 dB and -2.57 dB respectively. The standard deviations of were approximately 2.3 and 1.0 dB.

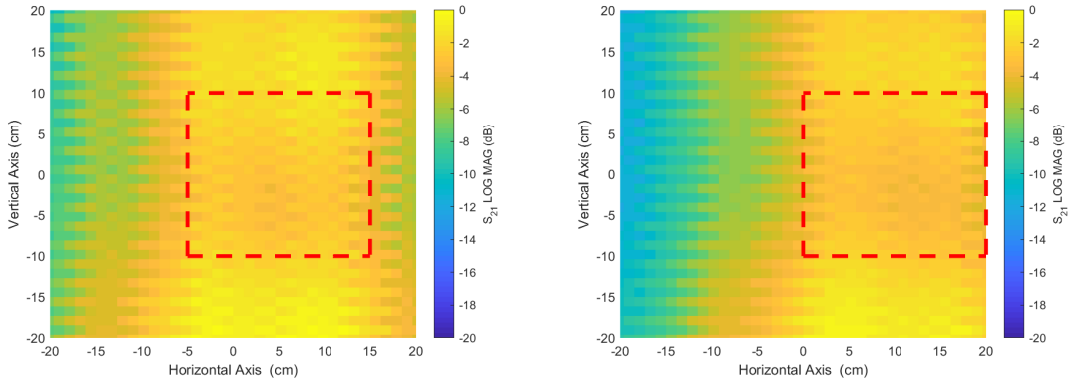

(a) Distribution of the signal in the measured plane J7.

(b) Distribution of the signal in the measured plane J10

Figure 30: Reflector 9 distribution of the power in the plane with the Uniform transmission mode

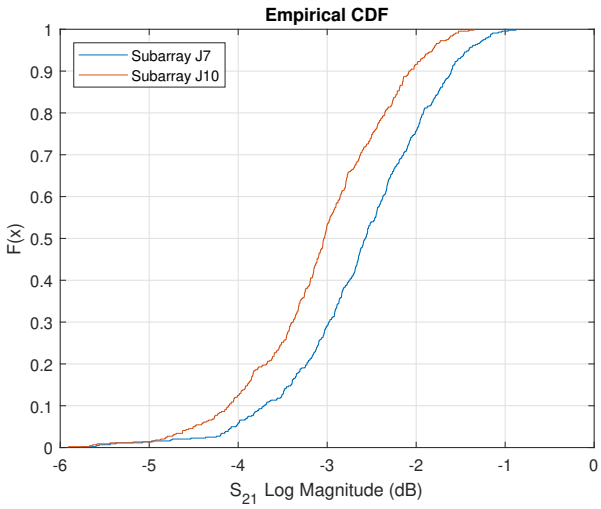

Figure 31: ECDF of the Test Zone from Reflector 9